

UNIVERSITY OF
BIRMINGHAM

College of Engineering and Physical Sciences

School of Chemical Engineering

PhD Thesis in Nanotechnology

M13 Bacteriophage: A Nanotool for the Fabrication of Novel Self-assembled Nanostructures

by

Paolo Passaretti

Supervisor
Dr Pola G Oppenheimer
School of Chemical Engineering

Co-Supervisor
Prof Tim R Dafforn
School of Bioscience

December 2019

UNIVERSITY OF
BIRMINGHAM

University of Birmingham Research Archive

e-theses repository

This unpublished thesis/dissertation is copyright of the author and/or third parties. The intellectual property rights of the author or third parties in respect of this work are as defined by The Copyright Designs and Patents Act 1988 or as modified by any successor legislation.

Any use made of information contained in this thesis/dissertation must be in accordance with that legislation and must be properly acknowledged. Further distribution or reproduction in any format is prohibited without the permission of the copyright holder.

To my Family,
Love and Friends

Acknowledgements

Writing this thesis would never have been possible without the contribution of the people who supported me along this challenging journey. Some of these were already part of my life, others I met along the way and here I want to take the opportunity to thank them all.

First of all, I would like to thank my supervisor, **Dr Pola Goldberg Oppenheimer**, for giving me the opportunity to continue my studies in her research group and to have supervised me throughout the entire project with great enthusiasm. Furthermore, I would like to thank my second supervisor **Prof Tim Dafforn** for his fundamental contribution to the study of the bacteriophage M13 and the realisation of the nanostructures on which I worked.

I would also like to thank the staff of the School of Chemical Engineering, which was always very kind and helpful, when I was performing my experiments and when I participated in the teaching laboratory demonstrations.

Thanks to all the members of the **ANMSA group** who have been with me over the years, for their support.

My experience as a PhD student gave me the chance to collaborate with many students and researchers involved in my projects as well as to contribute to the realisation of numerous other external projects.

Among the many Master's students that I have had the pleasure of supervising, I would like to thank those who have distinguished themselves for their outstanding work in the laboratory. In particular, **Kieran Chan** and **Rania Sebo**, who contributed to the *GraPhage13* project, **Connor James Linehan**, **Rachel Clayton**, **Joshua Murray**, **Cassidy Ooi**, **Max Ooi** who worked on GRX-N13 and finally **Xin Du** who participated to the SAS-M13 project.

I would like to continue by thanking **Prof Francesco Angelucci** and **Prof Rodolfo Ippoliti** for having hosted me again in L'Aquila in their laboratories, allowing me to produce the SmPRXI employed for the realisation of GRX-N13 and for always supporting my work. **Dr Matthew Tridgett** for inviting me to collaborate on one of his projects with M13 which was successfully published and for having always worked

constructively, also making time to share our opinions on music. **Maria Massoura** for being an excellent colleague and friend as well as for involving me in one of her projects that I hope will be published soon.

A special thanks to **Inam Khan** with whom a mutual collaboration was born during the last year. This has allowed us to work intensively side by side, completing multiple experiments. Therefore, I would like to thank him for his extreme kindness and availability, as well as for being a friend.

A huge thank you goes to **Dr Yiwei Sun** for having been a colleague and for being a great friend. We worked hard together realising that our different, but complementary background is extremely profitable. I am really grateful for the time spent together, for his precious critical thinking and for everything I learned from him. I hope we will have the chance to collaborate again in the future.

Furthermore, I would like to thank **Dr Daniel Escalera Lopez** for his kindness and willingness to help me with several concepts of electrochemistry. I would have loved to publish an article together and I hope that it can still happen in future.

I would also like to thank some of my friends who I had the pleasure of meeting here in the UK and others whom I have known since my childhood.

A special thanks to **Ivan** with whom I have collected many good memories so far. In particular, the fantastic evenings spent performing gigs in the pubs of Selly Oak together with **Josh**, **Jonathan** and **Sam**, as well as the pub crawls in town, dinners, barbecues and the board games nights together with **Zelu**, **Ninon**, **Oli**, **Tara** and many others. Thank you all for your friendship, support and for being an amazing part of my life in the UK.

Although at the moment we are separated by many miles and we meet only during the holidays, I want to thank all my friends spread across Italy. I would like you all to know that for me you are special because even though we see each other a couple of times a year, the little time spent together has the power of keeping our friendship alive and I am sure it will never dissolve. Thanks for being part of my life **Adolfo & Ilaria**, **Gianluca Nocera**, **Alessandro Picierno**, **Alessandro Croce**, **Antonio Loffredo**, **Francesco Calvanese**, **Enrico & Raffa** and all the **Munchkin group**.

Furthermore, I would like to thank **Nunzia** and **Donato** for their love and to have involved me in some of the most important steps of their life together. In particular, **Donato**, thank you for your true and special friendship, immutable despite the distance and the time passing.

Many thanks to all my family, especially my **dad**, my **mum** and my **sister** for their untiring love and encouragement. You have always believed in my dreams and supported my desire to pursue my studies both financially and morally. For this, I am immensely grateful.

Finally, the most important thanks to **Federica**. Without you, I do not know if I would have been able to make it. Thank you for taking care of me in the most difficult moments and for giving me the strength to carry on. Thank you for your love and for choosing me every day. You are extraordinary and I love you.

List of Publications

Peer-reviewed Journal Articles

Y. Sun, P. Passaretti I. Hernández, J. Gonzalez, W. Liu, F. Rodriguez, D. Dunstan, P. G. Oppenheimer and C. Humphreys. **Nanomechanics of Graphene Oxide-bacteriophage based Self-assembled Porous Composites.** Submitted.

P. Passaretti, Y. Sun, I. Khan, K. Chan, R. Sabo, H. White, T. R. Dafforn and P. G. Oppenheimer. **Multifunctional Graphene Oxide-Bacteriophage Based Porous Three-Dimensional Micro-Nanocomposites.** *Nanoscale* 11, (28): 13318-13329, (2019), DOI: 10.1039/c9nr03670a.

M. Tridgett, L. Lozano L., P. Passaretti, N. R. Desai, T. J. Proctor, H. A. Little, R. T. Logan, K. P. Arkill, P. G. Oppenheimer, and T. R. Dafforn. **Dye Aggregate-Mediated Self-Assembly of Bacteriophage Bioconjugates.** *Bioconjugate Chemistry* 29, (11): 3705–3714 (2018), DOI: 10.1021/acs.bioconjchem.8b00617.

Ardini M., G. Golia, P. Passaretti, A. Cimini, G. Pitari, F. Giansanti, L. D. Leandro, L. Ottaviano, F. Perrozzi, S. Santucci, V. Morandi, L. Ortolani, M. Christian, E. Treossi, V. Palermo, F. Angelucci and R. Ippoliti. **Supramolecular Self-Assembly of Graphene Oxide and Metal Nanoparticles into Stacked Multilayers by Means of a Multitasking Protein Ring.** *Nanoscale* 8, (12): 6739-53, (2016), DOI: 10.1039/c5nr08632a.

Posters

P. Passaretti, Y. Sun, I. Khan, K. Chan, R. Sabo, H. White, T. R. Dafforn and P. G. Oppenheimer. **Multifunctional Graphene Oxide-Bacteriophage Based Porous Three-Dimensional Micro-Nanocomposite** Size A1, ID: posPP03, DOI: 10.13140/RG.2.2.13760.28162. Presented at dstl Showcase 2019 Williams F1 Conference Centre, Grove, Wantage, UK.

P. Passaretti, Y. Sun, K. Chan, R. Sabo, T. R. Dafforn and P. G. Oppenheimer. **Self-Assembly of Graphene Oxide Sponges Using M13 Bacteriophage**' Size A3, ID: posPP02, DOI: 10.13140/RG.2.2.17115.72480. Presented at dstl Showcase 2018 John McIntyre Conference Centre, Edinburgh, UK.

P. Passaretti, R. Logan, F. Angelucci, R. Ippoliti, T. R. Dafforn and P. G. Oppenheimer. **Novel M13 Nanostructures as Metamaterials** Size A3, ID: posPP01, DOI: 10.13140/RG.2.2.24920.65288. Best PhD poster at EPS Research Conference 2016 at the University of Birmingham. This poster was also presented at Synthetic Biology UK 2016 Dynamic Earth, Edinburgh, UK and dstl Showcase 2017 University of Birmingham, Birmingham, UK.

Acknowledged Work

Luis J. Pérez-Córdoba; Ian T. Norton; Hannah K. Batchelor; Konstantinos Gkatzionis; Fotios Spyropoulos; Paulo J.A. Sobral. **Physico-chemical, antimicrobial and antioxidant properties of gelatin-chitosan based films loaded with nanoemulsions encapsulating active compounds.** *Food Hydrocolloids 79*: 544-559, (2018), DOI: 10.1016/j.foodhyd.2017.12.012. Acknowledged contribution for the support given in the AFM analysis.

Abstract

M13 is a filamentous bacteriophage that is constantly attracting the interest of several scientific communities. Since its discovery, it has been crucial in the progress of cloning vectors during the ’70s and later, in 1985, also for the development of ‘phage display’.

The latter introduced the use of genetically engineered bacteriophages for applications in many scientific fields, ranging from biology to chemistry and physical sciences, growing exponentially.

This thesis focuses on the application of M13 for the manufacturing of novel self-assembled nanostructures for the production of functional materials. For this purpose, M13 was also combined with additional building blocks including graphene oxide and proteins, producing novel composite materials.

In particular, the results obtained during this work show how to successfully assemble M13 and graphene oxide in a self-standing ultra-low-density porous material named *GraPhage13* and test its properties. Furthermore, other nano-architectures have been devised, for which the self-assembly process is based on non-covalent interactions or covalent bonds such as GRX-N13 and SAS-M13, respectively.

The fabricated structures can be potentially applied in the biomedical, environmental and energy fields, and in particular, used for the manufacture of batteries, supercapacitors, absorbers, biochemical sensors, optical and photonic devices.

Table of Contents

Table of Contents i

List of Figures vi

List of Tables ix

List of Equations and Reactions x

List of Abbreviations xi

CHAPTER I 1

1.1. Introduction to the Nanoworld 2

1.2. The Filamentous Bacteriophage M13 5

1.2.1. General Overview and History of M13 7

1.2.2. Genes and Proteins 10

1.2.2.1. *pI* – PI (PXI) 10

1.2.2.2. *pII* – PII (PX) 10

1.2.2.3. *pIII* – PIII 11

1.2.2.4. *pIV* – PIV 12

1.2.2.5. *pV* – PV 12

1.2.2.6. *pVI* – PVI 12

1.2.2.7. *pVII* – PVII 13

1.2.2.8. *pVIII* – PVIII 13

1.2.2.9. *pIX* – PIX 14

1.2.3. Infection Cycle 15

1.2.3.1. Adsorption 15

1.2.3.2. Insertion 15

1.2.3.3. Replication 17

1.2.3.4. Assembly 17

1.2.3.5. Extrusion 18

1.2.4. Propagation, Purification and Quantification 19

1.2.4.1. Propagation 19

1.2.4.2. Purification 20

1.2.4.3. Quantification 21

1.2.5. Modification and Applications 22

1.3. Graphenes and Carbon-based Materials 24

1.3.1. Graphenes 27

1.3.2. Production Methods 29
1.3.3. Graphene-Based Composite Materials 31
1.4. Peroxiredoxins 35
1.4.1. Recombinant PRXI of *Schistosoma mansoni* 36
1.5. Scope of the Thesis 38

CHAPTER II 42
2.1. Bacteria, Molecules and Compounds 43
2.2. Sample Preparation Methodologies 50
2.2.1. Bacterial Cultures and Purification Methods 50
2.2.2. Size Exclusion and Affinity Chromatography 52
2.2.3. Sonication 56
2.2.4. Substrate Preparation 57
2.2.5. Sputter Coating 59
2.2.6. Electrophoretic Deposition (EPD) 61
2.3. Characterisation Methodologies 65
2.3.1. Ultraviolet-Visible Spectroscopy (UV-Vis) 65
2.3.2. Fourier Transform Infrared Spectroscopy (FT-IR) 67
2.3.3. Raman Spectroscopy 69
2.3.4. Laser Diffractometry 71
2.3.4.1. ζ - potential 71
2.3.4.2. Particle Size Distribution 72
2.3.5. Scanning Electron Microscopy and Energy-dispersive X-ray Spectroscopy (SEM/EDX) 74
2.3.6. Atomic Force Microscopy (AFM) 75
2.3.7. Rheology 77
2.3.8. Brunauer, Emmett and Teller Method (BET) 80
2.3.9. Gel Electrophoresis 81
2.4. Additional Equipment Used 83
2.5. Software for the Data Analyses 83

CHAPTER III 85
3.1. Introduction 86
3.2. M13 Small Scale Production 87
3.2.1. Propagation in Batch Culture 87
3.2.2. Purification *via* PEG/NaCl Precipitation 88
3.2.3. UV-Vis Characterisation and Quantification 90
3.2.4. Morphological Characterisation 93
3.3. M13 Ionic Properties 95

3.3.1. Experimental Procedure 99
3.3.2. Results 101
3.4. M13 Stability in DIW and Buffers 102
3.4.1. Experimental Procedure 102
3.4.2. Results 102
3.5. Spectroscopic Characterisation 104
3.5.1. FT-IR Spectroscopy 104
3.5.2. Raman Spectroscopy 110
3.6. Summary and Outlook 114

CHAPTER IV 117
4.1. Introduction 118
4.2. GO Stock Preparation 119
4.2.1. UV-Vis Characterisation and Quantification 119
4.2.2. Morphological Characterisation 121
4.3. GO Stability in DIW 122
4.3.1. Experimental Procedure 123
4.3.2. Results 123
4.4. GO Stability in Buffers 125
4.4.1. Experimental Procedure 126
4.4.2. Results 126
4.5. Size Determination of GO Sheets 128
4.6. Spectroscopic Characterisation 130
4.6.1. FT-IR Spectroscopy 130
4.6.2. Raman Spectroscopy 132
4.7. Summary and Outlook 133

CHAPTER V 136
5.1. Introduction 137
5.2. Study of GPH in Water 140
5.2.1. Fundamental Experiments and Characterisation 140
5.3. Study of GPH in Buffer 145
5.3.1. pH Influence on the Hydrogel Self-Assembly 145
5.3.2. GO to M13 Reaction Ratio 148
5.3.3. The Rheology of GPH 152
5.4. GPA Characterisation 153
5.4.1. Morphological Characterisation 153
5.4.2. Calculations of the Volumetric Mass and the Surface Area 156
5.4.3. FT-IR Spectroscopy 160

5.4.4. Raman Spectroscopy 162
5.5. Summary and Outlook 165

CHAPTER VI 166
6.1. Introduction 167
6.2. Adjustable Porosity and Wettability of GPA 168
6.3. Gold Electrodeposition 171
6.3.1. Experimental Procedure 171
6.3.2. Results 172
6.3.3. Morphological and Compositional Characterisation 173
6.4. Functionalisation with Carbon Nanotubes 177
6.4.1. Experimental Procedure 178
6.4.2. Results 179
6.5. Summary and Outlook 180

CHAPTER VII 182
7.1. Introduction 183
7.1.1. GRX-N13 Nanostructured Surface 184
7.2. GO and M13 Preparation 186
7.3. SmPRXI Expression and Purification 187
7.3.1. Experimental Procedure 187
7.3.2. Results 188
7.4. M13 Modification 189
7.4.1. Experimental Procedure 190
7.4.2. Results 192
7.5. GRX-N13 Self-assembly 194
7.5.1. Experimental Procedure 194
7.5.2. Results 195
7.6. Summary and Outlook 196

CHAPTER VIII 198
8.1. Introduction 199
8.1.1. SAS-M13 Nanostructured Surface 199
8.2. M13 Preparation 200
8.3. SAS-M13 Self-assembly 201
8.4. SAS-M13 Characterisation 202
8.5. Summary and Outlook 205

CONCLUSIONS AND OUTLOOK 207

APPENDICES **213**

Appendix 1 M13 genome and proteins details **214**

Appendix 2 Protocol for the growth in batch of competent *E. coli* cells **226**

Appendix 3 Protocol for the propagation and purification of M13 through infection of *E. coli* and PEG/NaCl precipitation **227**

Appendix 4 Protocol for the propagation and purification of M13 through infection of *E. coli* and PEG/precipitation **229**

Appendix 5 GO-5' SEM/EDX **231**

Appendix 6 M13 SEM/EDX **232**

Appendix 7 *GraPhag13* SEM/EDX **233**

Appendix 8 Raman analysis - Tables **234**

Appendix 9 SmPRXI details **236**

Appendix 10 Protocol for the production and purification of SmPRXI **237**

Appendix 11 Amino acids classification table **241**

REFERENCES **242**

List of Figures

Figure 1.1. The filamentous bacteriophage M13 7

Figure 1.2. The infection cycle of M13 16

Figure 1.3. M13 components, potential modifications and application 23

Figure 1.4. Graphene, GO and rGO structures 27

Figure 1.5. PRXs oligomeric states 35

Figure 1.6. SmPRXI structure 37

Figure 2.1. Schematic representation of *E. coli* batch cultures 51

Figure 2.2. Schematic representation of SEC and AC 54

Figure 2.3. Schematic representation of the sonicator 57

Figure 2.4. Schematic representation of the snow jet and plasma cleaner 58

Figure 2.5. Schematic representation of the sputter coater 60

Figure 2.6. Schematic representation of PGSTAT and the electrolytic bath 63

Figure 2.7. Schematic representation of the spectrophotometer 66

Figure 2.8. Schematic representation of the FT-IR spectrometer 68

Figure 2.9. Schematic representation of the Raman spectrometer 70

Figure 2.10. Schematic representation of particle size analysers 72

Figure 2.11. Schematic representation of the SEM/EDX 75

Figure 2.12. Schematic representation of the AFM 77

Figure 2.13. Schematic representation of the rheometer 78

Figure 2.14. Schematic representation of the BET instrument 81

Figure 2.15. Schematic representation of the SDS-PAGE 82

Figure 3.1. M13 propagation and the purification procedure 88

Figure 3.2. UV-Vis characterisation and quantification of M13 91

Figure 3.3. AFM analysis of M13 and sample preparation 94

Figure 3.4. PVIII sequence and characteristics 97

Figure 3.5. ζ-potential and prediction of the charge distribution of M13 99

Figure 3.6. UV-Vis analysis for the stability of M13 in DIW and buffers 103

Figure 3.7. FT-IR analysis of PEG 106

Figure 3.8. FT-IR analysis of M13 contaminated by PEG 107

Figure 3.9. FT-IR analysis of M13 108

Figure 3.10. Comparison of FT-IR spectra 109

Figure 3.11. Raman analysis of PEG and M13 111

Figure 4.1. GO and its UV-Vis characterisation 119

Figure 4.2. GO and GO-5' calibration curves 120

Figure 4.3. AFM analysis of GO and sample preparation 122

Figure 4.4. GO stability and the effect of sonication 124

Figure 4.5. UV-Vis analysis for the stability of GO-5' in DIW and buffers 127

Figure 4.6. Particle-size distribution of GO 129

Figure 4.7. FT-IR analysis of GO-5' 131

Figure 4.8. Raman analysis of GO-5' 133

Figure 5.1. Schematic representation of the self-assembly mechanism 138

Figure 5.2. UV-Vis and AFM analysis of the individual components 140

Figure 5.3. UV-Vis analysis for the stability of the components 142

Figure 5.4. UV-Vis analysis of GO-M13 hydrogels 143

Figure 5.5. PVIII structure and ζ-potential 147

Figure 5.6. *GraPhage13* stability and alternative assembly conditions 149

Figure 5.7. UV-Vis analysis for the quantification of the reaction ratio 150

Figure 5.8. Rheological characterisation of *GraPhage13* hydrogel 153

Figure 5.9. SEM-EDX analysis of *GraPhage13* aerogel and its components 154

Figure 5.10. SEM images of *GraPhage13* at different magnifications 155

Figure 5.11. X-ray micro-CT analysis of *GraPhage13* aerogel 157

Figure 5.12. Pictures and image analysis of GPH and GPA 158

Figure 5.13. Comparison between the FT-IR spectra of GPA, GO and M13 161

Figure 5.14. Comparison between the Raman spectra of GPA, GO and M13 163

Figure 6.1. Different porosity of M13-based GPAs 168

Figure 6.2. Characterisation of GPA wettability 169

Figure 6.3. Gold electroplating CV and CA results 172

Figure 6.4. Optical microscope analyses of Au-GPA 174

Figure 6.5. SEM-EDX analysis of Au-GPA 176

Figure 6.6. SEM images of CNT-GPA at different magnifications 179

Figure 7.1. Schematic representation of GRX-N13 components and assembly 186

Figure 7.2. Purification, validation and quantification of SmPRXI 189

Figure 7.3. Chemical reaction to produce M13-NTA 191

Figure 7.4. SEC for the characterisation of M13-NTA 192

Figure 7.5. AFM analysis of M13-SmPRXI 193

Figure 7.6. AFM analysis of GRX-N13 196

Figure 8.1. Schematic representation of SAS-M13 assembly 200

Figure 8.2. AFM analysis of SAS-M13 and the intermediate samples 202

Figure 8.3. Raman analysis of SAS-M13 and the intermediate samples 204

Figure 8.4. Vis-NIR analysis of SAS-M13 and the intermediate samples 205

List of Tables

Table 1.1. M13 bacteriophage characteristics **6**

Table 1.2. Graphenes characteristics **28**

Table 3.1. M13 stocks production **93**

Table 3.2. PVIII protein pKa values **99**

Table 3.3. M13 stability in different buffer conditions **103**

Table 3.4. FT-IR peaks of PEG **106**

Table 3.5. FT-IR spectrum of M13 contaminated by PEG **107**

Table 3.6. FT-IR peaks of M13 ..... **108**

Table 3.7. Raman peaks of PEG **110**

Table 3.8. Raman peaks of M13 ..... **112**

Table 4.1. GO stability in DIW **125**

Table 4.2. GO stability in different buffer conditions **127**

Table 4.3. FT-IR peaks of GO-5' **131**

Table 5.1. GO, GO-5' and M13 stability in DIW **143**

Table 5.2. The pH values of GO, M13 and GPHs in DIW **146**

Table 5.3. The pH values of GO, M13 and GPHs in CB **148**

Table 5.4. GPHs stability in CB **151**

Table 5.5. Image analysis of GPH and GPA **158**

Table 5.6. BET surface area **159**

Table 5.7. Graphene-based sponges comparison **160**

Table 6.1. Contact angles of DIW on GPAs **170**

List of Equations and Reactions

Equation 2.1. Silicon dihydroxylation and hydroxylation (1) **59**

Equation 2.2. Silicon dihydroxylation and hydroxylation (2) **59**

Equation 2.3. General redox reaction for metals **62**

Equation 2.4. Hydrogen gas production in acid conditions **62**

Equation 2.5. Hydrogen gas production in basic conditions **62**

Equation 2.6. Beer-Lambert-Bouguer law **66**

Equation 2.7. Hook's law **75**

Equation 3.1. Phage concentration (virions mL^{-1}) **93**

Equation 3.2. Henderson-Hasselbalch equation **96**

Equation 3.3. M13 potential (B1) **100**

Equation 3.4. M13 potential (C1) **100**

Equation 3.5. M13 potential (B2) **101**

Equation 3.6. M13 potential (C2) **101**

Equation 3.7. M13 Precipitation (%) **104**

Equation 6.1. Gold sulfite reduction **171**

List of Abbreviations

°C	Celsius degrees
µg	Micrograms
µL	Microlitres
µm	Micrometre
0D	Zero-dimensional
1D	One-dimensional
2D	Two-dimensional
3D	Three-dimensional
A	Absorbance
Å	Ångström
aa	Amino acid
Abs	Absorbance
AFM	Atomic force microscope/microscopy
Am	Amide mode
AMP	Ampicillin
ANOVA	Analysis of variance
APTES	(3-Aminopropyl) triethoxysilane
AuNP	Gold nanoparticle
BMV	Brome mosaic virus
bp	Base pair
CAM	Chloramphenicol
CAS	Chemical abstracts service
CB	Citrate buffer
CCMV	Cowpea chlorotic mottle virus
CD	Circular dichroism
cm	Centimetre
CNT	Carbon nanotube
CP	Coat protein
CPMV	Cowpea mosaic virus
CVD	Chemical vapour deposition
Da	Dalton
DIW	Deionised water
DNA	Deoxyribonucleic acid
DO	Dissolved oxygen
EDX	Energy-dispersive X-ray
EGFP	Enhanced green fluorescent protein

EM	Electron microscope/microscopy
Ff	Filamentous phages
FF	Fully folded
FT-IR	Fourier-transform infrared
g	Times the gravitational force
g	Grams
GO	Graphene oxide
GPa	Gigapascal
GPA	*GraPhage13* aerogel
GPH	*GraPhage13* hydrogel
GPA$_{PC}$	GO and M13 in physical contact
h	Hours
HIV	Human immunodeficiency virus
HMW	High molecular weight
HPLC	High-performance liquid chromatography
HPV	Human papillomavirus
HSV	Herpes simplex virus
IEC	Ion exchange chromatography
IEP	Isoelectric point
IR	Infrared
J	Joule
K	Kelvin
k	Spring constant
kDa	Kilodalton
kHz	Kilohertz
L	Litres
LD	Linear dichroism
LMW	Low molecular weight
M	Molarity
mg	Milligrams
X-ray micro-CT	X-ray micro-computed tomography
min	Minute
mJ	Millijoule
mL	Millilitre
mm	Millimetre
MNP	Metal nanoparticle
mol	Moles
MPa	Megapascal

mRNA	Messenger RNA
MS	Mass spectrometry
MW	Molecular weight
N	Newton
n	Number on times
NB2	Nutrient broth No.2
nm	Nanometre
NMR	Nuclear magnetic resonance
OD	Optical density
Pa	Pascal
PBS	Phosphate-buffered saline
PEG	Polyethylene glycol
PFU	Plaque-forming unit
qPCR	Quantitative polymerase chain reaction
RCF	Relative centrifugal force
RF	Replicative form
rGO	Reduced graphene oxide
rpm	Revolutions per minute
s	Second
S	Svedberg
SD	Standard deviation
SEC	Size exclusion chromatography
SEM	Scanning electron microscope/microscopy
skl	Main chain skeleton
SLS	Static light scattering
ssDNA	Single-stranded DNA
SWNT	Single-walled carbon nanotubes
T	Temperature
TCN	Tetracycline
TEM	Transmission electron microscope/microscopy
TMV	Tobacco mosaic virus
TPa	Terapascal
tRNA	Transfer RNA
Trx	Thioredoxin
UV	Ultraviolet spectrum
V	Volts
Vis	Visible spectrum
VLP	Virus-like particle

W	Watts
WT	Wild type
XPS	X-ray photoelectron spectroscopy
ε	Molar attenuation coefficient
π	Bonding orbital
π*	Antibonding orbital
Ω	Ohms



UNIVERSITY OF
BIRMINGHAM

CHAPTER I

Biological and Carbon-based Components for Applications in Nanotechnology



Abstract

This chapter introduces essential concepts about synthetic biology and nanotechnology, providing an overview of the key components employed for the fabrication of the novel nanostructures described in the thesis. In particular, it describes the importance of nanotechnology and the impact of biological components. Moreover, the components such as M13, graphene oxide and SmPRXI are extensively described, in terms of structure, production methods and their employability in nanotechnology.

Paolo Passaretti

1.1. Introduction to the Nanoworld

The word 'Nano' derives from the Greek word *νάνος* (nànos) which means dwarf. In the scientific language and the International System of Units (SI), 'nano' is used as a prefix for units like meter, mole, second and others, to mean 1 billionth of the considered unit.

Nanoscience is defined as the study of the fundamental principles of molecules or structures that have dimensions between 1 and 100 nanometers. Everything that matches these characteristics is known as 'Nanostructures'.[1] At the same time, nanotechnology could be defined as the application of these nanostructures to design nanoscale devices.[1] However, these definitions are not sufficient to explain the wide world of nanoscale, and to better understand these concepts, it is important to know that nanoscale is a unique small scale. Nanostructures are the smallest architectures that are possible to assemble, given that only small molecules and free atoms are below the nanoscale. On the nanoscale, properties of materials like conductivity, hardness, or melting point change proportionally to the size of their nanocomponents.[1] A good definition of Nanoscience and Nanotechnology was written in 2001 by Mike Roco in the *National Science Foundation: Social implication of Nanoscience and Nanotechnology*:

"One nanometer (one billionth of a meter) is a magical point on the dimensional scale. Nanostructures are at the confluence of the smallest of human-made devices and the largest molecules of living things. Nanoscale science and engineering here refer to the fundamental understanding and resulting technological advances arising from the exploitation of new physical, chemical and biological properties of systems that are intermediate in size, between isolated atoms and molecules and bulk materials, where the transitional properties between the two limits can be controlled." Cit. Mike Roco[1]

There are numerous applications for nanomaterials spanning across every scientific field. Given the nanoscopic dimensions of their functional unit, nanomaterials are the perfect candidates for the realisation of advanced performing devices. For instance, nanomaterials are of interest in photonics, which is a scientific field that studies the transmission of photons and the energy from free electrons oscillation. In this field, the nanoscopic dimensions of these structures, are crucial for the studies involving the interaction with electromagnetic waves.[2]

There are several methods to manufacture these nanomaterials, such as nanolithography, which can guarantee high control and precision for the realisation of novel nanoarchitectures. However, the well-established methods, typically show limitations such as high costs of realisation, long production times and limited scalability. To overcome those limitations, scientists are treading alternative routes based on, for instance, synthetic biology. Such alternative methods focus on the use of biological components, such as viruses or virus-like particles (VLPs),[3] exploiting their natural assembly system and their extraordinary structural accuracy.[4–6]

Viruses are essentially comprised of a nucleic acid surrounded by a capsid, which consists of a variable number of one or more kinds of coat proteins (CPs). The possibility to modify their CPs with chemical groups, peptides, nucleic acids and more, opens a wide range of possibilities limited by one's imagination. Since their discovery, viruses have been broadly investigated in several scientific areas to better understand the biological role, their infection targets, the replication cycles and their structures. Viruses can be regrouped according to their natural host, such as for instance, animal cells (HIV, HPV, HSV and more), vegetable cells (CCMV, CPMV, BMV, TMV and more) and bacteria (M13, λ, T7 and more) as well as, by the genome type, as in the well-known Baltimore

classification.[7] Generally, viruses infect a specific host or a specific group of them to replicate themselves, taking advantage of the host replication system.

During the last two decades years, researchers exploited the self-assembly processes which lead the virus capsid formation, to produce high precision self-assembled 2D or 3D nanostructure through *bottom-up* approaches. Due to the achievements in this direction, many virus-based nanostructures and nanomaterials have been produced and characterised.[2,5,8–10]

The versatility of viruses has been revolutionising the biological, chemical and physical sciences, for a breadth of applications including, novel therapies,[11,12] drug delivery,[13] drug discovery,[14,15] bio-imaging,[16] biosensing,[17] electronics,[18,19] and the assembly of materials in general.[4,20]

Among many existing viruses, the filamentous bacteriophage M13 was chosen to play a key role in the realisation of the novel self-assembled nanostructures described in this thesis. This small virus played a pivotal role not only in biological sciences for the study of cloning vectors[21] and for the phage display,[22,23] but it also inspired and allowed to manufacture viral-based nanostructured materials.[5,24–26] Nowadays, M13 is employed in application ranging from the creation of electronic devices[18,27] such as batteries,[28] piezoelectric materials,[19] photovoltaic cells,[29] to scaffolds for tissue regeneration[30,31] and numerous sensing devices.[17,32–34] Therefore, it is essential and important to study and exploit viruses as potential building blocks to produce novel virus-based nano- macro-materials and miniaturised devices. This, in turn, will lay the groundwork for understanding and fabricating new materials with enhanced properties as well as advanced device technologies. Furthermore, in addition to M13 and viruses in general, nanotechnology has also yielded a broad spectrum of other materials and

biomolecules such as for instance graphene oxide (GO)[35,36] and the ring-like SmPRXI protein.[37–39] The following sections describe in detail these three components, employed and combined for the fabrication of the novel self-assembled nanostructures described in this thesis including *GraPhage13*, GRX-N13 and SAS-M13.

1.2. The Filamentous Bacteriophage M13

M13 is a small filamentous virus well known for its applications due to its extraordinary characteristics **(Table 1.1)**. It has revolutionised entire scientific fields such as virology, biological and environmental sciences, molecular biology, nanotechnology and material sciences. The studies on this bacteriophage had exponential growth over time, leading to the M13 to be considered more than a virus. Moreover, technological progress has always been strongly linked with the variety of applications in which M13 has been employed. For instance, the first designed nanostructures involving M13 are based on the employment of the phage display of specific peptides, which was a technique developed due to the discovery of restriction enzymes and the progress in manipulating the DNA sequences of organisms.

In this section, an overview of the history of M13 from its discovery to its applications is reported. Its genomic organization, protein structure and infection cycle is described in detail as well as methods of production, purification, quantification and storage. Furthermore, the employable approaches for its chemical and genetic modification will be discussed, alongside with some of the most successful and revolutionary applications, providing a clear view of the impact of M13 on the scientific communities.

Table 1.1. M13 bacteriophage characteristics

	Information	Ref.
Names	Heterotypic synonym: Escherichia virus M13, bacteriophage M13, coliphage M13, enterobacteria phage M13, M13 phage and phage M13.	
NCBI Taxonomy ID	1977402	
Lineage (Baltimore classification)	Domain: Acytota Group: Group II (ssDNA) Family: Inoviridae Genus: Inovirus	
Capsid	Non-enveloped Minor coat proteins PIII, PVI, PVII and PIX Major coat proteins PVIII	
Symmetry	Helical	
Structure	Filamentous, rod-shaped	40
Diameter	6.6 to 8 nm	40
Length	700 to 2000 nm	40
Inner diameter	2.0 nm	41
Molecular weight (MW)	16.8 ± 0.8 g mol^{-1}	42
DNA MW	2×10^6 g mol^{-1}	43
Isoelectric point (IEP)	4.1	35,43
Genome type	Circular ssDNA (+)	41
Genomic arrangement	Circular	41,44
Genome length	6407 bp	41
Genes	9 (11)	45
Genes order	IV – (I, VI) – III – VIII – VII – V – II with II and IV being contiguous on the circular map	46
Proteins	11	45
UV-Vis absorption peak	269 nm	47
Density (*p*CsCl)	1.29 g cm^{-3}	43
Molar extinction coefficient (ε)	3.84 ± 0.06 cm^2 mg^{-1}	47
Partial specific volume v_2	0.75 ± 0.03 ml g^{-1}	42
Rotational diffusion coefficient D_R^f at 20°C	21.4 ± 1.1 s^{-1}	42
Translational diffusion coefficient D_T^f at 20°C	$2.34 \pm 0.12 \times 10^{-8}$ cm^2 s^{-1}	42
Extrusion time	10 min	48
Simultaneous infecting phages per bacteria	~3	43
Optimal assembly temperature	32°C	49
Optimal growth temperature	28–37°C	50
Attachment range temperature	0–45°C	51
Inactivation temperature	80–85°C for 10 min	52,53
Multiplicity of infection (MOI)	0.05 pfu cfu^{-1}	54

1.2.1. General Overview and History of M13

M13 is a filamentous bacteriophage belonging to the genus *Inovirus*, together with other filamentous phages (Ff) such as f1 and *fd*. This phage is formed by a capsid that wraps around a single-stranded circular DNA molecule (ssDNA). The capsid is mainly formed by the major coat protein PVIII, and which covers the virus along its entire length. At both ends, there are four different minor coat proteins, such as PIII and PVI on one side, and PVII and PIX on the other **(Fig. 1.1)**. The M13 genome contains eleven genes coding for the five coat proteins previously mentioned and other genes coding for the proteins involved in its replication cycle. Its structural proteins as well as its genome, allow M13 to recognise the F-*pilus* of some *Escherichia coli* (*E. coli*) strains, infecting them and establishing a lysogenic replicative cycle.[8,43,55–57] A more detailed description of proteins, genome and replication cycle are provided in the following sections **(Chapter 1.2.2, 1.2.3)**.

M13 was first isolated by P. Hofschneider in 1963, who was able to understand that the filaments surrounding the bacteria that he was observing were filamentous viral particles rather than bacterial *pili*.[58]

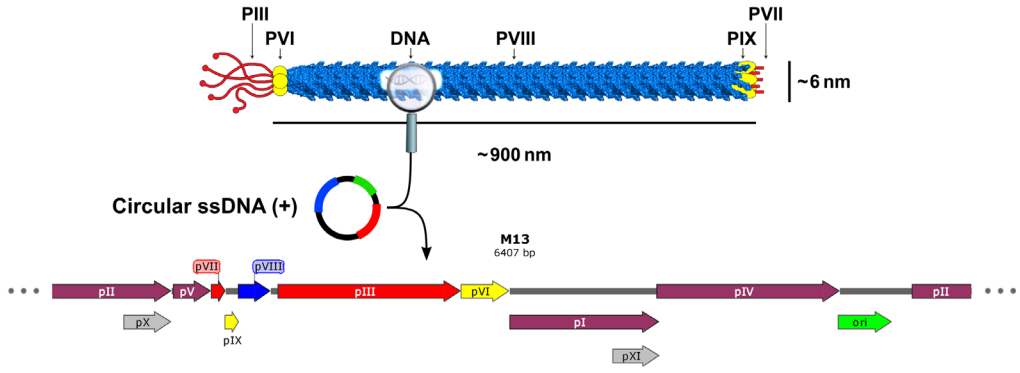


Figure 1.1. The filamentous bacteriophage M13

Schematic representation of the fully assembled M13 virion and the map of its genome linearised.

The first vitality studies carried out on *E. coli* bacterial cultures, coupled with CsCl gradient analyses of the extracted viral DNA, allowed to study the infection cycle of M13 for a long time.[43,55] Furthermore, UV-vis spectroscopy, X-ray diffraction and electron microscopy were employed to study the protein structure and morphology of M13.[43,55]

By the end of the '60s, breadth of information on M13 was established including, its molecular weight (MW), the DNA base composition and its genome type as well as the presence of different replicative forms of DNA during its infection cycle.[43,55] Furthermore, its infectivity and stability performance at different pH and temperature values were also characterised.[43,55]

During the '70s, the majority of studies related to M13 was focused on the infection cycle, genes and proteins. Moreover, the effects of the infection on the normal growth of *E. coli* were studied, including for instance, the loss of the *pilus* following the penetration of the phage DNA into the bacteria.[59] The studies related to the purification of M13,[60] revealed that there are different forms of M13 having different lengths.[61–63] Furthermore, Manning *et al.* described a bizarre behaviour of the phage in the presence of chloroform, which induces the contraction of M13 from its natural filamentous shape to a spheroidal (I-form).[64–66] Moreover, the advent of recombinant DNA techniques and the discovery of restriction endonucleases,[67] allowed M13 to become popular for the study of cloning vectors and DNA in general.

During the '80s, progress was made in the study of the protein structure of M13 and in particular, the study of PVIII, through nuclear magnetic resonance (NMR), Raman, electron spin resonance (ESR) and circular dichroism (CD). These led to a better understanding of the natural assembly process of M13, alongside with the development of study models for protein-protein and protein-membrane interactions.[68] At that time,

the progress in molecular biology produced a remarkable advancement in the characterisation of the M13 genome, allowing G. Smith in 1985 to develop the 'phage display'.[22] This technique consists of genetically engineered M13 modified with exogenous DNA, which can display foreign peptides/proteins fused with their PIII without compromise the virus ability to infect. The modified viruses were called 'fusion phages', and they demonstrated to be extremely versatile due to the variety of potentially displayable peptides and proteins on their native proteins.[23,69] This technique had such a great impact that G. Smith was awarded the Nobel Prize in Chemistry in 2018.

The applicability of phage display was further expanded by A. Belcher, who in 2000 demonstrated that it is possible to bind recombinant M13 phage libraries onto metal surfaces to produce nanostructured functional materials.[70] Due to this innovative approach, during the last 20 years, M13 have been employed as a building block for the fabrication of structured materials and devices, further increasing the interest of many scientific communities.[4,71–75] These *bottom-up* methodologies, used for the manufacturing of nanostructured materials, are usually based on self-assembly strategies. These are not only based on the display of peptides or proteins but also, these strategies involve the chemical groups naturally present on the viral capsid as well as the chemical modification of the phages.[10,76]

Nowadays, due to the inspiring work of A. Belcher and many other researchers, M13 is a very popular bio-nanotool employed in nanotechnology and material sciences to produce batteries,[27] supercapacitors,[19] piezoelectric,[19] sensors and nano-scaffolds[17,32,33,77] as well as detection systems,[78–80] imaging probes,[81] drug/gene delivery systems[12,13,74,82,83] and much more.

1.2.2. Genes and Proteins

The M13 bacteriophage consists of a positive single-stranded DNA genome (ssDNA+) with a length of 6407 bp including nine genes encoding for eleven different proteins.[41] Five of these, are structural (or coat) proteins and the remaining six, are involved in phage replication and assembly.[47]

The following subsections provide general information about each protein (indicated with capital letters), their encoding genes (indicated with italic lowercase letters), and their biological roles. More detailed specific characteristics about their peptide and corresponding nucleotide sequences as well as MW, isoelectric point (IEP) and molar extinction coefficient (ε), can be found in **Appx. 1**.

1.2.2.1. *pI* – PI (PXI)

The 1047 bp long *pI* encodes for the structural assembly proteins PI and a truncated translocation product named PXI,[45] composed of 348 and 108 aa respectively. PI and PXI play an essential role in phage assembly. Together with PIV, they form adhesion zones between the inner and outer membranes of *E. coli*, a complex through which the newly synthesised phage particles can be extruded.[41]

1.2.2.2. *pII* – PII (PX)

Proteins PII and PX are encoded by the 1233 bp long gene *pII*.[45] The 410 aa long protein PII is an endonuclease playing an essential role in the 'rolling circle' DNA replication mechanism.[45] Essentially, it nicks the replicative form (RF) and covalently binds the 5'–P, allowing the replication to initiate at the 3'–OH of the cleavage site. After one round

of rolling circle synthesis, PII is linked to the newly synthesised ssDNA and ligates the ends to generate a circular ssDNA ready to be packed.[41] PX is made of 111 aa and it is involved during the replicative phase. It binds to the viral double-stranded DNA (dsDNA), preventing hydrolysis by nucleases, including PII. Additionally, PX is an inhibitor of the DNA replication and it may have a role in the transition from RF to ssDNA, favouring the accumulation of the latter.[41]

1.2.2.3. *pIII* – PIII

The minor coat protein PIII is composed of 406 aa and is encoded by the 1272 bp long gene *pIII*. It is composed of three domains: N1, N2 and C, separated by glycine-rich areas. The two N-terminal regions regulate the infectious process, whereas the C-terminus maintains the stability of M13.[75] PIII is synthesised as a precursor and then processed into its mature form, after membrane insertion with the C-terminus reaching into the cytoplasm. PIII function is crucial in the penetration of the viral genome into the host cells *via* interaction with the F-*pilus* in the extrusion process. During the first phase of infection, PIII not only mediates adsorption the tip of the *pilus*, but its N1 domain, also interacts with the host entry receptor TolA, inducing penetration of the viral DNA into the host cytoplasm. During the extrusion process, PIII mediates the final phase of the phage particle extrusion.[41] Moreover, PIII is one of the most employed protein for display systems, given the presence of two insertion sites for exogenous polypeptides and proteins.[75] Those can be fused between PIII signal peptide and N1, or directly to the C-terminus. There is no limit to the size of the peptides or protein that can be displayed by PIII, however, there are only between three and five copies of this protein in each phage, which results in a relatively low number of proteins and polypeptides displayed.[75]

1.2.2.4. *pIV* – PIV

The phage protein PIV is composed of 426 aa and it is encoded by the 1278 bp long gene *pIV*. Fourteen monomers of PIV create secretin with an inner diameter of 80 Å. This is a channel, across the host cell outer membrane, through which, during the extrusion phase of the M13 life cycle, the newly synthesised phage particles are released.[41]

1.2.2.5. *pV* – PV

The 87 aa long protein PV is encoded by gene *pV* of 261 bp. It is a homodimer, in which each monomer is composed of eight β-strands. The midportion of the protein is arranged as a five-stranded anti-parallel β-sheet. From this core two β-hairpins, jointed by a connecting loop, protrude. The β-hairpins give to the molecule a crab-like appearance, in which the claws are the DNA-binding loops.[84] This protein not only determines the decrease of the synthesis of the replicative form, during the M13 infectious process,[85] it also binds to the positive strand of the ssDNA before the assembly phase.[41] The binding to ssDNA is highly cooperative, without pronounced sequence specificity and driven by electrostatic interactions between the positively charged DNA binding loops and the negatively charged DNA backbone.[86–90] During the synthesis of the new viral ssDNA, PV prevents its conversion into RF. PV is displaced by the capsid protein PV during phage assembly on the inner bacterial membrane.[41]

1.2.2.6. *pVI* – PVI

The minor coat protein PVI is comprised of 112 aa, encoded by 339 bp long gene *pVI*. It is located in the termination end of M13 with PIII. The formation of a PIII-PVI complex

is crucial to the correct termination of the assembly.[41] Before the phage assembly, protein PVI is stored within the inner membrane of the host bacteria. Its C-terminus region protrudes on the phage surface, making PVI an employable site for the insertion of exogenous proteins. Moreover, PVI has no signal peptide, thereby it does not affect the normal folding of proteins, which makes it more suitable to be a protein display system for cDNA libraries.[75]

1.2.2.7. *pVII* – PVII

PVII is a 33 aa long hydrophobic inner membrane protein, encoded by the 102 bp long gene *pVII*. PVII and PIX are both present at the first end, of the newly synthesised phage, to be released from the host cell.[41] PVII C-terminal residues, together with PIX, are involved in interactions with the packaging signal, that initiates the assembly process at the host cell inner membrane. In addition to its physiologic function, PVII was also proven to be suitable for display systems.[75,91]

1.2.2.8. *pVIII* – PVIII

The gene for the M13 procoat protein PVIII is a 222 bp long gene that encodes for a 73 aa long peptide, comprised of a leader peptide of 23 aa and the mature coat protein of 50 aa.[92] The PVIII, also known as major coat protein, can enter the host cell membrane *via* two different mechanisms. It can be deposited into the membrane during the insertion phase of the infection or it can be inserted into the plasma membrane as a newly synthesised protein, by the host machinery.[93]

Although the insertion of the newly synthesised major coat protein into the *E.coli* membrane is Sec translocase independent, it is mediated by the insertase YidC, which co-operates with the Sec translocase of the host.[94,95] Once inserted, the hydrophobic major coat protein is located into the plasma membrane of *E.coli*, with its negatively charged N-terminus into the periplasm and the hydrophilic, positively charged C-terminus protruding into the cytoplasm.[96–98]

At last, the leader peptide is removed to obtain the mature major coat protein PVIII. The latter has a continuous α-helix structure, with 10–13 aa in its positively charged C-terminus, interacting with the DNA, 19 mutually interacting aa, creating the intermediate region and 20 aa at the N-terminus exposed outside the virion.[75] About 2700 copies of PVIII subunits self-assemble in a helical arrangement around the viral genomic DNA. The capsid displays a filamentous structure with a length of 760–1950 nm and a width of 6–8 nm.[41] Due to the large number of copies, PVIII is employed for the display of multiple polypeptides. However, the N-terminus cannot fuse extremely long peptides, since it would cause the loss of infectivity due to steric hindrance.[91,99,100]

1.2.2.9. *pIX* – PIX

PIX is a hydrophobic protein consisting of 32 aa and encoded by the *pIX* gene of 99 bp.[75] As mentioned before, PIX and PVII colocalise at the end of M13 that is first released from the host *E. coli*, upon assembly.[41] PIX plays a very important role during the assembly. It interacts with the DNA packaging signal and assembly sites of other proteins.[75] This relatively small protein produces reduced steric hindrance, resulting in an employable site for display systems, that do not affect infectivity.[75,91]

1.2.3. Infection Cycle

M13 is a filamentous male-specific phage[40,58,101] that specifically infects gram-negative, F-episome carrying bacteria,[102] such as *E. coli*.[103] Upon active infection, M13 does not kill the host cells, rather it keeps producing and releasing phage particles, allowing the host to grow and divide. This infective cycle is defined as lysogenic and it is composed of five stages: adsorption, insertion, replication, assembly and extrusion.[45,103–106]

1.2.3.1. Adsorption

Essential to the start of the M13 infectious process is the absorption of the phage to the tip of the F-*pilus* of the host *E. coli*.[58,107–109] There are only a few of these *pili* per bacterium[107,108] corresponding to the adsorption sites,[51,110] which can be used only once **(Fig. 1.2e)**.[110,111] The *pilus* takes shape from a region where the cell wall and membrane adhere[43]. It is an elongated helical array of protein that retracts upon interaction with the N2 domain of the M13 protein PIII.[112] This allows M13 to get closer to the host and consequently, the N1 domain of PIII to bind to the host-encoded outer membrane protein TolA, belonging to the TolQRA complex.[113,114]

1.2.3.2. Insertion

During the insertion, the PVIII is removed from the phage surface and undergoes deposition into the inner membrane of the host. A precursor of the major coat protein (procoat protein), containing an extra amino acid leader sequence, is also synthesised and stored into the inner membrane, through the activity of YidC.[95,104] The hydrophobic PVI, that normally contributes to stabilising the phage particle acting as a sealing agent, is lost

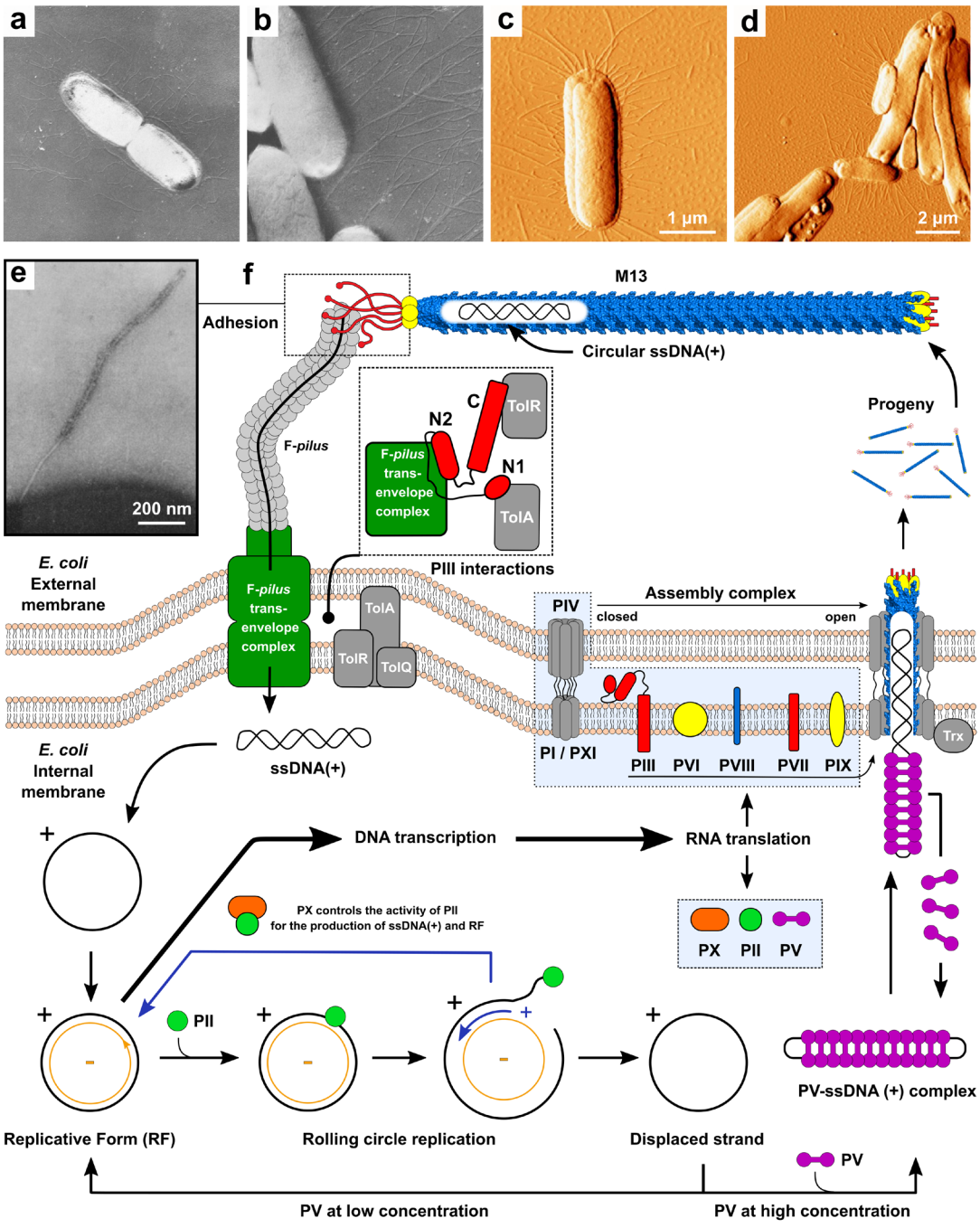


Figure 1.2. The infection cycle of M13

(a, b) M13 infecting *E. coli* cells imaged at 20 000× and 26 000× with the electron microscope (EM, no scalebar)[101] and **(c, d)** with the atomic force microscope (AFM).[48] **(e)** An individual bacteriophage connected to the F-*pilus* during the adsorption phase.[43] **(f)** Schematic representation of the infection cycle of M13.

resulting in a destabilised nucleoprotein particle. The circular ssDNA of M13 is then inserted into the host cell by a yet unclarified mechanism.[55,102,115] It is released into the cytoplasm, where new DNA and proteins are synthesised by the host cell machinery.[45,55]

1.2.3.3. Replication

Using the ssDNA(+) as a template, the RNA polymerase and DNA polymerase III of *E. coli* synthesise the complementary ssDNA(-) of the M13 genome, yielding a double-stranded circle,[45,116,117] known as the replicative form (RF).[118] RF accumulates to levels that are sufficient to sustain infection and M13 proteins production, without completely threatening *E. coli* growth. This parental RF is then used as a template for M13 DNA replication by a rolling-circle mechanism, involving the phage replication protein PII. The latter binds to a stem-loop structure in the RF and cleaves the (+) strand at 5'–P leaving a free 3'–OH for the host DNA polymerase III to start synthesising a new (+) strand.[119–121] The old (+) strand is then displaced, cut and ligated in a circle by PII itself.[119] During the early stages of replication, the production of RFs is favoured, to promote the accumulation of viral proteins. During later phases, as the concentration of phage proteins, especially PV, increases the rate of synthesis of RF DNA diminishes.[85,122]

1.2.3.4. Assembly

Before the assembly, all structural proteins, including the major coat protein and the newly synthesised procoat protein, are embedded into the inner membrane of the host cell, with their N-termini in the periplasm and their C-termini in the cytoplasm.[69] During assembly, the two α-helices composing PVIII rotate relative to one another to form a

continuous, α-helix within the new virus.[123–125] The packaging signal initiates the assembly when upon recognition by PVII and PIX, it interacts with the assembly complex. The latter is comprised of the ATPase/channel proteins PI and PXI, both located at the inner membrane[126,127] and the outer membrane channel PIV. These together form adhesion zones between the outer and inner membranes of *E. coli*,[128] that work as extrusion channels.[85,128] Furthermore, the phage assembly requires thioredoxin (Trx) association with the above-mentioned complex to progress successfully.[129]

1.2.3.5. Extrusion

Eventually, the extrusion phase begins. It is an energy-consuming event, during which PV is stripped off the DNA and about 2700 copies per phage of the major coat protein PVIII are assembled around the extruding DNA.[130] Finally, when the DNA is completely covered with PVIII, the minor coat proteins PIII and PVI are added to the virion and the assembled phage is released and ready to infect a new host.[114]

The M13 dynamics of infection has long been studied nevertheless, some of the mechanisms involved in this are still not completely understood or clarified. The review articles written by Rakonjac *et al.* and Loh *et al.* provide important information and reference for the study of the replication of the bacteriophage M13.[45,106]

1.2.4. Propagation, Purification and Quantification

1.2.4.1. Propagation

M13 causes lysogenic infections in *E. coli* strains showing the F-*pilus* and the viral genome consists of a circular ssDNA(+). Given the increasing interest in diverse applications of M13 for research and industrial practice, new approaches have been tested to improve the phage production on a large scale.[131] Although M13 production could be pursued through *in vitro* packaging, as frequently done for VLPs,[68,132–135] the preferred choice is often the exploitation of its natural capability of infecting bacteria and propagate within them **(Chapter 3.2.1)**. Therefore, many researchers tried to find the optimal conditions for bacterial growth when infected by M13. There are many parameters linked to bacterial growth such as, the growth medium, agitation, temperature (T), pH and dissolved oxygen (DO),[136,137] which have been extensively studied in the last few years. Although many propagation approaches have been attempted so far, the production in flasks seems to be the most convenient for laboratory research purposes.[50,54,138–140] However, the balance between the optimal conditions for bacterial growth, the translocation pathway for functional protein maturation and the phage particle assembly as well as the control of limiting factor, is crucial. These conditions can vary depending on the propagation purpose, which can be the production of ssDNA, a specific M13 protein or produce fully assembled and functional bacteriophages.

1.2.4.2. Purification

The M13 propagation methods are linked to the final product to be obtained (whole virion, its DNA or proteins) and consequently, there are different purification techniques specific for each desired component.[60]

During the initial studies of M13, the phage was successfully purified using polyethylene glycol (PEG), which allows its precipitation *via* centrifugation. This method is based on the 'salting out' mechanism of PEG and NaCl.[141] This precipitation process requires a considerably high amount of PEG (20%) and NaCl (2.5 M), some of which remains as a residue in the purified phage pellet.[142] McClendon in 1954,[143] was probably the pioneer in using PEG for precipitating fractions in heterogeneous mixtures[60] and Hebert in 1963 was the first who attempted to precipitate viruses with PEG and NaC1.[60] However, to meet specific needs, other purification techniques have been used such as, gel electrophoresis,[144,145] desalting spin column,[142] ion exchange (IEC)[146–148] and size-exclusion chromatography (SEC)[148,149] as well as high-performance liquid chromatography (HPLC) equipped with a methacrylate monolith column.[150] Moreover, Tang *et al.* described how divalent metal ions such as, Mg^{2+} or Ca^{2+} induce lateral aggregation of M13 at concentration > 100 mM, which is the optimal attractive interaction energy between phages.[151]

Although the techniques listed above show several advantages related to the specific contexts in which they were used, PEG purification seems to be the most convenient approach currently used by many researchers **(Chapter 3.2.2)**.[152] However, purification with PEG has the disadvantage of producing phage stocks with traces of PEG, which could hinder certain applications. To overcome this limitation, PEG purification can be accompanied by isoelectric precipitation.[60,153–155] The later can be carried out by bringing

the pH of the solution containing M13 to values close to the IEP of the analyte. This produces the neutralization of the charges exposed on the surface of the phages, which subsequently precipitate with a process called flocculation.

Regarding the purification of M13 DNA, there are several techniques such as glass fibre filter purification,[156] detergent extraction[157,158] and magnetic bead purifications.[159–162] However, all of these produce low yields.[53] Other methods developed over the time include zinc chloride precipitation,[163] for small scale preparations and the use of polyamines and cobalt hexamine.[164] However, the traditional approach is to precipitate the virus with PEG and subsequently extract the DNA with phenol. A further, high-performance technique, known for the purification of M13 DNA, is based on the method of Mardis and Roe,[158] which employs multichannel pipettes, bypassing both phenolic extraction and ethanol precipitation.[53]

1.2.4.3. Quantification

The quantification of M13 can be performed and expressed by different standardized methods used for viruses in general. These include titration, plaque-forming unit counts (PFU), DNA quantification by qPCR and UV-Vis spectrophotometry. The latter is also the most popular and direct method to quantify M13, *via* measuring its absorbance at 269 nm. Therefore, using the Lambert-Beer-Bouguer law **(Eq. 2.6)** and the molar extinction coefficient of M13 (ε = 3.84 ± 0.06 cm^2 mg^{-1}),[47] the absorbance can be converted into concentration.[165] More information can be found in **Chapter 3.2.3**.

1.2.5. Modification and Applications

M13 is essentially composed of proteins and DNA. During the last 50 years, its components as well as the entire virion, have been employed for several applications **(Fig. 1.3)**. The protein PVIII has been widely investigated structural biology as well as employed as a model in protein-protein and membrane bilayers interaction studies. M13 DNA was crucial in the development of cloning vectors, in testing sequencing techniques, in the study of the M13 replication cycle, and more recently in origami DNA, for the realisation of nano self-assembled architectures.[166]

Phage display played a crucial role in the development of novel phage modification approaches. This method is based on the genetic modification of M13 to show peptides, proteins, enzymes or antibodies fused on the native proteins of the phage without altering its natural infectious and assembly capacity **(Fig. 1.3)**. Subsequently, this concept was further extended by the studies of its potential interactions and by the development of alternative methods for its chemical modification, allowing M13 to be employed in numerous applications.

The minor and major coat proteins of M13 show a variety of chemical groups exposed on the external surface of the virus, available to react with other molecules. Furthermore, these exposed amino acids allow M13 to be negatively charged, at pH values ranging from 5 to 10.[35] Chemical modifications are strongly dependent on the groups available on the external surface of M13.[10,76,167] Small molecules and cross-linking agents are widely used to chemically functionalise the phage with chelating groups, nanoparticles, DNA and specific chemical groups. On the other hand, the phage display, which refers

exclusively to genetic modifications, is the preferred approach for the production of bacteriophages modified with fusion peptides and proteins on their surface **(Fig. 1.3)**.

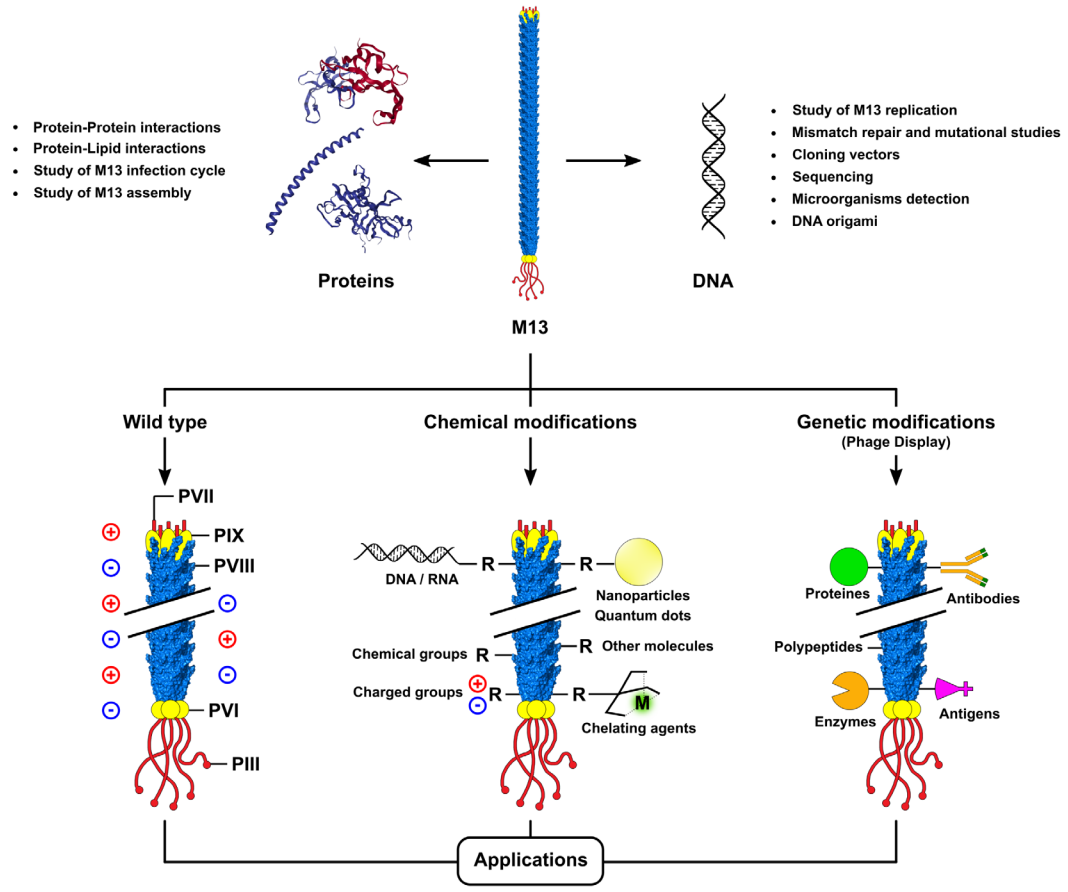


Figure 1.3. M13 components, potential modifications and application

M13 is comprised of a variable number of copies of five different coat proteins and a molecule of circular ssDNA. Its proteins and ssDNA can be used for different purposes as well as the entire virion can be functionalised *ad hoc* and employed in a variety of applications.

However, this does not exclude the possibility to chemically bind biomolecules to M13. Therefore, chemical and genetic modifications are two essential routes to modify M13 with small reactive groups as well as replace individual amino acids, providing the virus with different properties.

The extreme versatility of M13 and its predisposition to being modified and functionalised is therefore clearly evident. This makes it an extremely appealing nanotool for numerous applications in the biological, chemical and physical sciences for the development of novel nanotechnologies.

1.3. Graphenes and Carbon-based Materials

Graphene is defined as a single layer of sp^2-hybridized carbon atoms and it continuously triggers the interest of the scientific communities since its first characterisation in 2004.[168] It is a two-dimensional allotrope (2D) of carbon, characterised by a honeycomb network π-conjugated, which shows a variety of physical and chemical properties.[169]

Its intrinsic properties are also appreciated for the ability to effectively work and exhibit unique performance once combined with other nanomaterials. This is currently leading to the production of novel functional nanostructures and nanocomposites with advanced performances for many applications across several scientific fields.[36,170–175]

Graphene shows unique properties including, a half-integer quantum Hall effect for both electrons and holes, even at room temperature,[176–180] extraordinary high carrier mobility, and single-molecule detection.[181] Graphene also exhibits other remarkable electronic, mechanical and optical characteristics. These include ambipolar field-effect,[182] outstanding mechanical strength,[183] large specific surface area,[184] high-transparency[185,186] and excellent conductivity, both electric and thermal.[187]

Due to its extraordinary and superior properties, graphene has already shown its potential in a broad range of applications such as the manufacturing of capacitors, fuel cells,

batteries, sensors, transparent conductive films, high-frequency circuits, absorbers and flexible electronics.[185,188–192]

Despite its great potential for many applications, it is generally difficult to scale-up the properties of individual graphene nanosheets to macroscopic materials and considering that graphene shows zero band gap as well as inertness to many chemical reactions, it is less competitive for the fabrication of semiconductors and sensors. Due to these reasons, there is a considerable increase in the number of research studies aimed at the functionalisation of graphene and its derivates.[193]

Graphenes such as graphene, graphene oxide (GO) and reduced graphene oxide (rGO), can be functionalised *via* covalent bonds, which include for instance the addition of free radicals, dienophiles, chromophores and polymers as well as non-covalent bondings such as π-π, cation-π, anion-π, nonpolar gas-π and H-π interactions.[180]

Among the wide range of functionalisation, the biofunctionalisation of graphenes with nucleic acids, peptides, proteins and enzymes, for the production of graphene-based nanostructures, is particularly interesting and is leading to novel fields in biotechnology.[194] Graphenes are promising components in the development of fluorescent biosensors, due to their quenching capability toward various organic dyes and quantum dots[195–197] as well as fast DNA sequencing,[198] scaffolds for tissue regeneration[199] and other.[36,170–175]

Several studies showed that the biofunctionalisation of graphenes through weak intermolecular forces is an interesting alternative for the fabrication of graphene-based composite materials.[199] In particular, the biofunctionalisation is useful to design and produce composites with a *bottom-up* approach combining the components through self-

assembly strategies. Bio-components guarantee high-specificity of binding as well as the possibility to work at standard conditions of temperature, pressure and pH. Among the numerous advantages given by the bio-components and the biofunctionalisation, it is also important to remember the reduction of cost, scalability and environmental sustainability, without affecting the performances and quality of materials.[180,200]

Due to the presence of chemical groups containing oxygen and consequently, the superior dispersibility in water buffers, GO is considered a better candidate for biofunctionalisation compared to other more hydrophobic graphenes. In particular, the relatively lower toxicity,[188,199] makes GO a better choice for biomedical applications. Moreover, the possibility to treat GO with reducing agents to remove most of the oxygen groups producing rGO is also considered a good alternative to easily work in water buffers with GO and partially restore some of the properties shown by pure graphene (pristine graphene).[174]

Nevertheless, the biofunctionalisation is still a considerable challenge for the fabrication and employability of novel functional material and components. This is due to limitations related to the complexity of certain assembly strategies and durability of bio-components in the presence of incompatible agents or extreme conditions of temperature, pressure and pH. Therefore, it is crucial to pursue research in this direction. The finding of alternative bio-components for the functionalisation of graphenes as well as novel self-assembly strategies will produce a new generation of materials and devices with enhanced performances, quality and sustainability.

1.3.1. Graphenes

Individual graphene nanosheets were isolated for the first time by simply peeling a piece of graphite with scotch tape through a process called mechanical exfoliation, by Andre Geim and Konstantin Novoselov at the University of Manchester. Due to this extraordinary study published in 2004,[168] they were awarded the Nobel Prize in Physics in 2010. The resulting graphite monolayer, known as graphene **(Fig. 1.4a)**, is now considered the thinnest stable material known to exist so far and it completely revolutionised research across all scientific fields.[36,170–175] Since graphene has the thickness of a carbon atom characterised by extraordinary mechanical, electrical and thermal properties such as elastic stiffness 340 N m^{-1}, fracture toughness 4.0 MPa $m^{0.5}$, Young's modulus 1.0 TPa, electronic mobility 15 000–200 000 cm^2 V^{-1} s^{-1} and thermal conductivity 2000–5000 W m^{-1} K^{-1}, a large number of 2D heterostructures and composites have been produced by combining graphene sheets with other compounds.[174,180]

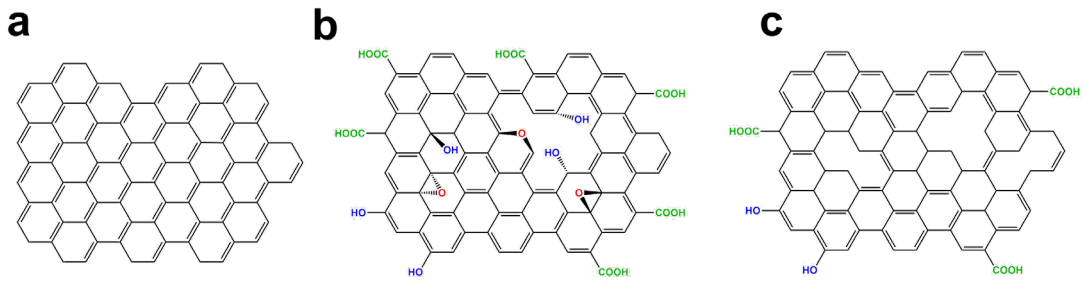


Figure 1.4. Graphene, GO and rGO structures

(a) Graphene is a single layer of carbon atoms arranged in a honeycomb lattice. **(b)** Graphene oxide (GO), has hydrophilic groups containing oxygen protruding outside its plane and edges. **(c)** Reduced graphene oxide (rGO) has less hydrophilic groups compared to GO, due to a reduction process. Contrarily to pristine graphene, the carbon atoms of GO and rGO do not lie in the same plane due to the structural defects.

Another appealing derivative of graphene is GO **(Fig. 1.4b)**, which is a 2D nanomaterial obtained from the oxidation of graphite. It has good biocompatibility and lower toxicity compared to graphene, therefore it is a good candidate for many biomedical applications.[199] One advantage of GO is given by its dispersibility in water buffers, due to the presence of groups containing oxygen such as carboxyls and epoxides distributed along the edges and on the planar surfaces of the sheets respectively, which provide electrostatic repulsion between the sheets. On one hand, these groups provide advantages in terms of water dispersibility and interaction with bio-components, but on the other hand, GO is not competitive with pristine graphene in terms of stiffness and electron mobility **(Table 1.2)**.

Table 1.2. Graphenes characteristics

Property	Graphene	Ref.	GO	Ref.	rGO	Ref.
Second- and third-order elastic stiffness	340 ± 50 N m^{-1} and -690 ± 120 N m^{-1}	201				
Area density	0.3818 $Å^{-2}$	202				
Breaking strength	42 N m^{-1}	201				
Cohesive energy	291 mJ m^{-2}	202				
Interlayer equilibrium spacing	3.41 Å	202				
Electronic mobility	200 × 10^3 cm^2 V^{-1} s^{-1} at electron densities of ~2 × 10^{11} cm^{-2}	203			2–200 cm^2 V^{-1} s^{-1}	204
Band gap	Zero					
Fracture toughness	4.0 ± 0.6 MPa $m^{0.5}$	205				
Intrinsic strength	130 GPa	201	76–293 MPa	206		
Magnetism	Strongly diamagnetic	207	Weak superparamagnetic	208	Weak superparamagnetic	208
Melting point	4510 K	209				
Opacity	2.3%	210	20%	211		
Optical transmittance	97.7%	210			80% for 550 nm light	211
Sheet resistance			276–2024 Ω/sq	212		
Solubility in water			6.6 μg mL^{-1}	213	4.74 μg mL^{-1}	213
Specific surface area	2630 m^2 g^{-1}	210				
Thermal conductivity	From 4.84 ± 0.44 × 10^3 to 5.30 ± 0.48 × 10^3	214				
Young's modulus	1.0 ± 0.1 TPa	201	324–529 GPa for 100–200 nm films	212		

Therefore, many reduction procedures have been developed to convert GO into graphene. These procedures aim to remove the oxygen-containing groups and structural defects to recover the π-conjugate honeycomb of graphene, restoring all its properties as well.[174]

This is the most important target of such procedures, however, although numerous efforts have been made, the reduction methods used so far have not reached the set expectations. Residual functional groups and other defects drastically alter the structure of the carbon plane and it is still not appropriate to refer to the rGO **(Fig. 1.4c)**, simply as if it was graphene, given that their properties are substantially different.[174]

1.3.2. Production Methods

Most of the research studies do not refer to pristine graphene due to the limited preparation yield.[174] Moreover, graphene derivatives such as GO and rGO are more commonly available and characterised by similar properties compared to graphene. Although most researchers call these materials 'graphene', it is misleading to identify them as such, given their heteroatomic irregularity, impurity and structural defects. Therefore, their nomenclature is expected to be corrected and standardised in the future. Interestingly, not many signs of progress have been made in the synthetic methodologies used to reduce GO into rGO since Boehm *et al.*[215] who first described the reduction of GO suspension with a series of chemical reducing agents,[216,217] apart from the thermal reduction.[218,219]

Although mechanical exfoliation can directly produce high-quality graphene, this method is not suitable for large-scale production. To overcome the limitation of this method, multiple approaches to produce graphene in bulk have been developed including, for

instance, epitaxial growth,[191] chemical vapour deposition (CVD),[192] liquid-phase exfoliation,[220] chemical peel[218,219] and organic synthesis.[221] Among these procedures, chemical exfoliation is of considerable interest because it does not require special equipment and produces large sheets of GO characterised by a high-density of functional groups, which facilitate the introduction of further functionalisation.[222] This method is known as the oxidation-exfoliation-reduction process, which generally consists of the chemical oxidation of graphite to graphite oxide, followed by the exfoliation of graphite oxide to produce single layers of GO, which finally reduced to rGO, generally characterised by a high carbon-oxygen ratio.[223]

The GO precursor is graphite oxide which exposes functional groups containing oxygen and retains a structure similar to that of stacked graphite. The history of the preparation of graphite oxide can be traced back to 1859 when steaming $KClO_3$ and HNO_3 were used to oxidize graphite powder, leading to the formation of a material with a carbon-oxygen ratio of about 2:1.[224] $KClO_3$ and HNO_3 must be though handled with particular caution due to the generation of highly toxic ClO_2 gas and the possibility of triggering an explosive reaction.[225] Hummers and Offeman, in 1958 developed an approach to synthesize graphite oxide with a similar level of oxidation but using different reagents (concentrated $NaNO_3$, $KMnO_4$, and H_2SO_4).[226] Through the Hummers method, the reaction can be completed in a relatively short time, avoiding the generation of ClO_2. The exfoliation of the graphite oxide in a single layer GO can be obtained by using additional energy inputs, such as mechanical agitation or ultrasound.[227] Several parameters, including starting materials, oxidation procedures and forms of energy for exfoliation, play an important role in controlling the size or number of layers of GO. By increasing the oxidation time or the number of oxidants, the average size of the GO flakes[228] can be

adjusted to 59 000-550 nm^2. Ultrasound is a more effective method for reducing the size of the GO sheets than mechanical shaking.[229] Finally, the number of layers of GO in the final products is strongly dependent on the size and crystallinity of the graphite precursors.[230]

The oxidation of graphite using strong oxidants leads to the breakage of the π-bonds and therefore, the conductivity of the oxidation products is drastically reduced. To remove the functional groups containing oxygen it is necessary to perform a reduction process which can partially improve the electrical conductivity by restoring the π-conjugated network.[231]

Several reduction strategies have been developed so far, including the chemical, electrochemical, hydrothermal or solvothermal, thermal, UV light and microbial reduction.[232] However, none of these methods is currently efficient enough to convert GO into high-quality graphene.

1.3.3. Graphene-Based Composite Materials

Graphene and its derivatives have given an incredible boost to the development of alternative carbon-based materials. The 2D structure of graphene, GO and rGO makes them very appealing components and potentially employable as versatile building blocks for the fabrication of 2D and 3D macroscopic materials.[173,174] Particularly, the resulting 3D macro-structures are self-supporting, exhibiting low density, extraordinary surface area, performing mechanical and electronic properties as well as chemical activity. This is particularly interesting for the fabrication of substrate-free components for applications in energy storage devices, sensors, catalysis and medicine.[173,174] These 3D hierarchical

assemblies attracted considerable attention and are expected to play a central role in commercializing their applications.

Graphenes act as the main constituents of novel materials as well as be incorporated into other composites producing novel materials with enhanced performances. The successful combination of two or more components can generate composite materials, which comprise both the individual properties from each component as well as reveal completely new characteristics. This, can expand the fields of application of existing materials and possibly open new avenues across different scientific fields, to overall enhance the technological progress.

There are several approaches for the fabrication of layered 2D graphene materials such as the Langmuir-Blodgett method, layer-by-layer assembly, electrochemical deposition, vacuum filtration and solvent evaporation.[173,174] Furthermore, there are alternative and more specific methods for the realisation of 3D graphene materials such as hydrothermal reduction, chemical reduction, template-directed method and the chemical vapour deposition.[232]

Generally, all these methods are limited by high costs, the use of expressly designed equipment, long incubation time and large reagents amounts as well as requirements for extreme conditions of temperature, pressure and pH. Although these methods provide in general positive results, there are alternative routes to assemble 3D graphene-based structures involving the use of cross-linking agents such as long-chain molecules, polymers and functionalised nanoparticles.[36,173,180] There are several limitations in the prevalent methods, including, for instance, the reduction of GO and functionalisation with nanoparticles generally requires toxic reductants such as hydrazine.[233] Moreover, the *in situ* growth of nanoparticles on the surface of graphenes often lacks control over the

reaction process, also altering the nature of graphenes.[180] The resulting compounds are mostly in the form of precipitates and therefore, not suitable for applications requiring well-dispersed materials. Currently, it is still difficult to obtain a homogeneous co-assembly of nanoparticles on individual graphenes sheets due to the presence of hydrophobic and hydrophilic contaminants which easily bind graphenes.

Alternatively, it is possible to employ biomolecules such as, nucleic acids,[234] proteins[38] and peptides[36,180] which can co-assembly with graphenes through non-covalent interactions (hydrogen bonds, electrostatic forces, van der Walls and π-π interactions).[180] These alternative assembly methods based on the employment of biomolecules show several advantages such as for instance the possibility to perform the reaction in standard conditions of temperature, pressure and pH as well as to easily carry out reversible reactions that do not destroy the nature of the individual components and simultaneously reduce the fabrication costs. Despite several limitations strongly linked to the nature of bio-components (due to their interacting surface complexity), they are highly appealing for applications of adhesion on graphenes surface. In literature, there are numerous studies concerning the production of composite materials, which exploit proteins to functionalise and induce the assembly of graphene-based composites through non-covalent interactions.[171,180]

As mentioned above, 3D materials are particularly interesting due to their structural properties, and therefore, many strategies have been developed for their production. One of the most common approaches to fabricate 3D graphene-based structures using bio-components is characterised by their assembly in a liquid environment. This permits the formation of hydrogels, which can be converted into porous aerogels through a drying process.[36,173,180] Hydrogels and aerogels have become increasingly popular as

immobilisation materials for cells, enzymes and proteins in biosensing applications.[36] In particular, enzymatic biosensors that use hydrogels as an encapsulant, have also shown improvements over other immobilisation techniques, such as cross-linking and covalent bonds.[235]

The 2D and 3D self-assembling materials based on graphenes functionalized with metallic nanoparticles, polymers and biomolecules, are promising candidates for bioelectrochemical applications, especially in the field of electrochemical biosensors and in that of biological fuel cells. Electrochemical biosensors with high sensitivity have found widespread uses in clinical diagnosis, in environmental monitoring as well as for quality controls in food industries and agricultural products.[236] Biofuel cells represent an important type of energy conversion devices, capable of transforming chemical energy from biomass, directly into high-efficiency electricity and with low or even zero-emission of pollutants. Biological fuel cells, therefore, can promote environmental remediation by being able to produce electricity.[237]

Finally, it is important to note that besides pristine graphene, GO and rGO, there are other zero and one dimensional (0D and 1D) carbon-based materials such as fullerenes, carbon dots, nanodiamonds, nanoribbons, single and multi-walled carbon nanotubes (CNTs), which also show various extraordinary properties, which can be an added value in the production of novel nanocomposites.[173]

This overview of carbon-based materials, in addition to describing the vastness of this scientific field, provides the basis for this dissertation on the characterisation of GO. It also lays the ground for the next chapter, in which a new three-dimensional graphene-based porous structure consisting of GO and M13 is described.

1.4. Peroxiredoxins

In the last few years, the Peroxiredoxin family (PRXs - EC 1.11.1.15)[237–239] has been considered as an interesting group of thiol-specific antioxidant proteins. These enzymes are vastly produced and widespread in a lot of different living beings, such as yeasts, bacteria, animals and plants. PRXs are located in cytoplasm, mitochondria, chloroplasts, membranes, peroxisomes and associated with nuclei.[240]

PRXs are considered moonlighting proteins, due to their double functionalities. In absence of oxidative stress, they are thioredoxin-dependent peroxidases, which protect cells from oxidative stress, reducing and detoxifying hydrogen peroxides (H_2O_2), peroxynitrites ($ONOO^-$) and other organic hydroperoxides (ROOH) **(Fig 1.5a)**.[240,241]

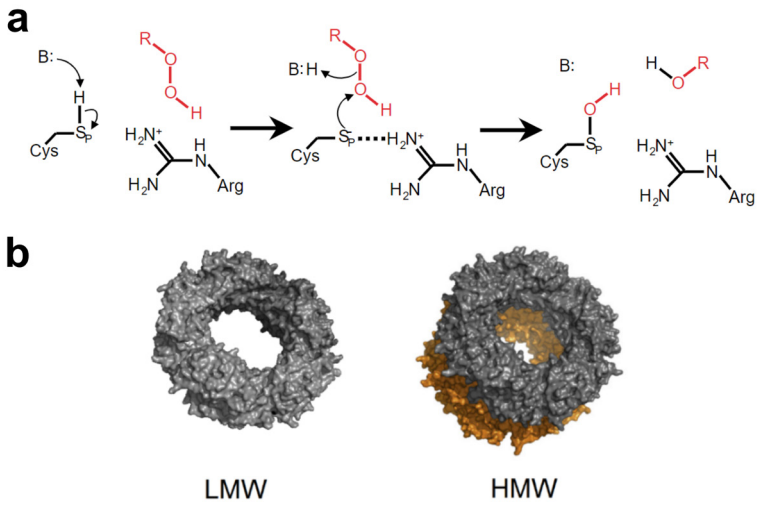


Figure 1.5. PRXs oligomeric states

(a) The first step of peroxide reduction, probably common to all peroxiredoxins.[240] This involves the nucleophilic attack by the peroxidatic cysteine (S_P) followed by the formation of the cysteine sulfenic acid intermediate (SP_{OH}). **(b)** A single PRX ring in the fully folded state (FF) that works as a peroxidase (left). Two PRX rings stacked in the unfolded state that works as a molecular chaperone (right).

Whereas, in presence of high H_2O_2 concentrations and low pH, they change their oligomeric state from low molecular weight (LMW) to high molecular weight (HMW) acting as holdases, which are a group of molecular chaperones involved in the proteins folding process **(Fig 1.5b)**.[242,243] PRXs are interesting not only for their physiological roles but also for their nanoscopic ring-like shape and their potential employability in nanotechnology. For example, a specific PRX named SmPRXI has been used for the fabrication of carbon-based composite material[38] and silver nanorings.[39]

1.4.1. Recombinant PRXI of *Schistosoma mansoni*

The specific PRX employed for the realisation of nanostructured surface described in **Chapter 7** is the SmPRXI, which is naturally expressed in a helminth which infects humans and mammals called *Schistosoma mansoni*.

Peroxiredoxins (PRXs) are generally characterised by having a ring-like structure, resulting from the assembly of several monomers. The monomer SmPRXI is a protein made of 185 aa and with MW of 25 273.5 Da.[243] The quaternary structure of SmPRXI is composed of 10 monomers organised in 5 homodimers organised in a ring-like shape, and rarely, it also forms dodecameric units. The SmPRXI has an external diameter of 13 nm, an inner diameter of 6 nm and a height of 4.5 nm.[243]

Due to the DNA cloning techniques, the SmPRXI was genetically engineered with a tail peptide made of 37 residues located at the N-terminal. This peptide includes a His-Tag comprised of six consecutive histidines (His) **(Fig. 1.6b)** to facilitate the protein purification through affinity chromatography (AC) with a HisTrap column. The column resin is functionalised with the chelating agent Nα, Nα-Bis(carboxymethyl)-L-lysine

(NTA) **(Chapter 2.1)**. The bond between the NTA on the column resin and the His-Tag peptide of the recombinant proteins is mediated through metallic bonds given by the presence of a hexacoordinated Ni atom interacting with one N atom and three O atoms exposed by NTA on a side and with two N atoms of the imidazole side chains of the His-Tag on the other **(Fig. 2.2c)**.

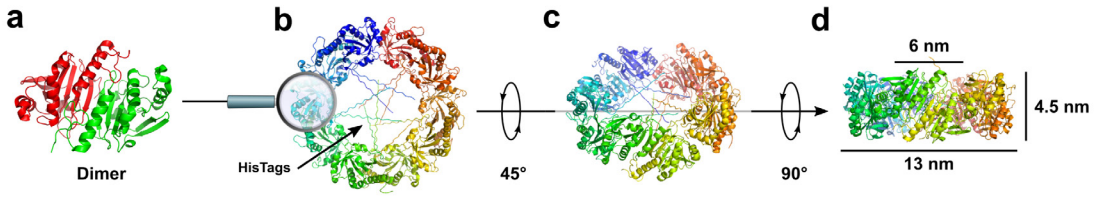


Figure 1.6. SmPRXI structure

(a) Two monomers (red and green) of SmPRXI forming a dimer. **(b)** The protein structure of the recombinant SmPRXI showing the His-Tag facing the internal cavity. Different views of the SmPRXI after **(c)** 45° and **(d)** 90° rotation from the top view orientation.

Furthermore, due to the His-Tag, the SmPRXI can be also used for the uptake or the *in situ* growth of metal nanoparticles (MNPs),[37,38] and this property is enhanced due to the presence of four additional aspartate (Asp) residues distributed on the tag peptides. Therefore, the decamer ring-like oligomeric state of this protein shows 10 peptide tails with 60 His and 40 Asp residues **(Appx. 9)**, ready to form useful bonds for purification and functionalisation purposes.

The binding between Ni-NTA and His-Tagged proteins or functionalised AuNPs (Gold nanoparticles), also requires the presence of imidazole (1,3-diazacyclopenta-2,4-diene), which is a molecule structurally identical to the variable group characterising the amino acid histidine. The presence of imidazole can be used to modulate the binding avoiding the formation of unspecific bonds.[38]

1.5. Scope of the Thesis

The field of nanotechnology is interconnected with numerous and different scientific fields where the nanoscaled dimensions of components for selective interaction at a molecular level and the assembly of the smallest possible functional structures are crucial.

Nanotechnology relies on a wide variety of 'nanotools'. In particular, bio-components such as viruses, proteins and small peptides as well as graphene derivatives such as graphene oxide and carbon nanotubes, are massively impacting the production of novel materials and technologies.

Although nanostructured materials and devices produced through the employment of biological components are sensitive to extreme conditions of pH, temperature and pressure, they have already proven to be extremely versatile, scalable, economical and environmentally sustainable. Moreover, among the wide range of components available in nature, viruses are one of the most versatile, and they are making the difference in numerous scientific communities.

This thesis focuses on the combination of M13 with other biological macromolecules and materials such as graphene oxide and carbon nanotubes, for the formation of self-assembled nanostructures for novel functional materials and devices. The entire study has revolved around the design, assembly and characterisation of novel porous nanostructured materials (*GraPhage13*) and nanostructured surfaces (GRX-N13 and SAS-M13). Furthermore, the in-depth characterisation and analyses of the newly fabricated structures are also detailed herein.

Chapter 1 is the introducing chapter where the state-of-the-art developing nanotechnologies have been described in detail, with particular focus on the advantages

and disadvantages of using biomolecules and viruses. M13 plays a central role for the assembly and properties of the three structures described in the thesis such as *GraPhage13*, GRX-N13 and SAS-M13. Therefore, a detailed description of the phage history, characteristics and its impact in various scientific fields is reported. This is fundamental for the development of novel assembly approaches and the study of interesting unexplored aspects of M13. In addition to M13, both GO and SmPRXI are other important components, assembled with M13, for the realisation of novel nanostructures. Therefore, this chapter contains fundamental information about the characteristics and implications in nanotechnology of these other two important components.

Chapter 2 provides a broad overview of the components used for the realisation of novel self-assembled structures as well as a concise description of the techniques used for their characterisation.

Chapter 3 introduces the results section, focusing on M13 and in particular on the methods of propagation, purification, quantification and storage employed during the entire project. Moreover, it includes an in-depth analysis of its structural properties, describing potential interactions with other components and identifying 'hot points' exploitable for potential novel and so far, unexplored modifications. M13 stability was also tested in different buffers and at different pH values as well as characterised through microscopy and spectroscopy techniques.

In **Chapter 4** the stability in different buffers and at various pH of graphene oxide (GO) is described. Furthermore, the effect of sonication was evaluated through the study of size distribution to understand how the reduced size of the carbon sheets can be related to the

stability of the graphene oxide in solution. Similarly to **Chapter 3**, the GO was also characterised using microscopic and spectroscopic techniques.

The results discussed in these two chapters are crucial to familiarize with the use of these two components and to obtain a solid background to continue with the study of the self-assembled nanostructures *GraPhage13*, GRX-N13 and SAS-M13 described in the following chapters.

Chapter 5 describes *GraPhage13*, a porous 3D structured aerogel, with high-surface-area and very low density, obtained by the self-assembly of M13 and GO through non-covalent interactions. *GraPhage13* realisation starts from the dispersion of the components in solution forming a hydrogel, which once freeze-dried converts into a very light aerogel. *GraPhage13* self-assembly strategies, the interaction between its two components under different pH conditions, the viscosity and density of the hydrogel (GPH) are described in this chapter as well as the morphology, density and surface area of the aerogel (GPA). Furthermore, the binding between the components of *GraPhage13* aerogel has been studied using various spectroscopy techniques.

Chapter 6 expands the description of preliminary experiments on *GraPhage13* aimed at analysing some of its characteristics to explore its properties and propose this material as an alternative source in a range of applications. In particular, it was found that the use of different formulations produces aerogels with variable porosity and that the aerogel shows peculiar hydrophobic properties. Furthermore, to improve its thermo-electric conductivity, *GraPhage13* was gold templated *via* electrodeposition and also carbon nanotubes were added to the reaction mixture to obtain more advanced hydrogels/aerogels.

Chapters 7 and **8** describe the self-assembly strategy of two nanostructured surfaces, the GRX-N13 and SAS-M13, based on the use of non-covalent interactions and covalent bonds, respectively. The realisation of both structures is aimed at the fabrication of metamaterials for optic and photonic applications. The two chapters describe the assembly strategies and the results of their characterisation.

The main purpose of this thesis was to investigate the employability of M13 in the fabrication of new self-assembling nanostructures for the production of functional materials that can be applied in the fields of biological, chemical and physical sciences, providing new insights into the development of novel micro- to nanotechnologies.



UNIVERSITY OF
BIRMINGHAM

CHAPTER II

Experimental Tools and Analytical Techniques



Abstract

This chapter contains the list of technical information about the materials, techniques and equipment employed to perform the experiments described in the other chapters. The experimental tool and the analytical techniques are described in individual paragraphs accompanied by images, schematics as well as a concise and referenced overview.

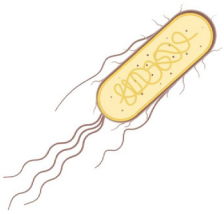
Paolo Passaretti

2.1. Bacteria, Molecules and Compounds



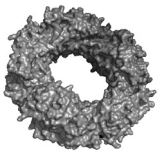
Filamentous bacteriophage M13

It is a virus which infects the *E. coli* strain showing the F-*pilus*. M13KE purchased from New England Biolabs was used to perform the following characterisation experiments as well as the fabrication of novel self-assembled nanostructures **(Chapters 1, 3 and Appx. 3, 4)**.



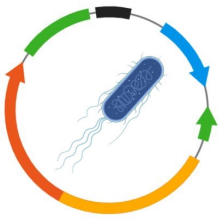
***Escherichia coli* Top10F'**

It is a specific strain of *E. coli* showing the following characteristics, F′{*lac*Iq Tn10 (TetR)} *mcr*A Δ(*mrr-hsd*RMS-*mcr*BC) Φ80*lac*ZΔM15 Δ*lac*X74 *rec*A1 *ara*D139 Δ(*ara-leu*)7697 *gal*U *gal*K *rps*L *end*A1 *nup*G. It was purchased from Thermo Fisher and used for the propagation of M13. The protocol for its self-propagation is described in **(Chapter 3 and Appx. 2)** (Thermo Scientific).



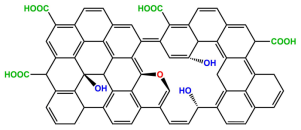
Peroxiredoxin I from *Schistosoma mansoni* (SmPRXI)

It is a thiol-specific antioxidant protein expressed in many different living organisms. Here, it was used for the fabrication of a novel nanostructure **(Chapter 7)**, and the protocol for its production is described in **Appx 9**. It was provided by the University of L'Aquila.



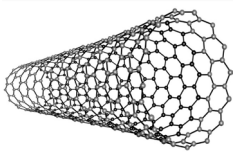
***Escherichia coli* BL21 Star (DE3) pLysS pRSETa-SmPRXI**

It is a specific strain of *E. coli* showing the following characteristics F$^-$ *ompT hsdS*$_B$ ($r_B^- m_B^-$) gal *dcm rne*131 (DE3) pLysS (Cam^R). The pLysS plasmid carried by this strain produces T7 lysozyme to reduce basal level expression of the gene of interest. pLysS confers resistance to chloramphenicol (Cam^R) and contains the p15A origin. It was provided by the University of L'Aquila **(Appx. 10)** (Thermo Scientific).



Graphene oxide (GO)

It is a 2D nanomaterial made of carbon, oxygen and hydrogen. It is a derivative of graphene obtained from the oxidation of graphite. It was purchased from Graphene Supermarket, characterised and used for the fabrication of novel self-assembled nanostructures **(Chapters 1, 4, 5, 7)**.



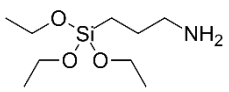
CoMoCAT single-wall carbon nanotubes (SWNTs)

Carbon nanotubes are materials that possess remarkable properties which find utility in a wide range of new and enhanced applications. It was purchased from Sigma-Aldrich and used to improve the conductivity performances of *GraPhage13* **(Chapters 1, 4, 6)**.



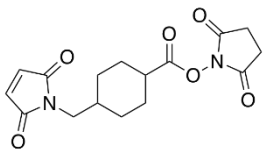
Silicon wafer (*p*-type)

It is a thin slice of semi-conductive crystalline silicon (c-Si) generally used as a substrate in several different fields such as energy, electronics and nano-engineering in general.



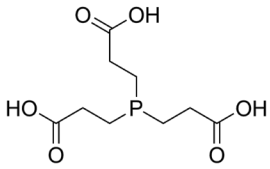
(3-Aminopropyl)triethoxysilane (APTES)

It is a common coupling agent used to functionalise the silicon wafers surface. It is composed of three ethoxy groups ($–OC_2H_5$) and an amino group ($–NH_2$) attached to a central Si. The latter can react with exposed O^- from oxidized silicon wafers to form siloxane bonds (Si–O–Si) organised in monolayers on the substrate surface (Sigma-Aldrich).



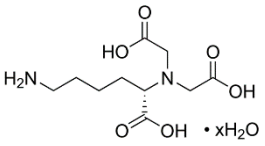
Succinimidyl 4-(N-maleimidomethyl)cyclohexane-1-carboxylate (SMCC)

It is a cross-linking agent containing an N-hydroxysuccinimide ester (NHS) and a maleimide group at opposite ends of the molecule. The NHS can react with an amino group forming an amide bond. On the other side of the molecule, the maleimide group can react with a thiol group (–SH) forming a thioether bond (Thermo Scientific).



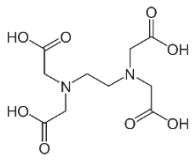
Tris(2-carboxyethyl)phosphine (TCEP)

It is a strong reducing agent. It can cleave the disulphide bond between two cysteine residues (R–S–S–R) into individual sulfhydryl groups with the oxidation of the phosphine. TCEP is highly soluble and stable in aqueous solutions over a wide range of pH values. It is specific towards the disulphide bond and lacks reactivity with other functional groups in biomolecules (Sigma-Aldrich).



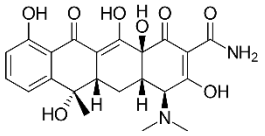
Nα, Nα-Bis(carboxymethyl)-L-lysine hydrate (NTA)

It is a chelating agent, which forms coordination compounds with metal ions such as Ni^{2+} Ca^{2+}, Co^{2+}, Cu^{2+}, and Fe^{3+} (Sigma-Aldrich).



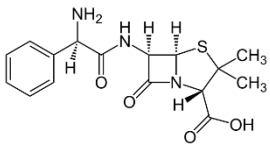
Ethylenediaminetetraacetic acid (EDTA)

It is a water-soluble chelating agent that can form complexes with metal ions similar to the NTA (Sigma-Aldrich).



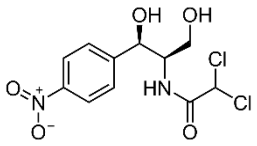
Tetracycline (TCN)

It is an antibiotic which passively diffuses through protein channels in the cell membrane, binding to 30S ribosomes and inhibits protein synthesis by preventing access of aminoacyl tRNA to the acceptor site on the mRNA-ribosome complex. It also binds to the bacterial 50S ribosomal subunit, altering the membrane and causing intracellular components to leak from bacterial cells (Sigma-Aldrich).



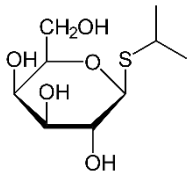
Ampicillin (AMP)

It is a semisynthetic penicillin and a β-lactam antibiotic that inhibits bacterial cell wall synthesis by inactivating the transpeptidases on the inner surface of the bacterial cell membrane (Sigma-Aldrich).



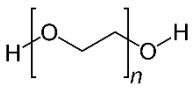
Chloramphenicol (CAM)

It is a synthetic antibiotic, which was first isolated from strains of *Streptomyces venezuelae*. It has a broad spectrum of activity against Gram-positive and Gram-negative bacteria. Chloramphenicol inhibits bacterial protein synthesis by blocking the peptidyl transferase step (elongation inhibition). It binds to the 50S ribosomal subunit and prevents attachment of aminoacyl tRNA to the ribosome (Sigma-Aldrich).



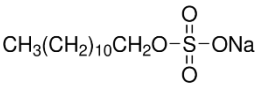
Isopropyl β-D-1-thiogalactopyranoside (IPTG)

It is commonly used in cloning procedures that require induction of β-galactosidase activity. It is used in conjunction with X-Gal in the blue-white selection of recombinant bacterial colonies that induce expression of the lac operon in *E. coli*. IPTG binds to the *lac*I repressor and altering its conformation, which prevents the repression of the β-galactosidase coding gene *lac*Z (Sigma-Aldrich).



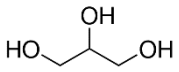
Polyethylene glycol (PEG)

It is a polyether compound with many applications, from industrial manufacturing to medicine. In the following experiments, it was employed in the M13 purification process (Sigma-Aldrich).



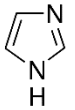
Sodium dodecyl sulfate (SDS)

Sodium dodecyl sulfate (SDS) is an anionic detergent that can form complexes with protein through hydrophobic interactions. Studies have reported that the hydrodynamic functions of protein-SDS complexes are governed by the length of their polypeptide chains. Thus, SDS-based electrophoretic techniques can separate protein molecules based on their molecular weights. Additionally, SDS can solubilize cell membranes and can extract membrane-bound proteins (Sigma-Aldrich).



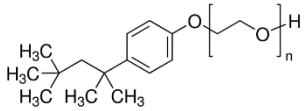
1,2,3-Trihydroxypropane (Glycerol)

It is used both in sample preparation and gel formation for polyacrylamide gel electrophoresis. In particular, here it was used as a protein stabilizer and storage buffer component (Sigma-Aldrich).



1,3-Diazole (Imidazole)

It is a five-membered heterocycle that is found in many naturally occurring compounds. It exhibits both acidic and basic properties. Here it was used to modulate the interaction between the protein His-Tag with the Ni-NTA groups during the SmPRXI purification through affinity chromatography (Sigma-Aldrich).



Octyl phenol ethoxylate (Triton X100)

It is a common non-ionic surfactant and emulsifier which is often used in biochemical applications to solubilize proteins. It is considered a comparatively mild detergent, non-denaturing, and is reported in numerous references as a routinely added reagent. It is utilized for lysing cells to extract protein and cellular organelles. It can also permeabilize the living cell membrane for transfection (Sigma-Aldrich).

NaCl

KCl

Na_2HPO_4

KH_2PO_4

Phosphate buffer saline (PBS)

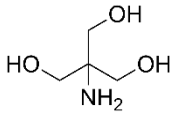
It is a buffer solution used in biological research. It is a water-based salt solution containing sodium phosphate, sodium chloride and, in some formulations, it contains potassium chloride and potassium phosphate. The osmolality and ion concentrations of the solutions match those of the human body (isotonic) and are non-toxic to most cells (Thermo Scientific).

$Na_3C_6H_5O_7$

$C_3H_5O(COO)_3^{3-}$

Citrate buffer (CB)

It is a buffer containing tri-sodium citrate and citric acid usually used for RNA isolation, due to its ability to prevent base hydrolysis. Here, it was used to study the stability of M13 and GO (Sigma-Aldrich).



2-Amino-2-(hydroxymethyl)-1,3-propanediol (TRIS base)

It is extensively used in biochemistry and molecular biology as a component of buffer solutions, especially to work with nucleic acids. It contains a primary amine and thus undergoes the reactions associated with typical amines (Sigma-Aldrich).

$NiSO_4\ (H_2O)_6$

Nickel(II) sulphate hexahydrate

It is a highly soluble blue-coloured salt and is a common source of the Ni^{2+} ion for several techniques. Here, it was used to functionalise the NTA group for the affinity chromatography and the modified M13-NTA (Sigma-Aldrich).

NaCl

Sodium chloride

It is an ionic compound with the chemical formula NaCl, representing a 1:1 ratio of sodium and chloride ions. Sodium chloride is the salt most responsible for the salinity of seawater and the extracellular fluid of many multicellular organisms (Sigma-Aldrich).

HCl

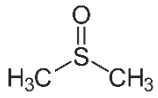
Hydrochloric acid

It is a strong acid which completely dissociates in aqueous solution. Hydrochloric acid is the simplest chlorine-based acid system containing water. It is a solution of hydrogen chloride and water, and a variety of other chemical species, including hydronium and chloride ions (Sigma-Aldrich).

NaOH

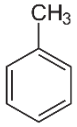
Sodium hydroxide

It is a highly caustic base and alkali that decomposes proteins at ordinary ambient temperatures. It is highly soluble in water and readily absorbs moisture and carbon dioxide from the air (Sigma-Aldrich).



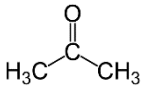
Dimethyl sulfoxide (DMSO)

It is an organosulfur compound with the formula $(CH_3)_2SO$. This colourless liquid is an important polar aprotic solvent that dissolves both polar and nonpolar compounds and is miscible in a wide range of organic solvents as well as water. It has a relatively high melting point (Sigma-Aldrich).



Methylbenzene (Toluene)

It is a mono-substituted benzene derivative, consisting of a CH_3 group attached to a phenyl group. As such, its IUPAC name is methylbenzene. Toluene is predominantly used as an industrial feedstock and a solvent (Sigma-Aldrich).



Propan-2-one (Acetone)

It is a colourless, volatile, flammable liquid and is the simplest and smallest ketone (Sigma-Aldrich).

CH_3CH_2OH

Ethanol (EtOH)

It is a simple alcohol, volatile and flammable, with a slight characteristic odour (Sigma-Aldrich).

H_2O

Deionised water (DIW)

Obtained with an Arium advance EDI – Type 2 Pure Water dispenser system.

2.2. Sample Preparation Methodologies

2.2.1. Bacterial Cultures and Purification Methods

Fermentation is the anaerobic catabolism of a single chemical compound using a series of redox transformations aimed to generate adenosine triphosphate (ATP) by substrate phosphorylation. This natural process is employed in industry and research in general for various purposes ranging from the production of wine and vinegar to the expression of proteins and drugs. These processes can be performed on a small or large scale, depending on the amount of product that is needed. To do this, there are several fermentation approaches called batch, fed-batch and chemostat. Batch cultures are used where large quantities of product are not needed. Then the microorganisms are made to grow suspended in a culture medium in which the growth stops when the nutrients end. In the batch system, the growth of microorganisms is generally characterised by a phase of latency (lag) in which the bacteria adapt to the new environment, an exponential growth phase in which the microorganisms are metabolically active, multiply very quickly producing the products of interest, a stationary phase in which growth stops and finally death in which the number of microorganisms begins to decrease. Batch cultures can be supplemented with the addition of nutrients that allow the cells in the culture medium to begin a new phase of exponential growth until the next nutrient depletion. In this case, they are called fed-batch and these are used to increase the production compared to the batch cultures. For large-scale fermentations the chemostat is usually used, also called continuous fermenter, in which the vessel containing the micro-organisms and the culture medium is constantly supplied with nutrients. Similarly, fermentation products are extracted from the fermenter through dedicated filtering systems depending on the

product. This makes it possible to keep the bacteria in a condition of constant exponential growth, maximizing the production.

To employ the bacteriophage M13 to produce new self-assembled structures, it was propagated by infecting batch cultures of *E. coli* **(Fig. 2.1a, b)**. These procedures are described in detail in the experimental section of **Chapter 3.2**. Furthermore, the protocols followed for the production of the *E. coli* to be infected and two different approaches for the propagation and purification of M13 adopted for all the studies described in the following chapters, are reported in **Appx. 2, 3** and **4**.

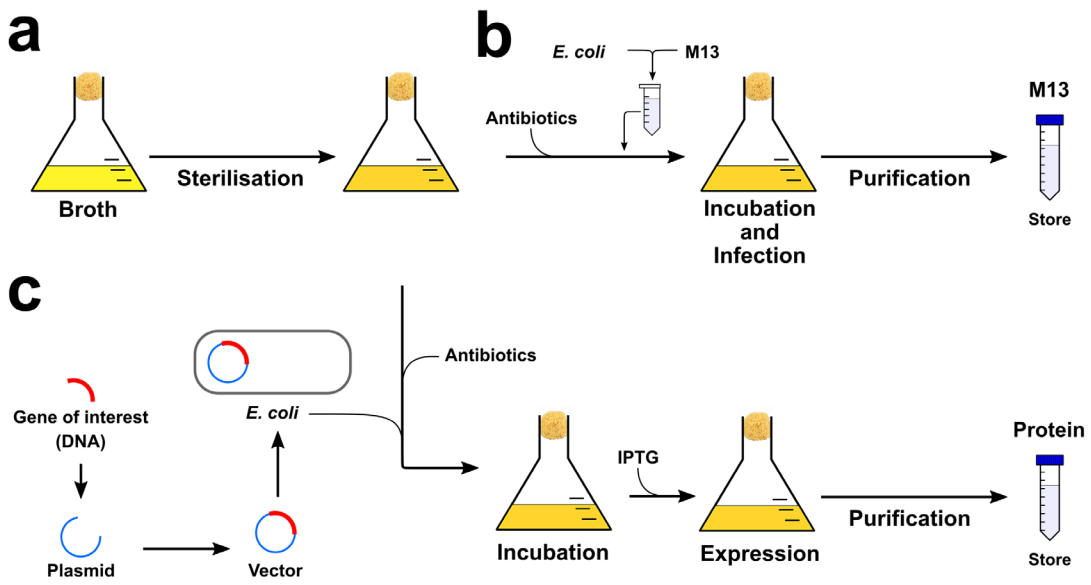


Figure 2.1. Schematic representation of *E. coli* batch cultures

(a) Nutrient broth preparation to produce M13 and SmPRXI through *E. coli* batch cultures. **(b)** The key step in the propagation of M13 which consists of the co-incubation of *E. coli* cells and phages promoting the natural infection process. **(c)** The artificial insertion of a recombinant gene into a plasmid, followed by the transformation of *E. coli* cells. This step precedes the incubation of transformed bacteria employed for the production of recombinant proteins. Both methods need purification techniques to obtain the final product.

The SmPRXI protein used for the assembly of the GRX-N13 structure **(Chapter 7)** was produced in collaboration with the University of L'Aquila. The approach used for its production was similar to the one used for M13 propagation. To produce SmPRXI, the wild type gene from *Schistosoma mansoni* was inserted inside a cloning vector and subsequently inserted inside *E. coli*. Once the bacteria that carried the plasmid containing the gene encoding the SmPRXI were modified and selected, they were grown in batch cultures and the expression of the protein was activated by administering IPTG during the exponential growth phase **(Fig. 2.1a, c)**. As for M13, the detailed protocol for its production is described in **Chapter 7.3** and **Appx. 10**.

2.2.2. Size Exclusion and Affinity Chromatography

Chromatography is a technique used to separate molecules based on specific interactions with an immobilized ligand (stationary phase). In 1903, for the first-time pigments extracted from plants were separated through adsorption chromatography by Mikhail Tswett, which used calcium carbonate as an adsorbent and a mixture of gasoline and ethanol as eluent.[244]

Chromatography is a chemical-physical method of separation based on the different distribution of compounds in two non-miscible phases. The chromatographic separation consists in exploiting the different capacity that each molecule or ion possesses in the distribution between the two phases.[244] The separation occurs during the passage of a mobile phase through a stationary phase. The phases can be solid, liquid or gaseous in various combinations depending on the type of chromatography.[244] There are many different types of chromatography, which can be classified based on the matrix used for the stationary phase and the type of mobile phase (thin layer, column, liquid and gas

chromatography) as well as the mechanism of interaction between the molecules to separate and the chromatographic system (size exclusion, ion exchange and affinity chromatography).[244]

Fast protein liquid chromatography (FPLC) was employed for the purification of the modified M13 (GRX-N13) and SmPRXI, both described in **Chapter 7** and **Appx. 10** respectively. These samples were specifically purified using size exclusion (SEC) and Ni-NTA affinity chromatography (AC), respectively. In both cases, the chromatography system is essentially composed of pumps, pipes and valves, which push the mobile phase through the dedicated (SEC or AC) column connected to the system, depending on the separation that needs to be performed.[244]

The purification through SEC **(Fig. 2.2a)** is a noninteractive separation mode usually used to separate analytes with a MW ranging between 1 up to 500 000 kDa. It is based on the capability of the stationary phase particles (Sephadex - Separation Pharmacia Dextran) to let smaller analytes to penetrate its porous structure, and therefore, slowing down their elution, while larger particles are quickly eluted in the interspace between the individual Sephadex beads. This promotes the separation of molecules with different MW, eluting the analytes with a velocity which is directly proportional to their mass **(Fig. 2.2a)**.[244] At the end of the elution column, there is usually a UV-Vis spectrophotometer which measures the absorbance at 280 nm for the detection of proteins. The peak intensity indicates the amount of the analyte eluted at a specific elution time/volume corresponding to a specific MW **(Fig. 2.2a)**.[244]

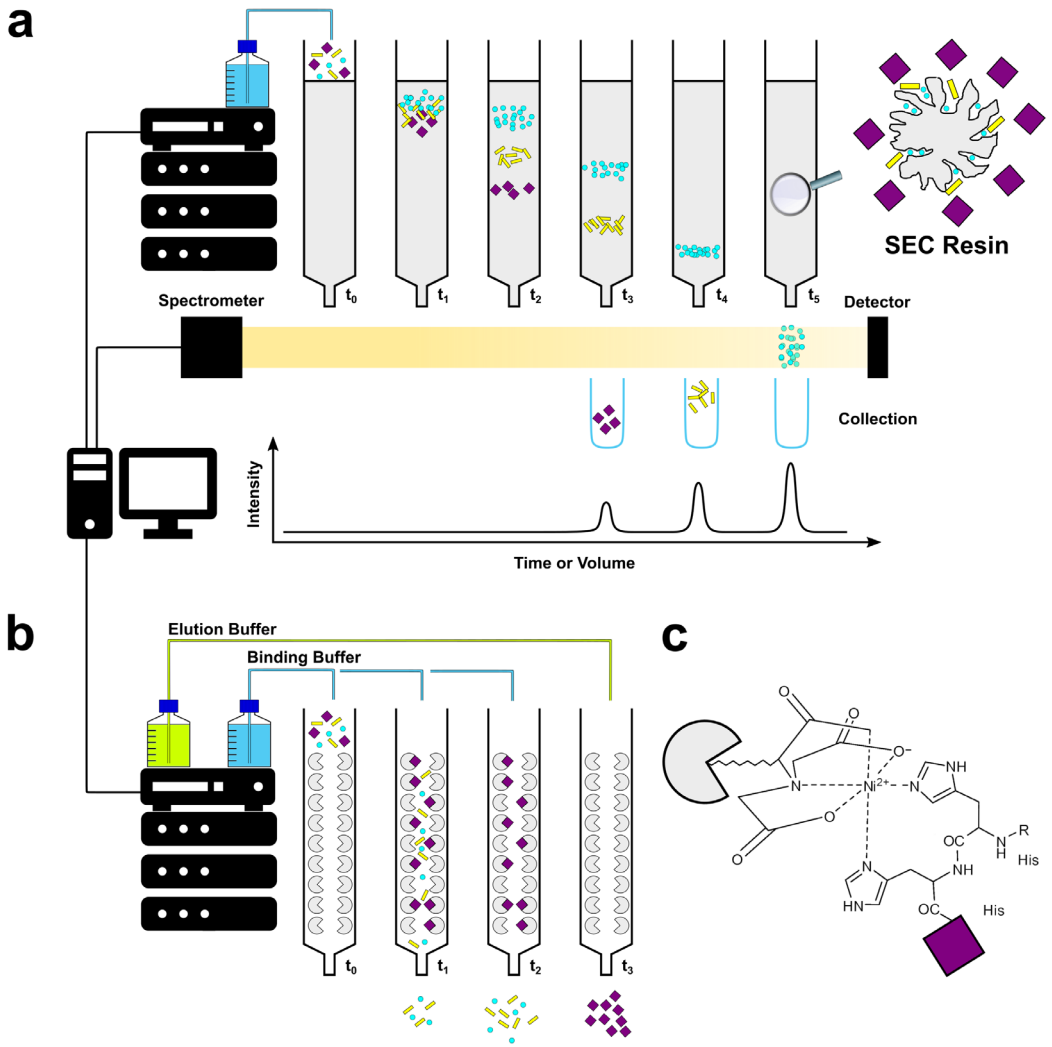


Figure 2.2. Schematic representation of SEC and AC

(a) Schematic representation of size exclusion chromatography. The sample containing a mixture of protein (t_0), is pushed through the column containing a resin made of small particles. This resin allows the bigger protein to flow faster around their external surface compared with smaller particles which flow slower due to the retention given by the presence of interspaces inside the resin structure (see insert). Therefore, the components inside the mixture are separated along the column based on their molecular weight. Once eluted the particles are detected and the intensity of the peaks is directly proportional to the amount of the eluted analyte. **(b)** Schematic representation of affinity chromatography through Ni-NTA interacting with His-tagged proteins. The sample containing a mixture of protein (t_0), including a recombinant protein modified with a His-Tag (purple) is passed through a HisTrap™ Ni-NTA column (t_1). The binding between the resin and the target protein **(c)** during t_1 and t_2 is shown in the insert and it is modulated by the presence of binding buffer with a low level of imidazole. Once the undesired proteins are eluted and the target protein is bound to the column resin, the elution buffer with a higher concentration of imidazole is passed through the column releasing the recombinant protein (t_3).

Differently, Ni-NTA AC **(Fig. 2.2b)** is one of the most commonly employed methods for the purification of recombinant proteins expressing the signalling peptides called His-Tag. The latter is essentially composed of a short amino acid sequence containing six consecutive His residues.

This separation method is based on the Ni mediated metallic bond between the stationary phase (Sephadex) functionalised with NTA groups, and the His-Tag peptide exposed by the recombinant proteins of interest **(Fig. 2.2c)**.[244] Briefly, the mixture containing the analyte of interest is eluted through the column using the binding buffer, which allows the His-Tag and the Ni-NTA to bind. This condition is kept constant until the chromatogram signal stabilises, indicating that all the unbound molecules have been removed from the column. Subsequently, a gradient of elution buffer, containing a high content of imidazole is passed through the column, displacing the His-Tag bound to the Ni-NTA, resulting in the selective release of the analyte. Once the analyte is unbound, it can be eluted and detected at the end of the column through a UV-Vis spectrophotometer.[244]

ÄKTA Prime Plus by GE Healthcare Life Sciences, equipped with HisTrap Excel 5 mL was used for the SmPRXI purification **(Chapter 7.3 and Appx. 10)**. ÄKTA Explorer FPLC System by GE Healthcare Life Sciences equipped with a HiLoad 16/10 Superdex 200 PG column was employed to perform a size-exclusion chromatography to purify a modified version of the bacteriophage (M13-NTA), conjugated with EGFP **(Chapter 7.4)**.

2.2.3. Sonication

Sound is a vibration transmitted through the movement of the particles constituting a medium, such as air or liquid. It is typically described as a wave characterised by a frequency and it is quantified in hertz (Hz), or cycles per second. The humans hearing ranges between 20 and 20 000 Hz and the fundamental measurement of loudness is the decibel (dB), named after Alexander Graham Bell.[245]

Sonication consists of applying sound energy to the sample to agitate its components for various purposes. In particular, ultrasonic frequencies (>20 kHz) are widely used in a process called ultrasonication, which can be performed in a bath or using a metal probe. Ultrasonication can be employed for several different purposes going from ultrasonic cleaning of surfaces, passing through dispersing nanoparticles for nanotechnology, to disrupting cell membranes to release their content in biological applications.[245]

Therefore, the main desired effect of ultrasonication is homogenisation, deagglomeration, extraction, disintegration and lysis. These are obtained due to the cavitation generated by introducing high-power ultrasound into the liquid medium where the sample is dispersed.[245]

The ultrasound waves transmitted through the fluid create high and low-pressure cycles (compression and rarefaction respectively) in the medium depending on the frequency. These cycles produce vacuum bubbles during the rarefaction, which collapse violently when they can no longer absorb energy during the compression phase. This phenomenon is responsible for the abovementioned effects and it is named ‘cavitation’, which generate high-temperature and pressure (5000 K and 2000 atm respectively) in small confined areas and liquid jets with a speed up to 280 m s^{-1} **(Fig. 2.3)**.[245]

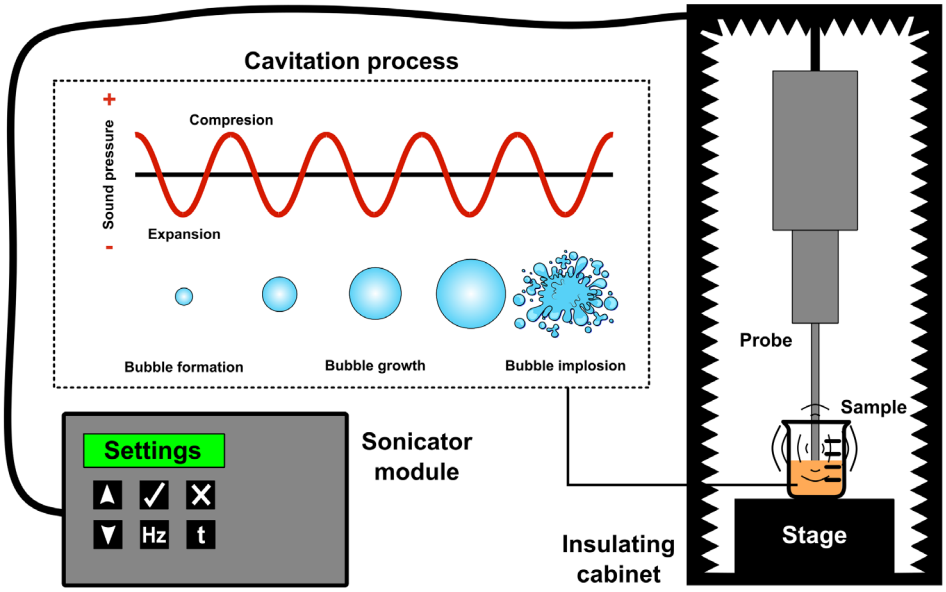


Figure 2.3. Schematic representation of the sonicator

Schematic representation of a probe sonicator and cavitation process.

The probe sonicator dismembrator Model 120 by Fisherbrand was employed to reduce the size of the GO nanosheets to improve its dispersibility **(Chapter 4)**. GO was subject to different sonication times of 5, 10, 15 and 30 min at 70% power with a pulse of 3 s ON and 9 s OFF.

2.2.4. Substrate Preparation

The silicon wafers employed as substrates were cleaved, cleaned and when necessary, functionalised following standard procedures. In particular, the substrates were always cleaned using a 'snow-jet' to remove potential contaminants and oxidised with a plasma cleaner to improve the spreadability of the drop cast samples. Snow-jet cleaning procedure first established by Hoenig S. A.[246] consists of placing the silicon wafer on a hot plate at 200°C and hit it with a high-pressure CO_2 jet using a spray gun.[247,248]

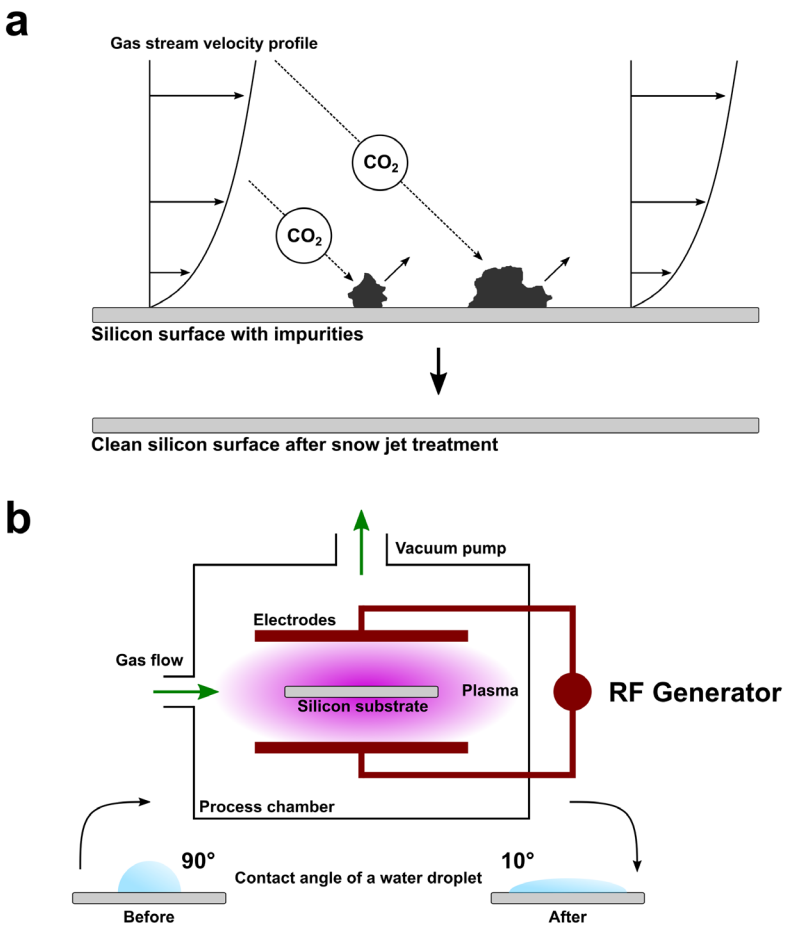


Figure 2.4. Schematic representation of the snow jet and plasma cleaner

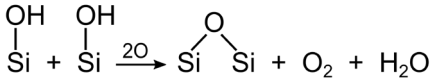
(a) Schematic representation of the snow-jet process. The CO_2 in the solid and liquid states, remove the impurity on the surface due to the momentum transfer and the solvent properties respectively. **(b)** Schematic representation of the plasma cleaner. The treated silicon substrate shows improved wettability after the treatment.

This method is based on the combined effects of momentum transfer given by the impacting dry crystals and the solvent properties of liquid CO_2. This impact provides sufficient momentum to remove sub-micron and micron-sized particles adhered to the surface. Also, the liquefied dry ice produced during the process, enhance the cleaning *via* dissolving organic residues **(Fig. 2.4a)**.

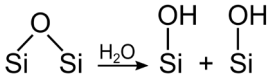
Plasma cleaning is a process to remove impurities from a surface using a plasma, which can be produced by gases such as argon, oxygen and nitrogen **(Fig. 2.4b)**. This procedure also enhances the hydrophilicity of the substrate surface, without changing the bulk properties of the material.[249] Plasma is a partially ionised gas where electrons, ions and neutral species coexist together, without the release of thermal energy.[249]

The plasma employed in the procedures described in this thesis was formed with a Harrick Plasma - PDC-32G-2 *via* oscillating the electric field with a radio frequency under vacuum and subsequently flowing air inside. The combination of these factors allows the gas to gain kinetic energy, therefore, it starts to ionise, breaking chemical species and creating radicals.[249]

Assuming that oxygen is responsible for the oxidation, they should follow the proposed dihydroxylation and hydroxylation, occurring in presence of the plasma **(Eq. 2.1)** and after the drop-casting of water onto the silicon **(Eq. 2.2)**, respectively.[249]



(2.1)



(2.2)

2.2.5. Sputter Coating

Sputter deposition is a plasma-based deposition method of thin-film deposition by sputtering. This implies ejecting material (Au, Pt, C, etc.) from a source called 'target', onto a substrate such as a silicon wafer.[250] This technique is extensively used in the

semiconductor industry to deposit thin films of various materials in integrated circuit processing. Since no high temperatures are required during the process, sputtering is considered an ideal method to deposit contact metals for thin-film transistors.[250]

Sputter coating is based on the capability of high-energy inert gas to enable the release of particles from the target *via* impacting on it at high-speed under certain conditions. There are several types of sputter coating instruments, in this case, all the experiments described in the following chapters were performed with magnetron sputter coaters **(Fig. 2.5)**.[250]

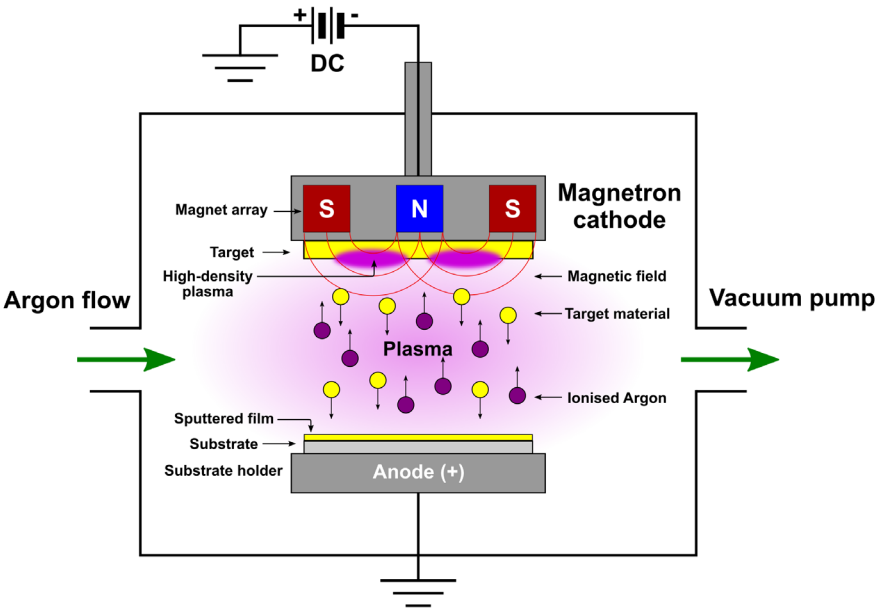


Figure 2.5. Schematic representation of the sputter coater

The figure shows a magnetron sputtering deposition. The instrument produces energetic ions *via* applying a negative charge to the target, which is inside a chamber together with the substrate to cover in the presence of plasma and an inert gas. These conditions allow the ions to accelerate towards the target and being ejected, creating a growing film onto the substrate.

This instrument employs magnets behind the cathode to trap electrons over the negatively charged target material. Subsequently, the free electrons flow produced from the negatively charged target, collide with the outer electronic shell of the Ar gas atoms,

which becomes positively charged due to the loss of electrons. In these conditions, the Ar ions are attracted to the target material at a very high-velocity due to the negative charge of the target. The impact of the Ar ions allows atomic size particles to be released from the target source material due to the momentum of the collisions. These resulting particles travel through the vacuum deposition chamber, depositing as a thin film of material on the surface of the substrate to be coated.[250]

The sputter coater SC7640 by Polaron was employed to coat the GPA and its corresponding control sample with platinum before the SEM analyses **(Chapter 5.4)**. Moreover, Automatic Sputter Coater by Agar scientific was employed to coat the GPAs samples with gold to study its wettability properties **(Chapter 6.2)**. To determine the deposition thickness, some calibration curves were obtained measuring the gold layer thickness at different times and current intensities.

2.2.6. Electrophoretic Deposition (EPD)

Electrophoretic deposition (EPD) or generally electrodeposition, is one of the most common approaches to functionalise and improve the performances of conductive due to the deposition of a thin layer of noble metals such as Au, Pt, Cu and Zn.[251] It is also used for applying coatings to metal fabricated products such as automobile bodies and parts, tractors and heavy equipment, electrical switchgear, appliances, metal furniture, containers and many other industrial products commonly used in the everyday life.[251]

Electrodeposition is based on the electrolysis of an aqueous solution containing the cations of the metal desired to cover the surface of an object. In the electrolytic cell, the object to be covered is used as a cathode. Therefore, it is connected to the negative pole

of a direct current source while the anode is connected to the positive pole and closes the electrical circuit. As soon as the current passes into the circuit, the free metal cations already dissolved in solution are discharged on the surface of the cathode, being reduced. In these conditions, the latter will acquire a number of electrons equal to its charge according to the following reaction **(Eq. 2.3)**.

$$M_{(aq)}^{n+} + n\,e^- \longrightarrow M_{(s)} \qquad (2.3)$$

Unfortunately, the reduction of metal cation always occurs in competition with the discharge of the H^+ ion from which hydrogen gas is obtained. This phenomenon decreases the quantity of metal deposited respect to that theoretically calculated, with a yield that in some cases is around 20%.[252] This is due to the fact that part of the current supplied in the electrolytic process is consumed by the development of hydrogen gas rather than used for metal deposition. Furthermore, the development of gaseous hydrogen has negative effects on the morphology of the deposited metal, causing inhomogeneous depositions and surface defects, which have negative consequences such as poor aesthetic, reduced mechanical properties and lower corrosion resistance.[252] The reactions which describe the production of hydrogen gas in acid and basic conditions are described in **Eq. 2.4** and **2.5**, respectively.[252]

$$2\,H^+ + 2\,e^- \longrightarrow H_2 \qquad (2.4)$$

$$2\,H_2O + 2\,e^- \longrightarrow H_2 + 2\,OH^- \qquad (2.5)$$

There are many electrochemical methods to study an analyte in an electrochemical cell such as linear sweep voltammetry, potentiometric stripping analysis as well as other chrono-methods and impedance spectroscopy.[253,254] In this particular study, to achieve the deposition of gold on the surface of *GraPhage13* aerogel (GPA) **(Chapter 6.3)**, cyclic voltammetry (CV) and chronoamperometry (CA) were employed, therefore, this paragraph focuses on them. Moreover, there are several potentiostat/galvanostat (PGSTAT) setups comprised of two, three or four electrodes. However, this paragraph only describes the three electrodes set up, equipped with counter (CE), reference (RE) and working (WE) electrodes **(Fig. 2.6)**.[253,254]

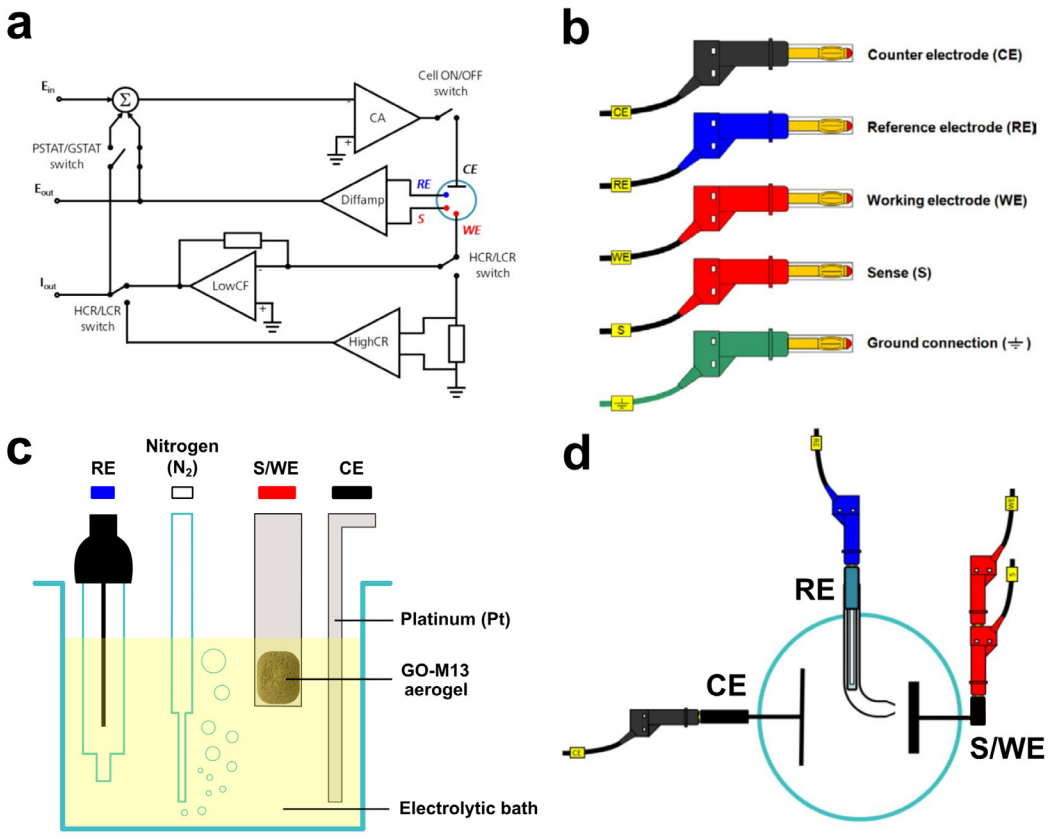


Figure 2.6. Schematic representation of PGSTAT and the electrolytic bath

(a) Schematic representation of the PGSTAT system and **(b)** its connectors.[253] **(c)** Side and **(d)** top views of the electrolytic cell set up.[253] The three electrodes set up consists of reference, working and counter electrodes as well as a glass nitrogen sparger.

CV is a type of potentiodynamic electrochemical measurement generally used to study the electrochemical properties of an analyte in solution or of a molecule adsorbed onto an electrode. Moreover, CV is employed to observe the electrochemical window in which the analyte is electrochemically active in certain conditions. This provides information on the reduction potential which better triggers the electrodeposition of the analyte onto the target (analyte).[255] CA is an electrochemical technique in which the potential of the working electrode is modulated producing a step in the current signal and the resulting current from faradaic processes occurring at the electrode is monitored as a function of time. Therefore, it allows an electrolyte to be electrodeposited at a specific voltage during a defined time.

As far as the PGSTAT setup is concerned, the CE is used to close the current circuit in the electrochemical cell and it does not participate in the electrochemical reaction without altering the process taking place at the WE. It is usually made of an inert material which in this case was platinum (Pt), but it could also be Au, graphite or glassy carbon. The RE is an electrode with a stable and well-known electrode potential regardless of the electrochemical potentials and currents employed, and it is used as a reference in the electrolytic cell for the potential control and measurement. The WE, coupled with the channel sense (S), is the electrode on which the reaction of interest occurs, which in this case was the GPA directly connected on a silicon wafer.[253,254]

In the three-electrode cell setup **(Fig. 2.6)**, the current flows between the CE and the WE. The potential is controlled between the WE and the CE and measured between the RE and S. Given that S/WE is kept at stable potential, by controlling the polarization of the CE, the potential difference between RE and WE is controlled all the time.[253,254] This mode is commonly used for the electrolytic cells in which a separate RE is used. It is

common practice to place the RE as close as possible to the WE to reduce the uncompensated resistance as well as the ohmic losses arising from this resistance. This can be obtained by physically placing the RE close to the S/WE or by using a Luggin-Haber capillary. The Potentiostat/Galvanostat Autolab PGSTAT204 was employed to perform cyclic voltammetry and chronoamperometry, to identify the reduction potential of the gold dissolved in the electrolytic bath and to perform its electrodeposition onto GPA, respectively **(Chapter 6.3)**.

2.3. Characterisation Methodologies

2.3.1. Ultraviolet-Visible Spectroscopy (UV-Vis)

It refers to the absorption or reflectance spectroscopy in part of the ultraviolet (UV) and the full, adjacent visible (Vis) spectral regions, that affects the perceived colour of the chemicals involved, due to the electronic transitions that atoms and molecules undergo in these regions of the electromagnetic spectrum. Absorption spectroscopy is complementary to fluorescence spectroscopy, in that fluorescence deals with transitions from the excited state to the ground state, while absorption measures transitions from the ground state to the excited state.[256]

Analytical chemistry often relies on UV/Vis spectroscopy, commonly carried out in solutions, for the quantitative determination of different analytes, such as transition metal ions, highly conjugated organic compounds, and biological macromolecules.[256]

The method is most often used in a quantitative way to determine concentrations of an absorbing species in solution, using the Beer-Lambert-Bouguer law **(Eq. 2.6)** where ***A*** is

the absorbance, $\boldsymbol{I_0}$ and $\boldsymbol{I}$ are the intensities of the incident and transmitted light at a given wavelength respectively, $\boldsymbol{\varepsilon}$ is the molar attenuation coefficient of a material ($cm^2\ mg^{-1}$ or $M^{-1}\ cm^{-1}$), $\boldsymbol{c}$ (mg mL^{-1} or M) is the concentration, which depending on the ε unit can be expressed in mg mL^{-1} or M and $\boldsymbol{l}$ is the path length (cm).[257,258]

$$A = log_{10}\ \frac{I_0}{I} = \varepsilon\ c\ l \qquad (2.6)$$

The spectrophotometer measures the amount of light absorbed by the sample. It is essentially made of a source of light, a monochromator that selects the specific wavelength, a sample holder, a detector and a computer that processes the data, usually shown as absorbance in the function of the wavelength **(Fig. 2.7)**.

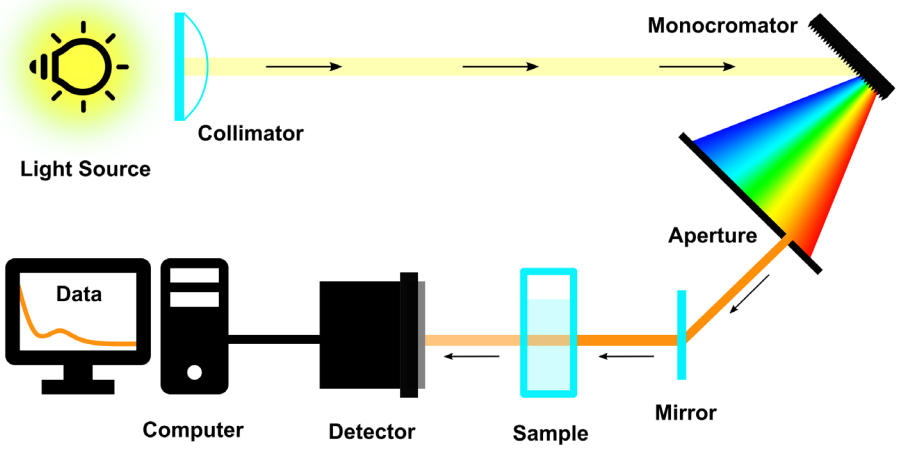


Figure 2.7. Schematic representation of the spectrophotometer

Schematic representation of the light pathway inside a standard spectrophotometer. The luminous radiation is collected with a collimating lens and directed to a monochromator, which separates the light in all its wavelengths. Subsequently, the desired wavelength is selected, and the light passes through an aperture which directs the beam to the sample which absorbs part of the light at specific wavelengths. Once passed through the cuvette containing the sample, the energy of the light is converted into an electric signal through a detector and analysed with a computer.

Through the Beer-Lambert-Bouguer law, the absorption of light can be related to the concentration and thickness of the material through which the light is passing. Therefore, is possible to calculate the concentration just by measuring the absorbance of the sample and knowing its ε, calculated at the maximum of its characteristic absorption peak.[257,258] Cary 60 UV-Vis spectrophotometer by Agilent Technologies was employed in numerous experiments in the following chapters. Thorlabs CV10Q1400 (1 cm light path) and Aireka QG10001 (0.1 cm light path) cuvettes were employed to analyse samples at low and high concentration respectively. Through the spectrophotometric analysis, M13 and graphene oxide (GO) absorption spectra were studied and used for their optical characterisation, quantification and study of their stability in different buffer conditions **(Chapters 3, 4)**. UV-Vis analyses were also crucial for the study of the self-assembly process between GO and M13 **(Chapter 5)**. Moreover, UV-Vis was employed for the quantification of SmPRXI and the detection of the enhanced green fluorescent protein (EGFP) connected to the modified M13 **(Chapter 7)**.

2.3.2. Fourier Transform Infrared Spectroscopy (FT-IR)

Fourier transform infrared spectroscopy (FT-IR) is a technique used to acquire the infrared absorption or emission spectra of samples in a solid, liquid or gas state. FT-IR is used in several research fields like geology, chemistry, materials and biology, to identify unknown materials and to analyse biomolecules, such as proteins.

It is based on the ability of some chemical groups to absorb the energy coming from infrared (IR) light and transfer it to the chemical bonds that characterise them, producing detectable vibrational modes, such as rocking, twisting, wagging, symmetric and anti-symmetric stretching.[259]

The FT-IR spectrometer is based on a Michelson interferometer, and it is composed of a source that produces IR monochromatic light, which after being divided by a splitter and reflected by two mirrors, one fixed and one moving, is recombined in a single beam, in phase, and transmitted to a detector, through the sample **(Fig. 2.8)**. The presence of the moving mirrors allows to alternate constructive and destructive interferences in the combined beam, which produces an interferogram, finally converted into a spectrum, using the Fourier transform, on a computer.[259]

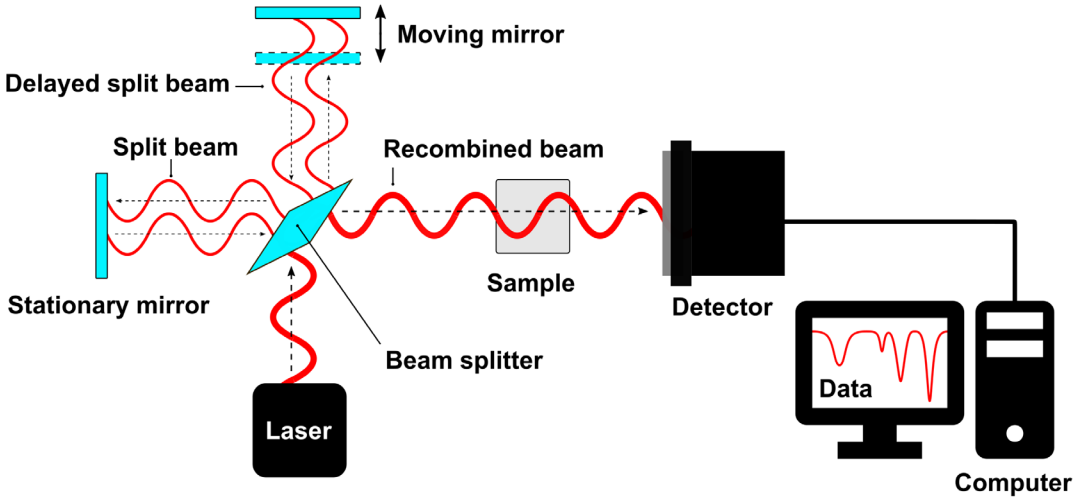


Figure 2.8. Schematic representation of the FT-IR spectrometer

Schematic representation showing the main components of an FT-IR spectrometer, which is essentially an interferometer. It consists of a source of light, a beam splitter, a static and a moving mirror. When the light goes through the splitter the beam is split into two beams directed to the static and the moving mirror respectively. After being reflected, these beams recombine again at the beam splitter and the resulting beam is directed to the detector, passing first through the sample. The path difference between these two beams produces an interference diffraction pattern, which is converted into a spectrum by the computer using the Fourier transform.

Nicolet 6700 FT-IR spectrometer by Thermo Fisher Scientific was employed to produce the fingerprint spectra of M13 and GO, to study their characteristic peaks **(Chapters 3.5.1, 4.6.1)**. In particular, in the study of M13, FT-IR allowed to detect PEG

contamination, due to the purification process. Lastly, this technique helped to study the interaction between GO and M13 in *GraPhage13* aerogel **(Chapter 5.4.3)**.

For these analyses, samples were prepared by grinding 200 mg of pre-dried potassium bromide (KBr) together with 2 mg of the sample. The mortared samples were subsequently transferred into a 13 mm diameter compression mold and compressed using a pressure of 10 Tons. This procedure led to the production of a transparent disk, ready to be scanned with an FT-IR spectrometer in transmission mode. Before analysing the samples, another disk containing only KBr was prepared following the same procedure and it was used as a blank to obtain the background spectrum. FT-IR spectroscopy was performed in transmission mode. The spectral region between 400–4000 cm^{-1} was scanned with a resolution of 4 cm^{-1} and 100 scans were acquired to obtain the final spectra.

2.3.3. Raman Spectroscopy

Raman spectroscopy is a technique used to observe vibrational, rotational, and other low-frequency modes in a system. It is generally used in chemistry to identify molecules by means of a structural fingerprint.

The Ramen effect was firstly observed by C. V. Raman and K. S. Krishnan in 1928 while experimenting on the scattering of light. This phenomenon is based on the inelastic scattering of monochromatic light (Raman scattering), that describes the excitation of photons to virtual energy states and the energy gained or lost due to the interaction of light, with the vibrational modes of the specific chemical bonds within the sample.[260]

The Raman spectrometer consists essentially of a laser beam that illuminates the sample which reflects part of the radiation, collected by a lens, and sent through a monochromator. Subsequently, the scattered radiation, corresponding to the laser wavelength (Rayleigh scattering), is filtered out while the rest of the light is collected by a detector **(Fig. 2.9)**. The acquired signal is elaborated with a computer, which produces the final spectrum.[260]

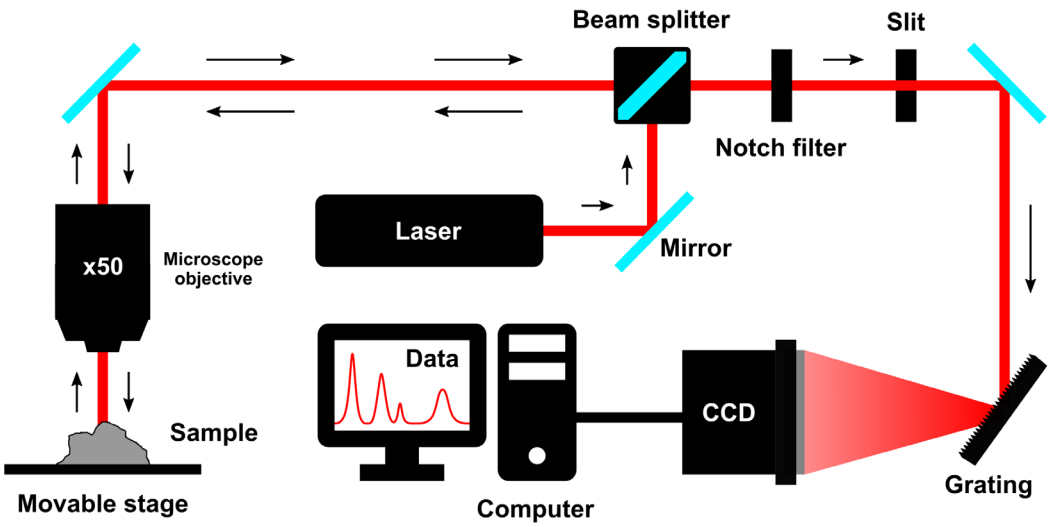


Figure 2.9. Schematic representation of the Raman spectrometer

Schematic representation showing the main components of a Raman spectrometer. The laser beam is split due to a beam splitter and directed to the objective aiming at the sample. Subsequently, the scattered radiation is directed to the detector connected to a computer, which analyses the signal providing the final fingerprint spectrum.

InVia Qontor Raman Spectrometer system by Renishaw equipped with a Leica confocal microscope DM2500, 633 nm RL633 Class 3B HeNe and 785 nm lasers were used to acquire the Raman spectra of M13, GO and *GraPhage13* aerogels implementing the FT-IR data **(Chapters 3.5.2, 4.6.2, 5.4.4)**.

For these analyses, non-polarised Raman spectra were obtained using a Renishaw inVia Qontor Raman Microscope system with a confocal microscope (Leica DM2500 equipped

with a 50× objective) at room temperature. Suitable edge filters for the lasers were used as well as single 1200 grooves mm^{-1} grating the resolutions of the spectra is 1.5 cm^{-1}. The laser power on the sample was always kept below 5 mW for both lasers, to avoid laser-heating effects on the probed samples and the concomitant softening of their Raman peaks. Representative Raman spectra of M13, GO and GPAs on silicon substrates were averaged out of 100 spectral acquisitions collected on a 100 μm^2 area in static mode for 30 s each, enabling optimisation of Raman signal while avoiding saturation of the detector. Silicon is commonly used as substrate and reference since it just shows one characteristic, strong and sharp peak at ~520 nm, without interfering much with the other peaks in the spectrum.[261,262]

2.3.4. Laser Diffractometry

2.3.4.1. ζ- potential

The zeta-potential (ζ) is expressed in Volts (V) and it is defined as the electric potential difference between the stationary layer of fluid attached to the analysed dispersed particle and the surrounding dispersion medium. The electric potential that originates at the interface between a solid surface and its liquid medium **(Fig. 2.10a)**.[263] The measurement of ζ-potential is possible due to the presence of anions and cations, dissolved in a medium, which can be attracted, and distribute in layers on the surface of other suspended particles, according to their charge.[264]

The instrument is made of a laser light source (red laser at 632.8 nm), a measurement cell connected to two electrodes which allow the current passing through to measure the ζ-potential and a series of detectors placed in different positions (175° or 90° depending

on the model). The signal is subsequently analysed with a computer connected to the machine **(Fig. 2.10b)**.

Zetasizer Nano ZS by Malvern Panalytical was employed to estimate the ζ-potential of M13 and to study its charge properties, to identify potential interactions with other components involved in the self-assembly of novel nanostructures **(Chapters 3.3.1, 5.3)**.

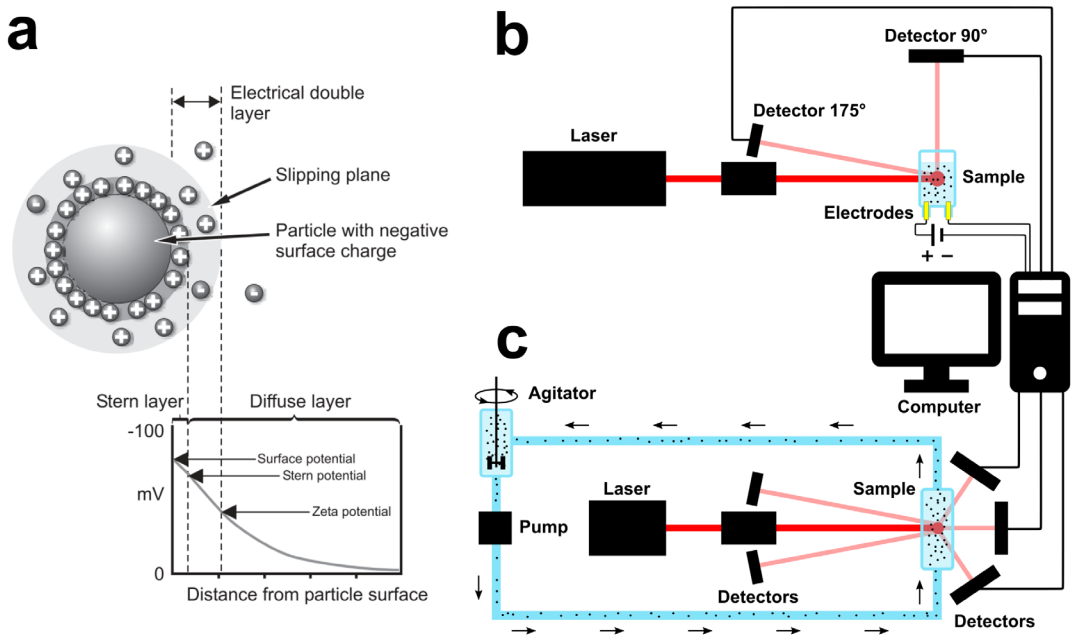


Figure 2.10. Schematic representation of particle size analysers

(a) Schematic of the diffuse layer surrounding a spherical particle.[264] Schematic representation of **(b)** the Zetasizer Nano and **(c)** the Mastersizer 2000 by Malvern.

2.3.4.2. Particle Size Distribution

The accepted theory which accurately predicts the light scattering behaviour of all materials particles under all conditions, and that overcome the limitations of the Fraunhofer model, is known as Mie theory.[265–269] It was developed to describe the scattering behaviour of spherical particles and the way light passes through or is absorbed by them. This theory is very accurate, but it needs to be integrated with specific

information about the analysed particle, such as its refractive index and absorption. Therefore, if the size of the particles and other structural details are known, the way these will scatter light can be accurately predicted. Each size of particle will have a characteristic fingerprint scattering pattern, that is unlike any other size of the particle.

The Malvern Mastersizer uses laser diffraction techniques, based on the principles of static light scattering (SLS) and Mie theory[270] to calculate the size distribution of particles in samples. These could be suspensions of solid particles, emulsion droplets, or dry powders. By the SLS principle, small particles scatter light at larger angles than large particles. The resulting scattering pattern is recorded, and the distribution of particle sizes can be calculated by applying Mie scattering theory.[265–269]

The instrument is essentially composed of two light sources (blue LED laser at 466 nm and red HeNe gas laser at 633 nm), a measurement cell connected to a pump, which keeps the sample constantly mixed and a series of detectors placed in different positions, acquiring many snapshots of the scattering pattern (typically 1000 snapshots per second) **(Fig. 2.10c)**. Once the measurement is completed, a computer processes the raw data calculating which size of particle created that pattern, through a dedicated software which uses the theory mentioned above.[271]

Mastersizer 2000 by Malvern Panalytical was used to measure the GO particles size distribution **(Chapter 4.5)**.

2.3.5. Scanning Electron Microscopy and Energy-dispersive X-ray Spectroscopy (SEM/EDX)

The scanning electron microscope (SEM) coupled with energy dispersive X-ray (EDX) spectroscopy is widely used for the characterisation of inanimate samples (which can also be biological samples) to obtain high-resolution images and detect their elemental composition.[272]

SEM is a type of electron microscope that produces images scanning the surface of samples with a focused electron beam. The electrons interact with the atoms of the sample, producing various signals containing information about the surface topography of the sample with nanoscale resolution.[272] SEM can also be coupled with EDX which is an analytical technique used for the elemental analysis or chemical characterisation of samples. It consists of a source of X-ray exciting the sample which produces a unique electromagnetic emission corresponding to its specific atomic structure.[272] This can be plotted into a spectrum which shows specific peaks for each element of the periodic table.

The SEM/EDX is essentially made of an electron gun which generates an electron beam passing through an anode and focused by magnetic lenses onto a movable stage where the sample is placed. The microscope has separate hardware for the EDX, which include a source of X-ray, all controlled by a computer **(Fig. 2.11)**.[272]

XL30 ESEM FEG by Philips equipped with an INCA X-sight by Oxford Instruments was used for the morphological study and the elemental composition analysis of *GraPhage13* aerogel **(Chapter 5.4)**. Moreover, Tabletop Microscope TM3030 by HITACHI was employed for the study of *GraPhage13* aerogel, subject to gold-electrodeposition and functionalisation with carbon nanotubes (CNTs) **(Chapters 6.3, 6.4)**.

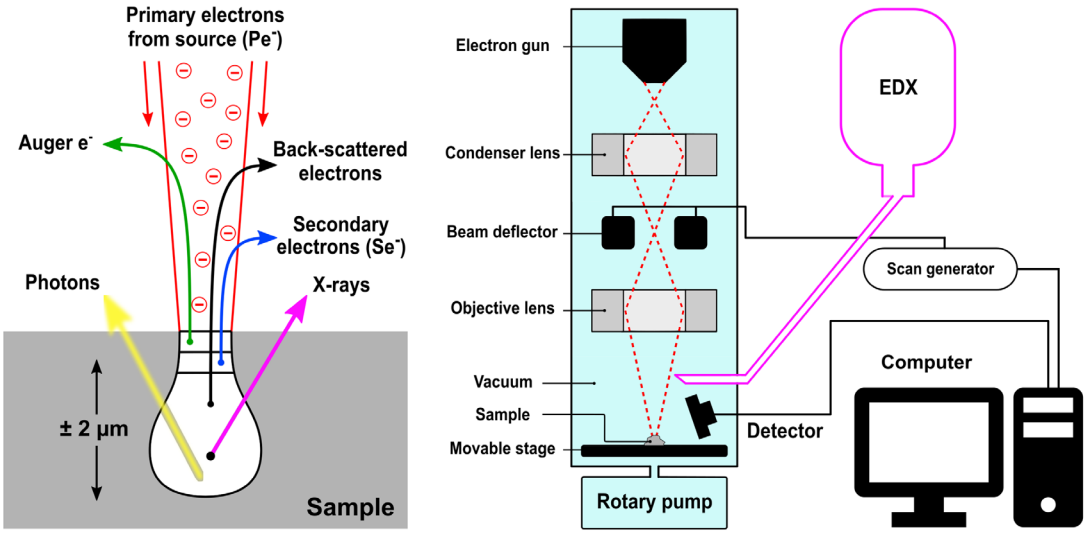


Figure 2.11. Schematic representation of the SEM/EDX

At the left, an electron beam hitting the surface of a sample, producing several phenomena detectable by the SEM/EDX. At the right side, the schematic representation of a conventional SEM. It is composed of an electron gun and a series of lenses, which focus the electron beam on the sample surface producing detectable electron species and signals, subsequently converted into images by the computer.

2.3.6. Atomic Force Microscopy (AFM)

The atomic force microscope (AFM), also referred to the scanning force microscope (SFM), is part of a larger family of instruments named scanning probe microscopes (SPMs).[273] Commonly, all SPM techniques use a very sharp tip mounted onto a cantilever scanning across the surface of the sample. When the tip is brought into proximity of the sample surface, the force acting between the sample and the tip (***F***) can be described with the Lennard-Jones potential curve **(Fig 2.12a)**, and calculated with the Hooke's law **(Eq. 2.7)** knowing the stiffness of the cantilever (***k***) and the distance that the lever is bent (***x***).

$$F = k\,x \qquad (2.7)$$

AFM measures different forces such as mechanical contact, van der Waals, capillary, chemical bonding, electrostatic, magnetic and solvation forces **(Fig. 2.12a, b)**. There are several modes that AFM can operate depending on the specific application, such as imaging in contact, intermittent contact (tapping) and non-contact modes as well as operate as a force sensor or nanomanipulator. For what concerns the application of AFM for imaging purposes, the interactions between the probe and the surface, allow the microscope to acquire very high-resolution three-dimensional topographic images of the sample surface. Moreover, depending on the technique and sharpness of the probe tip, sub-nanometre scale resolution can be achieved.[273]

The AFM was first described by Binnig *et al.* as a new technique for imaging the topography of surfaces at high-resolution.[274] It was created to overcome the limitations of STM, which was able to image only conductive samples in vacuum.

The AFM is usually installed onto an antivibration stage and surrounded by an insulation cabinet to avoid any vibration from the surrounding. The core of this microscope consists essentially of a probe comprised of a tip mounted at the apex of a flexible cantilever, a piezoelectric crystal, a laser light source and a detector, all connected to a computer **(Fig 2.12)**.

The probe is mounted on a piezo crystal, allowing it to scan the sample surface along the X, Y and Z axes. Before scanning, the probe approaches the sample while the vertical and lateral deflection of the cantilever is constantly monitored. The movement of the cantilever is recorded by a laser directed on its reflecting surface and reflected onto a detector. Therefore, the laser spot moves onto the detector accordingly to the movement of the cantilever and the signal acquired is subsequently elaborated by the computer providing the final images **(Fig 2.12c)**.[273]

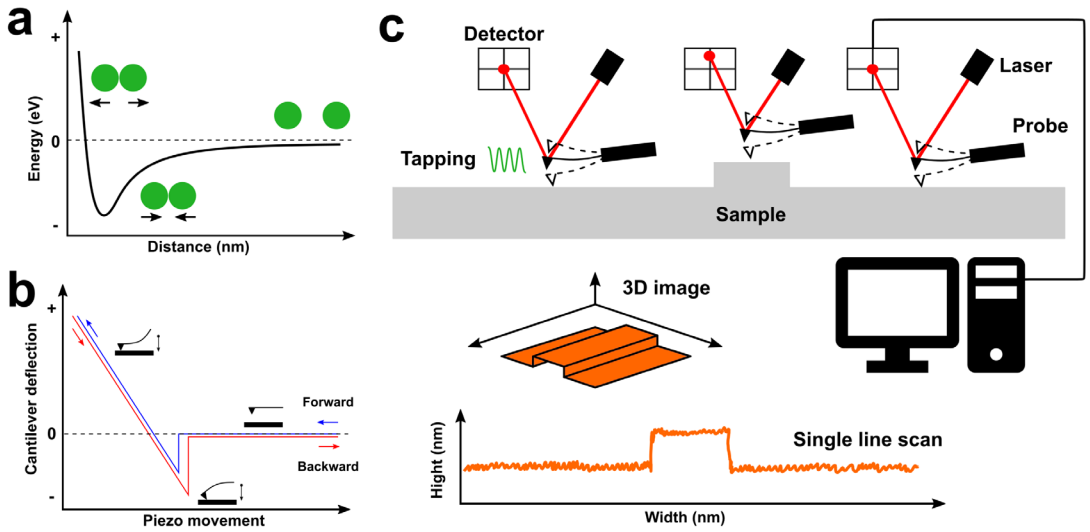


Figure 2.12. Schematic representation of the AFM

(a) Lennard-Jones potential curve indicating the attraction/repulsion energy between two particles. **(b)** AFM force diagram illustrating how the cantilever bends depending on the distance from the surface of the sample. **(c)** Schematic representation of an AFM in tapping mode scanning on a surface presenting a step. The oscillating cantilever scans on the sample surface while a laser beam reflected on its surface is projected to a detector to be recorded. The movement of the laser corresponding to the movement of the probe is converted in numerous single line scans, which together form a topographical 3D image of the sample surface.

NanoWizard II by JPK equipped with a BRUKER RTESPA-300 probe (Thickness: 3.4 µm; Length: 125 µm; Width: 40 µm; Resonant frequency: 300 kHz; Spring constant: 40 N m^{-1}) was used in tapping mode for the characterisation of M13 **(Chapter 3)**, GO **(Chapter 4)** and their derived nanostructures **(Chapters 5, 7, 8)**.

2.3.7. Rheology

Rheology is a branch of physics used to describe and study deformation and flow behaviour of materials under certain conditions in response to an applied force. This provides information that can be used to classify liquid, viscous and solid materials.[275]

Using a rheometer to monitor the shear stress versus the shear rate of a sample, provides important data to characterise its viscoelasticity. This, for instance, can be subsequently used to test different formulation of the analyte as well as identify potential applications.[275]

Focusing on the study of fluids, when the viscous stresses arising from its flow, are linearly proportional to the local strain rate which is changing over time, at every point, that fluid is defined as Newtonian **(Fig. 2.13a)**.

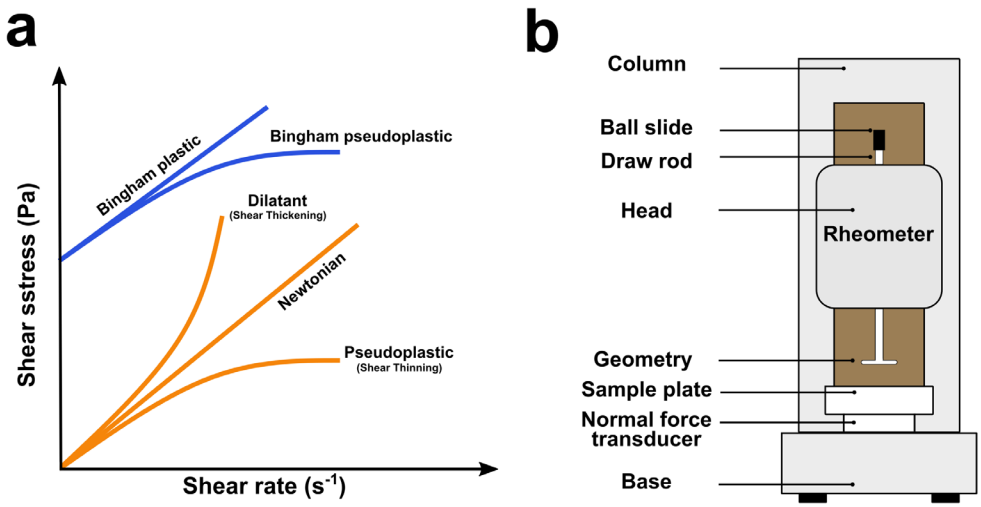


Figure 2.13. Schematic representation of the rheometer

(a) The shear stress as a function of shear rate functions for different kinds of fluid. **(b)** Schematic representation of a rheometer and its components.

This is considered the simplest mathematical model of fluids to describe viscosity. Interestingly, no real fluid fits this definition perfectly, however, the behaviour of many common liquids and gases, such as water and air, can be approximate to a Newtonian for practical calculations under ordinary conditions.[275] On the other hand, when fluids do not follow Newton's law of viscosity, they are defined as non-Newtonian. These fluids do not show a linearly proportional relation between the shear stress and the shear rate and a

constant coefficient of viscosity cannot be defined.[275] Non-Newtonian fluids can be studied through several other rheological properties *via* relating stress and strain rate tensors under several different flow conditions using different devices or rheometers.

Non-Newtonian fluids can be also categorised in shear thickening and shear thinning when the viscosity of the fluid appears to increase when the shear rate increases and *vice versa*, respectively. Moreover, there are Bingham plastics which are fluids showing a linear shear stress/shear strain relationship which require finite yield stress before they begin to flow as well as anti-thixotropic and thixotropic fluids, which require a gradually increasing shear stress to maintain the strain rate constant and *vice versa*, respectively.[275]

The rheometer is an instrument that measures how a liquid or suspension flows, as a response to applied forces. This is possible because when their molecules and/or particles are put into motion, they are forced to slide along each other producing a flow resistance caused by the internal friction.[275]

The rheometer can be essentially divided into two parts, the 'head' and the 'platform'. The first one is composed of a motor which moves a kind of piston called 'geometry' (this is due to the vast range of shapes that are commercially available), which directly applies a shearing force on the sample. The platform, located underneath the geometry, is where the sample is deposited and usually is equipped with a temperature control system. Finally, the applied force applied to the sample placed between the geometry and the platform is measured with a torque sensor and analysed through the computer **(Fig. 2.13b)**.[275]

An HR-1 Discovery Hybrid Rheometer by TA Instruments with a TA geometry 991437 (cone angle: 20° 0' 14", cone diameter 20 mm and truncation 55 μm) was employed for

the characterisation of *GraPhage13* hydrogel (GPH), which is an intermediate product in the production of GPA **(Chapter 5.3.3)**.

2.3.8. Brunauer, Emmett and Teller Method (BET)

Brunauer, Emmett and Teller (BET) is a technique aimed to explain the physical adsorption of gas molecules on a solid surface, providing data to calculate the specific surface area of materials through the BET theory.[276]

The specific surface area of a sample is determined by the physical adsorption of a gas (usually N_2) on its surface and by calculating the amount of adsorbed gas corresponding to a molecular monolayer. Physical adsorption is due to the relatively weak forces between the adsorbed gas molecules and the adsorbent surface area of the sample. The measurement is usually carried out at the temperature of liquid nitrogen and the amount of gas adsorbed can be measured by a volumetric or continuous flow procedure. The specific surface area determined by BET relates to the total surface area. This corresponds to the reactive surface adsorbing the gas molecules, which is normally larger than the surface area determined by air permeability **(Fig. 2.14a)**.[276]

The instrument consists of a pump to purge the nitrogen in the analytical chamber where is the sample, a dewar filled with liquid nitrogen to keep the sample temperature low and the data acquisition system connected to a computer, which analyses the raw data **(Fig. 2.14b)**.[276]

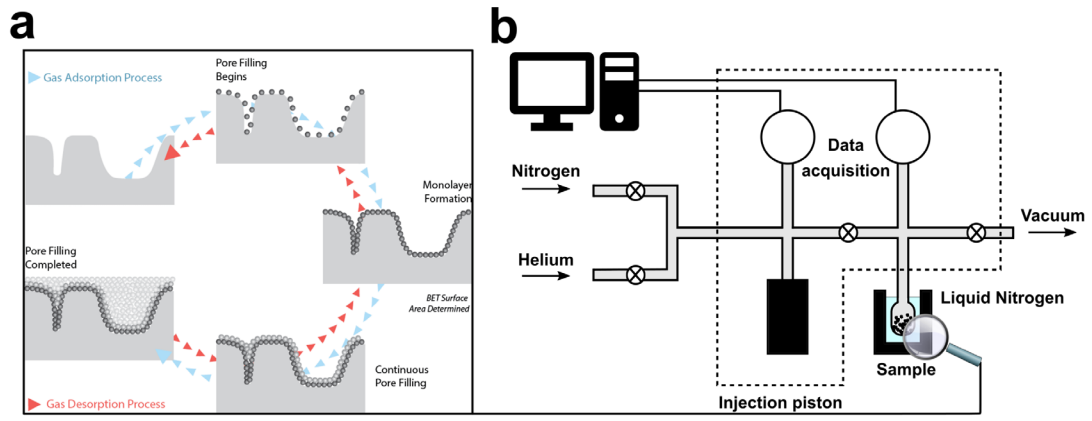


Figure 2.14. Schematic representation of the BET instrument

(a) The adsorption/desorption cycle performed into the BET apparatus. **(b)** The schematic representation of a BET system.

3 Flex Physisorption by Micrometrics was used to estimate the surface area of GPA samples **(Chapter 5.4.2)**. Before the analysis, samples were dried with a nitrogen flow or under vacuum at 40°C overnight. Subsequently, the volume of gas adsorbed to the surface of the particles was measured at -196°C. The amount of adsorbed gas is then correlated to the total surface area of the particles, including pores in the surface and the final calculation based on the BET theory is performed by the computer.

2.3.9. Gel Electrophoresis

Gel electrophoresis is a technique employed to separate biological macromolecules, such as DNA, RNA and proteins, according to their charge and size.[277] This technique involves the use of acrylamide or agarose gels immersed in an electric field, that act as size-selective sieves for the fragments running through them.

In particular, to allow protein separation in a size range from 5 to 250 kDa, the most popular form of electrophoresis is the sodium dodecyl sulfate-polyacrylamide gel

electrophoresis (SDS-PAGE).[277] SDS is a negatively charged detergent that denatures proteins by breaking their non-covalent internal bonds. Moreover, SDS binds proteins through non-covalent interactions, imparting them an overall negative charge, which is proportional to the protein mass. Therefore, the SDS and PAGE system allows the protein migration through the gel, separating proteins depending on their MW.[277]

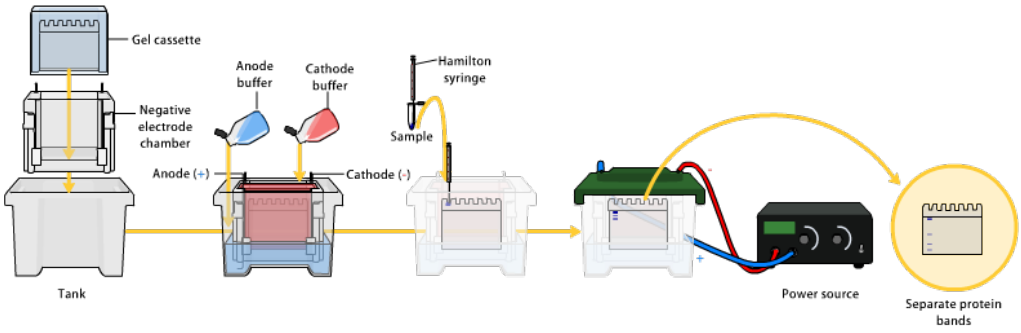


Figure 2.15. Schematic representation of the SDS-PAGE

The essential steps to perform the electrophoresis. Briefly, the tank is assembled and filled up with the appropriate running buffers, while a Hamilton syringe is used to load the samples in the wells of a polyacrylamide gel. Subsequently, the tank is connected to a power source which applies a potential which allows the protein separation within the gel.

In SDS-PAGE applications, a vertically oriented polyacrylamide gel is mounted between two buffer chambers, in such a way that the only electrical path between the buffers is through the gel itself **(Fig. 2.15)**. The top part of the gel is characterised by a series of wells in which the protein samples are loaded. Once the current is applied across the buffer chambers, the proteins are forced to travel through the pores of the gel, being separated in bands of smaller, low molecular weight proteins, that migrate faster through the matrix and bigger, high molecular weight proteins that accumulate in higher sections of the gel.[277]

This technique was performed with a BIO-RAD electrophoresis apparatus, and it was employed in **Chapter 7.3** to check the SmPRXI purity obtained through affinity chromatography purification.

2.4. Additional Equipment Used

Apart from the equipment listed so far, additional small scale instruments were employed to perform the experiments, such as analytical balance Pioneer PA114C by OHAUS, Genlab classic oven, Airstream Class I Biological Safety Cabinet (E-series) by ESCO, pH meter FiveEasy equipped with InLab Microprobe by Mettler Toledo, MaxQ 4450 Incubated Orbital Shakers by Thermo Fisher Scientific, benchtop centrifuge SciSpin MICRO by SciQuip, ultracentrifuge J2-21 equipped with a JA 10 rotor by BECKMAN Coulter, vacuum chamber equipped with a rotary vacuum pump E2M2 by Edwards, optical microscope DM2500 by Leica equipped with a camera DMC2900 and dedicated designed UV-Vis-IR spectrometer by Horiba.

2.5. Software for the Data Analyses

All figures were composed using Inkscape 0.92.4 and the references organised with Mendeley. Microsoft Office Excel 365, OriginLab 2019b, Wolfram Mathematica and GraphPad PRISM 6 were used for calculations and final data plotting of all spectra and charts. Error bars represent mean ± SD. Statistical significance was assessed performing 2-way ANOVA with a post hoc test of the relevant pairs of samples. $*p < 0.05$,

$^{**}p < 0.01$, $^{***}p < 0.001$, $^{****}p < 0.0001$. PyMOL® 1.7.x was used to illustrate protein structures and calculate alternative pKa values through the additional tool PROPKA. UV-Vis spectra data collection was performed using the dedicated software CaryWinUV by Agilent Technologies. FT-IR analyses and data collection were performed using the dedicated software OMNIC by Thermo Scientific. Raman analyses and data collection were performed using the dedicated software WiRE 5.0 by Renishaw. M13 potential data collection was performed using the dedicated Zetasizer Software v7.12 PSS0012 by Malvern. Particle size distribution data collection was performed using the dedicated software M2000 v560 PSS0002 by Malvern. Optical Microscopy images were collected using the Leica Application Suite X (LAS X). SEM/EDX images were acquired using the Microscope control Kewell software by Philips. The AFM images were edited using JPK SPM Data Processing 5.1.8 and Gwyddion 2.53. Rheology analyses and data collection were performed using the dedicated software TRIOS v4.4.0.41128 by TA Instruments. BET isotherm curves were acquired using the dedicated Micrometric software. The electrochemical experiments were controlled with the dedicated software NOVA 2.1.3 by Metrohm-Autolab. The contact angle of water on *GraPhage13* was measured using ImageJ. Affinity and Size exclusion chromatography were controlled, and the data acquired using PrimeView and Unicorn 5.11 by General Electric Healthcare Life Science, respectively.



UNIVERSITY OF
BIRMINGHAM

CHAPTER III

M13 Characterisation



Abstract

M13 completely revolutionised science in several scientific fields, ranging from virology to molecular biology, up to nanotechnology for the manufacturing of smart components and functional materials employed in numerous applications. This chapter has the intent to show some of the production methods and procedures to characterise M13, through bioinformatics, microscopy and spectroscopy methods as well as report fundamental information about its structural composition and properties.

Paolo Passaretti

3.1. Introduction

M13 is more than a simple virus, as indicated by the vast range of applications in which this nanoscopic biological entity has been employed over the last fifty years. **Chapter 1** provides an extensive description of how M13 research changed over time, starting from the initial studies predominantly focused on its nature (protein structure, genome and infective cycle), to the employment in phage display systems and more sophisticated applications.

As M13 plays a pivotal role in the fabrication of the novel nanostructures discussed in this thesis, crucial studies were performed to characterise and understand the fundamental properties of this extraordinary nanoscopic building block.

The work reported in this chapter focuses on the methodologies employed for the production and characterisation of M13. A detailed description of the methodologies adopted is reported starting from the propagation, purification and quantification of M13, to its characterisation through several microscopy and spectroscopy analyses. These methods are also important to study M13 assembled with other components forming the novel composite materials described in the following chapters.

The production of M13 was accomplished by exploiting its natural infectivity against *E. coli* strains showing the *F-pilus*.[43] Therefore, the phage was propagated *via* infected *E. coli* batch cultures[49,54,138] and purified through PEG/isoelectric precipitation.[154,155] UV-Vis spectroscopy was employed to quantify the virus in water or buffers as well as to study its stability in different pH conditions. The study of the PVIII protein through a bioinformatics approach, together with the measurement of the ζ-potential was used to characterise the external surface charge of M13.[278–280] Due to its nanoscopic dimensions,

atomic force microscopy (AFM) was used to characterise the phage morphology.[281] Finally, Raman and Fourier transform infrared spectroscopies (FT-IR) were employed to obtain the fingerprint spectra, which are essential for the characterisation of potential chemical interactions and to validate the presence of residual contaminating PEG in the new M13 stocks after the purification procedures.[282]

3.2. M13 Small Scale Production

3.2.1. Propagation in Batch Culture

M13 bacteriophage (M13KE) was purchased from New England Biolabs as double-stranded DNA (dsDNA) and transferred into One Shot™ TOP10F′ Chemically Competent *E. coli* through heat shock. Subsequently, the phage was self-propagated in batch cultures in the *E. coli* strain TOP10F′, exploiting its natural infection process **(Fig. 3.1)**.

The infection procedure started with the preparation of 2.22 L of 25 g L^{-1} nutrient broth (NB) No. 2 split into 6 conical flasks of 2 L (370 mL each), which were subsequently autoclaved at 120°C for 20 min. When the flasks had cooled down to room temperature, 370 µL of tetracycline (TCN) 5 mg mL^{-1} was added to each flask under aseptic conditions. Then, 500 µL of *E. coli* TOP10F' and 0.05 g of M13 were added into each flask and incubated in an incubator overnight (16–18 h) at 32°C and agitated at 150 rpm.

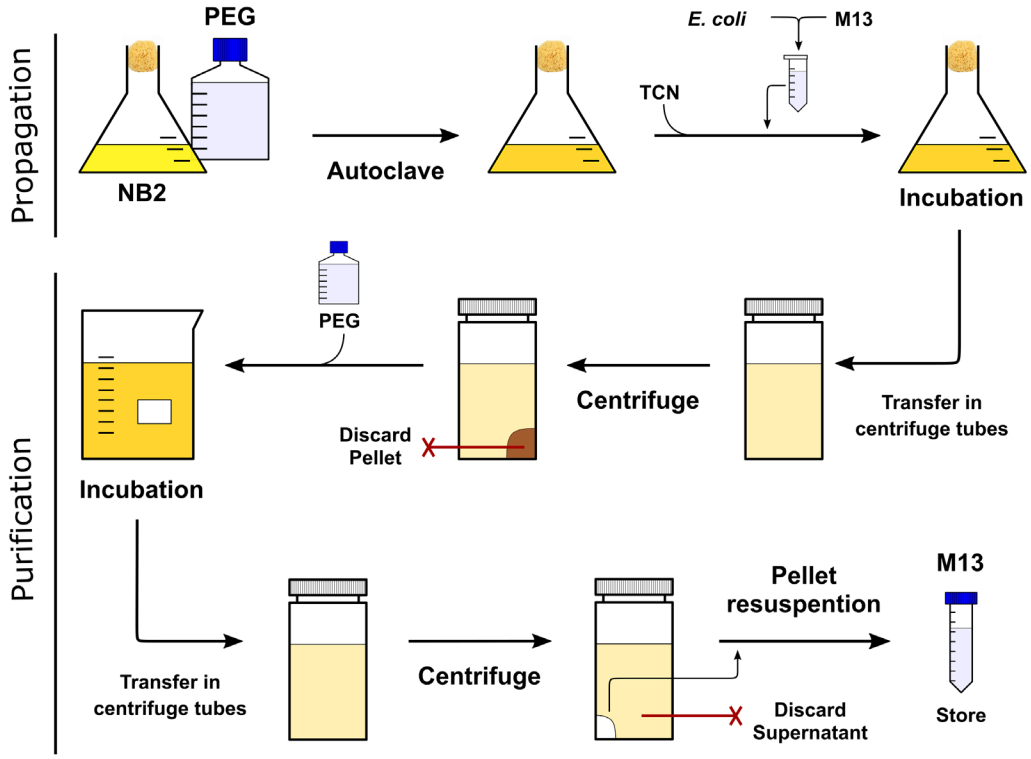


Figure 3.1. M13 propagation and the purification procedure

Schematic representation of the main procedural steps for the propagation and purification of M13. In the first row, the co-incubation of *E. coli* and M13, which is part of the propagation procedure is shown. Following, the essential steps of the phage purification through PEG precipitation.

3.2.2. Purification *via* PEG/NaCl Precipitation

Cultures within the flasks appeared turbid after 24 h due to bacterial growth. The broth containing *E. coli* and M13 was removed from the incubator, transferred in the appropriate tubes (500 mL) and centrifuged with an ultracentrifuge at 8000 rpm (RCF = 11 295.1 *g*) for 30 min at 4°C to pellet the cells. The supernatant was carefully collected from each tube, while the pellet consisting predominantly of *E. coli*, was discarded. This process was repeated twice to ensure that most of the *E. coli* were removed from the solution.

Approximately 80% of the remaining supernatant (300 mL) from each flask was transferred into a 3 L beaker and mixed with a 1:5 ratio PEG/NaCl (polyethylene glycol 6000 and sodium chloride) solution and left stirring on ice for 90 min. The PEG/NaCl stock solution was previously prepared by mixing 250 g of PEG and 146 g of NaCl in 1 L of deionised water (DIW) and then autoclaved at 120°C for 20 min. The addition of PEG/NaCl to the supernatant caused the precipitation of M13, then through several further centrifugations, the bacteriophage was purified.

The M13-PEG solution was split into six centrifuge tubes and centrifuged at 10 000 rpm (RCF = 17 648.6 *g*) for 30 min at 4°C. The supernatant was discarded and the white pellet containing M13 was resuspended by adding 1–2 mL of DIW in each tube depending on the size of the pellet. Once resuspended, all the pellets were merged in one beaker and incubated with PEG/NaCl for another 90 min as in the previous step.

The M13-PEG solution was then separated into some microtubes, placed in a benchtop centrifuge and spun at 15 000 rpm for 15 min (RCF = 15 100 *g*). The resulting supernatant for each tube was discarded, and the white pellet containing M13 was resuspended in 0.1–1 mL of DIW (or other saline buffers). To remove further *E. coli* or big residues which were potentially contaminating the final stock solution, further centrifugation at 15 000 rpm for 5 min (RCF = 15 100 *g*) was performed and the resulting brown pellet was discarded. The brown pellet should mainly contain residual *E. coli* cells, cellular detritus and other impurities from the growing media.

All the supernatants were carefully collected in a single tube and stored in the fridge at 4°C. M13 can be also stored in a freezer at -20°C or -80°C by adding 25–50% glycerol to protect the phage from the formation of ice crystals, which can damage its structure.[283]

The resuspension of M13 in a saline buffer, such as PBS (Phosphate-buffered saline, pH 7.33), allows for better stability due to its natural pH and ionic strength.[283] However, the resuspension of M13 in DIW allows for ease in the deposition of the phage onto substrates (e.g. a silicon wafer) commonly required for several analyses. The deposition through drop-casting of M13 in DIW avoids the formation of salt crystals on the substrate, which could interfere with most analyses. M13 stability in DIW and other buffers were tested with the results discussed within this chapter.

The final concentration of new stocks was calculated by performing a serial dilution and spectrophotometric analysis. The production method described so far can be considered the standard and was adopted during most of the project. However, other methods characterised by marginal differences have been tested and described in **Appx. 3** and **4**.

PEG precipitation is the most convenient method to purify M13, however, residual PEG can contaminate the new stocks. This can be difficult to be removed and its presence can hamper the phage reactivity with other components.[155] To reduce the residual amount of PEG, isoelectric precipitation was performed by adjusting the pH to 4.1 with 5 M HCl. This method causes the proteins to precipitate by reducing their solubility at pH values closer to their IEP.[155] Once the pH was reduced, the solution immediately showed evident flocculation with white agglomerates, therefore, the sample was quickly precipitated *via* centrifugation and resuspended in PBS or DIW.

3.2.3. UV-Vis Characterisation and Quantification

To estimate the concentration of M13, UV-Vis spectrophotometry and the Beer-Lambert-Bouguer law were employed **(Chapter 2.3.1)**.

Given that viruses are essentially made of protein and nucleic acids, the UV-Vis spectrum of M13 appears very similar to the spectra of DNA and proteins, combined.[284]

DNA absorbs the light in the range of 150–300 nm showing two main peaks. The contribution to the absorption below 180 nm is due to the deoxyribose and the absorption between 180–300 nm comes from the nitrogenous bases.[285]

Proteins absorb the light in the range of 180-300. Around 180–230 nm is almost entirely due to the $\pi \rightarrow \pi^*$ transitions in the peptide bonds. On the other hand, the absorption in the range of 230–300 nm is due to the aromatic side-chains of tryptophan (Trp), tyrosine (Tyr), and phenylalanine (Phe) residues, and there is also a weak contribution by disulfide bonds near 260 nm.[286–289]

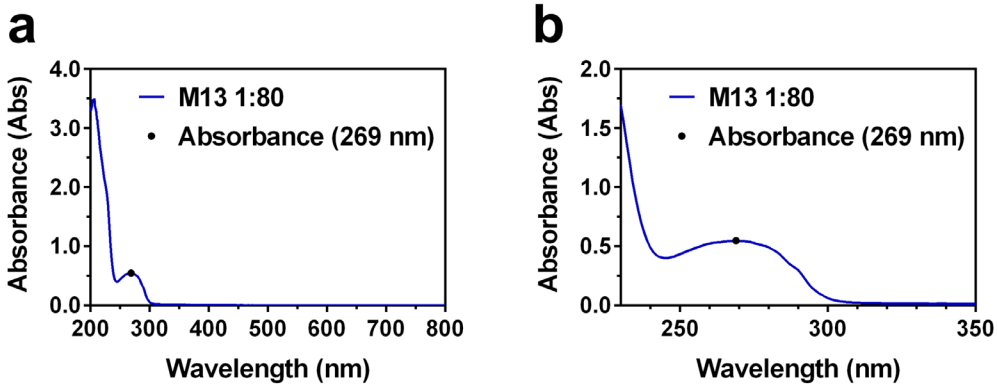


Figure 3.2. UV-Vis characterisation and quantification of M13

UV-Vis spectra of an M13 stock diluted 80 times is shown. This stock was obtained with the previously described procedure. **(a)** The blue line represents the absorbance of M13 across the entire UV-Vis spectrum. **(b)** Shows the M13 spectra between 230–350 nm for clarity. The black dots indicate the absorbance at 269 nm used to estimate the phage concentration.

In general, the UV-Vis quantification of DNA and proteins is based on the absorption at 260 and 280 nm respectively. Therefore, the presence of a peak at 269 nm and a higher

absorption in the region below 240 nm in the UV-Vis spectrum of M13 **(Fig. 3.2)** is coherent with the previous considerations.[290]

To estimate the phage concentration, an absorbance between 0.1 and 2 should be measured at 269 nm. A value outside this range will be affected by stray light disrupting the linear correlation between concentration and absorbance.[291] However, modern spectrophotometers produce reliable data at absorbance values > 2. For this reason, when the stock is too concentrated is necessary to dilute it before the analysis. Moreover, to check the quality it is important that the spectrum shows the minimum around 245 nm and very low absorption at 320 nm.[290] The absence of the minimum at 245 nm could be due to general impurities in the solution, while, the absorption at 320 nm, that is due to a little light absorption from phage chromophores, is meant to crudely correct for light scattering from phage particles and non-phage particulate contaminants.[290]

The UV-Vis spectrum of an M13 stock is shown in **Figure 3.2**. For this measurement, 500 μL of M13 diluted in DIW (1:80) was loaded in a quartz cuvette (1 cm light path) and analyzed with the UV-Vis spectrophotometer. The sample was scanned in the wavelength range of 200–800 nm. Finally, M13 concentration was calculated with the Beer-Lambert-Bouguer law **(Eq. 2.6)**, using $A_{269\,nm} = 0.549$ and $\varepsilon = 3.84 \pm 0.06$ mg^{-1} cm^2.[47] The concentrations of this specific M13 stock was 11.44 mg mL^{-1}.

To calculate the phage concentration, there is also another technique pioneered by George P. Smith and based on the measurements by L. Day and R. Wiseman.[290] This approach considers the constant relationship between the length of viral DNA and the amount of the PVIII, which together are the major contributors to the absorption spectrum in the UV range **(Eq. 3.1)**, where $\boldsymbol{A_\lambda}$ is the absorbance at a specific wavelength.[290]

$$\frac{\text{virions}}{\text{mL}} = \frac{(A_{269} - A_{320}) \cdot 6 \times 10^{16}}{\text{number of bases} \cdot \text{virion}^{-1}} \quad (3.1)$$

Spherical phages are characterised by equal weight ratios between protein and DNA. On the other hand, filamentous phages have approximately six times more proteins.[290] Therefore, the PVIII contributes substantially to the total absorption in the range between 260–280 nm.

M13 was propagated and purified many times during this project showing different yields **(Table 3.1)**. Different factors such as temperature, pH, dissolved oxygen and contaminations could be the potential reasons behind these differences. However, the amount of phage produced with the method previously described was adequate to perform all the experiments.

Table 3.1. M13 stocks production

Date (aaaa/mm/dd)	Concentration (mg mL^{-1})	Volume (mL)	Quantity (g)
2017-05-19	7.07	11.4	80.6
2017-07-07	1.65	23.5	38.8
2017-07-18	7.63	10.7	81.6
2017-11-19	5.35	13.6	72.7
2017-11-27	11.44	8.4	96.1
2018-01-29	5.03	15.4	105.3
2018-01-29	5.32	18.9	100.6

3.2.4. Morphological Characterisation

Given the nanoscopic dimensions of M13, its morphology was characterised *via* AFM **(Chapter 2.3.6)**.

The sample used for the AFM analysis was simply prepared by depositing a drop of M13 dispersed in DIW on a clean substrate and left to air dry. The substrate used was a cleaned and oxidised *p*-type silicon wafer previously cleaved from a larger silicon wafer in a small square of ~0.5 cm^2 **(Chapter 2.2.4)**. The oxidation of the silicon substrate *via* plasma etching improves the spreadability of the sample drop onto its surface. This causes that the phages are distributed on the substrate well-spaced each other, facilitating the detection of individual viruses.

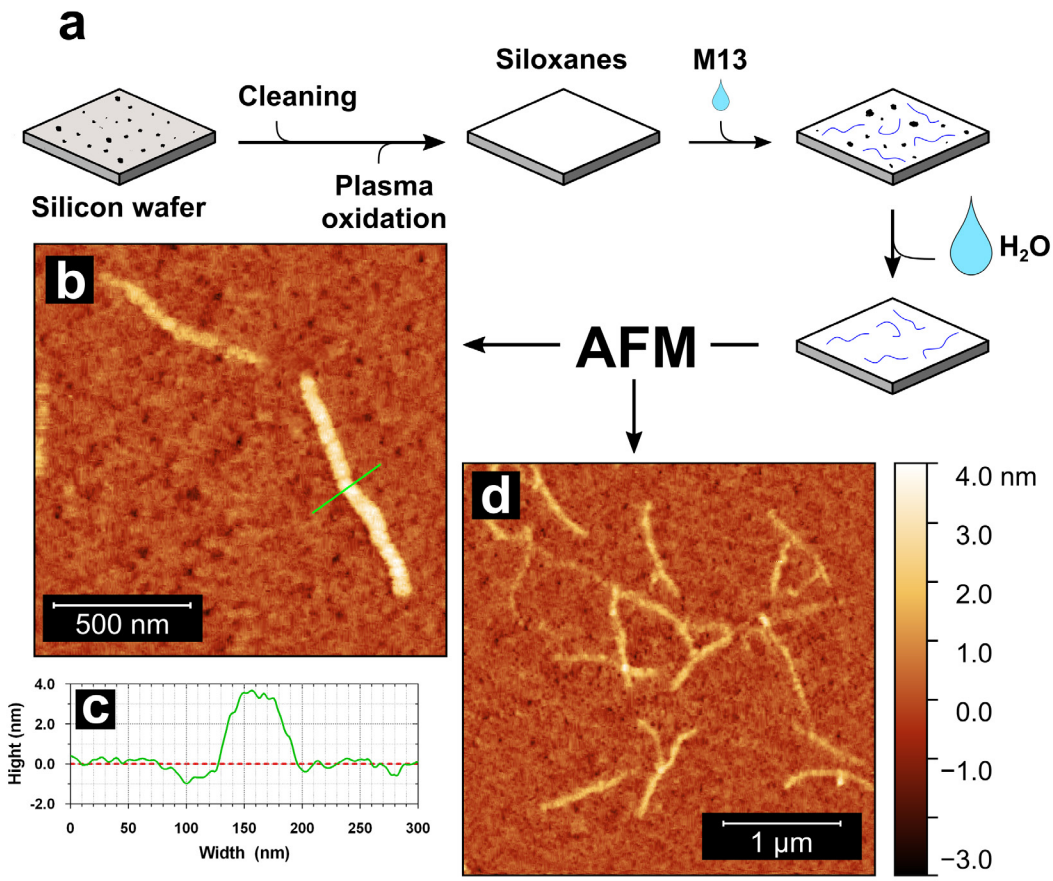


Figure 3.3. AFM analysis of M13 and sample preparation

(a) Schematic procedure for AFM sample preparation. **(b)** AFM images of individual M13 phages with **(c)** the relative cross-section of one of them. **(d)** AFM image of a group of M13 bacteriophages lied on the surface with some overlap.

Therefore, 10 μL of M13 0.005 mg mL^{-1} in DIW was deposited onto the substrate and left to air dry. This specific volume and concentration were found to be the best combination to obtain a nice distribution onto the substrate to easily observe M13 avoiding agglomeration as well as tangled or overlapped viruses.

After being rinsed with DIW **(Fig. 3.3a)**, the sample was analysed *via* AFM. The results **(Fig. 3.3b–d)** show that the phages measure ~900 μm in length and ~60 nm in width. The cross-section of the virus does not appear circular as expected, but it shows the height and width of 4 nm and 70 nm respectively. This situation can be explained considering the hydration level of the viruses, which can retain a small level of moisture from the air that together with the effect of the tip convolution, can increase the phage dimensions up to ten times.[281]

3.3. M13 Ionic Properties

Although, **Chapter 1** contains an extensive amount of detailed information about M13, a more in-depth study on the PVIII protein was necessary to clarify some aspects related to the ionisable species distributed along the phage body.

Studying the PVIII protein is crucial to understand which chemical bonds can be employed for the display of functional groups as well as predict possible intramolecular and intermolecular interactions for the design of self-assembly systems. Despite the vast amount of studies describing the ionic properties of other similar filamentous phages, such as *fd* and Pf1,[278] there is no clear information in the literature about M13. Therefore, to clarify which PVIII amino acids contribute to the total charge of M13 and,

consequently which chemical groups could be involved in the fabrication of supramolecular structures, M13 was studied combining bioinformatic data and measurement of the ζ-potential **(Chapter 2.3.4)**.

Before discussing in detail the structure of PVIII to understand its ionic properties, it is necessary to recall some concepts related to the acid-base balance of titratable groups. Among the 20 native amino acids in the proteins, approximately half of them contain side chains that are titratable groups. These groups can show negative or positive charge, such as Glu and Lys respectively.[292,293] Their charge depends on their pKa and the pH of their local environment. At the pH value corresponding to their pKa, half of the molecules are protonated (**HA**) and half deprotonated ($\mathbf{A^-}$), as described by the Henderson-Hasselbalch equation **(Eq. 3.2)**.

$$\mathrm{pH} = \mathrm{pKa} + \log\frac{[\mathrm{A^-}]}{[\mathrm{HA}]} \qquad (3.2)$$

For example, the side chain of Glu has a pKa of 4.25,[292] therefore, a solution containing this amino acid at pH 4.25 is at the equilibrium (50% protonated and 50% deprotonated). Increasing the pH by two or three units, the deprotonation of the amino acid will be up to 90% and 99% respectively. Similarly, by reducing the pH starting from 4.25, glutamate begins its protonation, no longer showing its charge, and follows the same trend of deprotonation.[294] On the other hand, amino acids with a positive charge such as Lys (pKa = 10.53),[292] show their charge when protonated and no charge when deprotonated.

PVIII is the main component of M13, therefore, the information regarding the pKa values of its amino acids was crucial to understand the total charge of M13 at pH values ranging from 2 to 11 and to calculate its IEP.

The mature form of the PVIII is made of 50 amino acids. Thirteen of these, including the N- and the C-terminus can sensibly contribute to the total charge of this protein **(Fig. 3.4a)**. The PVIII is an α-helix protein, which forms a helical capsid wrapping the viral genomic ssDNA.[278] The C-terminus and the Lys_{40}, Lys_{43}, Lys_{44} and K_{48} residues are not available for potential interactions as they are only exposed in the internal cavity of the phage. These residues stabilise the entire phage structure, by interacting with the negative charges distributed along the sugar-phosphate backbone of the ssDNA during capsid self-assembly.[278]

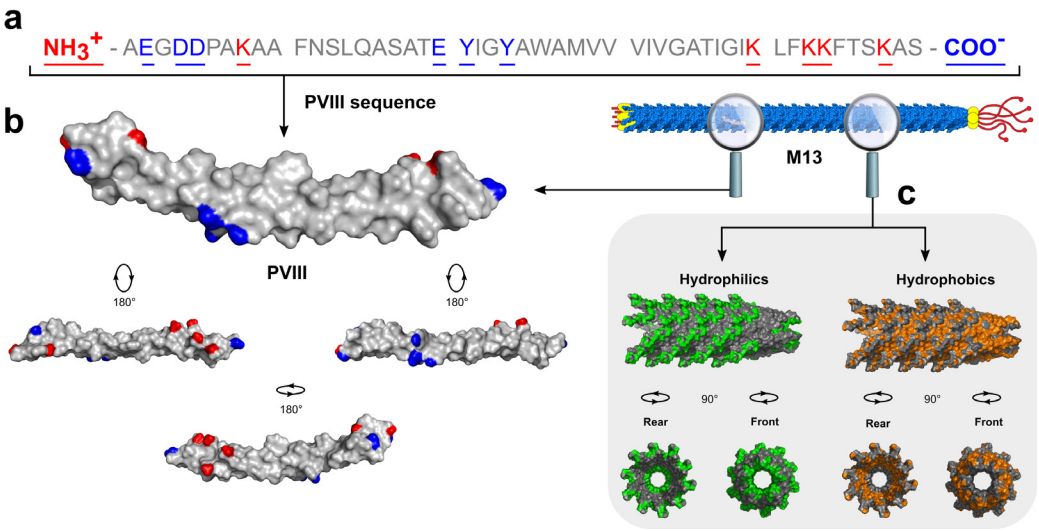


Figure 3.4. PVIII sequence and characteristics

(a) The sequence of the PVIII protein and **(b)** its 3D structure from different angles. **(c)** The figure shows a section of the phage structure made of 35 copies of the PVIII, assembled in the quaternary structure (PDB: 2MJZ).[280] The hydrophilic surface corresponding to the amino acids Arg, Lys, His, Glu, Asp, Asn, Gln, Thr, Ser and Cys is shown in green, while the hydrophobic surface (orange) corresponds to the amino acids Ala, Gly, Val, Ile, Leu, Phe and Met.

Tyr_{21} and Tyr_{24} residues are mostly embedded in the protein structure, moreover, exhibiting high pKa values, they make their contribution to the total charge considerably at pH > 10. Therefore, the N-terminus and the Glu_2, Asp_4, Asp_5, Lys_8 and Glu_{20} residues seem to be the main contributors for the overall charge of M13 **(Fig. 3.4a, b)**.

By using the software PyMOL® it was possible to analyse the protein structure of M13 **(Fig. 3.4c)**. The capsid portions made of PVIII proteins were coloured in green and orange to highlight the areas where the phage is hydrophilic or hydrophobic, respectively. The distribution of hydrophobic residues is within the inner part of the capsid, while the hydrophilic residues are exposed to the solvent on both, the external surface and the internal cavity, where the ssDNA is located.

To further corroborate the hypothesis by which the charge of M13 is mainly due to a certain group of amino acids and calculate the IEP of the phage, the ζ-potential of M13 across the pH 2–11 range was measured and compared to several models of charge potential curves **(Fig. 3.5)**.

The charged amino acids are listed in **Table 3.2** together with their corresponding pKa, referred to their variable portion (pKa_1).[292] It is important to consider that the pKa of the amino acids can vary depending on their chemical surrounding, especially if they are part of a polypeptide, as it is in the case of M13 capsid. Therefore, an alternative pKa_2 of each amino acid was calculated with PROPKA.[295–297]

This software predicts the pKa of the amino acid variable portion, considering the influence of nearby chemical groups that can alter their standard pKa. The amino acids in **Table 3.2** are divided into three groups based on their position. These groups are exposed on the external surface of the phage (External), the middle portion of the PVIII protein (Intermediate) and the internal cavity of the viral capsid (Internal).[41] Moreover, the

calculation done by PROPKA is based on the 3D structure of the protein, considering for each amino acid its exposure to the solvent in percentage.[295–297]

Table 3.2. PVIII protein pKa values

Protein portion	M13 amino acid		Part	Charge	pKa_1	pKa_2	Exposure
External	A_1	Ala	N-terminus	+	9.69	8.62	100%
	E_2	Glu	Variable group	-	4.25	3.45	100%
	D_4	Asp	Variable group	-	3.65	3.11	100%
	D_5	Asp	Variable group	-	3.65	4.02	58%
	K_8	Lys	Variable group	+	10.53	11.56	100%
	E_{20}	Glu	Variable group	-	4.25	5.21	75%
Intermediate	Y_{21}	Tyr	Variable group	-	10.07	14.74	30%
	Y_{24}	Tyr	Variable group	-	10.07	13.14	77%
Internal	K_{40}	Lys	Variable group	+	10.53	9.67	63%
	K_{43}	Lys	Variable group	+	10.53	11.17	61%
	K_{44}	Lys	Variable group	+	10.53	9.91	48%
	K_{48}	Lys	Variable group	+	10.53	8.16	30%
	S_{50}	Ser	C-terminus	-	2.21	2.18	47%

3.3.1. Experimental Procedure

To determine the total charge of the phage and study which amino acids are contributing to its value, ζ-potential was measured and compared to the predicted values obtained through several mathematical models **(Fig. 3.5)**.

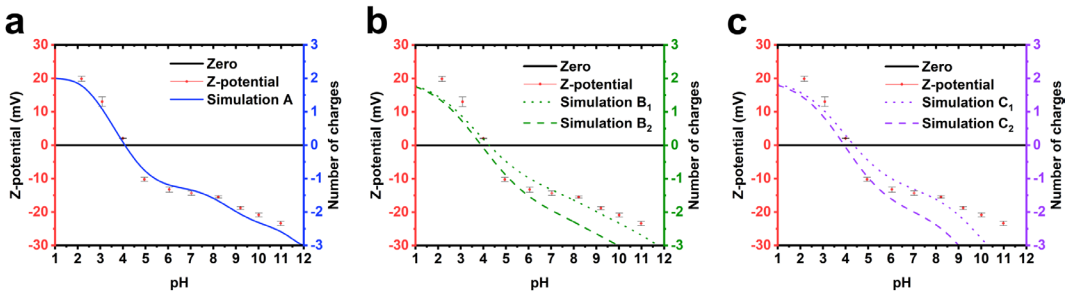


Figure 3.5. ζ-potential and prediction of the charge distribution of M13

(a) Model A fitting the measured ζ-potential of M13. **(b)** Models B_1 and B_2 plotted with the M13 ζ-potential. **(c)** models C_1 and C_2 plotted with the M13 ζ-potential.

M13 of 1 mg mL^{-1} was dispersed in several tubes with 10 mM NaCl with a pH ranging from pH 2 to 11 and analysed with the particle analyser **(Chapter 2.3.4)**.

The analysis shows that M13 charge ranges from -23.36 ± 0.65 to 19.88 ± 0.74 at pH 10.98 and 2.17 respectively **(Fig. 3.5)**. The total charge of M13 is given by the sum of the charges of each considered amino acid. For the calculation of these theoretical models, the number of negatively charged residues was subtracted from the number of positively charged residues using the following equations.

The ionisation state of the amino acids in model A **(Fig. 3.5a)** was obtained using the Henderson-Hasselbalch equation **(Eq. 3.2)**. Therefore, the degree of ionisation of each ionizable amino acid was calculated considering that 99% of the species were protonated or deprotonated between ± 2 pH units to the pH corresponding to their pKa_2. The amino acids from Ala_1 to Tyr_{24} were considered as well as the exposure of each amino acid. It is important to notice that despite the inclusion of Tyr_{21} and Tyr_{24} in this calculation, the total charge is not affected for pH ≤ 13.14.

The other four simulations were calculated using different equations containing small variations, for example, pKa value and whether the exposure (***E*** = exposure/100) was considered **(Eq. 3.3–6)**.[294–297]

$$B_1 = \left\{ \frac{e^{-log_{10}(pH-pKa_2)}}{1 + e^{-log_{10}(pH-pKa_2)}} \right\} \cdot E \qquad (3.3)$$

$$C_1 = \left\{ \frac{e^{-log_{10}(pH-pKa_1)}}{1 + e^{-log_{10}(pH-pKa_1)}} \right\} \cdot E \qquad (3.4)$$

$$B_2 = \frac{e^{-log_{10}(pH-pKa_2)}}{1+e^{-log_{10}(pH-pKa_2)}} \quad (3.5)$$

$$C_2 = \frac{e^{-log_{10}(pH-pKa_1)}}{1+e^{-log_{10}(pH-pKa_1)}} \quad (3.6)$$

At the same time, the ζ-potential of M13 was measured and plotted together with the models of the potential charge curves **(Fig. 3.5)**.

3.3.2. Results

The results show that the models B_1, B_2, C_1 and C_2, do not fit the ζ-potential curve. The better fit shown by B_1 compared with C_1 indicates that pKa_2 is probably the most accurate approximation of the pKa in the PVIII protein. Similarly, the better fit shown by B_2 compared with C_2 indicates that the exposure of the amino acids is another parameter that can affect the accuracy of this charge estimation. However, the model A shows the best fit with the calculated ζ-potential, indicating that M13 charge mostly depends on the amino acids Ala_1, Glu_2, Asp_4, Asp_5, Lys_8, Glu_{20}, Tyr_{21} and Tyr_{24} with a pKa influenced by their surrounds (pKa_2) and level of exposure.

From the results, the IEP of M13 was established at pH 4.1 from both the ζ-potential and the theoretical curves. Similar values were previously measured for *fd* bacteriophage, which has an identical, mature PVIII protein, excluding the substitution Asn35Asp and for F-specific filamentous viruses (Ff).[41,43,278–280] Moreover, the charge of the filamentous phage M13 is distributed on a surface of 18 730 nm^2 considering that its external surface can be approximated to the one of a cylinder measuring 900 nm in length with a diameter of 6.6 nm.[278,290]

3.4. M13 Stability in DIW and Buffers

Given that the charge of M13 depends on the pH of the surrounding environment, additional experiments were carried out to evaluate M13 stability in different buffer conditions. The following study provides information about the range of pH in which M13 can be dispersed and defines some of the conditions to maintain during the self-assembly with other components.

3.4.1. Experimental Procedure

M13 dispersed in DIW showed a pH of 6.97 ± 0.06, which corresponds to the expected pH for water. To understand if the M13 dispersion is stable, a series of centrifugations were performed keeping M13 of 0.3 mg mL^{-1} in four different conditions. These were DIW, and citrate buffer (CB) at pH values of 3.5, 4.9 and 6.9. Subsequently, the samples were centrifuged at 15 000 rpm for 1 min (RCF = 15 100 *g*) and the supernatant extracted and analysed at the UV-Vis spectrophotometer **(Fig. 3.6a–d)**.

3.4.2. Results

The UV-Vis spectra of M13 in DIW, CB pH 3.5, 4.9 and 6.9 are shown in **Fig. 3.6**. Looking at the peak at 269 nm, M13 drastically precipitates after centrifugation in CB pH 3.5, while it appears stable in solution at all other conditions. The bar chart in **Fig. 3.6e** shows statistical differences between M13 concentrations in each buffer.

M13 appears stable in DIW and CB at pH > 4.1, where approximately less than 10% of the total phage dispersed precipitates after centrifugation. On the contrary, at lower pH

values, M13 starts to visibly aggregate and precipitate on the bottom of the microtube due to its IEP. In the latter case, after centrifugation, ~92% of the phage was precipitated and the formation of agglomerates altered the natural absorption spectrum of the M13 dispersed in solution **(Fig. 3.6b)**. All the related data of absorbance and concentration are listed in **Table 3.3**.

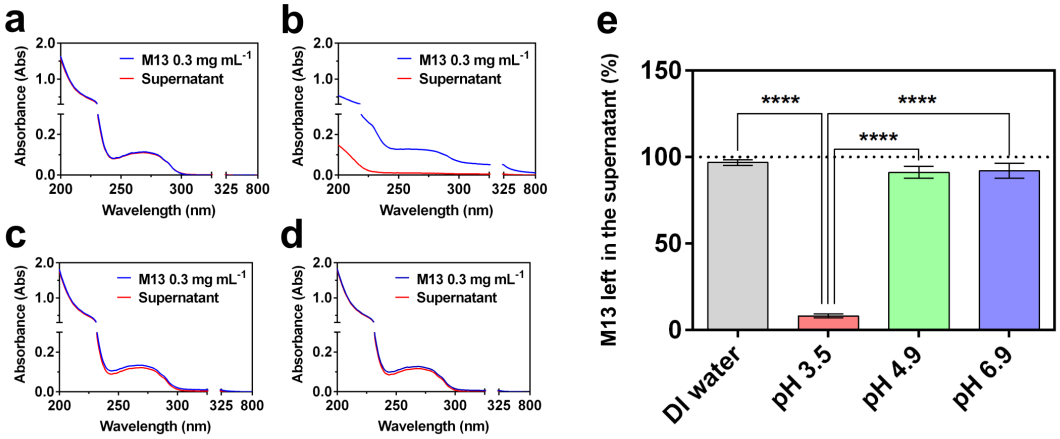


Figure 3.6. UV-Vis analysis for the stability of M13 in DIW and buffers

The figure shows the spectra o M13 and its relative supernatant in **(a)** DIW, **(b)** CB pH 3.5, **(c)** CB pH 4.9 and **(d)** CB pH 6.9. **(e)** Bar chart representing the amount of M13 left in the supernatant after centrifugation in percentage. Error bars represent mean ± SD. Statistical significance was assessed performing 2-way ANOVA with post hoc Tukey's multiple comparisons tests ****$p < 0.0001$.

Table 3.3. M13 stability in different buffer conditions

	Absorbance (Abs)	*n*	Concentration (mg mL^{-1})	M13 Precipitated (%)
DIW	0.114 ± 0.012	3	0.296 ± 0.025	3.11 ± 6.60
Supernatant	0.110 ± 0.013	3	0.286 ± 0.028	
CB (pH 6.9)	0.127 ± 0.013	3	0.330 ± 0.027	7.92 ± 4.28
Supernatant	0.116 ± 0.007	3	0.303 ± 0.015	
CB (pH 4.9)	0.134 ± 0.016	3	0.348 ± 0.005	8.87 ± 3.45
Supernatant	0.122 ± 0.010	3	0.316 ± 0.005	
CB (pH 3.5)	0.126 ± 0.030	3	0.328 ± 0.008	91.89 ± 1.14
Supernatant	0.010 ± 0.001	3	0.026 ± 0.003	

The concentration of M13 was calculated using the **Eq. 2.1**, while the fraction of precipitated phage was calculated comparing the absorbance of M13 0.3 mg mL^{-1} with the absorbance of its supernatant after centrifugation. This approach provides information on the amount of phage still dispersed in the supernatant and subtracting this from the total amount, it is possible to quantify the precipitated fraction **(Eq. 3.7)**.

$$\text{M13 Precipitated (\%)} = \frac{A_{super}}{A_{sample}} \cdot 100 \qquad (3.7)$$

3.5. Spectroscopic Characterisation

3.5.1. FT-IR Spectroscopy

FT-IR is one of the most popular spectroscopy methods for the characterisation of functional groups, therefore, it was chosen to study the presence of contaminants and the occurring interactions of M13 with other components **(Chapter 2.3.2)**.

Before characterising the virus combined with other components, a detailed analysis was performed to produce a fingerprint FT-IR spectrum of M13. Although the purification of M13 through PEG is one of the preferred methods, the phages purified are often contaminated with a relevant amount of PEG that can potentially compromise the phage interactions,[298] hence, reducing the quality of the purified product. FT-IR is a valid method to check PEG contamination as well as evaluate further interaction in the fabrication of supramolecular structures containing M13.

Samples of PEG, M13 purified through PEG precipitation ($M13_{PEG}$) and $M13_{PEG}$ being resuspended in DIW after isoelectric precipitation (M13) were analysed with an FT-IR spectrometer **(Chapter 2.3.2)**.

PEG is a polyether with formula $H{-}(O{-}CH_2{-}CH_2)_n{-}OH$. The sample was prepared and analysed following the procedure described in **Chapter 2.3.2**, and the obtained spectrum normalised and fitted for the characterisation of peaks **(Fig. 3.7)**. The spectrum shows a variety of peaks ascribable to the PEG structure and they are all listed in **Table 3.4** alongside their position, intensity and assignment. In the same way, $M13_{PEG}$ was analysed and its spectrum **(Fig. 3.8)** shows a greater number of peaks compared to PEG, however, some similarities indicate the presence of PEG **(Table 3.5)**. The spectrum of M13 after isoelectric precipitation appears similar to $M13_{PEG}$, but with a notable reduction of the characteristic peaks of PEG **(Fig. 3.9 and Table 3.6)**.

The FT-IR spectra of these samples are vastly reported in the literature.[260,298–302] However, it is still not clear which chemical groups or bonds are contributing to the peaks below 1000 cm^{-1}. The spectrum of PEG shows the presence of distinctive peaks such as 510, 529, 842, 947 and 962 cm^{-1}, while $M13_{PEG}$ and M13 show a few distinct peaks, together with an unclear absorption region until ~800 cm^{-1}. The peaks in the range between 1000−1900 cm^{-1} were assigned to several bonds involving carbon such as C–O stretching of aliphatic ethers, O–H and C–O–H stretching and alkyl aryl ether C–O stretching as well as the amide band I, II and III **(Table 3.4, 5, 6)**. Finally, the absorbance between 2500−4000 cm^{-1} is due to O−H stretching or O−H and N−H groups involvement in hydrogen bonds.

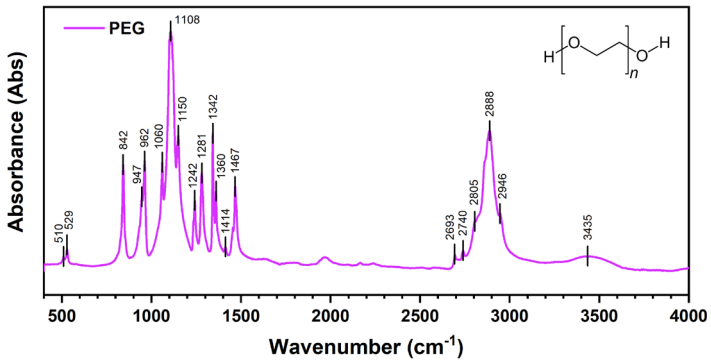


Figure 3.7. FT-IR analysis of PEG

The figure shows the absorption spectrum of PEG (pink). The peaks intensity was normalised, and the baseline subtracted. The insert at the top right corner represents the chemical structure of PEG.

Table 3.4. FT-IR peaks of PEG

	Wavenumber (cm^{-1})	Intensity (arb. unit)	Assignment	Ref.
1	510	0.06		260,299–301
2	529	0.11		
3	842	0.44	C–C skeletal vibration	
4	947	0.31		
5	962	0.46		
6	1060	0.45	C–O stretching aliphatic ether	
7	1108	1.00	O–H and C–O–H stretching	
8	1150	0.57	C–OH stretching	
9	1242	0.30	C–O–C asymmetric stretching	
10	1281	0.41	O–H and C–O–H stretching	
11	1342	0.57	C–H bending	
12	1360	0.33	Alkyl C–H deforming	
13	1414	0.10		
14	1467	0.35	C–H bending	
15	2693	0.07	C–H stretching	
16	2740	0.09		
17	2805	0.21		
18	2888	0.58	Alkyl C–H stretching	
19	2946	0.24		
20	3435	0.06	O–H stretching	

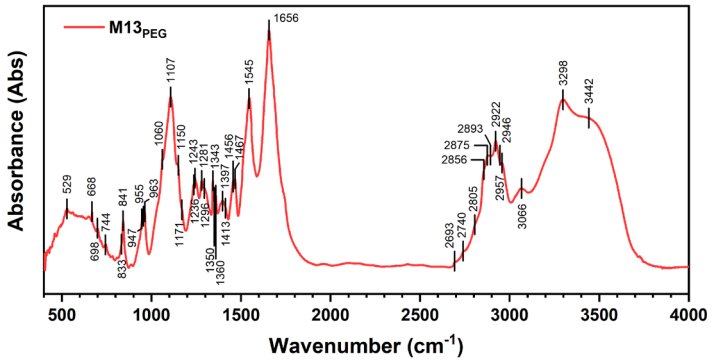


Figure 3.8. FT-IR analysis of M13 contaminated by PEG

The figure shows the absorption spectrum of M13 contaminated by PEG (red). The peaks intensity was normalised, and the baseline subtracted.

Table 3.5. FT-IR peaks of M13 contaminated by PEG

	Wavenumber (cm^{-1})	Intensity (arb. unit)	Assignment	Ref.
1	529	0.25		260,298–302
2	668	0.24		
3	698	0.17		
4	744	0.11		
5	833	0.11		
6	841	0.20	C–C skeletal vibration	
7	947	0.21		
8	955	0.22		
9	963	0.24		
10	1060	0.46	C–O stretching aliphatic ether	
11	1107	0.72	O–H and C–O–H stretching	
12	1150	0.44	C–OH stretching	
13	1171	0.25	C–C and C–O–H stretching	
14	1236	0.36	Amide III band: C–N stretching, N–H in-plane bending and C–H_2 wagging	
15	1243	0.38	alkyl aryl ether C–O stretching	
16	1281	0.37	O–H and C–O–H stretching	
17	1296	0.34		
18	1343	0.37	C–H bending	
19	1350	0.30		
20	1360	0.31	Alkyl C–H deforming	
21	1397	0.29	Symmetric C–H_3 bending	
22	1413	0.26		
23	1456	0.37	C–H_2 scissoring, C–H_2 bending and asymmetric C–H_3 bending	
24	1467	0.38	C–H bending	
25	1545	0.71	Amide II band: amide plane N–H bending and C–N stretching	
26	1656	1.00	Amide I band: Amide plane C=O stretching	
27	2693	0.04	C–H stretching	
28	2740	0.08		
29	2805	0.19	O–H and N–H groups involved in hydrogen bonds	
30	2856	0.42		
31	2875	0.48		
32	2893	0.48	C–H stretching	
33	2922	0.54	O–H and N–H groups involved in hydrogen bonds	
34	2946	0.48		
35	2957	0.45		
36	3066	0.34		
37	3298	0.71		
38	3442	0.63		

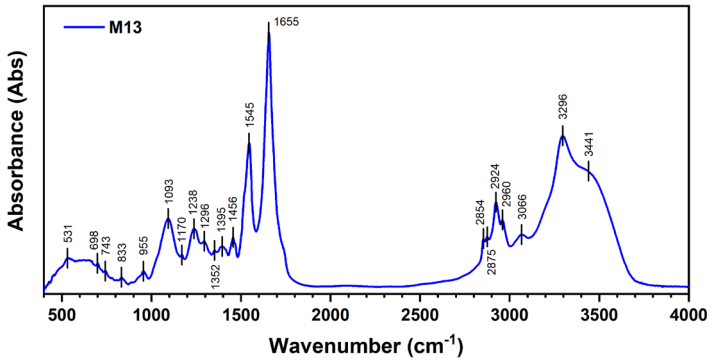


Figure 3.9. FT-IR analysis of M13

The figure shows the absorption spectrum of M13 (blue). The peaks intensity was normalised, and the baseline subtracted.

Table 3.6. FT-IR peaks of M13

	Wavenumber (cm^{-1})	Intensity (arb. unit)	Assignment	Ref.
1	531	0.14		260,298–302
2	698	0.12		
3	743	0.09		
4	833	0.06	C–C skeletal vibration	
5	955	0.09		
6	1093	0.29	O–C=O stretching	
7	1170	0.15	C–C and C–O–H stretching	
8	1238	0.25	Amide III band: C–N stretching, N–H in-plane bending and C–H_2 wagging	
9	1296	0.20		
10	1352	0.17		
11	1395	0.18	Symmetric C–H_3 bending	
12	1456	0.22	C–H_2 scissoring, C–H_2 bending and asymmetric C–H_3 bending	
13	1545	0.58	Amide II band: amide plane N–H bending and C–N stretching	
14	1655	1.00	Amide I band: Amide plane C=O stretching	
15	2854	0.21	O−H and N−H groups involved in hydrogen bonds	
16	2875	0.22		
17	2924	0.35		
18	2960	0.28		
19	3066	0.23		
20	3296	0.60		
21	3441	0.47		

The differences between the three samples (PEG, $M13_{PEG}$ and M13) is evident when comparing the spectra **(Fig. 3.10)**.

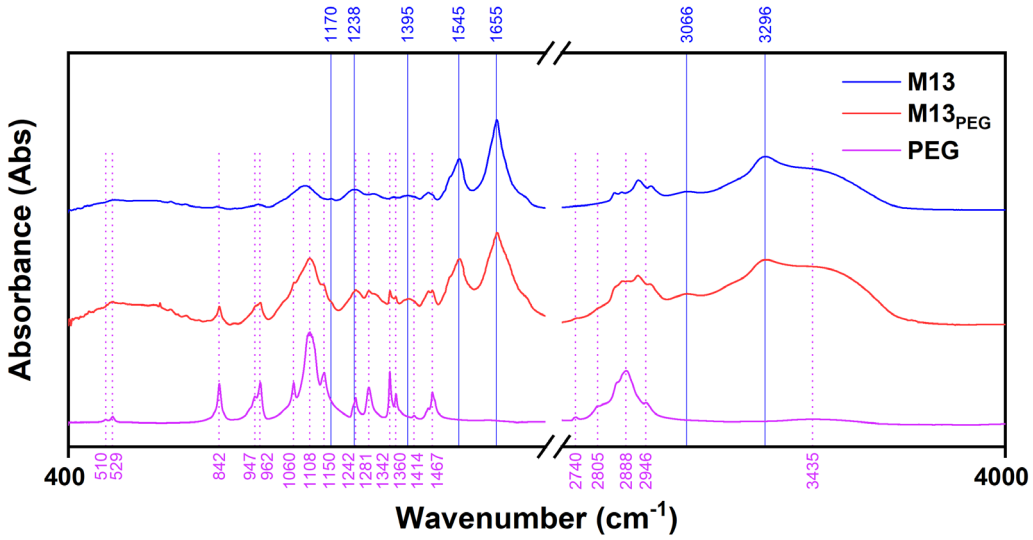


Figure 3.10. Comparison of FT-IR spectra

The figure shows the comparison between the spectra of M13 contaminated with PEG (red) and M13 (blue) after the precipitation and buffer exchange. The spectrum of PEG (pink) is included for clarity.

The Amide bands I and II respectively at 1544 and 1652, together with the broad absorption peak after 3000 cm^{-1}, are distinctive characteristics of the M13 fingerprint spectrum. Similarly, the strong and sharp peaks between the ranges 800–1500 cm^{-1} and 2700–3000 cm^{-1}, are distinctive of PEG. The comparison of the spectra clearly shows that the presence of residual PEG in the sample $M13_{PEG}$ can be reduced through isoelectric precipitation and buffer freshening. The spectra show an evident reduction of the PEG peaks while there is a constant intensity of the M13 amide bands I and II. This implies that $M13_{PEG}$ was contaminated by PEG and its presence can be reduced through an additional step in the purification process, that in this case was the isoelectric precipitation.

3.5.2. Raman Spectroscopy

As well as FT-IR, Raman spectroscopy was employed to produce a fingerprint spectrum of M13 to study its interaction with other components and the presence of PEG after purification. PEG flakes were placed onto a clean silicon wafer and illuminated with the laser following the standardised procedure described in **Chapter 2.3.3**. M13 dispersed in DIW was deposited onto a silicon wafer and subsequently dried in a vacuum chamber for 1 h before being analysed with the Raman spectrometer. Raman spectra of PEG and M13, are already reported in the literature[260,282,303–307] and given the nature of PEG already described above, its Raman spectrum **(Fig. 3.11a)** shows several peaks attributed to several vibrational modes from chemical groups containing carbon such as CH_2 rocking vibration, C–C and C–O stretching, CH_2 wagging and twisting vibration, CH_2–CH_2 symmetric and anti-symmetric bending vibration as well as skeletal vibrations **(Table 3.7)**.

Table 3.7. Raman peaks of PEG

	Wavenumber (cm^{-1})	Intensity (arb. unit)	Assignment	Ref.
1	583	0.06		260,303–307
2	845	0.78	Skeletal vibrations	
3	861	0.49		
4	934	0.05	CH_2 rocking	
5	945	0.04		
6	1064	0.28	C–O stretching and CH_2 rocking	
7	1072	0.20		
8	1127	0.38	C–C and C–O stretching	
9	1143	0.49	C–C stretching and CH_2 rocking	
10	1235	0.36	CH_2 twisting	
11	1282	1.00		
12	1364	0.09	CH_2 wagging and twisting	
13	1398	0.16		
14	1446	0.27	CH_2–CH_2 anti symmetric bending	
15	1477	0.73		
16	1485	0.86	CH_2–CH_2 symmetric bending	

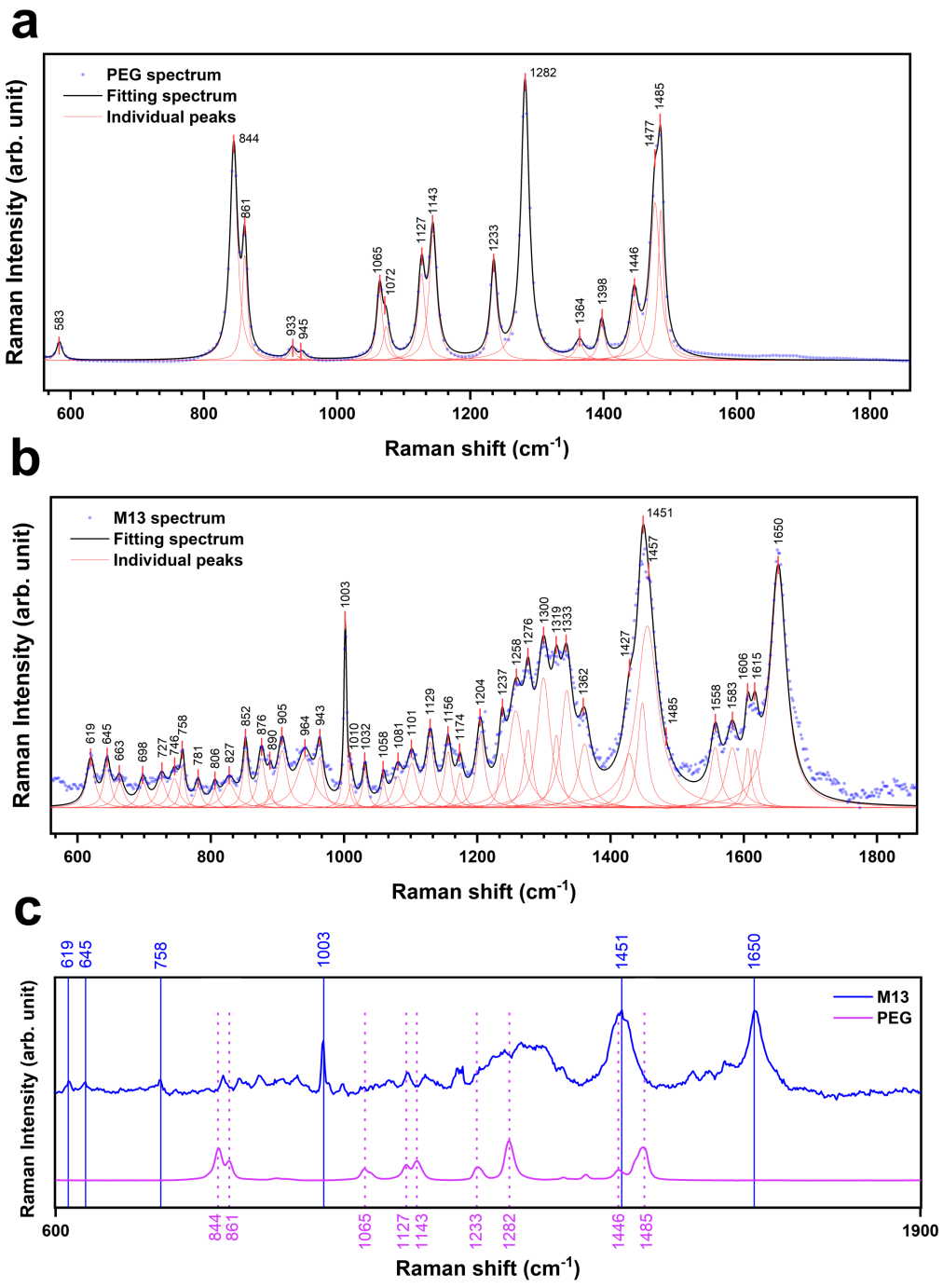


Figure 3.11. Raman analysis of PEG and M13

The figure shows the Raman spectra (blue dots) of **(a)** PEG and **(b)** M13 with the corresponding data fitting (cumulative fitting spectrum in black and individual peaks in red) and peaks. **(c)** Comparison between PEG and M13 spectra.

Table 3.8. Raman peaks of M13

	Wavenumber (cm^{-1})	Intensity (arb. unit)	Assignment	Ref.
1	619	0.21	Phe	
2	645	0.20	Tyr	
3	663	0.13	thy, gua	
4	698	0.13	AmV	
5	727	0.14	ade	
6	746	0.15	thy	
7	758	0.22	Trp	
8	781	0.11	cyt	
9	806	0.11	backbone	
10	827	0.12	Tyr	
11	852	0.27	Tyr	
12	876	0.24	Trp	
13	890	0.18	Gly; backbone	
14	905	0.27	Ala	
15	964	0.27	Ile	
16	943	0.23	C–C–C deformation	
17	1003	0.66	Phe	
18	1010	0.19	Trp	
19	1032	0.17	C–C, C–N, C–O stretching	
20	1058	0.14	C–C, C–N, C–O stretching	
21	1081	0.17	C–C stretching; backbone	260,282
22	1101	0.22	Ala	
23	1129	0.30	C–C str	
24	1156	0.28	C–C str	
25	1174	0.20	Tyr	
26	1204	0.35	Tyr, Trp	
27	1237	0.36	AmIII; thy, cyt	
28	1258	0.49	AmIII; thy, ade	
29	1276	0.56	AmIII; Tyr	
30	1300	0.64	–CH, $–CH_2$ deformation	
31	1319	0.58	$–CH_2$ deformation	
32	1333	0.60	$–CH_2$, $–CH_3$ deformation; Trp	
33	1362	0.36	Trp	
34	1427	0.42	$–CH_2$, $–CH_3$ deformation	
35	1451	1.00		
36	1457	0.89	$–CH_3$, $–CH_2$ deformation	
37	1485	0.27	ade, gua	
38	1558	0.32	Trp	
39	1583	0.32	Trp; gua, ade	
40	1606	0.43	Phe, Tyr	
41	1615	0.40	Tyr	
42	1650	0.99	AmI	

On the other hand, M13 which is comprised of a circular ssDNA molecule encapsulated in a protein capsid shows a wider multitude of peaks due to the presence of many more chemical groups and conformations **(Fig. 3.11b)**. **Table 3.8** lists the assignments including the M13 amino acids side chains (three-letter symbols), main chain skeleton (skl), or amide modes (AmI, AmIII, AmV, AmVII) as well as DNA nucleotide bases (three-letter symbols) and backbone.[282]

Overlapping the PEG and M13 spectra **(Fig. 3.11c)**, it is possible to identify their peaks and evaluate the presence of PEG within the analysed M13 sample. In particular, PEG peaks of greater intensity, such as 844, 1282 and 1485 cm^{-1}, can be used to detect its presence within the spectrum of the virus.

Looking at **Fig. 3.11c** it is noticeable that the peaks at 844 and 1282 cm^{-1} assigned to skeletal vibration and CH_2 twisting respectively are in the same region of other peaks coming from the spectrum of M13, which makes difficult to attribute them to one or the other component. On the other hand, the peak at 1485 cm^{-1} of PEG might be easier to identify as it lays in a region of the spectrum where there are no M13 peaks. However, this was detected with extremely low intensity in the M13 spectrum. Although with the available data it is not possible to make an accurate quantification of the mass ratio between the two components, it is possible to say that a small amount of PEG might be still present within the sample.

The use of Raman spectroscopy represents a good method to distinguish the different components of composite materials. Therefore, M13 peaks of predominant intensity, such as 1003, values between 1230 and 1260, 1451,1457 and 1650 cm^{-1}, can be used to detect its presence in new self-assembled nanostructures. Furthermore, their variations can be

used to study possible modifications, which include the addition of amino acids and specific chemical bonds.

3.6. Summary and Outlook

This chapter provides the results and important information for the characterisation and employability of M13 in the fabrication of novel functional structures. It also includes several methodologies that were subsequently used to study and characterise the self-assembled structures described in the following chapters.

The propagation and the purification of M13 performed through infecting *E. coli* in batch culture and subsequently purified *via* PEG/isoelectric precipitation, were extensively studied. The methodology used to produce M13 is the result of an in-depth study of the approaches already described in the literature. This guarantees the production of highly concentrated stocks of M13 with a lower quantity of contaminating PEG, presence of which hampers the reactivity of M13. Furthermore, for the production of M13 for research purposes, its propagation in batches was confirmed to be more convenient than using continuous fermenters, given the ease of preparation without employing sophisticated and expansive instruments.

Since its discovery, M13 has been characterised using various techniques, including TEM, CsCl gradients, NMR, CD, LD and MS. In contrast, this chapter reports the study of M13 through additional techniques, already described in the literature, but not listed above.

UV-Vis spectroscopy was employed for the quantification of the phages dispersed in solution. This was possible due to the ability of M13 to absorb the light at 269 nm. Therefore, in addition to its quantification, this technique can be crucial for the analysis of M13, in solution, combined with other components which show specific absorption peaks such as fluorophores and nanoparticles.

AFM was employed for the morphological characterisation of M13. This particular microscope can acquire high-resolution images of individual viruses and the nanostructures produced with it.

Computational structural studies of the major coat protein PVIII, associated with the measurement of the ζ-potential, led to the estimation of M13 total charge across the whole range of pH. Furthermore, this study provides an accurate calculation of the IEP of M13, corresponding to 4.1. This is pivotal for the study of possible non-covalent interactions between M13 and other components.

Finally, FT-IR and Raman spectroscopies were employed to validate M13 purity after the purification process, alongside the study of M13 and characterisation of possible covalent bonds and non-covalent interactions. Due to the Raman and FT-IR results it is possible to observe a reduction of the PEG signal in the M13 samples further purified with isoelectric precipitation. This showed the effectiveness of this approach. In addition, the purity of the samples produced can be validated in a short time and with greater simplicity using FT-IR and Raman spectroscopies. These two techniques are extremely effective in the study of composite materials based on M13 since they are able to detect the variations of chemical bonds, which can be introduced with the addition of new components.

The technological progress and the employment of this small bacteriophage in a constantly increasing number of applications require further studies and thorough characterisation, exploiting techniques not employed so far to expand the knowledge about its properties. This will provide a groundwork for new ideas and possible applications in the future, more advanced technologies.



UNIVERSITY OF
BIRMINGHAM

CHAPTER IV

Graphene Oxide Characterisation



Abstract

As well as bronze marked the end of the stone age, graphene ousted silicon by opening the doors to the carbon age. This consideration already gives us an idea of the importance of this extraordinary material that generated over 45 000 publications in the last ten years. This chapter has the intent to show certain characterisation methods employed for the study and development of the new composite materials that will be discussed in the subsequent chapters.

Paolo Passaretti

4.1. Introduction

Graphene Oxide (GO) is one of the most commonly employed graphene-like material for the fabrication of carbon-based composites involving biomolecules. **Chapter 1** provides an extensive description of the properties of graphene and its derivatives as well as a description of the most common production methods and applications.

GO together with M13, are essential components for the fabrication of the novel nanostructures described in the following chapters. Therefore, it is crucial to perform a series of fundamental studies on GO and familiarize with this extraordinary nanomaterial.

The work reported in this chapter was an important step to understand and optimise all the methodologies employed for the characterisation of GO itself, and the novel self-assembled composite *GraPhage13* described in **Chapter 5**.

Following, there is a detailed description of the methodologies adopted for these studies starting from the GO stock preparation and quantification, to its characterisation through several microscopy and spectroscopy analyses. Particularly, UV-Vis spectrophotometry was employed to obtain quantitative information of the concentration in solution and to study its stability in different conditions. GO was also subject to several sonication procedures and analysed with a laser diffractometer to determine the nanosheets size average. Moreover, AFM was employed for its morphological characterisation, while GO fingerprint spectra were obtained with FT-IR and Raman spectroscopy.

4.2. GO Stock Preparation

The GO employed in this research was purchased from Graphene Supermarket®. It was in the form of a water dispersion of 5 mg mL^{-1}, with a composition of carbon and oxygen of 79% and 20% respectively **(Fig. 4.1a)**.

4.2.1. UV-Vis Characterisation and Quantification

The GO stock solution looks dark brown and depending on the dilution factor, it can appear clearer and even transparent **(Fig. 4.1a)**.

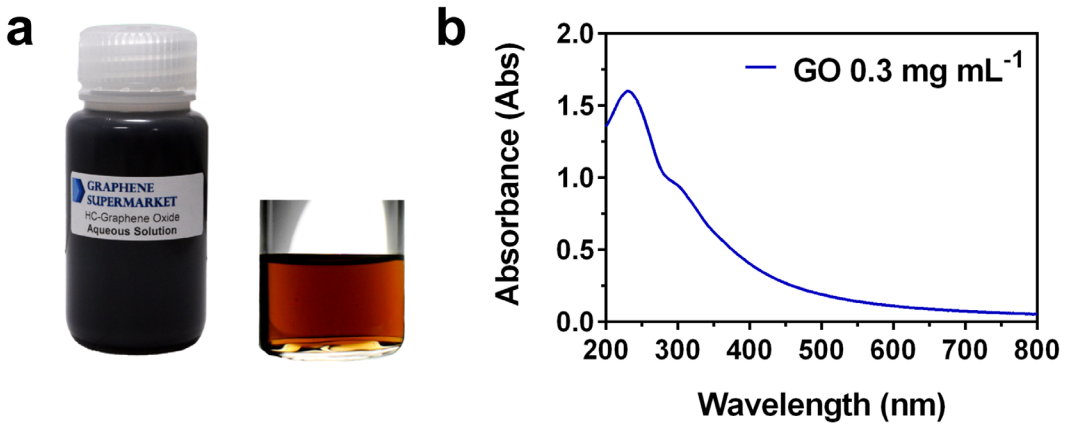


Figure 4.1. GO and its UV-Vis characterisation

(a) Purchased stock of graphene oxide and 10% diluted sample in DIW. **(b)** The typical UV-Vis spectrum of diluted GO in DIW.

For this analysis, 5 mg mL^{-1} GO was first diluted in DIW to a concentration of 0.3 mg mL^{-1}, transferred into a cuvette (0.1 cm light path) and scanned with the UV-Vis spectrophotometer in the wavelength range of 200–800 nm **(Chapter 2.3.1)**. GO has a typical spectrum characterised by a constant increasing absorption across the entire

spectrum, the $\pi \rightarrow \pi^*$ plasmon peak at 230 nm and a shoulder corresponding to the $n \rightarrow \pi^*$ plasmon peak around 310 nm **(Fig. 4.1b)**.[308]

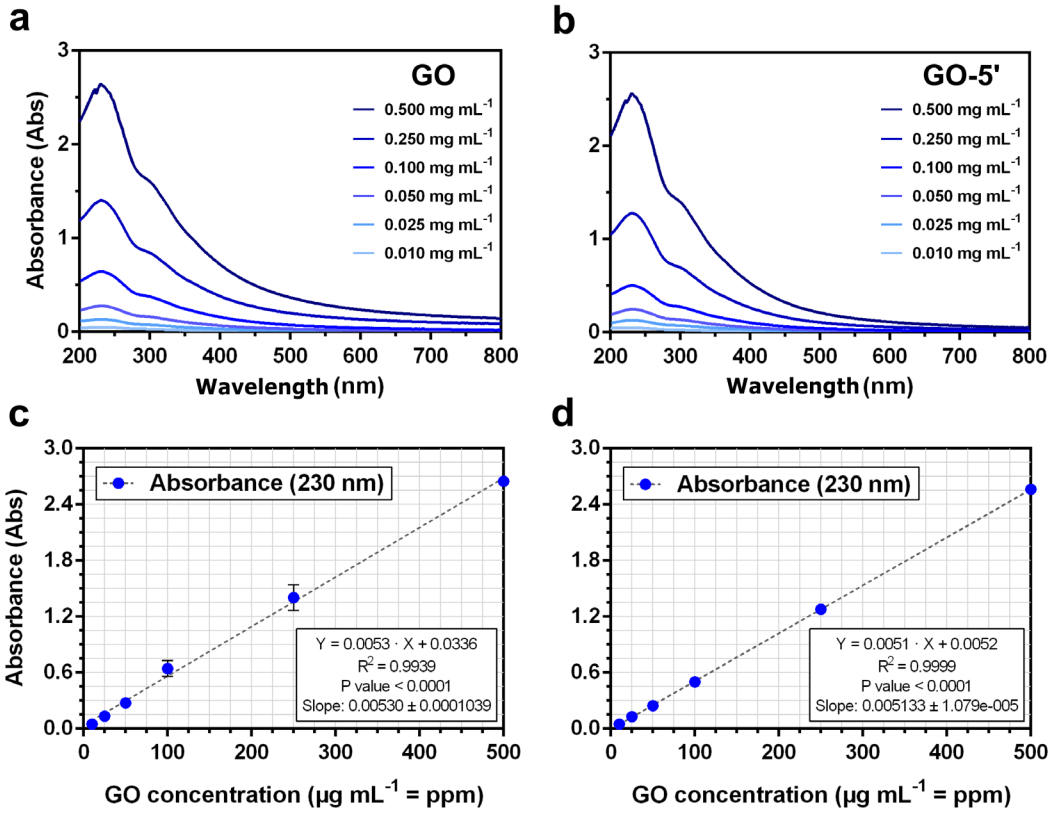


Figure 4.2. GO and GO-5' calibration curves

(a) GO and **(b)** GO-5' UV-Vis spectra at different concentrations. **(c)** GO and **(d)** GO-5' calibration curves calculated using the absorbance at 230 nm in a concentration range comprised between 0.01–0.5 mg mL^{-1}.

Considering the absorption properties of GO, its concentration was monitored *via* UV-Vis spectroscopy. This approach was extremely convenient to quantify the amount of GO involved in the assembly processes used to produce composite material with other components. Due to the heterogeneous shape and dimensions of the GO nanosheets, this material does not have a well-defined molar attenuation coefficient. Therefore, to correlate the absorption values to the corresponding concentrations, several samples with

an increasing concentration were prepared from the purchased stock and their UV-Vis spectra acquired. The values of the absorption peak at 230 nm were plotted against the established concentration, and the calibration curve equations calculated **(Fig. 4.2)**.

This method was also used to estimate the concentration of sonicated GO (in particular GO-5'). Lastly, the GO and GO-5' spectra were analysed to determine any differences between the two samples. The results indicate that, although the GO-5' shows a slightly lower peak intensity compared to GO, the difference between the two is not significant, therefore, the sonication does not significantly change the absorption properties of GO.

4.2.2. Morphological Characterisation

The morphological characterisation of GO was performed *via* AFM. The sample was prepared by soaking a clean *p*-type silicon wafer functionalised with (3-aminopropyl) triethoxysilane (APTES) into a GO solution. This procedure allowed GO to adhere to the surface without being washed away during sample preparation. This is due to amino groups provided by the APTES, which react forming a covalent bond with the GO carboxyl groups **(Fig. 4.3a)**. Functionalisation of the silicon wafer involved an incubation period of 30 min in acetone and water with a volume ratio of 5:1 and 10 mM APTES.[309] Subsequently, the Si-APTES wafer was soaked for 3 s in a solution of GO 1 μg mL^{-1} and extensively rinsed with DIW to remove any unbound material. Images were acquired in tapping mode with the AFM **(Chapter 2.3.6)**. GO micro-nanosheets were too heterogeneous to be defined through the AFM images, however, the individual micro-nanosheets thickness was accurately measured, showing a typical value of ~1 nm **(Fig. 4.3b, c)**.[310,311]

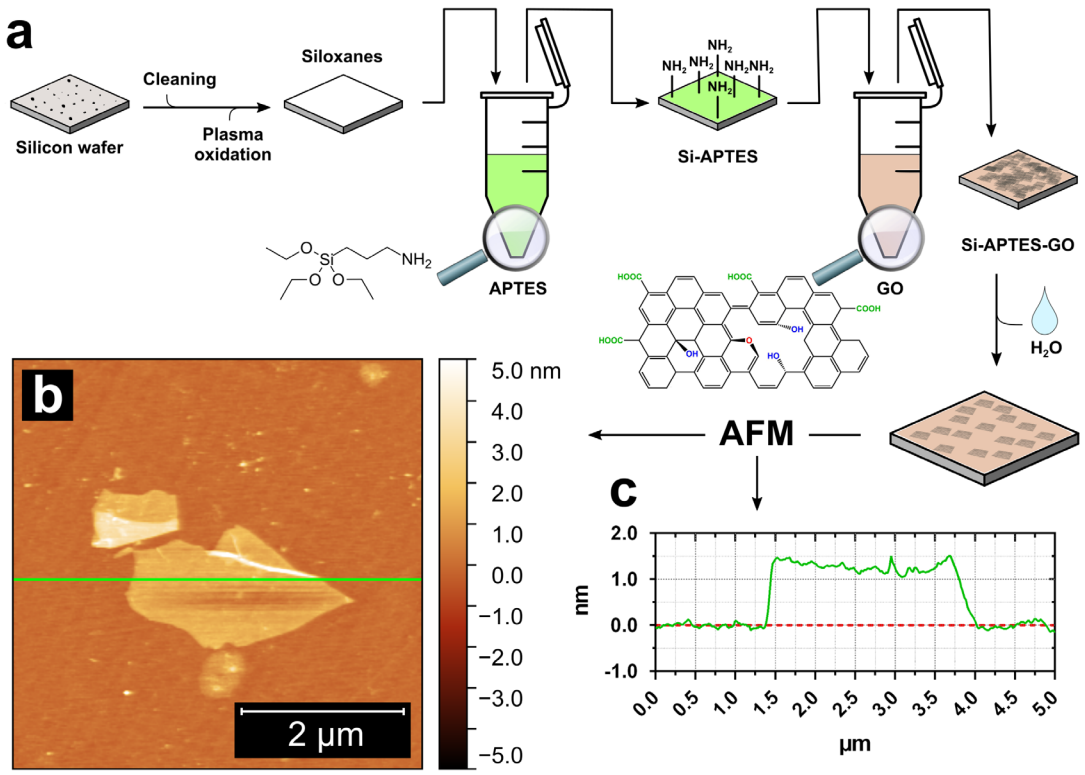


Figure 4.3. AFM analysis of GO and sample preparation

(a) Schematic procedure for AFM sample preparation. **(b)** AFM images of individual GO microsheets with **(c)** the relative cross-section of one of them.

4.3. GO Stability in DIW

Once diluted in DIW, GO forms relatively stable dispersions which precipitate over time if not disturbed.[312] This was experimentally confirmed *via* monitoring samples of GO 0.5 mg mL^{-1} after 24, 48 and 72 h **(Fig. 4.4a)**. Notably, after one day, the dispersion already showed sedimentation of GO, which increases to form a visible pellet after 2–3 days. GO instability is attributed to the presence of large micro sheets and clusters that can reduce the stability of the carbon-based material when dispersed in DIW. This

instability could negatively affect the assembly process between GO and other components as well as hamper the characterisation of GO itself.

4.3.1. Experimental Procedure

To improve the dispersibility of GO, it was sonicated in glass vials using a probe sonicator **(Chapter 2.2.3)** at 70% power for 5, 10, and 30 min (GO-5', GO-10' and GO-30') with a pulse of 3 s ON and 9 s OFF. During the sonication, the vial was kept on ice to avoid GO overheating. This procedure was adopted to mechanically disaggregate the clusters, separate the layered GO and break the large flakes into small GO nanosheets.[312] These samples were subsequently centrifuged at 15 000 rpm for 1 min (RCF = 15 100 *g*) to speed up the precipitation process. For a more accurate characterisation, the samples were analysed with both the UV-Vis spectrophotometer and the AFM.

4.3.2. Results

The effect of sonication to improve the GO stability was already evident by observing the pellets after centrifugation **(Fig. 4.4b)**. While GO formed a dark pellet and showed a clear supernatant, the sonicated samples produced a small pellet, inversely proportional to the sonication time and a clear brown supernatant, which indicates the presence of GO.

Comparing the absorbance intensity at 230 nm of GO and GO-5' supernatants **(Fig. 4.4c)**, there is a considerable difference between the two samples. In particular, while GO-5' showed negligible precipitation (5.49 ± 1.54%), GO was almost entirely precipitated after centrifugation (92.95 ± 0.80%) **(Table 4.1)**.

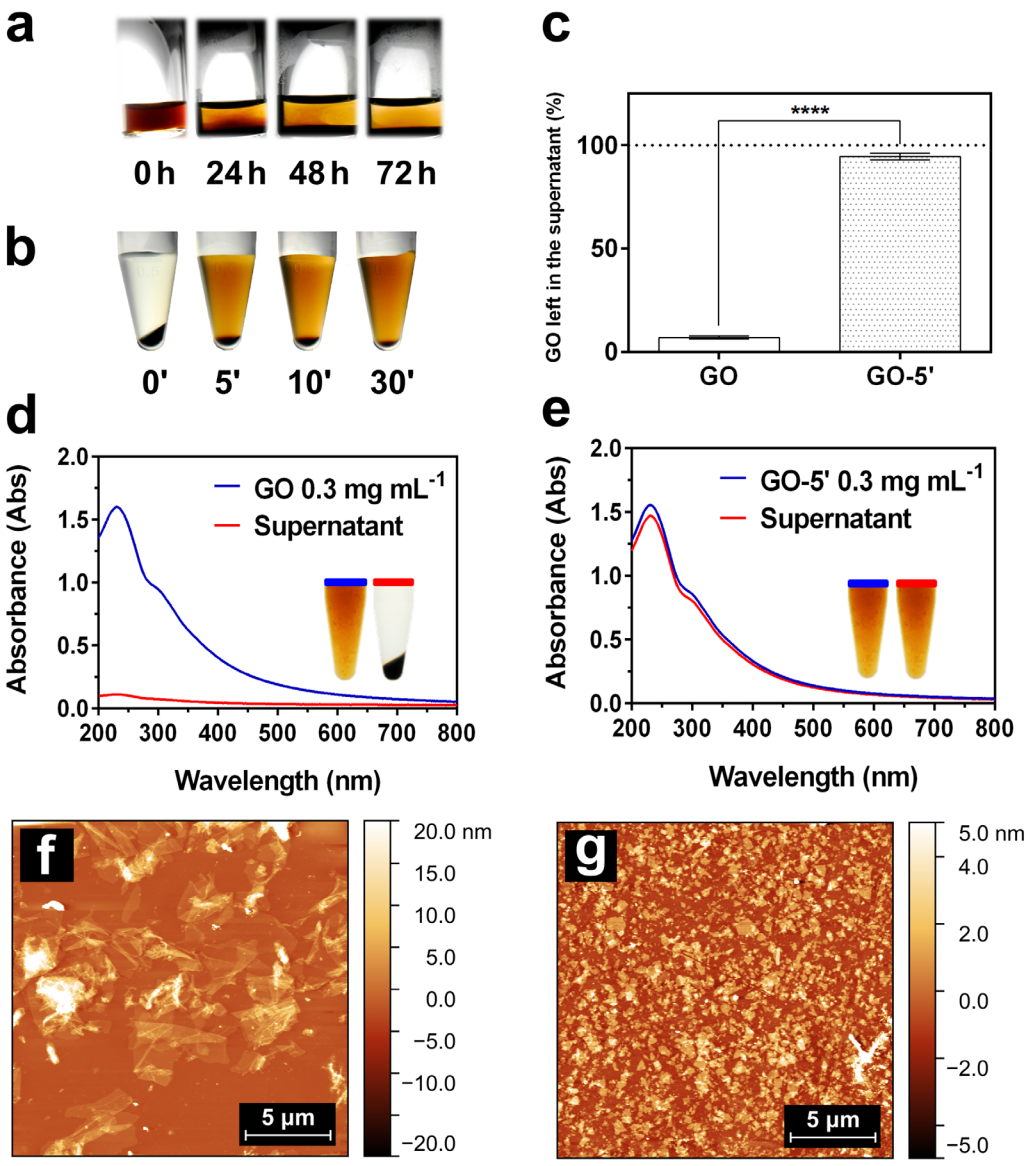


Figure 4.4. GO stability and the effect of sonication

(a) GO dispersion showing precipitation over time. **(b)** GO at different sonication times showing that the pellet decreases at longer sonication times. **(c)** Bar chart showing the comparison of the amount of GO and GO-5' left in the supernatant after centrifugation. **(d, e)** The UV-Vis spectra with the corresponding **(f, g)** AFM images of GO and GO-5'.

Table 4.1. GO stability in DIW

	Absorbance (Abs)	*n*	Concentration (mg mL^{-1})	Precipitation (%)
GO	1.602 ± 0.007	3	0.309 ± 0.001	92.95 ± 0.80
Supernatant	0.113 ± 0.016	3	0.028 ± 0.002	
GO-5'	1.556 ± 0.023	3	0.304 ± 0.004	5.49 ± 1.54
Supernatant	1.471 ± 0.013	3	0.288 ± 0.002	

This can also be observed by looking at the UV-Vis spectra of both samples before and after centrifugation. The spectra clearly show the drastic absorbance difference between GO and its supernatant after centrifugation **(Fig. 4.4d)**, compared with GO-5' spectra, which do not show much difference before and after centrifugation. This indicates that most of the sample is still dispersed in solution **(Fig. 4.4e)**.

AFM images provided morphological information about GO. The presence of larger flakes and clusters in the GO sample is evident, while GO-5' shows the presence of smaller sheets **(Fig. 4.4f, g)**. These results indicate that the procedure to improve GO stability through sonication was successful. From this moment on, GO-5' was considered the standard sample as it showed satisfying stability in DIW, after short sonication time.

4.4. GO Stability in Buffers

The stability of GO in DIW is correlated to the size of the sheets. By considering the presence of hydroxyl and epoxide on the top and bottom planes as well as carboxyl and carbonyl groups located at the edges of the GO sheets, the pH could play an important role for its stability. Therefore, understanding the chemistry behind the aqueous

dispersibility of GO nanosheets at different pH conditions is crucial to improve its processability and to understand associated phenomena.

The chemical groups containing oxygen distributed on GO sheets have different pKa. Phenolic groups and carboxylic groups have a pKa of 9.8 and 6.6, respectively.[313] However, some carboxylic residues are stabilised by hydrogen bonds, due to the presence of nearby carboxylate anions which give them an alternative pKa ($pKa_2 = 4.3$).[313] GO acts as an acid in solution, due to the presence of these chemical groups, which can be protonated or deprotonated depending on the pH conditions. As a consequence, GO shows an increasing amount of negative electrostatic charge starting from pH 3 to 12.[313] This characteristic could is crucial for the interaction between individual nanosheets, which can be enhanced or reduced by adjusting the pH at lower or higher values respectively.

4.4.1. Experimental Procedure

To further study GO-5', this was dispersed in DIW and citrate buffer (CB) at pH 3.5, 4.9 and 6.9. It was subsequently centrifuged, and the supernatants were analysed at the UV-Vis spectrophotometer to evaluate any change.

4.4.2. Results

The results show that there is no significant difference between the samples and their corresponding supernatant in CB at different pH values. All samples showed small precipitation ranging between 5–7% **(Fig. 4.5 and Table 4.2)**. These results were anticipated, as the ζ-potential values of the GO are negative in the pH range from 2 to 12.

Furthermore, for pH values above 3.5, the ζ-potential of the GO is less than -30 mV. These values provide sufficient repulsion force between the nanosheets to define the colloidal suspensions as stable.[263]

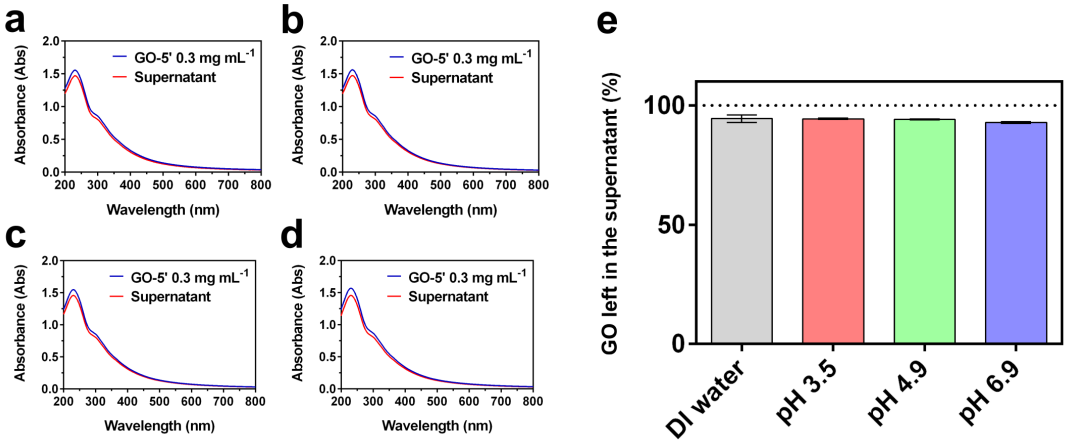


Figure 4.5. UV-Vis analysis for the stability of GO-5' in DIW and buffers

The figure shows the spectra of GO and its relative supernatant in **(a)** DIW, CB pH **(b)** 3.5, **(c)** 4.9 and **(d)** 6.9. **(e)** Bar chart representing the amount of GO left in the supernatant after centrifugation in percentage. Error bars represent mean ± SD. Statistical significance was assessed performing 2-way ANOVA with post hoc Tukey's multiple comparisons tests.

Table 4.2. GO stability in different buffer conditions

	Absorbance (Abs)	*n*	Concentration (mg mL^{-1})	Precipitation (%)
GO-5' DIW	1.556 ± 0.023	3	0.304 ± 0.004	5.49 ± 1.54
Supernatant	1.471 ± 0.013	3	0.288 ± 0.002	
GO-5' CB pH 3.5	1.561 ± 0.016	3	0.305 ± 0.003	5.61 ± 0.27
Supernatant	1.473 ± 0.020	3	0.288 ± 0.003	
GO-5' CB pH 4.9	1.548 ± 0.019	3	0.303 ± 0.003	5.84 ± 0.20
Supernatant	1.458 ± 0.015	3	0.285 ± 0.002	
GO-5' CB pH 6.9	1.570 ± 0.022	3	0.307 ± 0.004	7.12 ± 0.40
Supernatant	1.458 ± 0.015	3	0.285 ± 0.002	

4.5. Size Determination of GO Sheets

Although GO-5' was identified as the standard sample throughout the project due to its superior dispersibility compared with non-sonicated GO, the latter was analysed with the AFM and a laser diffractometer to define the size of the sheets and compared to other GO samples subjected to different sonication times, such as 0, 5, 10 and 30 min **(Fig. 4.6)**. AFM was employed to characterise the size and morphology of GO and GO-sonicated samples. Samples were prepared by soaking Si-APTES wafers into the GO dispersions and subsequently analysed at the AFM **(Chapter 2.3.6)**. The samples are visibly different and show, that the size of the sheets decreases by increasing the sonication time **(Fig. 4.6a, c, e, g)**. Unfortunately, ImageJ analysis of AFM acquired images to determine size distribution is difficult. In some cases, the sheets were too large to be counted and, in others, too small to be distinguished from the background. Furthermore, the thresholding procedures to determine the outlines of the sheets with ImageJ were hampered by the overlapping of those and for an accurate analysis, a larger number of images would have been required.

To overcome the limitations encountered with AFM images, without having to change the sample preparation strategy, the GO stocks were analysed with a laser diffractometer **(Chapter 2.3.4)**.

For this analysis, several GO samples subject to different sonication time were analysed. A water dispersion of GO 5 mg mL^{-1} was sonicated for 0, 5, 10 and 30 min and 3 mL of each sample was transferred into the mixing pump connected to the diffractometer. The mixing pump was already filled with DIW at pH 8.0, previously adjusted with 100 mM NaOH.

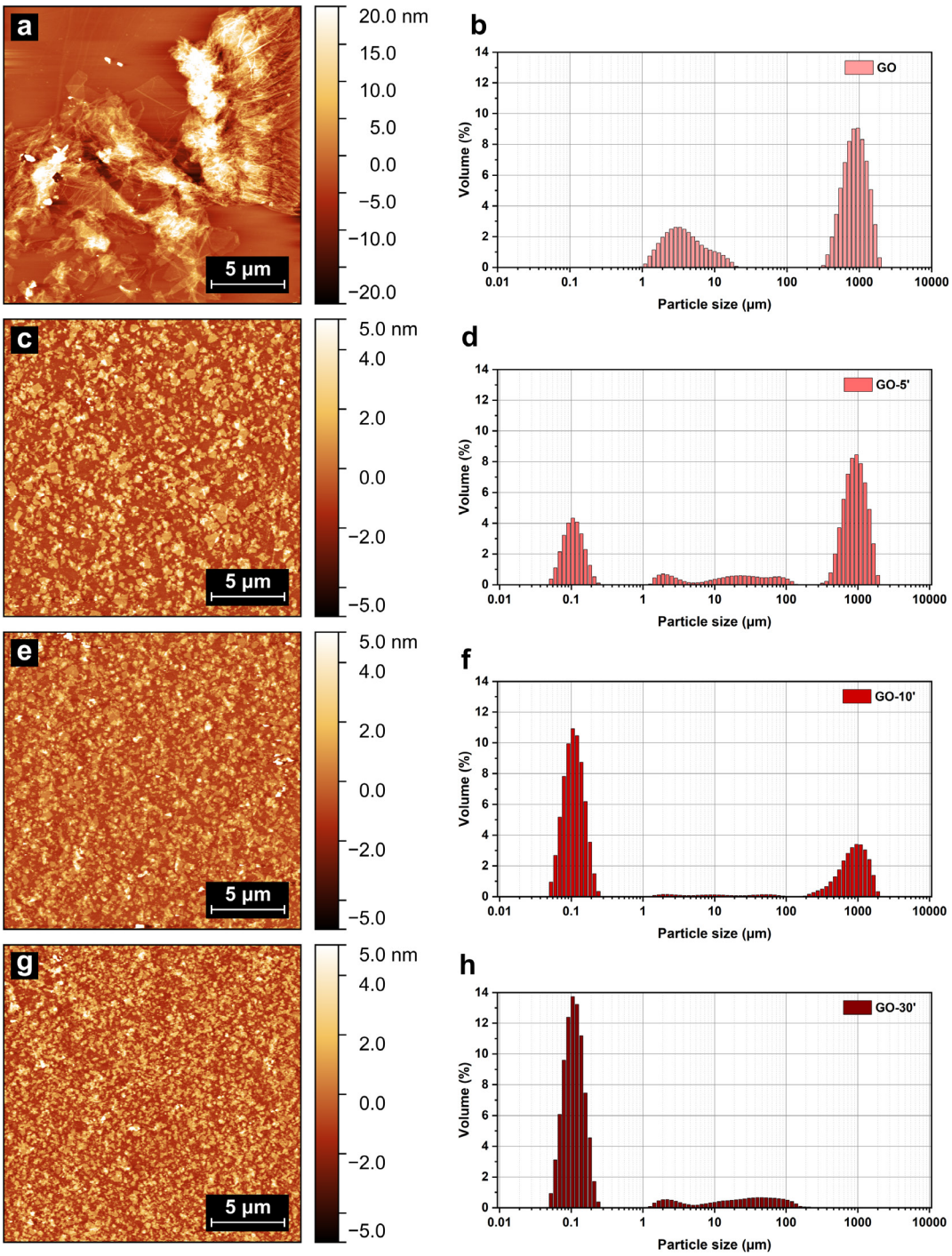


Figure 4.6. Particle-size distribution of GO

On the left side the AFM images of **(a)** GO, **(c)** GO-5' **(e)** GO-10' and **(g)** GO-30' while on the right side **(b, d, f, h)** the corresponding histograms of their particles size distribution, are shown.

This strategy was adopted to increase the repulsing forces between the GO nanosheet, *via* deprotonating the functional groups of GO, which prevents any possible aggregation inside the measuring cell during the analysis.

After measuring the background, five replicas of the samples were analysed using the same parameters. The mixing was kept constant at 1500 rpm, the obscuration comprised between 10–20, 10 s acquisition time and 10 000 measurement snaps. The refractive index used for GO and dispersant were 2.7 and 1.33 respectively.[264,271,314]

The results show different size distributions for each sample **(Fig. 4.6b, d, f, h)**. GO (GO-0') is characterised by particles with a size ranging from 0.1 to 1 mm, in particular, with a higher concentration of the latter. On the other hand, the sonicated samples (GO-5', GO-10' and GO-30') show a gradual decrease of the distribution peak around 1 mm together with the formation and increase of a peak around 0.1 μm. Sonication produces the deagglomeration of clusters, the separation of stacked GO sheets as well as their breaking, directly proportional to the sonication time.[227,312] This is confirmed by the particle size distributions and the corresponding AFM images.

4.6. Spectroscopic Characterisation

4.6.1. FT-IR Spectroscopy

GO-5' was analysed *via* FT-IR and Raman spectroscopies to acquire its fingerprint spectra, following the approach described in the methodologies section. FT-IR spectroscopy in transmission mode was performed on a transparent disk prepared by pressing dried GO-5' grained together with KBr **(Chapters 2.3.2)**. The FT-IR spectrum

obtained is comprised of several peaks which correlate to other GO spectra described in the literature.[260,301,315–319]

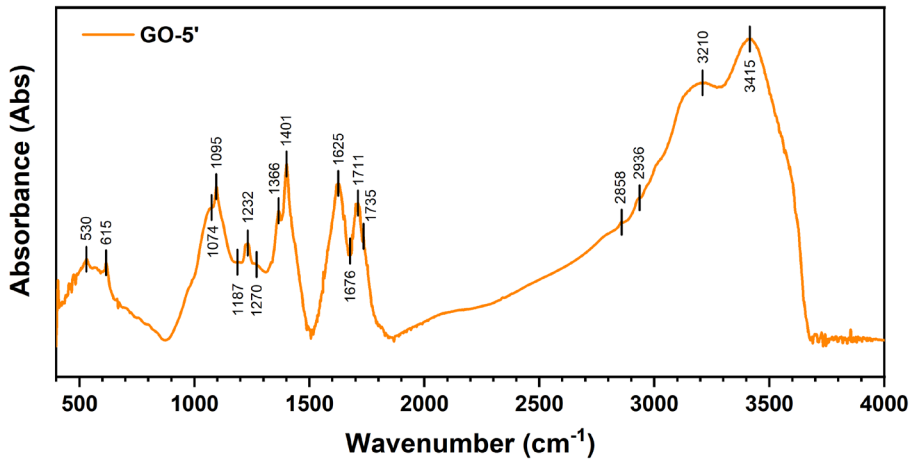


Figure 4.7. FT-IR analysis of GO-5'

The figure shows the absorption spectrum of GO-5' (orange). The peaks intensity was normalised, and the baseline subtracted.

Table 4.3. FT-IR peaks of GO-5'

	Wavenumber (cm^{-1})	Intensity (arb. unit)	Assignment	Ref.
1	529	0.28		
2	615	0.27		
3	1074	0.45	C–O alkoxy stretching	
4	1095	0.52	C–O	
5	1186	0.27	C–O epoxy stretching	
6	1231	0.33	C–O epoxy stretching	
7	1269	0.27		
8	1366	0.44		
9	1400	0.59	Tertiary C–OH groups	260,301,315–319
10	1625	0.53	C=C stretching	
11	1676	0.31	C=C stretching	
12	1710	0.47	C=O carbonyl stretching	
13	1734	0.36	C=O carbonyl stretching	
14	2857	0.40	C–H stretching	
15	2935	0.48	C–H stretching	
16	3209	0.86	O–H stretching	
17	3414	1.00	O–H stretching	

The FT-IR spectrum of GO-5' **(Fig. 4.7)** shows an intense absorption band between 2800–3700 cm^{-1} due to the C–H and O–H stretching and other lower intensity peaks in the fingerprint region such as 1186, 1231, 1400, 1625, 1676, 1710 and 1734 cm^{-1}. These other peaks correspond to C–O epoxy stretching and tertiary C–OH groups as well as C=C and C=O carbonyl stretching **(Table 4.3)**.

4.6.2. Raman Spectroscopy

In addition to FT-IR, Raman spectroscopy is one of the most employed techniques for the characterisation of graphene-based materials. It provides important information on the electronic structure and staking of graphene sheets.[170] In this study, Raman spectroscopy was performed to produce the fingerprint spectra of GO using the standardised approach described in **Chapter 2.3.3**. For this purpose, 20 µL GO of 5 mg mL^{-1} was deposited onto a silicon wafer, dried under vacuum and illuminated with two different lasers of 633 and 785 nm separately.

The resulting spectra **(Fig. 4.8)** show the typical D band at ~1350 cm^{-1} which indicates the lattice distortions and many sp^3-like defects caused by the oxidation process. Moreover, the presence of the G band at ~1584 cm^{-1} given by the E_{2g} vibrational mode, provides important information regarding the graphene sheets stacking.[170] GO is characterised by a sensible alteration of the basal plane due to the presence of several groups containing oxygen. This condition makes the D band particularly broad, hindering the assignment of the G band and consequently the determination of the crystallite thickness.[170]

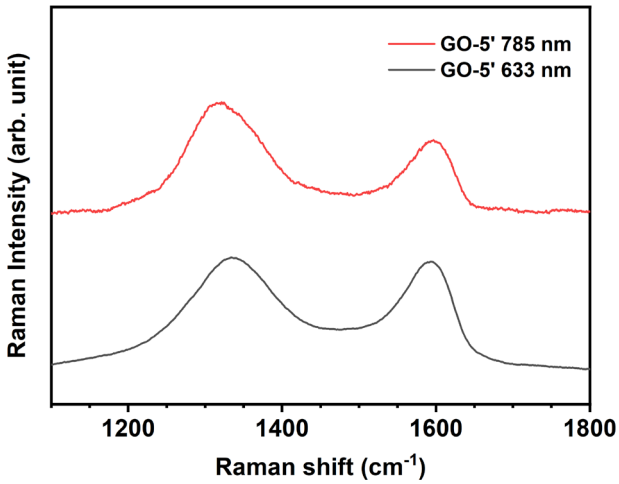


Figure 4.8. Raman analysis of GO-5'

The figure shows the Raman spectra of GO-5' obtained with two different lasers the 633 nm (RL633 Renishaw Class 3B HeNe) and 785 nm (RL785 Class 3B). Spectra coloured in black and red respectively.

4.7. Summary and Outlook

This chapter provides fundamental results and important information for the study and employability of graphenes, and in particular GO, in the fabrication of novel functional structures. It also contains the description of several methodologies employed to study and characterise the self-assembled structures, reported in the following chapters.

GO is comprised of carbon and decorated with chemical groups, containing oxygen which makes it easy to disperse in water buffers. Morphological characterisation of GO can be obtained *via* AFM, with UV-Vis, FT-IR and Raman spectroscopies, providing important qualitative and quantitative information.

The concentration of GO can be calculated and monitored through the calibration curves obtained using UV-Vis absorption spectra of standardised samples. For this reason, UV-Vis spectroscopy is an important method to check the stability of GO in different solvents and pH conditions.

Apart from the characterisation methods mentioned above, the aggregation and particles size of GO affecting its dispersibility were investigated. Combining UV-Vis spectroscopy, laser diffractometry and AFM for the analysis of GO subject to different sonication times, it was possible to show that they produce smaller GO flakes, leading to an improved dispersibility.

The cavitation generated by ultrasound favours the exfoliation of the GO and its fragmentation into smaller sheets. Due to their reduced size, the repulsive forces between the nanosheets are strong enough to prevent them from agglomerating, therefore, improving their dispersibility.

Due to its structure and functionalities, graphene is an intriguing material which could be used as a building block for the fabrication of novel 2D and 3D materials. Therefore, numerous approaches have been developed so far for the manufacturing of these graphene-based materials. Most of them, aim to preserve the extraordinary properties of pristine graphene and to improve their functionalities through the introduction of other elements, metals, specific chemical groups, nanoparticles, peptides, proteins, enzymes and nucleic acids.

Despite the considerable achievements in this field during the last fifteen years, there are not many successful studies on GO which resulted in practical applications. This will require further research efforts of the scientific communities, through the integration of

several disciplines including physics, chemistry materials and engineering, yet without underestimating the great potential to emerge from the biological sciences.

Several methods can boost research and provide a substantial advance in the production and applicability of graphene-based materials such as synthesising monodisperse graphene sheets with controlled sizes, shapes and functionalities. Of particular interest are the electrical properties and the procedures to remove sheet defects, enhancing the component performances.

Finally, it is crucial to explore the procedures for rational design and synthesis of these materials given the strong correlation between the accomplishable structures and their properties. This will undoubtedly expand the knowledge related to the graphene-based materials and possibly, broaden the range of applications for future advanced devices and technologies.



UNIVERSITY OF
BIRMINGHAM

CHAPTER V

GraPhage13



Abstract

Graphene oxide and M13 are two revolutionary components, which individually, produced an enormous impact across numerous scientific fields. The importance of their characterisation, functionalisation and application, was recognised by the entire scientific community, which awarded the brilliantly minded, authors of these studies, with the Nobel prize in physics and chemistry. In this chapter, a novel composite material originated from the self-assembly of these two components, GO and M13, is described. Furthermore, the self-assembly process is studied, and the mechanism is discussed and established with a corresponding, extensive structure characterisation.

5.1. Introduction

Carbon-based nanomaterials including graphene, graphene oxide (GO), carbon fibres and carbon nanotubes (CNTs) have been extensively studied for their potential exploitation in improving performance, functionality and durability of advanced materials.[36] Therefore, they can be employed in a wide range of applications, ranging from composite materials with tailored functionality, through materials for electrochemical sensors and absorbers, to energy storage and conversion.[36,320]

Graphene is a two-dimensional (2D) material consisting of sp^2-hybridised carbon atoms, exhibiting high-electrical and thermal conductivity as well as large surface area, high in-plane stiffness and ultra-thin thickness.[36,180] Since the demonstration of the mechanical exfoliation for its production[168] several alternative methods have been developed, including chemical vapour deposition (CVD),[321–323] direct exfoliation of graphite[36,324] and liquid phase exfoliation,[220,325,326] with the latter method producing GO as an intermediate product,[226,327] which can be reduced to partially restore its pristine structure (rGO).[328–330]

GO is comprised of several functional groups containing oxygen, namely hydroxyl which is epoxied to the top and bottom planes as well as carboxyl and carbonyl groups, located at the edges of the GO sheets **(Fig. 5.1a)**.[331,332] These functional groups render GO hydrophilic and therefore, make it easy to disperse in water, however, at the same time, they reduce its conductivity relative to graphene.[36]

Despite the continuous developments, it is still a considerable challenge to exploit the properties of graphene, GO and rGO for the fabrication of novel functional materials by assembling these 2D materials into three-dimensional (3D) architectures through facile and scalable procedures. Concurrently, however, the production of GO (rGO and pristine

graphene) sponges, which refers to foams, templates and aerogels, is a rapidly growing field of research.[36] Such sponges are characterised by a 3D structure with, particularly low-density, porous network, large surface area and high-conductivity.[36]

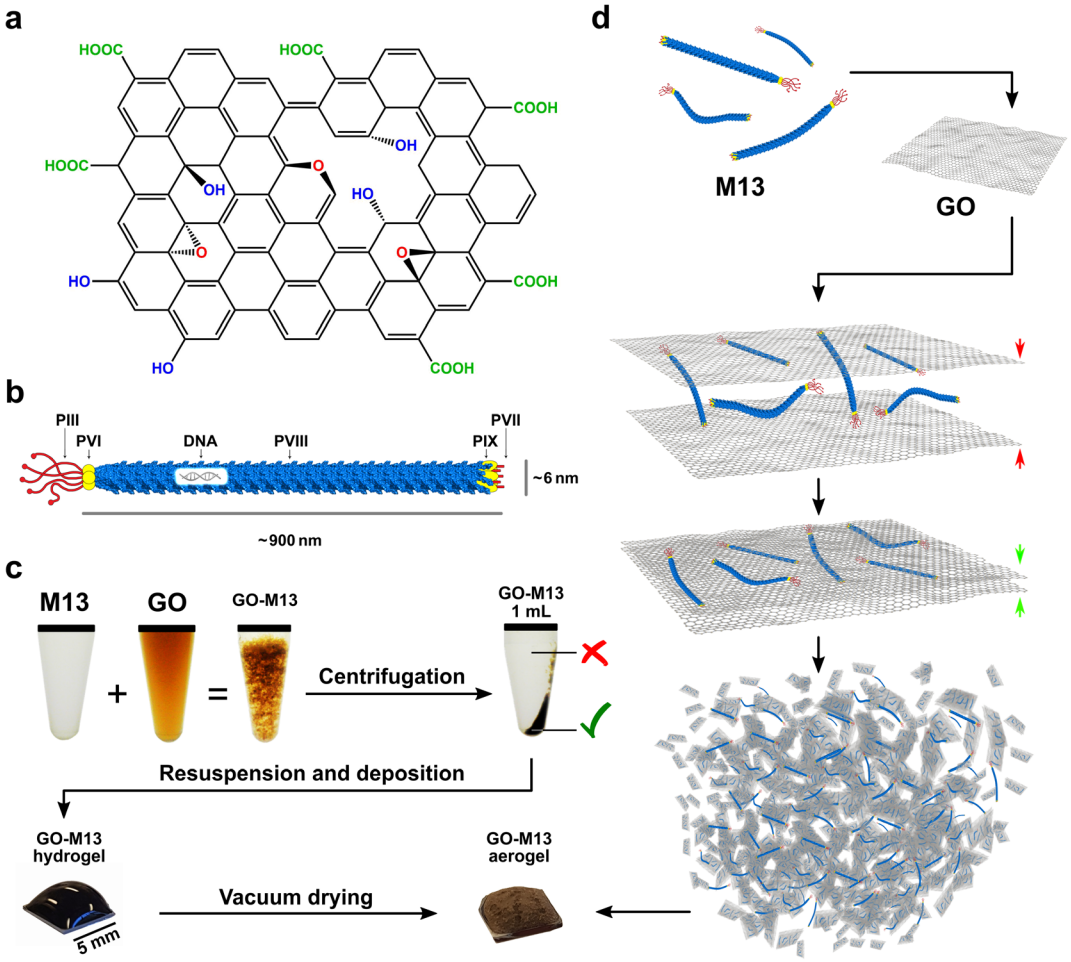


Figure 5.1. Schematic representation of the self-assembly mechanism

(a) Graphene oxide and **(b)** M13 bacteriophage structures. **(c)** Overview of the fabrication process of the *GraPhage13* and **(d)** a schematic representation of the self-assembly mechanism with M13 acting as a cross-linking agent for the GO nanosheets in DIW. Once the two components are mixed, M13 acts as a bridge to interconnect GO nanosheets assembling a hydrogel which is subsequently dried and converted into a porous 3D structure.

Several methods have been developed to assemble GO in a scalable manner into functional bulk materials, including, for instance, treatments at extreme conditions of

high-temperature or high-pressure as well as in combination with polymers,[333,334] DNA,[234] proteins[38] and peptides.[36] Usually, the latter methods require the formation of a hydrogel, merely based on non-covalent interactions[180,310,311,335] and subsequent drying processes, both crucial for sponge formation.[36] However, viral building blocks have not been previously exploited to fabricate GO micro-nano sponges.

In this chapter, is described a novel route for *bottom-up* self-assembly of GO into a 3D porous structure spanning the micro- and nanoscales, yielding a unique hierarchical GO sponge based on a synthetic biology approach, by exploiting the bacteriophage M13, acting as a cross-linker between the graphene nanosheets.

M13 phage has typical dimensions of approximately 900 nm in length and 6.6 nm in width, and it is composed of a circular ssDNA, encoding ten genes encapsulated in a flexible rod-like shape capsid, consisting of 2700 copies of its major coat protein PVIII. At the ends, there are five copies of each minor coat protein, PIII and PVI on one side and PVII and PIX on the other **(Fig. 5.1b)**.[41,47,336]

This facile method to fabricate GO-M13 sponges (*GraPhage13* aerogel or simply GPA), is performed without the need of extreme conditions of temperature, pressure or pH rendering it an environmentally friendly and scalable material, further characterised by ultra-low-density and high-surface-area. The fabrication of GPA is based on four main steps: (i) assembly reaction in aqueous buffers to form a hydrogel (GPH), (ii) hydrogel separation through centrifugation, (iii) drop-casting onto a silicon wafer and (iv) drying under vacuum **(Fig. 5.1c, d)**. Furthermore, M13 can be functionalised through the many specific chemical groups on its surface with a broad range of functional molecules such as peptides, antibodies, proteins and enzymes.[10,23,76] These hybrid micro-nano sponges

have potential applications for the development of electrochemical energy storage and conversion devices, absorbers, sensors or composite scaffolds.[36]

5.2. Study of GPH in Water

5.2.1. Fundamental Experiments and Characterisation

Initially, GO and M13 were combined in DIW, each at a concentration of 0.3 mg mL^{-1}. Upon mixing of the two components, they immediately react forming an aggregate which is separated from the supernatant and subsequently deposited on the bottom of the microtube *via* centrifugation **(Fig. 5.1c)**.

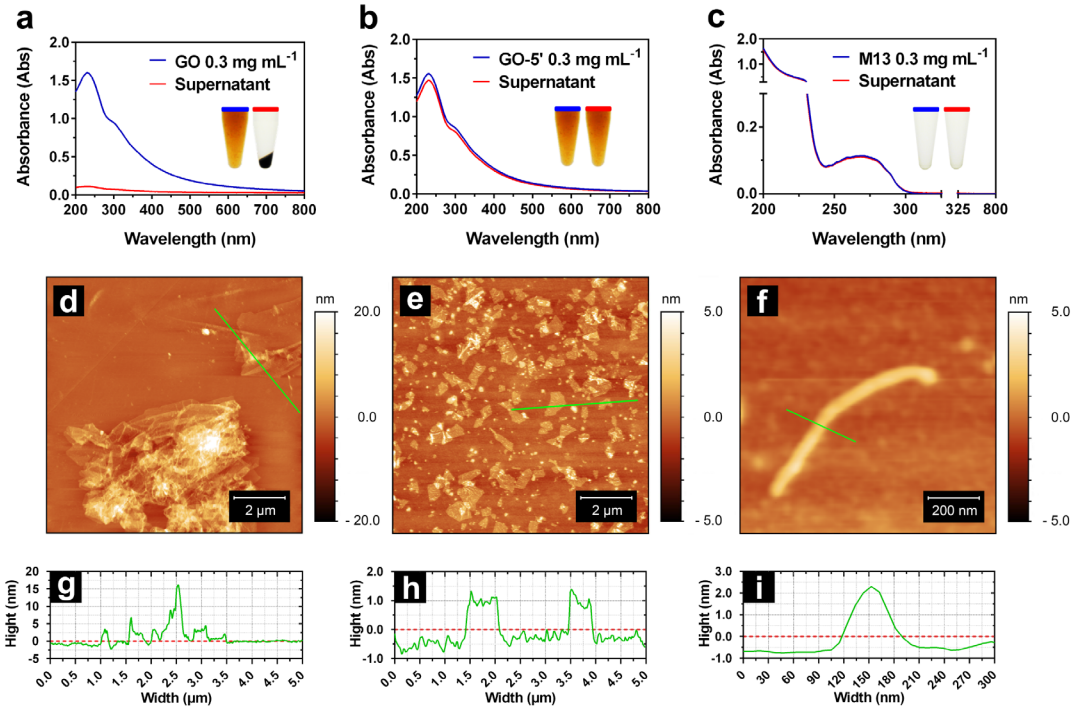


Figure 5.2. UV-Vis and AFM analysis of the individual components

UV-Vis spectra of **(a)** GO dispersion in DIW (blue) and its supernatant (red), **(b)** GO-5' dispersion in DIW (blue) and the corresponding supernatant (red), and **(c)** M13 in DIW (blue) and the corresponding supernatant (red). Inserts: Photographs of each sample (left) and the corresponding supernatant (right). AFM height channel images of the **(d)** layered GO, **(e)** GO-5' flakes and **(f)** individual M13 phage with the corresponding **(g–i)** cross-sections.

To establish the optimal self-assembly conditions, the formation of the hydrogel was studied by systematically analysing the UV-Vis spectra of the supernatants after centrifugation **(Fig. 5.2a–c)**. While the dispersed M13 was not producing a visible pellet post centrifugation **(Fig. 5.2c)**, GO yielded a dark pellet with a clear supernatant **(Fig. 5.2a)**. The precipitation of GO occurred due to its moderate instability in DIW, combined with the large size of the dispersed sheets and the presence of clusters of sheets.[312]

Under these conditions, it was not possible to distinguish between the GO precipitation due to the self-assembly processes or its clustering, therefore, hampering the spectrophotometric analysis of the hydrogel formation. To improve its stability, GO of 5 mg mL^{-1} from the stock solution, was sonicated for 5 min (GO-5'), obtaining a new stock. Moreover, the concentrations of the samples prepared by diluting both stocks (GO and GO-5' of 5 mg mL^{-1}), were estimated using calibration curves calculated by measuring the absorbance of serial dilutions **(Fig. 4.2)**. The sonication allowed to separate the layered flakes and to produce smaller GO sheets, achieving a more stable dispersion **(Fig. 5.2b)**.[312]

AFM height images **(Fig. 5.2d–f)** and the corresponding cross-sections **(Fig. 5.2g–i)** of the dispersed GO, GO-5' and M13 bacteriophage clearly show that while the GO samples consist of large flakes and aggregates of a heterogeneous thickness **(Fig. 5.2d)**, the GO-5' is predominantly composed of small, well-distributed nanosheets with a typical thickness of ~1 nm **(Fig. 5.2e)**.[310,311] The M13 bacteriophages measure, on average, 880 μm in length, 40 μm in width and 3 μm in height **(Fig. 5.2f)**. The apparent non-circular cross-section of the filamentous bacteriophage is due to a variety of conditions and in particular, the relative humidity of the sample, the applied force on the surface during the scan and tip convolution effects, caused by the curvature radius of the tip itself.[281]

UV-Vis spectra of GO exhibit a $\pi \rightarrow \pi^*$ plasmon peak at 230 nm and a shoulder corresponding to the $n \rightarrow \pi^*$ plasmon peak around 310 nm **(Fig. 5.2a)**.[308] The spectra of M13 show high absorbance values in the region between 200–230 nm, mostly due to the $\pi \rightarrow \pi^*$ transitions in the peptide bonds[286] and the typical peak at 269 nm of M13 bacteriophages which is due to the combination of the viral DNA and its major coat protein PVIII.[290]

The comparison of the absorbance intensities before and after the centrifugation enabled the stability of GO dispersion in DIW to be studied **(Fig. 5.2a–c)**. It was found that only 7.05 ± 0.80% of the GO remained in the supernatant, while GO-5', on the other hand, exhibited considerably better stability with a higher spectral absorbance intensity, corresponding to 94.51 ± 1.54% of the GO-5' remaining within the supernatant. Also, 96.89 ± 6.60% of M13 remained dispersed in the supernatant after centrifugation **(Fig. 5.3 and Table 5.1)**. Therefore, GO-5' has been identified as the optimal GO preparation for the fabrication of *GraPhage13*.

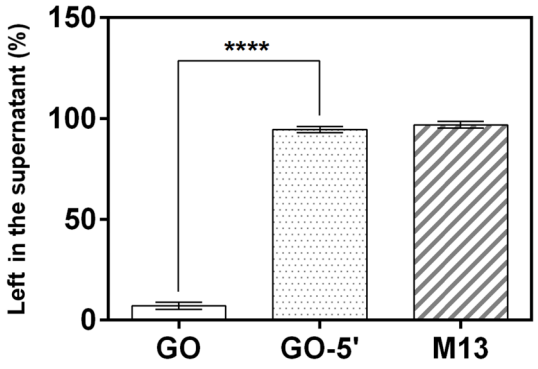


Figure 5.3. UV-Vis analysis for the stability of the components

The bar chart shows the amount of GO, GO-5' and M13 left in the supernatant after centrifugation. This bar chart corresponds to the data in **Table 5.1**. Error bars represent mean ± SD. Statistical significance was assessed performing 2-way ANOVA with post hoc Tukey's multiple comparisons tests ****$p < 0.0001$.

Table 5.1. GO, GO-5' and M13 stability in DIW

	Absorbance (Abs)	*n*	Concentration (mg mL^{-1})	Precipitation (%)
GO	1.602 ± 0.007	3	0.309 ± 0.001	92.95 ± 0.80
Supernatant	0.113 ± 0.016	3	0.028 ± 0.002	
GO-5'	1.579 ± 0.062	3	0.304 ± 0.004	5.49 ± 1.54
Supernatant	1.471 ± 0.013	3	0.288 ± 0.002	
M13	0.114 ± 0.012	3	0.296 ± 0.025	3.11 ± 6.60
Supernatant	0.110 ± 0.013	3	0.286 ± 0.028	

To establish the optimal weight ratio between the two components for the formation of *GraPhage13* hydrogel (GPH) self-assembly, GO-5' was mixed with M13 in DIW at different weight ratios of 2:1, 1:1 and 1:2. GO concentration was kept constant at 0.3 mg mL^{-1} in all the samples, while M13 was of 0.15 mg mL^{-1} (GO-M13$_{03015\text{-}5'}$), 0.3 mg mL^{-1} (GO-M13$_{0303\text{-}5'}$) and 0.6 mg mL^{-1} (GO-M13$_{0306\text{-}5'}$), respectively **(Fig. 5.4a–c)**.

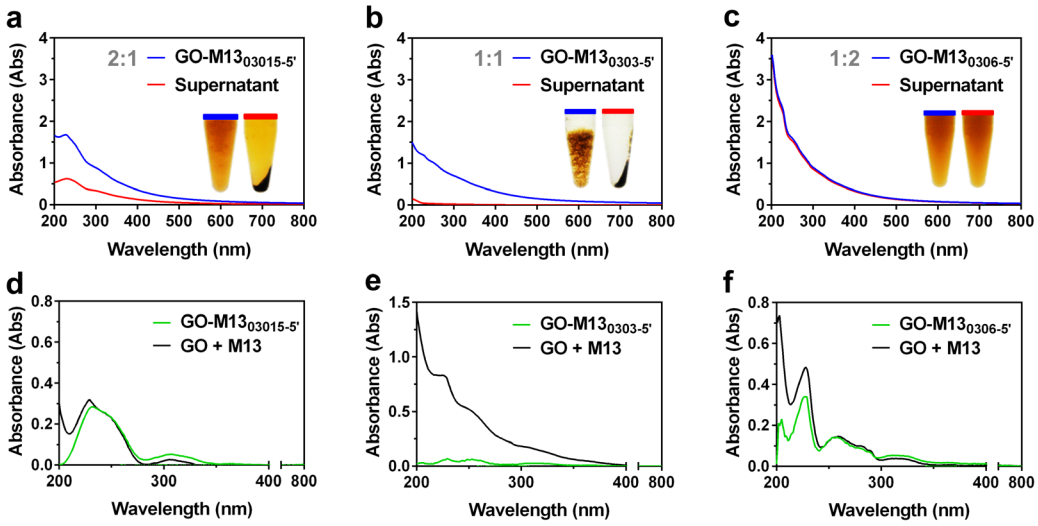


Figure 5.4. UV-Vis analysis of GO-M13 hydrogels

UV-Vis spectra of GPH at various concentration ratios of **(a)** GO-M13$_{03015\text{-}5'}$ **(b)** GO-M13$_{0303\text{-}5'}$ **(c)** GO-M13$_{0306\text{-}5'}$. Insert: the corresponding photographs of each sample and its supernatant. **(d–f)** UV-Vis spectra at the same three wt:wt ratios (green) in comparison to the theoretically calculated spectra obtained by summing the individual spectra of the two components at the same concentrations used to make the corresponding sample (black).

GO-M13$_{03015\text{-}5'}$ exhibited a minor aggregation and the characteristic spectrum of pure GO in solution, although, due to the presence of M13 in solution, with a slightly increased absorbance at 200 nm. Following the centrifugation, a dark pellet and a transparent light brown supernatant were formed indicating the presence of GO **(Fig. 5.4a)**. GO-M13$_{0303\text{-}5'}$ exhibited an evident formation of the hydrogel **(Fig. 5.4b)**, which is separated from the supernatant with the corresponding spectrum showing a continuous increase of absorbance due to the macroaggregates of the hydrogel, responsible for the light scattering.

The supernatant itself appeared transparent, and the lack of characteristic GO and M13 peaks in the UV-Vis spectrum, suggests the nearly complete precipitation of both components in the pellet. GO-M13$_{0306\text{-}5'}$ on the other hand, appeared clear with no apparent hydrogel formation and the corresponding spectrum exhibiting the fingerprint features of GO and M13 individually **(Fig. 5.4c)**. Furthermore, following the centrifugation, only a small pellet was formed. The supernatant spectrum was found to almost completely overlap with the spectrum of the GO-M13$_{0306\text{-}5'}$, suggesting that the two components did not interact, and they were still fully dispersed in the solution.

Given that the absorbance of two or more components in solution is derived by the sum of the individual absorbance values,[257] the spectra of each sample were compared to the one obtained by the sum of their respective components, measured individually **(Fig. 5.4d–f)**, to investigate the interaction between the two components. Interestingly, there was a reduction in the total absorbance in each case and in particular, for GO-M13$_{0303\text{-}5'}$ **(Fig. 5.4e)**. Furthermore, this composition does not exhibit the characteristic peaks of absorbance of the individual GO and M13 components. In contrast, the GO-M13$_{0306\text{-}5'}$ spectrum almost entirely overlaps with the corresponding one obtained

by the sum of the respective components **(Fig. 5.4f)**, suggesting that GO and M13 were absorbing the light in the same manner as they would if they were freely dispersed in DIW. These results indicate that GO and M13 in the form of a hydrogel scatter the light, not exhibiting their typical absorption peaks.

5.3. Study of GPH in Buffer

5.3.1. pH Influence on the Hydrogel Self-Assembly

Two possible mechanisms can lie at the origin of the observed GPH self-assembly. The first is the result of the electrostatic forces acting between the negatively charged groups of GO and the positively charged groups of M13. The second mechanism relies on the non-covalent interactions involving π-systems which may exist due to the increasing proximity between the two components and the progressive GO sheets stacking.[180] Therefore, the proposed mechanisms were further experimentally examined to understand which is the dominant one, responsible for the assembly.

The absence of the hydrogel formation in the case of GO-M13$_{0306\text{-}5'}$, whereas a pellet and an excess of M13 was expected in the supernatant **(Fig. 5.4c)**, suggested that pH might play an important role in the GPH self-assembly. Subsequently, the effect of pH was systematically verified by adding set volumes of 1 M NaOH or HCl to the aqueous GO-M13$_{0303\text{-}5'}$ solution. While the excess of HCl led to hydrogel assembly, NaOH yielded a reverse outcome of disassembly. Moreover, the pH values of GO-M13$_{03015\text{-}5'}$, GO-M13$_{0303\text{-}5'}$ and GO-M13$_{0306\text{-}5'}$ in DIW were measured and found to be 3.77 ± 0.02, 4.85 ± 0.02 and 5.7 ± 0.02, respectively **(Table 5.2)**.

Table 5.2. The pH values of GO, M13 and GPHs in DIW

Medium	*n*	Sample	pH
DIW	3	$GO_{0.3\ mg\ mL^{-1}}$	3.49 ± 0.02
	3	$M13_{0.3\ mg\ mL^{-1}}$	6.97 ± 0.06
	3	$GO\text{-}M13_{03015\text{-}5'}$	3.77 ± 0.02
	3	$GO\text{-}M13_{0303\text{-}5'}$	4.85 ± 0.02
	3	$GO\text{-}M13_{0306\text{-}5'}$	5.72 ± 0.02

GO in DIW at a concentration of 0.3 mg mL^{-1} exhibited a pH of 3.49 ± 0.02, due to its acidic properties given by the presence of phenolic (pKa = 9.8) and carboxylic (pKa_1 = 6.6 and pKa_2 = 4.3) functional groups on its surface.[313] These groups are responsible for its negative charge at pHs ranging from 2 to 12, and a stable dispersion can be typically achieved at pH ≥ 3.[227,313]

On the other hand, M13 in the same conditions showed pH 6.97 ± 0.06 and stability at pH ≥ 4.8. M13 is almost entirely comprised of its major coat proteins PVIII, which is made of 50 amino acids, and 13 of these, including the N- and the C-terminus contribute to the total protein charge **(Fig. 5.5a)**. The C-terminus and the residues Lys_{40}, Lys_{43}, Lys_{44} and Lys_{48} face the internal cavity of the phage, stabilising the negative charge of the ssDNA during the capsid self-assembly mechanism.[337] Moreover, Tyr_{21} and Tyr_{24} residues, mostly embedded in the protein structure, and exhibiting high pKa values **(Table 5.2)**, do not contribute to the total charge of the virus. Therefore, just the N-terminus and the residues Glu_2, Asp_4, Asp_5, Lys_8 and Glu_{20} could be responsible for the M13 overall charge distributed on a surface area of ~18 300 nm^2.[278]

This hypothesis was further corroborated by measuring the ζ-potential of M13 and comparing it to the theoretically predicted values **(Fig. 5.5b)**. The charge of each amino acid was assigned at each corresponding pH value, based on its pKa and following the Henderson-Hasselbalch equation **(Eq. 3.2)**.[294] The theoretical values of the pKa of each

amino acid were calculated by taking into consideration their chemical surrounding **(Table 5.2)**. The IEP of M13 was established as pH 4.1 from both the ζ-potential and the theoretical curves **(Chapter 2.3.4)**.

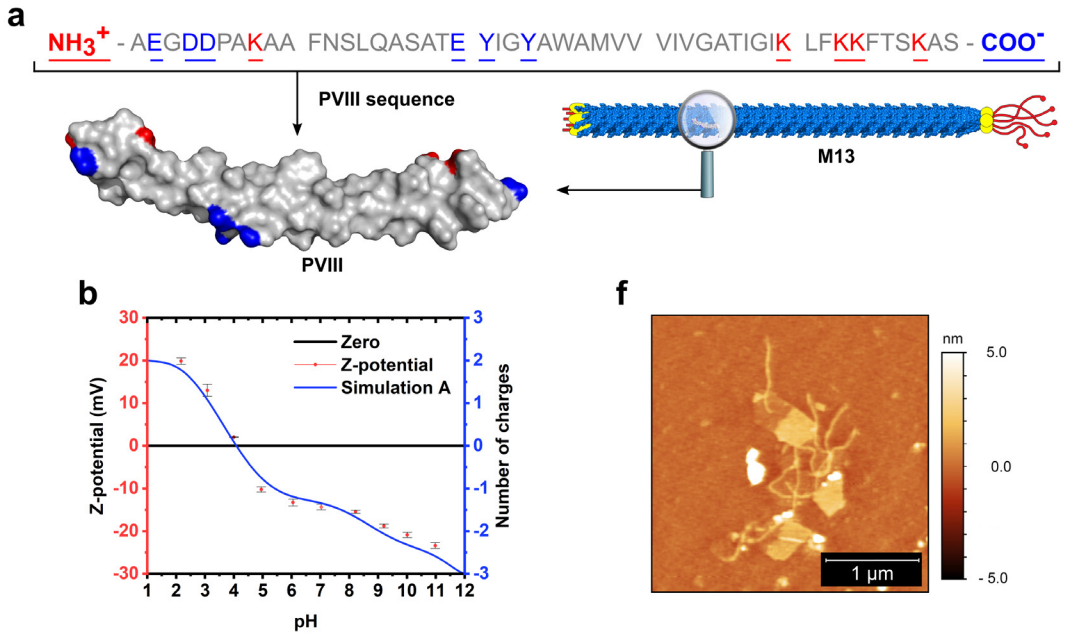


Figure 5.5. PVIII structure and ζ-potential

(a) M13 major coat protein PVIII sequence and structure. **(b)** The ζ-potential of M13 at different pH values (red) overlapping the calculated values of M13 electrostatic charge in equivalents (blue). **(c)** AFM height image of the M13 bacteriophages interacting with GO on a silicon wafer substrate. The unbound phage was washed with CB 10 mM at pH 4.9.

To establish the pH at which the assembly of GPH occurs, an acid titration, from pH 12 to 2, was performed. At pH 5.4, a minor aggregation started occurring, which further dissolved upon mixing followed by a more substantial non-soluble aggregation at pH ≤ 4.8. Notably, the self-assembly occurred at pH values where both components are stably dispersed in solution. The calculated ζ-potential and pH values indicate that the interaction between the two components is most probably due to the reduction of repulsion between the deprotonated carboxylic groups of the GO and the negatively

charged amino acids present on M13, at the pH range 4.8–5.4. Moreover, after the protonation of Glu_{20}, the interaction between the positively charged N-terminus and K_8 with the carboxylic groups on the GO can trigger the self-assembly process, further enabling the self-assembly of the GPH. Although this suggests that the electrostatic interactions dominate the self-assembly process, other non-covalent interactions involving π-systems are not excluded.

5.3.2. GO to M13 Reaction Ratio

The significant effect of pH on the interaction between the two components was further used to determine the optimal reaction conditions to form the GPH. Therefore, the stability of GO and M13 was tested in 10 mM citrate buffer (CB) at three specific values of pH 3.5, 4.9 and 6.9 **(Table 5.3)**. UV-Vis analysis demonstrates that both components are stable at all the above-analysed pH conditions, except at pH 3.5, at which M13 has precipitated considerably due to its IEP **(Fig. 5.6a, 5.7a–d)**.

Table 5.3. The pH values of GO, M13 and GPHs in CB

Medium	*n*	Sample	pH
CB pH 3.5	3	$GO_{0.3\ mg\ mL^{-1}}$	3.19 ± 0.06
	3	$M13_{0.3\ mg\ mL^{-1}}$	3.44 ± 0.05
CB pH 4.9	3	$GO_{0.3\ mg\ mL^{-1}}$	4.80 ± 0.02
	3	$M13_{0.3\ mg\ mL^{-1}}$	4.95 ± 0.02
	3	$GO\text{-}M13_{03001\text{-}5'}$	4.77 ± 0.03
	3	$GO\text{-}M13_{00103\text{-}5'}$	4.94 ± 0.02
	3	$M13\text{-}GO_{00103\text{-}5'}$	4.80 ± 0.01
	3	$M13\text{-}GO_{03001\text{-}5'}$	4.96 ± 0.03
CB pH 6.9	3	$GO_{0.3\ mg\ mL^{-1}}$	6.71 ± 0.06
	3	$M13_{0.3\ mg\ mL^{-1}}$	7.02 ± 0.06
	3	$GO\text{-}M13_{03001\text{-}5'}$	6.50 ± 0.05
	3	$GO\text{-}M13_{00103\text{-}5'}$	6.85 ± 0.04
	3	$M13\text{-}GO_{00103\text{-}5'}$	6.50 ± 0.06
	3	$M13\text{-}GO_{03001\text{-}5'}$	6.83 ± 0.02

Further UV-Vis analyses were performed to establish and quantify the assembly-ratio between the two components at optimal assembly conditions. GO was transferred into CB and mixed with a 30 times weight excess of M13 (GO-M13$_{00103\text{-}5'}$) and reciprocally, M13 was mixed with 30 times excess of GO inside the buffer (M13-GO$_{00103\text{-}5'}$). Moreover, two other samples were prepared by inverting the order of addition of the two components to evaluate if the mixing was affecting the reaction ratio (M13-GO$_{03001\text{-}5'}$, GO-M13$_{03001\text{-}5'}$) **(Fig. 5.6b, c, 5.7)**.

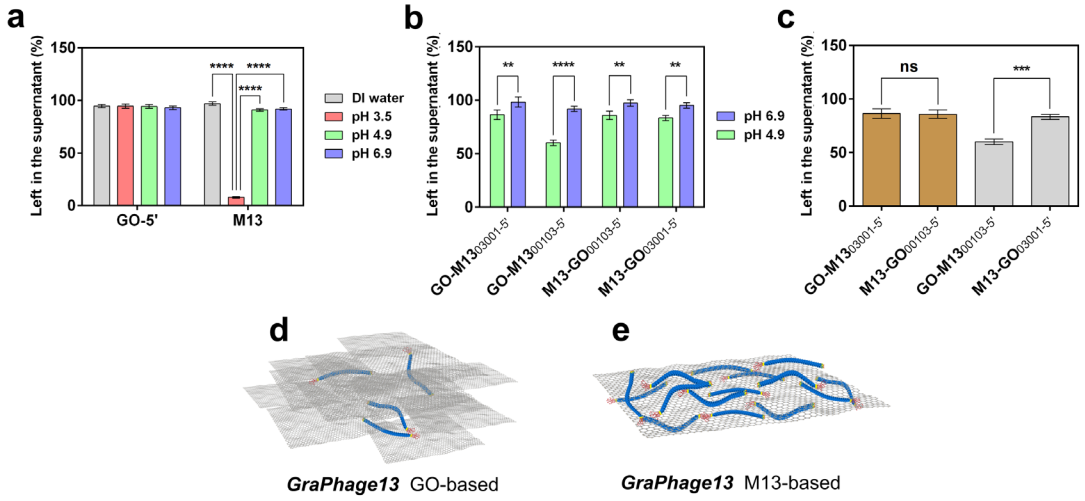


Figure 5.6. *GraPhage13* stability and alternative assembly conditions

The bar charts show **(a)** the amount of GO and M13 left in the supernatant after centrifugation in different media conditions such as DIW and CB pH 3.5, 4.9 and 6.9. **(b)** The comparison between several GO-M13 formulations at two different pH conditions at which GO and M13 self-assemble (green) and where they do not interact. **(c)** The amount of GO (brown) and M13 (grey) left in the supernatant after centrifugation of several GO-M13 formulations in CB pH 4.9. Schematic representation of two different *GraPhage13* hydrogel/aerogel compositions **(d)** GO-overloaded and **(e)** M13-overloaded.

Due to the instability of M13 at pH ≤ 4.8 **(Fig. 3.6)**, the self-assembly of GPH was carried-out at pH 4.9, which is slightly above its IEP, and compared to the control solutions at pH 6.9, at which no interaction was expected to occur.

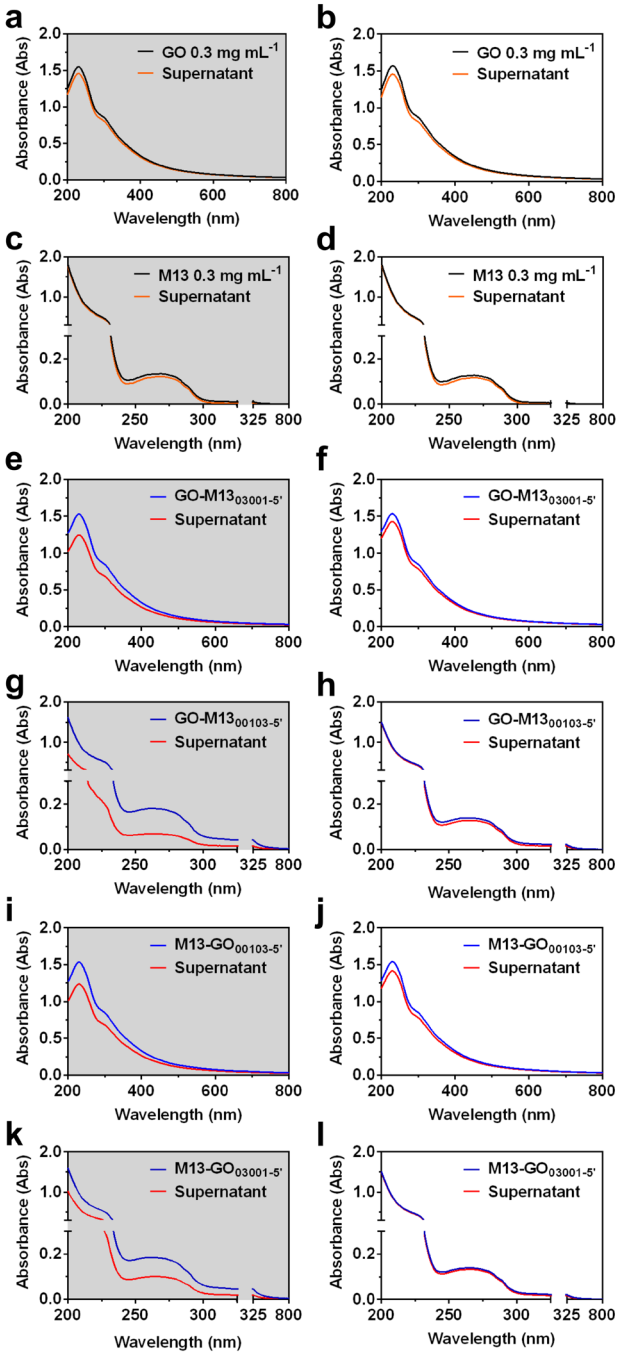


Figure 5.7. UV-Vis analysis for the quantification of the reaction ratio

This figure shows the UV-Vis spectra of GO, M13 and GO-M13 samples in assembly (grey background) and disassembly pH conditions (white background), corresponding to pH 4.9 and 6.9 respectively. The reduced absorbance signal shown by the supernatants of the samples in assembly conditions indicates that after centrifugation, a portion of the components precipitated due to the assembly process. Contrarily, the samples in the disassembly condition show no differences after centrifugation, indicating that the components are still freely dispersed in solution.

The UV-Vis analyses further corroborated the significance of the pH on the interaction between the GO and M13 **(Fig. 5.6b)**. Furthermore, the mixing is of significant importance **(Fig. 5.6c)** for the self-assembly process.

At optimal pH values for the self-assembly, it is possible to modulate the reaction by varying the ratios of each component, to yield the two different assembly conditions called, *GO-* and *M13-based* **(Fig. 5.6d, e)**, depending on which of the two is in excess. GO:M13 weight ratio ranges from 4:1 to 1:5, nevertheless, inverting the order of addition of the two components the *M13-based* hydrogel ratio can increase up to 1:12 **(Table 5.4)**.

Table 5.4. GPHs stability in CB

		Absorbance (Abs)	*n*	Concentration (mg mL^{-1})	Precipitation (%)
CB pH 4.9	**GO-5'**	1.548 ± 0.019	3	0.303 ± 0.003	5.84 ± 0.20
	Supernatant	1.458 ± 0.015	3	0.285 ± 0.002	
	***M13**	0.134 ± 0.016	3	0.348 ± 0.035	8.87 ± 3.45
	***Supernatant**	0.122 ± 0.010	3	0.316 ± 0.022	
	GO-M13$_{03001\text{-}5'}$	1.531 ± 0.004	3		13.72 ± 1.53
	Supernatant	1.246 ± 0.029	3	0.244 ± 0.005	
	***GO-M13$_{00103\text{-}5'}$**	0.178 ± 0.005	3		40.20 ± 7.93
	***Supernatant**	0.068 ± 0.013	3	0.177 ± 0.028	
	M13-GO$_{00103\text{-}5'}$	1.537 ± 0.010	3		14.26 ± 1.27
	Supernatant	1.237 ± 0.024	3	0.242 ± 0.004	
	***M13-GO$_{03001\text{-}5'}$**	0.181 ± 0.008	3		16.97 ± 0.89
	***Supernatant**	0.099 ± 0.001	3	0.258 ± 0.003	
CB pH 6.9	**GO-5'**	1.570 ± 0.022	3	0.307 ± 0.004	7.12 ± 0.40
	Supernatant	1.458 ± 0.015	3	0.285 ± 0.002	
	***M13**	0.127 ± 0.013	3	0.330 ± 0.027	7.92 ± 4.28
	***Supernatant**	0.116 ± 0.007	3	0.303 ± 0.015	
	GO-M13$_{03001\text{-}5'}$	1.536 ± 0.022	3		-0.28 ± 1.86
	Supernatant	1.431 ± 0.035	3		
	***GO-M13$_{00103\text{-}5'}$**	0.138 ± 0.007	3		-0.12 ± 5.90
	***Supernatant**	0.127 ± 0.010	3		
	M13-GO$_{00103\text{-}5'}$	1.540 ± 0.023	3		0.99 ± 0.50
	Supernatant	1.415 ± 0.009	3		
	***M13-GO$_{03001\text{-}5'}$**	0.138 ± 0.005	3		-3.02 ± 2.13
	***Supernatant**	0.131 ± 0.004	3		

The absorbance values and the respective concentrations of the samples in **Fig. 5.6b, c** and **5.7** are reported in **Table 5.4**. The concentrations of starred samples (*) were calculated using the Beer-Lambert-Bouguer law (λ = 269 nm) **(Eq. 2.6)**, and similarly, the concentrations of the non-starred once were calculated using the calibration curves in **Fig. 4.5** (λ = 230 nm).

The precipitation values refer to the amount of GO or M13, expressed in percentage, that was precipitated after centrifugation. These were calculated using the difference between the sample and the respective supernatant concentrations, also considering the precipitation percentage of the component if dispersed individually.

These extreme assembly conditions are highly-appealing since they can potentially enable tailoring the properties and functional applications of GPA such as porosity, surface area and stiffness.

5.3.3. The Rheology of GPH

Following the GPH assembly, the subsequent second step (ii) included the hydrogel separation **(Fig. 5.1)**. The sample was centrifuged at 15 000 rpm for 1 min (RCF = 15 100 *g*) and 90% of the clear supernatant was discarded. After that, the pellet was resuspended, yielding the final *GraPhage13* hydrogel (GPH). The viscosity and stress of the standard GPH formulation (GO-M13$_{0303\text{-}5'}$), were analysed using a rotational rheometer **(Chapter 2.3.7)**. GPH was analysed by depositing 75 µL on the rheometer platform and analysed by varying the shear rate from 0.1 to 1000 s^{-1} at 25°C. The hydrogel density was predicted to be 1.003 mg cm^{-3} and subsequently calculated by weighing three samples of 1.0 mL on an analytical balance. The rheometer results in **Fig. 5.8** show

shear-thinning indicating that GPH behaves as a non-Newtonian fluid and the hydrogel density was estimated at 1.005 ± 0.003 g cm^{-3}.

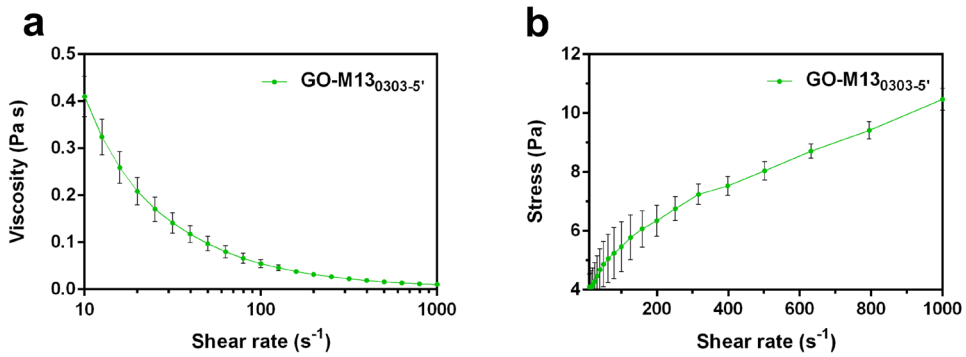


Figure 5.8. Rheological characterisation of *GraPhage13* hydrogel

GraPhage13 aerogel shows shear-thinning, a characteristic of non-Newtonian fluids.

5.4. GPA Characterisation

5.4.1. Morphological Characterisation

After the centrifugation, 900 µL of the supernatant was removed, and the pellet was well resuspended in the remaining supernatant. 50 µL of the final hydrogel were deposited onto the Si substrate and finally, dried for 1 h in a vacuum chamber until reaching the pressure of ~90 Pa. Before the secondary electrons image acquisition, all the samples were sputter-coated with platinum for 4 min at 30 mA **(Chapter 2.2.5)** and subsequently analysed with the SEM/EDX at 15 kV **(Chapter 2.3.5)**. GPA exhibited a layered and porous 3D sponge-like structure with a random distribution of micro and nanopores **(Fig. 5.9, 5.10)**. GO, on the other hand, exhibited a very fine and fragile structure **(Fig. 5.9f)**, while the M13 appeared to be of an amorphous morphology with tangled fibres **(Fig. 5.9g)**. The unique sponge-like structure of GPA arises from the intertwined

M13 nanowires, acting as threads in-between the thin GO nanosheets, forming the hierarchical 3D architectures with embedded microporous morphology. While GO was predominantly comprised of carbon and oxygen, M13 and GPA exhibited the presence of elements such as N, S, P, Na and Cl from the amino acids, DNA and traces of salts **(Fig. 5.9i–k)**. The Si peak is due to the underlying supporting substrate on which the free-standing 3D sponge with an average thickness of ~2 mm was generated. EDX analysis at three random locations across the macro-sponge yielded identical elemental composition throughout, indicating a homogeneous distribution of GO and M13 inside the 3D sponge **(Appx. 5–7)**.

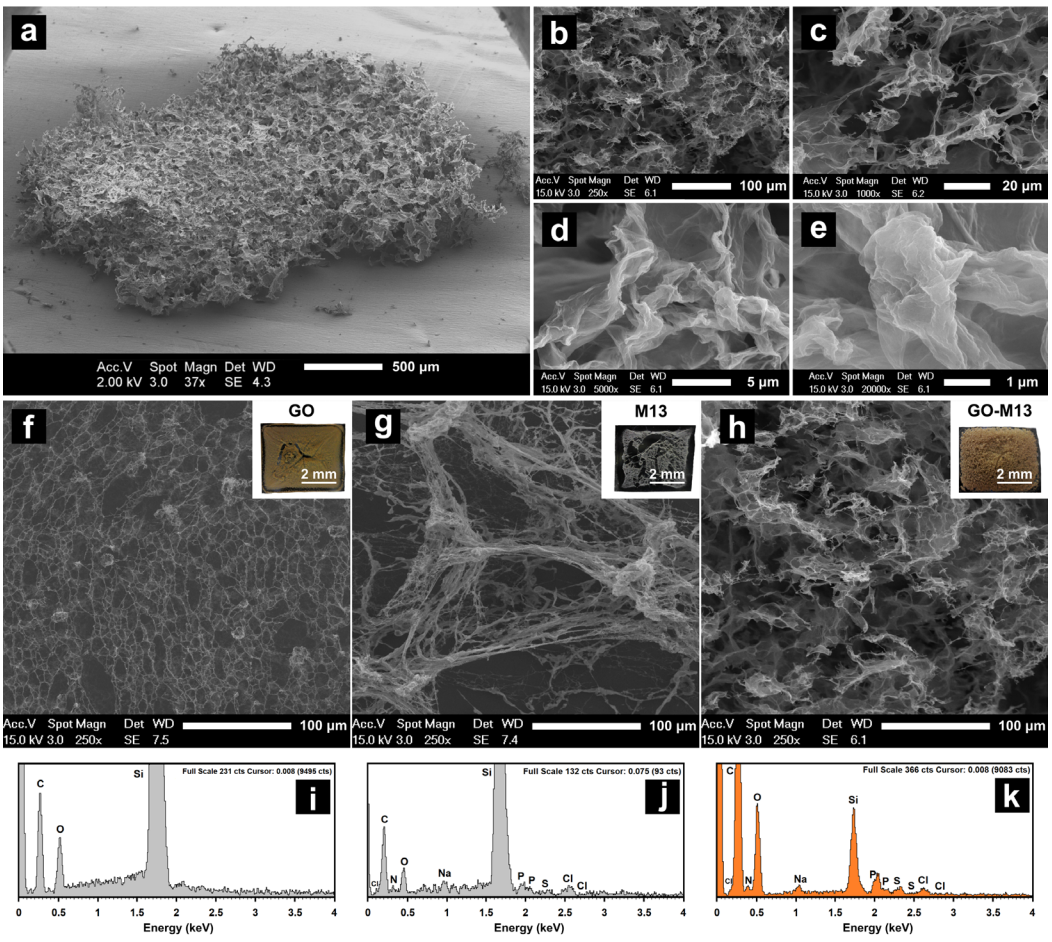


Figure 5.9. SEM-EDX analysis of *GraPhage13* aerogel and its components

(a–e) SEM images of GO-M13$_{0303\text{-}5'}$ aerogel (GPA) at different magnifications. **(f)** GO-5', **(g)** M13 and **(h)** GPA. Inserts: Picture of the sample and the at the bottom **(i–k)**, the corresponding EDX spectra.

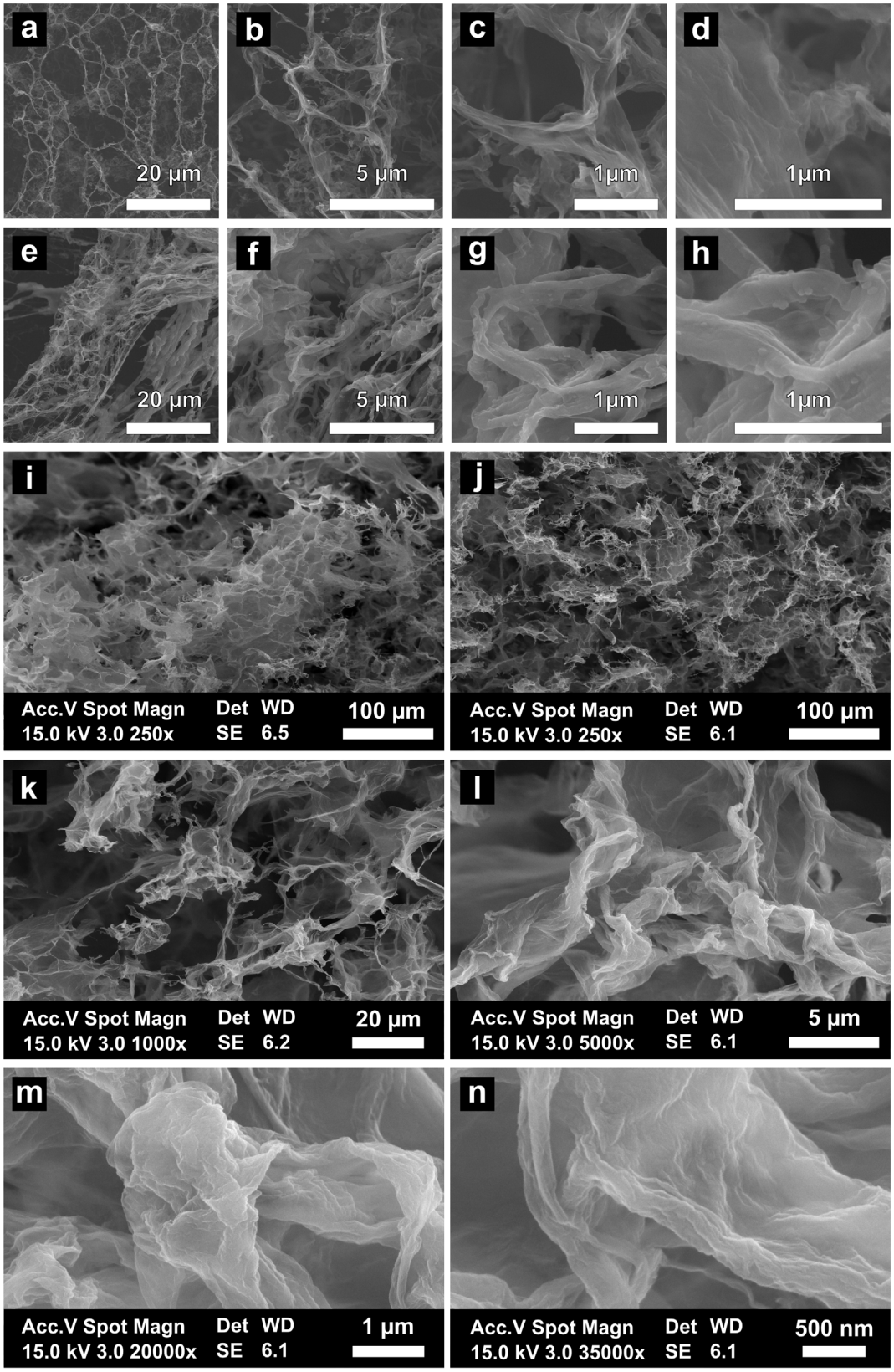


Figure 5.10. SEM images of *GraPhage13* at different magnifications

SEM images of **(a–d)** dry GO-5', **(e–h)** M13 and **(i–n)** GPA at different magnifications.

5.4.2. Calculations of the Volumetric Mass and the Surface Area

The drop-casting (iii) and the drying (iv) steps are characterised by the deposition of 50 μL of the hydrogel onto a silicon wafer and the subsequent placing in a vacuum chamber. As the drying process progressed, caused by the vacuum evaporating the water, the hydrogel changed into an extremely light 3D porous aerogel (GPA). The produced aerogel was further investigated to calculate its density and surface area, which are commonly calculated for this class of materials.

In the first instance, the volumetric mass of GPA was measured with He-gas pycnometer (Micrometrics AccuPyc II 1340®) which is the instrument generally used for this type of characterisation in a non-destructive manner.[338] This technique is based on Boyle's law and it detects the pressure change resulting from the displacement of gas by a solid object. The instrument measures the pressure inside a chamber filled with a gas (usually He). Subsequently, the pressure inside the chamber containing the same amount of gas is measured, however, this time in the presence of a sample. The difference between the two pressures combined with the volume of the empty chamber and the sample mass is used to determine the sample volume and density.[338] Unfortunately, due to the detection limit of the instrument and the apparently extremely low-density of GPA, the measurement was not possible at this instance.

GPA was also attempted to be analysed through X-ray microtomography (micro-CT preclinical tomography system/high-resolution - SKYSCAN 1172), a non-destructive technique that uses X-rays to recreate 3D virtual models of physical objects.[339] The analysis of the 3D models obtained with this technique provides a breadth of information

on porous materials such as the GPA, including the porosity, pore size distribution, pore connectivity, surface area, hydraulic radius and aspect ratio.[339] Also, these measurements did not go according to the plan, most probably due to the low density of the GPA and further studies will be required to successfully characterise these properties. Interestingly, an image of GPA deposited on top of a silicon wafer shows that the sponge cannot be distinguished from the air background and the support on which it was deposited for the analysis **(Fig 5.11)**.

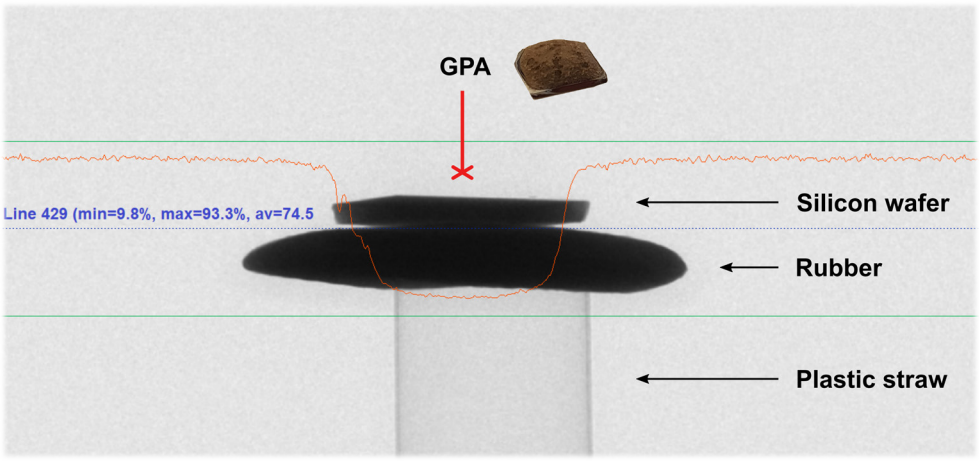


Figure 5.11. X-ray micro-CT analysis of *GraPhage13* aerogel

The figure shows the silicon wafer on which a GPA was deposited, connected on the top of a plastic straw through a small rubber, used as support for the rotating stage of the micro-CT scanner. The area on top of the silicon wafer should show the porous structure of GPA which appears 'invisible', with a contrast similar to that of air.

Due to the small dimension and irregular shape of each sponge sample as well as its extremely low weight, an alternative method was conceived for the calculation of the density. The latter consisted of demonstrating that the volume of GPA was not varying considerably compared to the volume of the GPH used for its production, and subsequently weight the sponge with a microbalance.

To estimate the change in volume between GPH and GPA, a rotating stage with a fixed camera was used and each GPH sample was photographed at 0°, 90°, 180° and 270°. After drying, the fresh GPA was photographed in the same way and the profile pictures of GPH and GPA were overlapped **(Fig. 5.12 and Table 5.5)**.

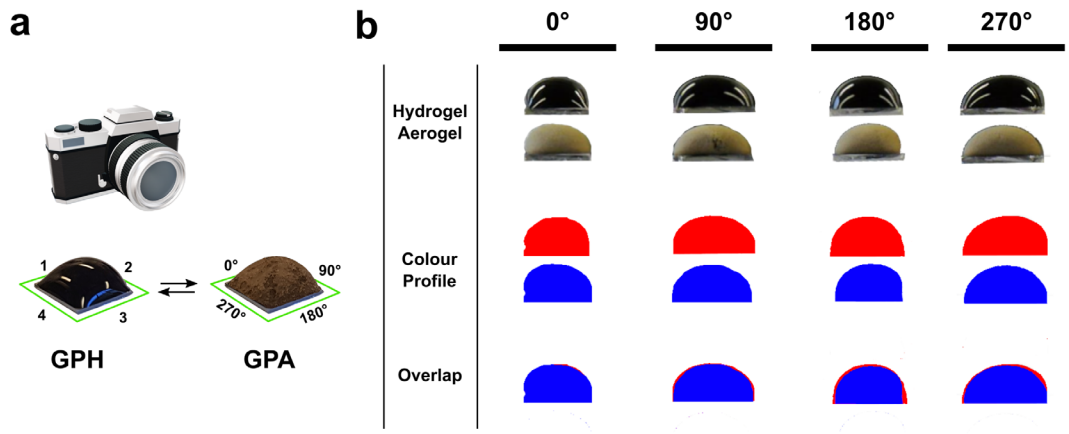


Figure 5.12. Pictures and image analysis of GPH and GPA

(a) Schematic representation of the rotating stage and camera to acquire the pictures of GPH and GPA. **(b)** The pictures at 0°, 90° 180° and 270° with their corresponding monochromatic images used for the comparison between GPH and GPA are shown.

Table 5.5. Image analysis of GPH and GPA

	Hydrogel area (px)			Aerogel area (px)		
	1	**2**	**3**	**1**	**2**	**3**
0°	6736	5564	6063	6228	5723	6636
90°	5909	4890	5138	5266	4444	5946
180°	6346	5783	5844	6004	5557	6410
270°	5471	5207	5279	5272	4584	5892
Total	68 230 px			67 962 px		
Difference	268 px 0.393%					

The comparison of the areas in pixels of GPH and GPA shows that there is a difference of 0.4% and therefore, it is possible to assume that GPA and GPH have the same volume (50 mm^3). To measure the weight of an individual sponge, a microbalance from a

Dynamic Vapour Sorption apparatus (DVS Advantage - Surface Measurement Systems®) was employed. The average of each sponge was divided by the average volume yielding an ultra-low-density of 8.82 ± 0.03 mg cm^{-3}.

The surface area of GPA was measured *via* a BET apparatus **(Chapter 2.3.8)**. The analysis was performed three times using a sample composed of approximately thirty GPA sponges (corresponding to a total mass of ~0.011 mg), dried overnight at 40°C in the oven (Genlab Classic Oven) before the analysis. The results show that the GPA has a high-surface-area of 325.147 ± 34.307 m^2 g^{-1} **(Table 5.6)**.

Table 5.6. BET surface area

	Samples			Average	SD
	1	2	3		
BET Surface Area (m^2 g^{-1})	793.48	859.95	1054.88	902.77	110.93
Single point surface area (m^2 g^{-1})	276.72	346.80	351.92	325.15	34.31
p/p°	0.273514205	0.273432514	0.27342998	0.27346	0.00004

Other graphene-based sponges reported in the literature show a density in the range of 0.16–90 mg cm^{-3} and surface area in the range of 166–1500 m^2 g^{-1} **(Table 5.7)**.[36,340–344] Although *GraPhage13* does not show superior properties, its values of density and surface area are comparable with most of the other graphene-based sponges.

The ultra-flyweight aerogels (UFAs) assembled by Sun *et al.* using GO and carbon nanotubes (CNTs) are interesting materials which can be easily scaled up, and their electrical conductivity and absorption properties have been already tested.[340] However, even though UFAs can reach extremely low density **(Table 5.7)**, *GraPhage13* shows a

slightly larger surface area. Moreover, the aerogels developed by Zhang *et al.*,[345] Zhao *et al.*[343] and Luan *et al.*[346] show surface areas in the same range of *GraPhage13*, which on the other hand has a lower density. Considering that some other sponges show surface areas >1000 m^2 g^{-1},[344,347] to overcome these limits, it is important to develop alternative strategies to assemble newer version of *GraPhage13* with lower density and increased surface area.

Table 5.7. Comparison of graphene-based aerogels

	Components	Surface area (m^2 g^{-1})	Density (mg cm^{-3})	References
Laser-scribed graphene (LSG)	• GO	1520		[344]
Gelation of a graphene oxide *via* resorcinol-formaldehyde (RF) sol-gel chemistry	• GO • Resorcinol-formaldehyde (RF)	584–1200	16–25	[347]
Reduced graphene oxide hydrogel (rGH)	• GO • Ethylene diamine (EDTA)	745		[346]
Graphene oxide with L-ascorbic acid	• GO • L-ascorbic acid	512	31–96	[345]
Polypyrrole graphene foams (PPyG)	• GO • Polymer of polypyrrole (PPy)	166–463	5–40	[343]
GraPhage13 (GPA)	• GO • M13 bacteriophage	325	8.82	
Ultra-flyweight aerogels (UFAs)	• GO • Carbon nanotubes (CNTs)	272	0.16–22	[340]
Graphene sponge (GS)	• GO	79–150		[348]
Graphene oxide–epoxy composite aerogel (GEA)	• GO • Epoxy resin		90	[342]

5.4.3. FT-IR Spectroscopy

FT-IR was employed to characterise GPA by comparing its spectrum with the spectra obtained from its components individually. Samples were prepared following the procedure and using the equipment described in **Chapter 2.3.2**.

The results show that the GO and M13 produce two different and distinguishable spectra **(Fig. 5.13)**. In particular, the predominant peaks which characterise M13 are centred at 1545, 1655, 3296 cm^{-1} and the band between 2800–3000 cm^{-1}. These peaks refer to O–C=O stretching, C–N stretching, amide bands I, II and III, O−H and N−H groups involved in hydrogen bonds **(Chapter 3.5.1)**. On the other hand, GO can be identified through the peaks at 1366, 1400, 1625, 1710, 3209 e 3414 cm^{-1}, assigned to O–H, C=C, C–H, C=O stretching and tertiary C–OH groups **(Chapter 4.6.1)**.

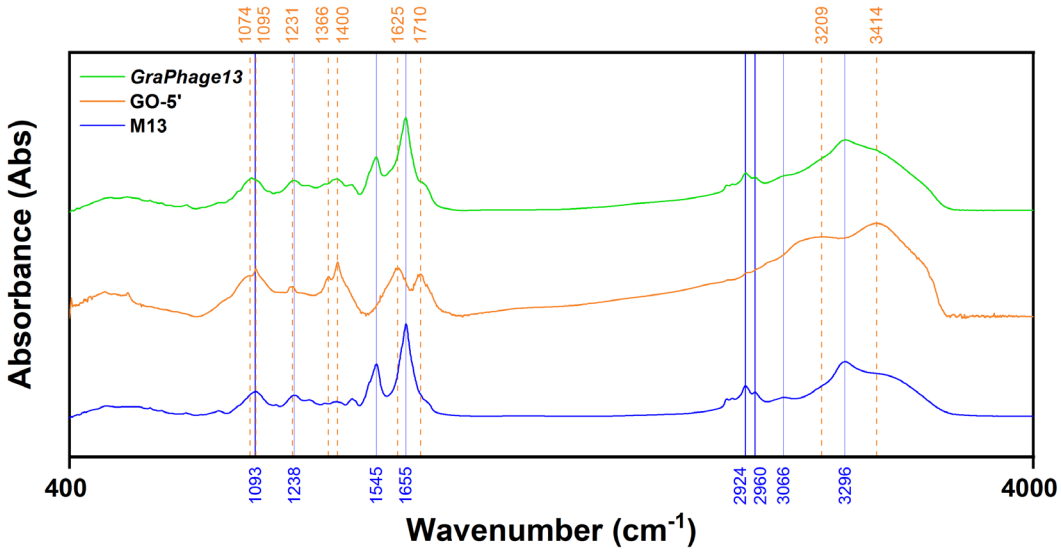


Figure 5.13. Comparison between the FT-IR spectra of GPA, GO and M13

The figure shows the comparison between the spectra of M13 (blue), GO-5' (orange) and *GraPhage13* (green).

The spectrum of GPA shows the typical peaks of both GO and M13, which do not present any significant change in terms of intensity ratios among the peaks in the same spectrum as well as no significative peak shifts. This is an indication that there is no change in the number and nature of the chemical bonds already present in the individual components.

These results support the hypothesis that the GPA self-assembly is predominantly based on non-covalent interactions.

5.4.4. Raman Spectroscopy

Raman spectroscopy was further carried out on the GO, M13 and GPA to quantify the effects of the interaction between GO and M13 in the sponge on the original bonds of each component. The Raman analysis was performed following the methods and using the equipment described in **Chapter 2.3.3** for the characterisation of GO and M13 individually.

To further study the interaction between GO and M13, their spectra were compared with GO-M13$_{0303\text{-}5'}$ (GPA) and a control sample comprised of M13 and GO dried separately and grained together with no sponge formation, but of merely physical contact (GO-M13$_{PC}$ also named GPA$_{PC}$).

The Raman spectra of GO and GPA exhibited two clear peaks at 1350 and 1600 cm^{-1} at the excitation wavelengths of 633 and 785 nm **(Fig. 5.14a)**. Differently, M13 exhibited three strong peaks at 1310, 1650 and 1590 cm^{-1} **(Fig. 5.14a)**, agreeing with the literature.[282] For the control sample GPA$_{PC}$, Raman spectra exhibited highly similar fingerprints to those of GO and GPA **(Fig. 5.14a)**.

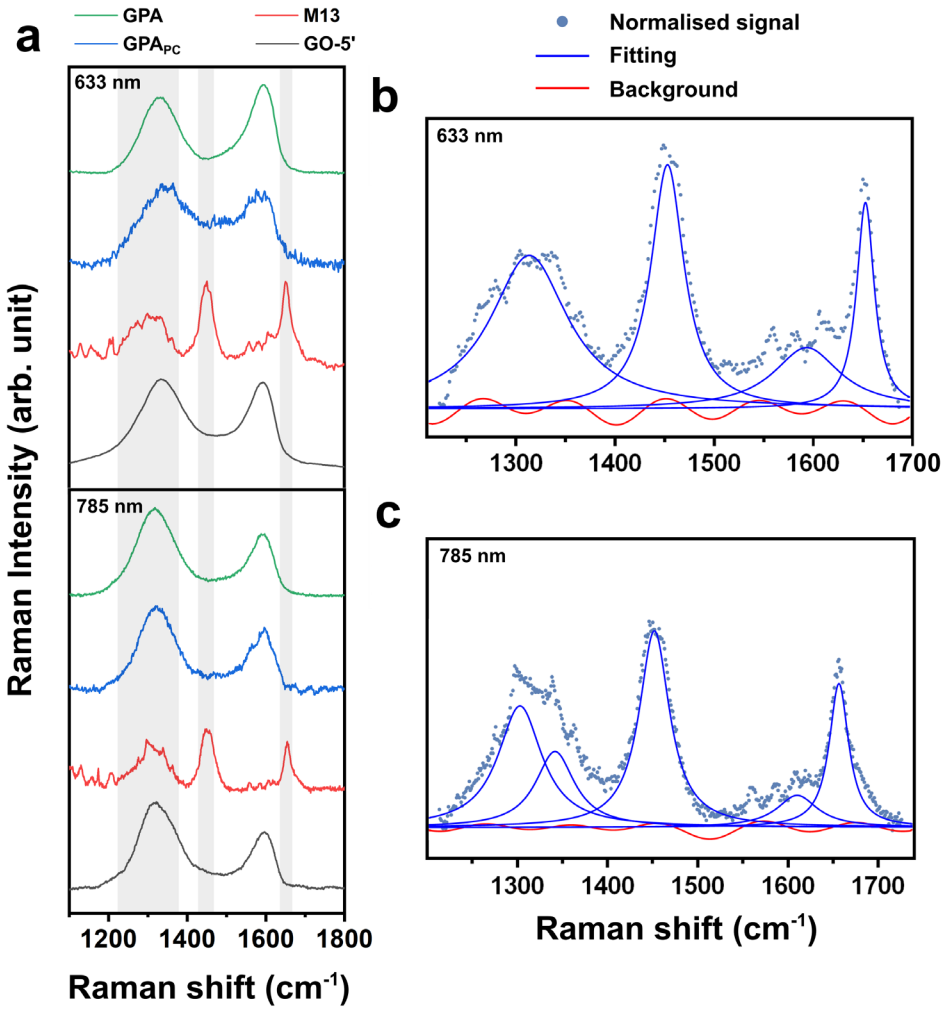


Figure 5.14. Comparison between the Raman spectra of GPA, GO and M13

(a) The Raman spectra of GO (black), M13 (red), the GPA_{PC} (blue) and the GPA (green) at 633 and 785 nm laser excitations, labelled respectively, are presented. The spectra are vertically shifted for clarity. The best fit of the spectra of M13 at 633 **(b)** and 785 nm **(c)** are shown. These best fits consist of 4 and 5 Lorentzians for Raman peaks (blue) and Fourier series of five and six terms for the background (red), respectively for the 633 and the 785 nm signals. The spectra were subtracted by a straight line to make flat (blue dots).

From Raman analysis, it is evident that the spectra of both GPA and GPA_{PC} contain contribution mainly from GO rather than the M13. It was anticipated that due to the interaction between GO and M13 during the assembly of the sponge, two main peaks of GPA would be shifted, while those of GPA_{PC} will not, indicating a change of the GO

bonds. Considering that all the spectra exhibited broad peaks with a large background, and the employment of fitting procedure, a subjective choice of the number of peaks and background could affect the position of fitted peaks. Baseline-subtraction was not applied to the acquired spectra in **Fig. 5.14a**. Maximum likelihood estimation was employed to obtain the peak positions in the model (the peak shape, number of peaks, parameters of each peak and background) optimal for the acquired data **Table A8.1–4 (Appx. 8)**.

Each spectrum was initially subtracted using a straight line for flattening, and subsequently, a corresponding number of Lorentzians and Fourier series of a range of terms were applied to give a fit for each spectrum **(Fig. 5.14b, c)**. Finally, by comparing the Bayesian information criteria (BIC) of the fits, the optimal fit was established for each spectrum. To note, no subjective input was provided to the BIC fitting, except setting two rational constraints: amplitudes of Lorentzians are positive, and coefficients of the Fourier series are comparatively small and, therefore, that they do not fit the peaks. The optimal fitting parameters of all the spectra are shown in **Table A8.1–4 (Appx. 8)**.

The BIC fitting shows that the spectrum of the GPA_{PC} consists of two peaks, which correspond to the unmodified sp^2 (G mode) and sp^3 (D mode) bonds of the GO.[349] In the spectrum of the GPA, Raman G mode of GO splits, with approximately 30% upshifted and the rest remains unchanged. While the effect of charge transfer usually shifts the entire Raman peak, this observation can be interpreted as approximately 30% of the sp^2 bond of GO stiffened by ~2%, due to the interaction between M13 and GO. These results confirm that the interaction between GO and M13 in the fabricated sponge is strong enough to modify the original sp^2 bonds.

5.5. Summary and Outlook

This study introduces a novel, rapid and facile method to self-assemble and control GO into 3D hierarchical morphologies using M13 as integrated biological nanocomponent. The new graphene-viral sponge has been in-depth characterised, establishing the preferable conditions for the optimal self-assembly process, enabling the control over the stability as well as laying platform towards controllable pore dimensions. Investigating the formation mechanism of the hydrogel, signposted the electrostatic interaction as the driving force responsible for the self-assembly at specific pH conditions in solution. The porous structure of the micro-nano-composite exhibits ultra-low-density and high-surface-area with further advantages, compared with typical GO sponges, including the ease of assembly, low concentration of the reagents, scalability, environmental sustainability and low-production costs. GPA holds promise for numerous applications including functional scaffolds, absorbers, filters, gas-sensors, chemical catalysis, supercapacitors and optoelectronics. Moreover, the M13 may provide a straightforward route for incorporating chemical functions by functionalisation along their longitudinal filament axis, rendering the *GraPhage13* potentially useful for the development of rapid-response biological and chemical sensors for environmental and biomedical applications, where selective and targeted detection of biochemical molecules is crucial.



UNIVERSITY OF
BIRMINGHAM

CHAPTER VI

GraPhage13 Applications



Abstract

GraPhage13 was previously introduced and extensively described as an alternative graphene-based composite material, characterised by a porous 3D network, showing extremely low-density, high-surface-area. This chapter describes preliminary experiments on GraPhage13 to explore its properties and define some potential application exploiting its architecture as well as exploring further functionalisation with gold and carbon nanotubes.

Paolo Passaretti

6.1. Introduction

In addition to the development of the self-assembly process and the characterisation of the new composite *GraPhage13* in the form of hydrogels and aerogels, this chapter includes some preliminary results of additional experiments aimed to functionalise these new materials and in particular, to test some properties of GPA.

It was observed that by modifying the concentration ratios between the two components (GO and M13) and the water content of GPH, it is possible to modulate the pore size of GPA. The obtained different porosity can be used for the production of GPAs showing interesting wettability properties.

Gold electrodeposition was performed to replicate the porous structure of GPA **Chapter 2.2.6**, moreover, carbon nanotubes (CNTs) were successfully integrated into the composite, obtaining a novel GO-M13-CNTs sponge. Both conditions have been tested to improve the chemical-physical properties of GPA, in particular, the mechanical properties and electro-thermal conductivity.

The results obtained from these further experiments are reported in the following pages. The PGSTAT was mainly used to perform the electrodeposition, and the samples were characterised by an optical microscope and SEM coupled with EDX **Chapter 2.3.5**. In addition, there are some images of the different porosities obtained, measurements of the contact angle with DIW.

The following experiments opened alternative routes for the study of this novel graphene-based material, showing potential functionalisation and application. Nevertheless, more experiments need to be performed to optimise the methodologies and obtain more reproducible results.

6.2. Adjustable Porosity and Wettability of GPA

In **Chapter 5** is shown the formation of different versions of GPHs and GPAs, named GO- and M13-based obtained by varying the concentration ratios between GO and M13. These different formulations can improve or even confer new characteristics to both hydrogels and their corresponding aerogels. An example of that is given by the possibility of adjusting the porosity of the GPAs, starting from M13-based GPHs such as GO-M13$_{0303\text{-}5'}$, GO-M13$_{0306\text{-}5'}$ and GO-M13$_{0309\text{-}5'}$. The GPAs obtained from the previously listed M13-based GPHs showed different morphologies immediately visible from a picture without using any particular equipment **(Fig. 6.1)**.

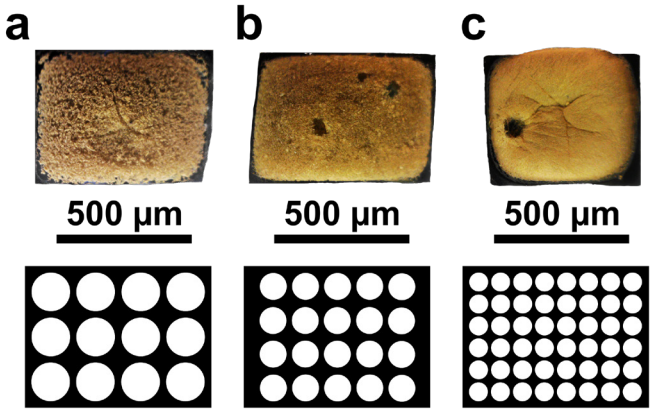


Figure 6.1. Different porosity of M13-based GPAs

(a) GO-M13$_{0303\text{-}5'}$, **(b)** GO-M13$_{0306\text{-}5'}$ and **(c)** GO-M13$_{0309\text{-}5'}$ aerogels. Below the pictures, a schematic representation of the different porosity of the samples.

Although the sponges thus obtained were extremely fragile, they showed to be durable over time if stored in normal plastic containers, avoiding subjecting them to strong compressions.

Given the nature of the components of which GPAs consist, it is expected that the aerogels can be drastically affected by water and other solvents. Therefore, to test the durability of

the standard GPA (GO-M13$_{0303\text{-}5'}$) in contact with water, a small 5 µL drop of DIW was deposited with a pipette on top of the sponge. The drop instantaneously dissolved the aerogel and its porous structure, rapidly diffusing in the entire porous network **(Fig. 6.2a)**. The same experiment was also performed on the other M13-based GPAs, GO-M13$_{0306\text{-}5'}$ and GO-M13$_{0309\text{-}5'}$ shown in **Fig. 6.2b, c** respectively. Contrary to the standard GPA, the M13-based aerogels did not allow the DIW to penetrate and dissolve their structure.

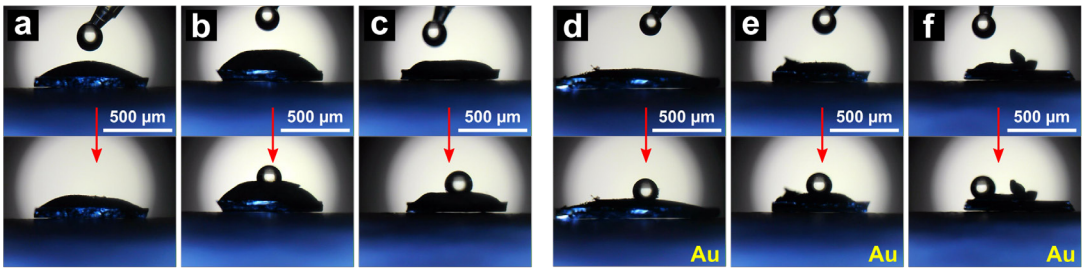


Figure 6.2. The characterisation of GPA wettability

(a) GO-M13$_{0303\text{-}0'}$, **(b)** GO-M13$_{0306\text{-}5'}$ and **(c)** GO-M13$_{0309\text{-}5'}$ aerogels, compared with **(d)** GO-M13$_{0303\text{-}0'}$, **(e)** GO-M13$_{0306\text{-}5'}$ and **(f)** GO-M13$_{0309\text{-}5'}$ aerogels after being sputter coated with gold. The different porosity and characteristics of these aerogels are associated with different wettability.

Given this surprising result, the water repellency properties of these GPAs were characterised *via* measuring the contact angle between the drops and the corresponding GPAs surfaces. Furthermore, using a gold sputter coater, several other M13-based sponges were coated with gold and tested to compare their performances with the uncoated sponges to understand if more stable and durable golden replicas of the GPAs showed superior waterproof performance **(Fig. 6.2d–f)**.

The contact angle measurement results listed in **Table 6.1** indicate that increasing the amount of M13 producing M13-based GPAs, results in a superior hydrophobicity of the corresponding sponges ranging from 92.1° ± 1.21 to 130.07° ± 2.78 degrees. On the other

hand, Au-GPAs showed slightly better performances on average, independent of the GO-M13 concentration ratio.

Table 6.1. Contact angles of DIW on GPAs

	GO-M13$_{0303\text{-}0'}$	GO-M13$_{0306\text{-}5'}$	GO-M13$_{0309\text{-}5'}$	GO-M13$_{0303\text{-}0'}$	GO-M13$_{0306\text{-}5'}$	GO-M13$_{0309\text{-}5'}$
	0	93.691°	126.175°	132.739°	139.192°	131.649°
	0	90.773°	132.455°	130.135°	139.035°	132.709°
	0	91.843°	131.576°	130.978°	138.783°	130.326°
Mean	0	92.10°	130.07°	131.28°	139.00°	131.56°
SD	0	1.21	2.78	1.08	0.17	0.97

Therefore, the observed hydrophobic effect could be due to several factors. One of these could be that the hydrophobic areas exposed on the surfaces of GO and M13 do not interact with the water molecule, generating the hydrophobic effect.

However, over time, this does not prevent the drop from disassembling the GPAs, restoring the hydrogel state, with a speed inversely proportional to the size of the pores of the sponge. Another factor could be the micro-nanotexture of the sponge, which does not allow the drop of water to easily penetrate in depth. Moreover, all Au-GPAs with different porosities showed an enhanced hydrophobic effect due to the gold layer and its superior water-repelling properties.[350] Therefore, this hydrophobic effect may not exclusively be due to the chemical properties of the sponge, but also to its micro-nanoarchitecture.

These results encourage to pursue the studies in this direction to consolidate more precise procedures to assemble and categorise more advanced versions of the GPA as well as to extend its range of applications.

6.3. Gold Electrodeposition

Porous aerogels similar to GPA are arousing great interest in the scientific communities, in particular their properties and their potential for many applications in the fields of energy, materials and medicine.[36] Unfortunately, the majority of these graphene-based aerogels are not durable and sometimes the functionalisation process reduced their conductivity performance. Therefore, one of the most common approaches to functionalise and improve the performances of these materials, is the electrodeposition of specific metals such as Au, Pt, Cu and Zn, which are particularly good conductors **(Chapter 2.2.6)**.[251] In this particular case, the experiment aims to determine the reduction potential of gold sulfite and electrodepositing gold onto the GPA surface following the reaction in **Eq. 6.1** using a constant potential.[251,351,352]

$$[Au(S_2O_3)_2]^{3-} + e^- \longrightarrow Au + 2\,S_2O_3^{2-} \qquad (6.1)$$

6.3.1. Experimental Procedure

The PGSTAT (Autolab PGSTAT204) used to electroplate gold onto GPA was composed of three electrodes namely counter (CE), reference (RE) and working (WE) electrodes.[253,254] The sample was assembled on top of a cleaned *p*-type silicon substrate and connected to the WE channel of the PGSTAT system. Similarly, the CE and the RE consisting of a Pt wire and an Ag/AgCl in 3 M NaCl (BAS Inc. Cat. No 012167) respectively, were connected to the corresponding channels and finally soaked in the electrolytic bath. It is good practice to clean the Pt wire *via* flaming, stabilise the RE by leaving it 24 h in 1 M NaCl before running the experiment and purge the bath with

nitrogen (N_2) to remove dissolved oxygen for at least 30 min.[251,351,352] The electrodeposition was performed at 25°C using a commercial full bright cyanide-free gold plating solution (Metalor ECF 60) containing gold of 10 g L^{-1} at pH 9.5. To determine the reduction potential of GPA on the silicon wafer substrate, CV was performed over a range of potentials between -0.8 to 0.2 V and a scan-rate of 0.1 mV s^{-1}.

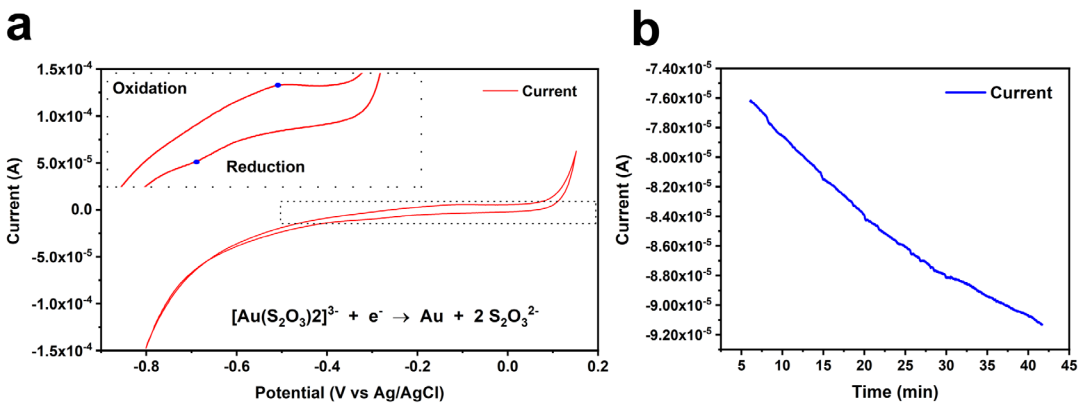


Figure 6.3. Gold electroplating CV and CA results

(a) The cyclic voltammogram showing the reduction peak of gold and the oxidation of GO at specific potential values. **(b)** The chronoamperogram obtained from the electrodeposition of gold onto a GPA showing the typical signal decay.

6.3.2. Results

The resulting cyclic voltammogram **(Fig. 6.3a)** shows an oxidation reaction around -0.1 V and a reduction at -0.3 V. Given that gold sulfite can be hardly oxidised in these conditions,[251,351,352] the positive peak **(Fig. 6.3a)** is most probably due to the further oxidation of GO and/or other groups on the M13 surface, however, this still needs to be clarified. On the other hand, the reduction peak at -0.3 V can be assigned to the gold sulfite reduction on the WE surface.[251,351,352] This specific reduction potential found through CV was employed to set up the CA and obtain a gold-coated *GraPhage13* aerogel

(Au-GPA). CA was performed on a fresh GPA using a constant reduction potential of -0.3 V for 40 min **(Fig. 6.3b)**. The chronoamperogram shows the characteristic exponential decay of a diffusion-controlled process. Given that the solution was not being stirred, the signal appears as a current decay due to the depletion of gold from the electrode-electrolyte interface.

6.3.3. Morphological and Compositional Characterisation

The resulting Au-GPA sample was subsequently observed with an optical microscope, and an SEM coupled with EDX to determine its elemental composition.

The optical microscope images **(Fig. 6.4)** were obtained in reflection mode with several objectives at different magnification (10×, 20× and 50×), and the images were acquired using a Leica camera DMC2900. The images show the same portion of Au-GPA sample at different magnification as well as with a polariser filter. In **Fig. 6.4a** it is possible to see the silicon substrate in the background, and a dark sponge-like structure in the middle of the image, which is the Au-GPA. Increasing the magnification **(Fig. 6.4c, e, g)**, it is possible to observe the gold-coated areas (coloured in yellow) distributed on the surface of the Au-GPA. Moreover, using a polarizer filter **(Fig. 6.4b, d, f)**, it is possible to have a better contrast in the entire image, especially on the edges of the pores, providing a better view of the porous network compared with the unfiltered images. To further characterise the Au-GPA areas where the gold was successfully deposited, the samples were imaged with an SEM/EDX (Hitachi TM3030), which provided higher resolution images as well as the elemental analyses to confirm that the yellow areas detected under the optical microscope are effectively made of gold **(Fig. 6.5)**.

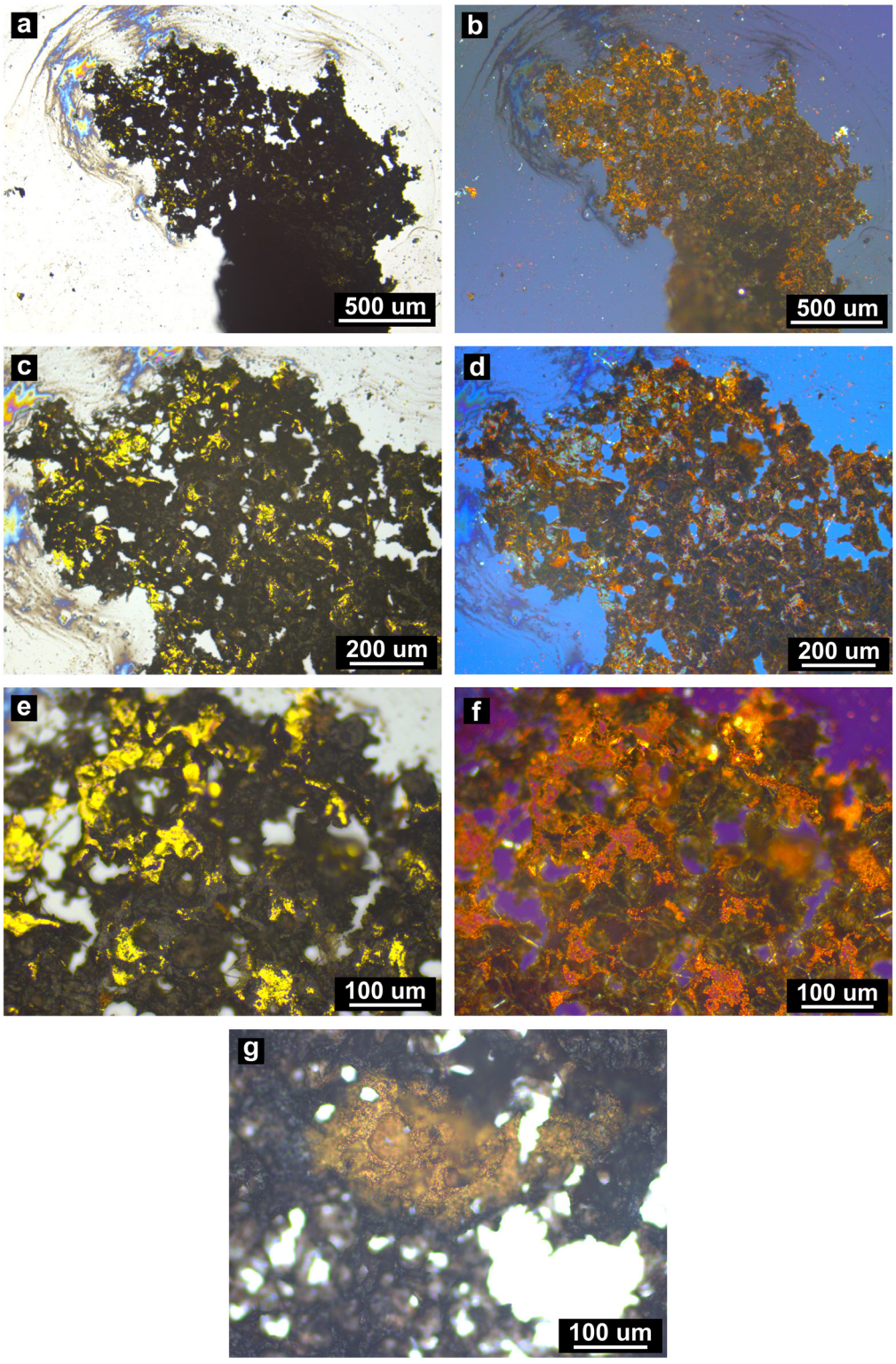


Figure 6.4. Optical microscope analyses of Au-GPA

Microscope images of GPA partially coated with gold and magnified **(a, b)** 10×, **(c, d)** 20× and **(e, f, g)** 50×. **(b, d, f)** were obtained using a polariser filter placed through the light path of the microscope to enhance the differences between the coated and non-coated areas of Au-GPA.

The SEM images show some small fragments of Au-GPA at different magnifications **(Fig. 6.5a-d)** where it is possible to distinguish portions of the porous network covered by nucleated gold, also partially covering the silicon substrate in the background. A different location of the same sample was imaged **(Fig. 6.5e)** and analysed with the EDX **(Fig. 6.5f–k)**. The EDX analysis, assigned a different colour to each different element detected in the sample **(Fig. 6.5f)**.While in the graph in **Fig. 6.5g** the signal corresponding to Si, C, N and Au are reported, in **Fig. 6.5h–k** each channel is visualised with the colour code on the targeted area. In particular, it is possible to see that the area corresponding to the background is labelled just with the colour pink. On the other hand, the area of the image which includes the Au-GPA is coloured in cyan, red and green indicating the presence of GO, M13 and gold respectively.

The optical microscope and SEM/EDX results show that the replica in gold of GPA was successful, but did not entirely cover the porous structure. This can be due to the substrate and/or sample conductivity as well as the buffer condition or the parameter used during the electrodeposition.

Moreover, this electrodeposition procedure visibly affected the sample structure altering its porous morphology. This is due to the instability of GPA in water-based solvents, which can disassemble its structure based on non-covalent interactions. Therefore, considering that the electrodeposition was performed in a water-based bath at pH 9, which is a particularly unfavourable condition for assembly between GO and M13, the partial disassembly of the sample during the experiment was expected.

Despite the limitation of this methodology, it is still an approach which can be further studied and improved.

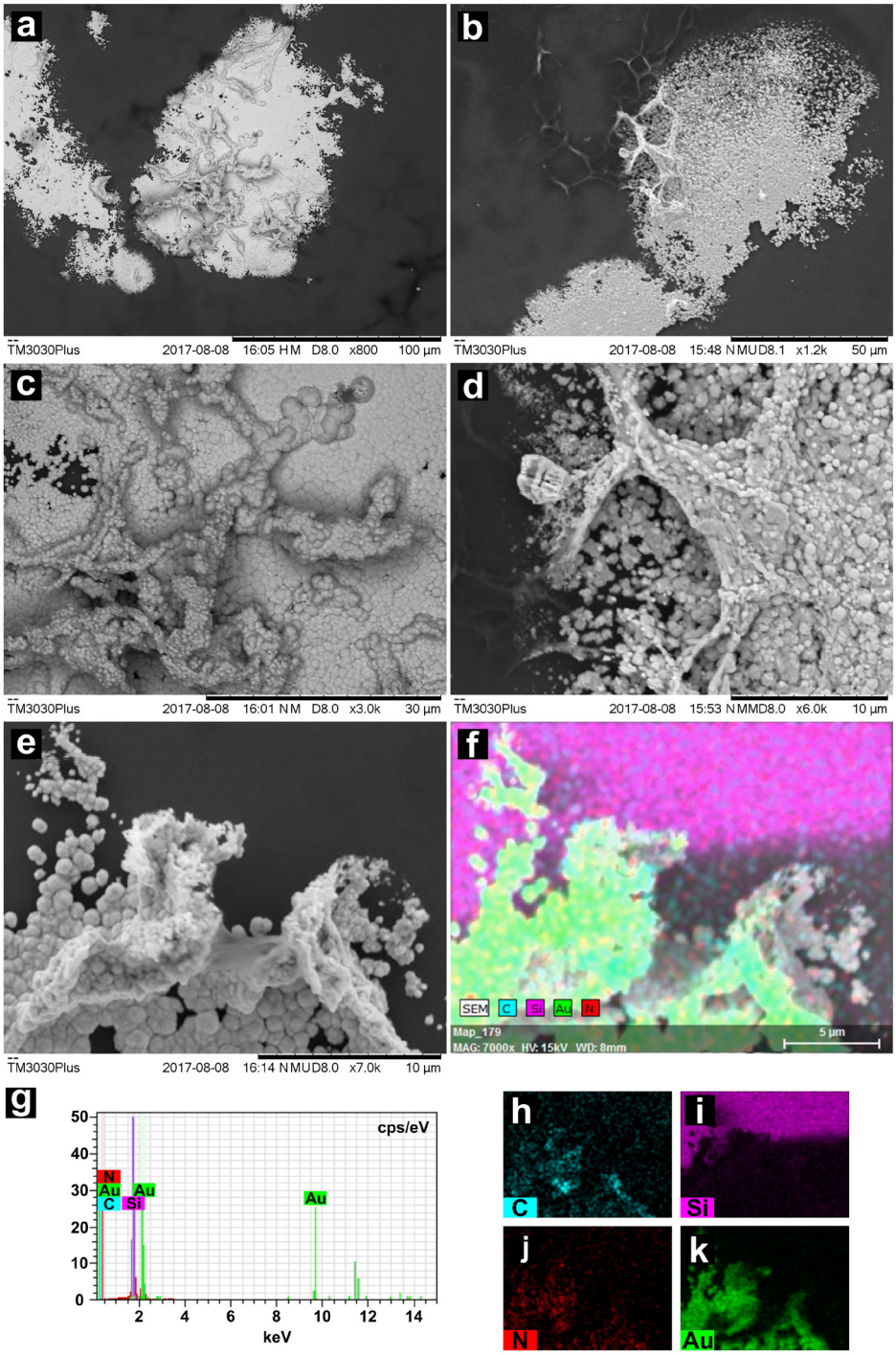


Figure 6.5. SEM-EDX analysis of Au-GPA

(a–e) SEM images of Au-GPA at different magnifications. **(f)** SEM/EDX image of Au-GPA highlighting with different colours the four elements expected to be found in the material and substrate. **(g)** Shows the corresponding spectrum with the relative intensities of the elements detected in the picture area. The elements found in the sample were: **(h)** carbon due to the presence of both GO and M13 (blue), **(i)** silicon (pink) due to the substrate, **(j)** nitrogen associated to the proteins of M13 (red) and **(k)** gold (green) as result of the electrodeposition.

6.4. Functionalisation with Carbon Nanotubes

Due to their remarkable properties, CNTs are considered good candidates for improving the mechanical properties and electro-thermal conductivity of GPA. Therefore, to include CNTs into the GPA, a stock solution containing CNTs was prepared and added to the reaction mixture forming the hydrogel and subsequently dried to obtain an alternative version of the GO-M13 aerogel named CNT-GPA.

Carbon nanotubes are particularly appealing materials employed in many research fields such as electronics, sensing, medicine, energy and more. Since their discovery in 1991 by Iijima,[353] single-walled nanotubes (SWNT) had a great impact on both the global research community and industry, promoting conspicuous investments in their manufacturing methods, characterisation and application development.

SWNTs are an allotrope of carbon made of sp^2 hybridized carbons similar to fullerenes and graphene but arranged to form cylindrical tubes. They show remarkable properties such as a tensile strength ~100 times greater than steel at $1/16^{th}$ the weight,[354] current-carrying capacities of 109 A cm^{-2},[355] thermal conductivity comparable to that of diamond or in-plane graphite, distinct optical absorption and fluorescence response.

There are several methods to produce SWNTs, and these include laser ablation, carbon arc-discharge and chemical vapour deposition (CVD) processes, either involving a gaseous[356] or supported catalyst.[357] Nowadays, the CVD process is the most popular approach to the bulk production of SWNTs. To produce the CNT-GPA, GO and M13 were obtained from the same stock solutions previously described for the assembly of the standard GPA and the CNTs stock solution was separately prepared as follows.

6.4.1. Experimental Procedure

The CNTs employed in this experiment were the CoMoCAT SWNTs purchased from Sigma-Aldrich, and 5 mg of CNTs were dissolved in 1 mL of DIW to obtain a stock solution of 5 mg mL^{-1}. CNTs tend to agglomerate into bundles due to highly attractive van der Waals forces resulting in poor dispersions within most aqueous media. Therefore, the stock was sonicated for 30 min using a probe sonicator at 70%, and sodium dodecyl sulfate (SDS) was subsequently added to the final concentration of 10 mg mL^{-1}. The sonication process, together with the use of surfactants like SDS, helped to form stable dispersions.[358] The dispersion quality was tested *via* centrifugation, similarly to GO **(Chapters 4.3, 4.4)**. The achieved stability in DIW of CNTs through the procedure previously described was not studied in depth as with GO. However, the obtained CNTs stock was stable enough to perform the preliminary experiments to include CNTs in the GO-M13 hydrogel/aerogel.

To assemble CNT-GPA a reaction microtube was prepared adding GO, CNTs and M13 from the corresponding stocks. Each component with a final concentration of 0.3 mg mL^{-1} was dispersed in the reaction microtube containing citrate buffer (CB) pH 4.9. Similarly to the GPH preparation, upon mixing the three components immediately react forming an aggregate, which is separated from the supernatant and deposited on the microtube bottom. While the supernatant was clear, indicating the absence of GO and CNTs, the inclusion of CNTs produced a black pellet, contrarily to the typical dark brown pellet of GPH. Subsequently, the CNT-GPH was further precipitated *via* centrifugation at 15 000 rpm for 1 min (RCF = 15 100 *g*), and 90% of the supernatant removed. Therefore, 50 µL of the obtained CNT-GPH was deposited onto a pre-cleaned *p*-type silicon substrate and dried for 1 h in a vacuum chamber until reaching

a pressure of ~90 Pa. Once dried, the hydrogel turns into a black aerogel (CNT-GPA) that was further investigated with the SEM, similarly to GPA.

6.4.2. Results

The SEM images at different magnification **(Fig. 6.6)**, show that the CNT-GPA is characterised by a porous network where the three components cannot be distinguished. Although CNT-GPA and GPA **(Fig. 5.9, 5.10)** are indistinguishable through their SEM images, more experiments need to be performed to characterise the mechanical and conductive properties of the upgraded sponge material.

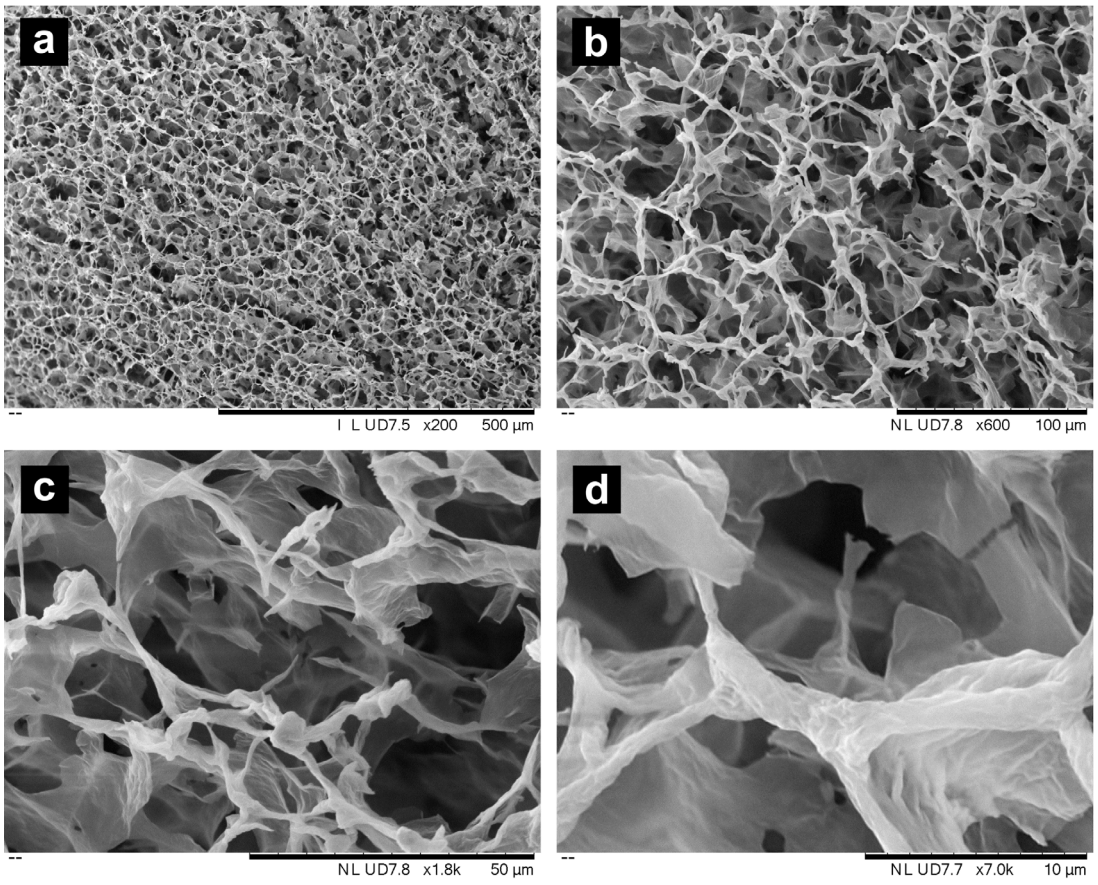


Figure 6.6. SEM images of CNT-GPA at different magnifications

(a–d) SEM images of CNT-GPA at different magnifications showing the material porosity.

6.5. Summary and Outlook

This chapter provides preliminary results and important information for the study and employability of *GraPhage13*, especially about its adjustable porosity and hydrophobic properties as well as the possibility to replicate its structure *via* gold electrodeposition and also, introduce CNTs to improve the material robustness and thermo-electric conductivity.

GraPhage13 porosity can be modulated by modifying the concentration ratios between the components during the assembly process. Unfortunately, this mechanism has not been completely clarified yet and it needs further experimentation to reach a satisfactory level of reproducibility. However, seems that a key factor influencing this phenomenon is the hydrogel density.

Some *M13-based* GPAs have been tested to assess their durability when in contact with water. Surprisingly these showed peculiar hydrophobic characteristics probably due to their micro-nanotexture. In particular, *M13-based* GPAs presented this property, unlike the standard GPA (GO-M13$_{0303\text{-}5'}$). The same types of sample were also covered with a layer of gold through sputter coating **(Chapter 2.2.5)** to evaluate possible changes in hydrophobic performances. The results indicate that regardless of the concentration ratios used for their production, all the gold-covered samples showed similar hydrophobic abilities, slightly higher than the non-gold covered samples.

Given that sputter coating does not guarantee the production of durable structural replicas, alternative methods such as electrodeposition have been tested for their production. Although the reasonable sensitivity of GPA in a liquid environment was observed, the deposition of colloidal gold by electrodeposition, which needs GPAs to be submerged in

an electrolytic bath, was successfully performed. As expected, the structure of GPA was significantly damaged after the process due to the presence of water and the high pH value, which favoured the disassembly of the components. However, some portions of the sample were successfully covered in gold demonstrating that this approach can be feasible for more resistant GPAs versions which can be produced in the future through improved assembly strategies.

Finally, considering the poor performance of GPAs in thermo-electric conductivity due to the individual characteristics of the two components, CNTs were introduced in the self-assembly process. This allowed to produce an aerogel morphologically indistinguishable from the standard GPA. However, in addition to establishing more detailed and accurate self-assembly procedures to have higher reproducibility, the thermal and electrical conductivity properties of CNT-GPA have not been tested yet as well as those were not compared to GPA and other similar structures to evaluate the effective competitiveness.

GraPhage13 has shown extraordinary potential in several diverse applications. Although these positive and encouraging results, more experiment are still needed to refine the samples preparation as well as standardise the procedures and test its performances compared to similar materials.



UNIVERSITY OF
BIRMINGHAM

CHAPTER VII

GRX-N13 Nanostructured Surface



Abstract

M13-based nanoarchitectures can be arranged into high-ordered patterns. These, due to the nanoscopic dimensions of phages can potentially interact with a broad range of electromagnetic radiation, and of particular interest with visible light. This opens the way to numerous applications in optics and photonics, overall for the possibility to create metamaterials which can potentially produce unique optical effects like invisibility. This chapter describes a bottom-up strategy to self-assemble M13 onto a silicon substrate forming a structure named GRX-N13. This approach is based on non-covalent interactions and involves also GO and a specific ring-like protein called SmPRXI, which already showed great potential in the fabrication of nanostructured material in combination with nanoparticles.

7.1. Introduction

Given its filamentous shape and nanoscopic dimensions, M13 is a perfect candidate for the production of nanostructured surfaces for optical and photonic applications. In particular, M13 can be used as liquid crystals for the production of colourimetric sensors and highly ordered repeated patterns as in the case of metamaterials.[2,359,360] These applications require the use of extremely small and versatile components, capable of interacting with electromagnetic radiations at specific wavelengths.[361,362] Among many applications for metamaterials, the fabrication of surfaces with a negative refractive index is of great interest. This could be crucial for the development of materials with unique optical properties such as for instance invisibility.[361,362] Currently, it is a big challenge to produce metamaterials and exploit their extraordinary optical properties. Conventional manufacturing methods for the production of these nano-metamaterials such as nanolithography can guarantee high control and precision during the production process, but at the same time, they have several limitations in terms of cost, production time and scalability.[36]

Alternatively, a different route based on the use of biological components is offering a variety of different assembly strategies.[27,77,363] These usually are *bottom-up* approaches, based on the self-assembly of proteins, nucleic acids, biopolymers as well as entire viruses employed like LEGO® building blocks.[364–366] These biomolecules can be functionalised and assembled into specific architectures, producing functional materials with enhanced performance compared to their synthetic competitors.[36] The bio-self-assembly approach shows many advantages in terms of cost, production time, scalability and environmental sustainability as well as producing durable materials.[27,36,77,363]

This chapter focuses on the study of a self-assembled nanostructured hierarchical surface through non-covalent interactions, using GO, M13 and a particular protein called SmPRXI, for applications in optics and photonics. The structure is assembled on a silanised silicon substrate, onto which a monolayer of GO is deposited. Subsequently, PIII proteins of M13 are chemically modified to selectively bind SmPRXI forming a complex binding the substrate and completing the structure called GRX-N13. Once assembled, the structure is subjected to templating treatments to cover the nanoarchitecture with noble metals such as Au, Pt, Ag, Pd and Cu, to improve the thermo-electric conductivity and durability performance. Unfortunately, the templating and characterisation steps have not been studied yet and it will be the primary area to examine in future studies.

Here, the procedure of expression and purification of SmPRXI as well as the detailed assembly strategy and the characterisation of GRX-N13, are described.

7.1.1. GRX-N13 Nanostructured Surface

The hierarchical 3D nanostructured surface proposed in this project is composed of GO **(Fig. 7.1a)**, a ring-like protein (SmPRXI) **(Fig. 7.1b)** and M13 **(Fig. 7.1c)**, mainly assembled through non-covalent interactions. All these components have already been described in **Chapter 1**. To better understand the GRX-N13 self-assembly strategy, it is important to recall some of the fundamental characteristics of each component.

Contrary to the major coat protein PVIII which does not have Cys residues within its sequence, the PIII has six of them involved in the formation of disulfide bridges (R–S–S–R).[76,367] The latter can be reduced with the use of reducing agents, which break

the bond between the two sulfur atoms producing thiol groups (-SH) available for site-specific reactions. SmPRXI in its decameric form is a ring-like protein showing peroxidasic and chaperonic activities. The recombinant version of SmPRXI used in this project has a signal peptide called His-Tag located at the N-terminus of each monomer, primarily used for its selective purification **(Appx. 9)**. Finally, the GO has affinity through non-covalent interaction with both SmPRXI[38] and M13 **(Chapter 5)** at pH 7 and 4.9 respectively as well as being covalently linked to silicon substrates using APTES.

Given the following considerations, a self-assembly procedure was designed involving the functionalisation of a silicon substrate with APTES, allowing the exposure of reactive amino groups on its surface. Therefore, the latter react with the oxygen-containing groups arranged on the GO surface, forming covalent bonds producing a layer of GO onto the modified silicon surface. The His-Tag exposed into the central cavity of the SmPRXI structure mediates the binding with the NTA through a Ni atom (Ni-NTA). The Ni-NTA are groups covalently linked to the PIII through the crosslinking agent SMCC. This is possible due to the action of the reducing agent TCEP which produces free thiol groups on the PIII. Therefore, the modified M13 (M13-NTA) can bind the SmPRXI in solution at pH 7. The GRX-N13 self-assembly process is completed when the M13-NTA-SmPRXI complex, formed in solution, is finally deposited on the silicon substrate functionalised with GO **(Fig. 7.1d)**. Once GRX-N13 is obtained, this can be subjected to a templating process such as sputter coating or electrodeposition and subsequently characterised.

The process for the study of GRX-N13 conducted so far can be summarised into three main steps such as (i) the self-assembly procedure, (ii) the templating and (iii) the optical properties characterisation **(Fig. 7.1d)**.

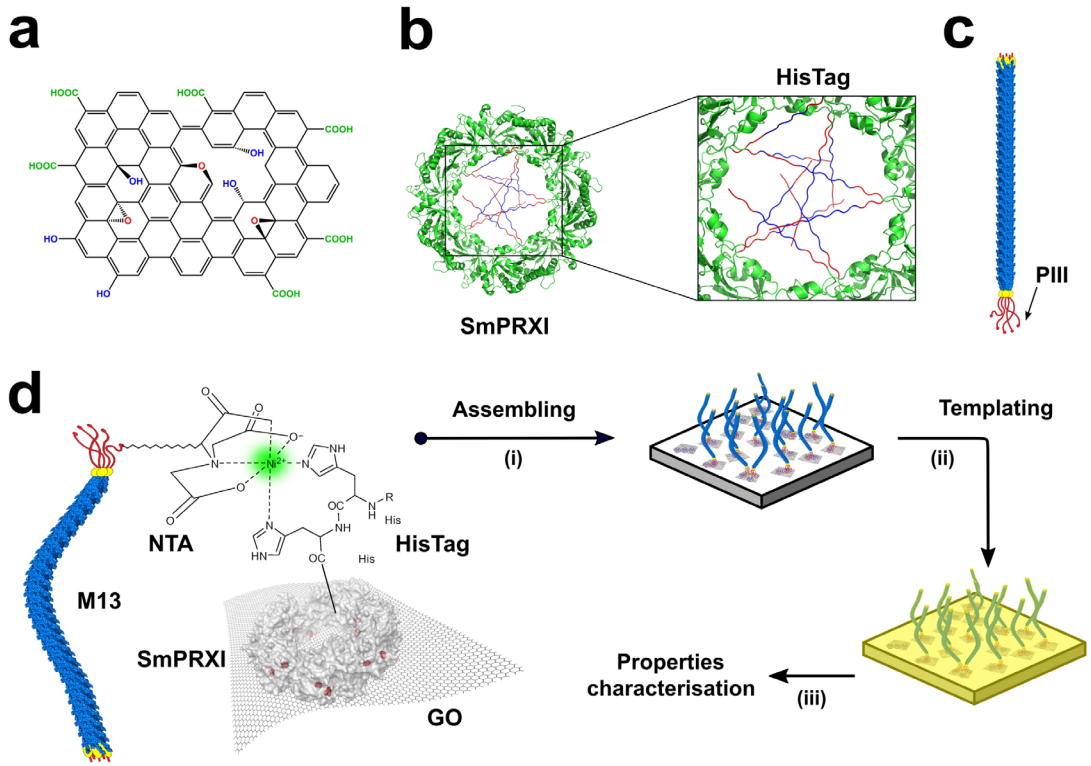


Figure 7.1. Schematic representation of GRX-N13 components and assembly

The figure shows **(a)** the structure of GO, **(b)** SmPRXI decamer, with a zoom on the His-Tag peptides exposed in the central cavity and **(c)** the location of the PIII protein on M13. **(d)** The schematic representation of the GRX-N13 and an essential flowchart which describes the main steps of the project.

7.2. GO and M13 Preparation

During this project M13 and GO **(Fig. 7.1a, c)** were prepared and characterised following the procedures described in **Chapters 2, 3** and **4**. Specifically, GO was purchased and M13 propagated *via* infection of *E. coli* batch cultures.

7.3. SmPRXI Expression and Purification

It is possible to produce large amounts of recombinant SmPRXI using an *E. coli* expression system.[38,368] Therefore, this procedure is summarised below and described in a detailed protocol in **Appx. 10**.

7.3.1. Experimental Procedure

The procedure for SmPRXI production was studied and optimised at the University of L'Aquila in the laboratory of Prof Rodolfo Ippoliti and Prof Francesco Angelucci, with the collaboration of Dr Matteo Ardini. The process can be divided into three main phases such as expression, purification and stock validation.

Initially, the SmPRXI gene was inserted into the pRSET-A vector, which was subsequently introduced into BL21 (DE3) pLysS cells through thermal shock. The cells carrying the SmPRXI gene correctly inserted into the vector, therefore, correctly transformed, were positively selected on solid media containing two antibiotics ampicillin (AMP) and chloramphenicol (CAM).

For the production of SmPRXI stocks, a single colony was taken with an inoculation loop from the previously described plates, transferred into 50 mL of growth medium and left in overnight incubation. Subsequently, the inoculum was transferred into a flask containing fresh growing medium, in which bacteria can continue to grow, monitored *via* UV-Vis absorbance. Once the exponential growth phase was reached, IPTG was added, activating the Lac operon which controls the expression of the recombinant SmPRXI. After a few hours of induction, the cells were removed from the flask, transferred into centrifuge tubes and separated from the medium *via* centrifugation. Subsequently, the

obtained pellets were resuspended in buffer and sonicated to release the protein accumulated inside the bacteria during the growth **(Chapter 2.1)**.

To purify SmPRXI *via* FPLC, the obtained cell lysate was eluted within an affinity chromatography column, where the SmPRXI was selectively retained through the bond between His-Ni-NTA, and separately eluted. Given the high concentration of imidazole in the elution buffer, the purified protein was subjected to dya-filtration with filtering centrifuge tubes. This procedure is used to concentrate the protein and at the same time to replace the buffer removing the imidazole.

Finally, the purity of the protein was validated *via* electrophoretic gel (SDS-PAGE) and the concentration was estimated through UV-Vis absorbance at 280 nm and ε = 26 065 M^{-1} cm^{-1} **(Chapter 2.3.1, 2.3.9)**.

7.3.2. Results

The SmPRXI was successfully purified at the University of L'Aquila as well as at the University of Birmingham. This is confirmed by the chromatogram, SDS-PAGE bands and the UV-Vis spectrum **(Fig. 7.2)**.

The chromatogram in **Fig. 7.2a** shows the absorbance signal at 280 nm, in which a peak appears approximately after the elution of 75 mL of elution buffer. This indicates that the protein was eluted when the elution buffer concentration was between 60-80%. The eluted fractions corresponding to that peak were collected and the buffer exchanged with PBS using membrane filtering tubes. To remove the elution buffer, the purified samples were dya-filtrated *via* centrifugation using membrane filtering tubes and subsequently analysed through SDS-PAGE and UV-Vis spectrophotometry. Dya-filtration is necessary to

remove the elution buffer which contains a high concentration of imidazole which affects the stability of SmPRXI, hampering the UV-Vis analysis.

To investigate the purity of SmPRXI, SDS-PAGE was performed **(Fig. 7.2b)**. The stained gel shows a single band at 25 kDa for each eluted fraction, which confirms the presence of SmPRXI only, also due to the absence of other bands at different MW.

Lastly, the concentration of SmPRXI was successfully estimated using the absorbance at 280 nm **(Fig. 7.2c)**.

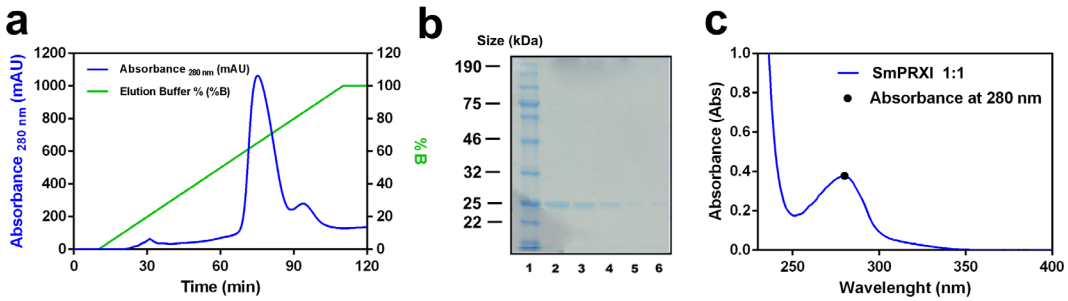


Figure 7.2. Purification, validation and quantification of SmPRXI

(a) The chromatogram shows the elution peak of SmPRXI (blue) and elution buffer concentration gradient (green). When the concentration of the elution buffer is between 60–80% the high concentrated imidazole allows the SmPRXI to be eluted from the Ni-NTA resin *via* bonding competition. **(b)** SDS-PAGE of the marker (1) and the eluted fraction corresponding to the elution peak (2–6). **(c)** UV-Vis spectra of SmPRXI showing the characteristic protein peak at 280 nm.

7.4. M13 Modification

The GRX-N13 assembly procedure involves the chemical functionalisation of M13 with NTA groups on the protein PIII. The devised strategy to perform the modification consists of several steps. Initially, NTA is mixed with SMCC and left to react, while in a different vial, TCEP is reducing the disulphide bonds of the PIII, producing free reacting thiol

groups on M13. Once individually reacted, NTA and M13 can be mixed to form the chemically modified M13-NTA **(Fig. 7.3)**.

This reaction was successfully performed and the modified M13 was studied *via* size exclusion chromatography (SEC) and AFM **(Chapter 2.2.2, 2.3.6)**. In particular, SEC elution was monitored using the absorption signals given by M13, Ni and enhanced green fluorescent protein (EGFP) at 269, 393 and 488 nm respectively.

EGFP is an enhanced fluorescent version of the GFP, which is a fluorescent protein derived from *Aequorea victoria*,[369] provided by Prof. Tim Dafforn group at the University of Birmingham.

Similarly to SmPRXI, this EGFP is a recombinant protein that presents a His-Tag to facilitate its purification. The presence of this peptide allows the creation of the M13-EGFP complex, which can be used as an indirect method to qualitatively and quickly confirm the successful modification of M13 *via* SEC. This method is based on the possibility of simultaneously monitoring several wavelengths during the elution. M13-EGFP in permissive conditions of assembly should show the elution peaks of M13 and EGFP, appearing at the same retention volume (R_v) during the elution, contrary to what should be observed if the two components do not form the complex. Therefore, in these conditions, the presence of two peaks corresponding to the MW of M13 and EGFP should be observed.

7.4.1. Experimental Procedure

Initially, 10 mM NTA and SMCC (previously dissolved in dimethyl sulfoxide - DMSO) were mixed in 1 mL DIW, while 1 mg mL^{-1} M13 was dispersed, in presence of 10 mM

TCEP, in 1 mL PBS. The reactions were performed in two separated microtubes, incubated at 25°C for 1 h. The M13/TCEP solution was subsequently mixed with the NTA/SMCC and incubated at 25°C for 1 h to form the chemically modified M13-NTA.

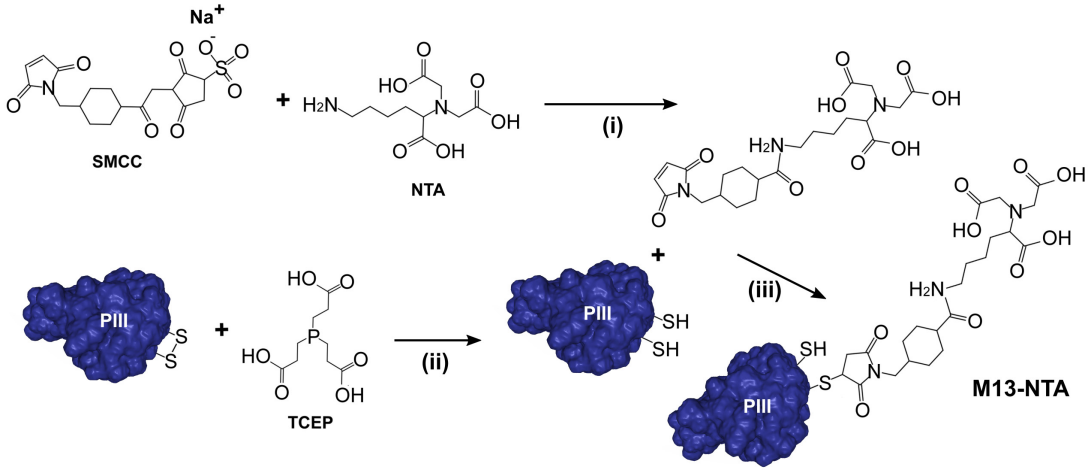


Figure 7.3. Chemical reaction to produce M13-NTA

The schematics show the steps leading to the formation of the chemically modified M13-NTA. At the top left SMCC reacts with the NTA, while in a separate reaction tube the disulphide bonds on the PIII protein of M13 are reduced with TCEP. Lastly, the NTA-SMCC and the M13 with available thiol groups are mixed to react, forming the chemically modified M13-NTA.

To complete the functionalisation of M13-NTA, 10 mM $NiSO_4$ was added to bind the NTA, making the Ni-NTA groups ready to interact with the His-Tags. After 5 min incubation, 0.123 mM EGFP was added and the final sample was loaded and eluted in PBS through SEC. The elution of the complexes M13-Ni-NTA and M13-EGFP were separately eluted while monitoring the wavelengths corresponding to the components of interest.

Moreover, the purified sample of M13-Ni-NTA was mixed with 0.123 mM SmPRXI and analysed at the AFM following the methodology described in **Chapter 2.3.6**.

7.4.2. Results

To qualitatively check the successful chemical modification of M13, two elutions were performed. During the first experiment, M13-NTA was eluted through SEC after being mixed with $NiSO_4$ **(Fig. 7.4a, b)**, subsequently, M13-NTA was eluted through SEC after being mixed with $NiSO_4$ and EGFP to form the complex M13-EGFP **(Fig. 7.4c, d)**.

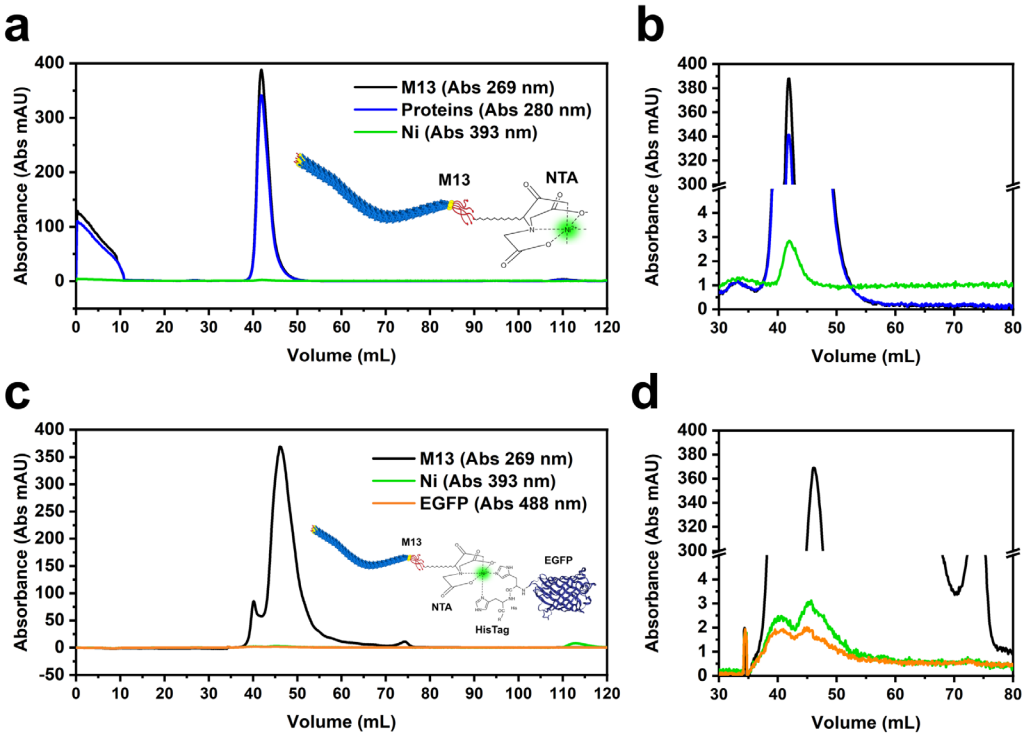


Figure 7.4. SEC for the characterisation of M13-NTA

(a) The chromatogram of M13-Ni-NTA shows a weak Ni signal **(b)** at the same R_v of M13 indicating that the two analytes were co-eluted. **(c)** Similarly, the chromatogram of M13-EGFP shows two weak signals **(d)** corresponding to Ni and EGFP. The presence of peaks having the same R_v, but associated with different wavelengths, is a clear indication of the analytes co-eluted, and this is probably due to the successful self-assembly between the components.

In the first case (M13-Ni-NTA), the monitored absorbances of M13 and Ni show their co-elution. This corresponds to the overlapping of the elution peak of the signal at 269 nm (M13) and the peak of the signal at 393 nm (Ni) **(Fig. 7.4a, b)**. In the second case

(M13-EGFP), the monitored absorbances of M13, Ni and EGFP show the co-elution of M13, Ni and EGFP. This corresponds to the overlapping of the elution peak of the signal at 269 nm (M13), 393 nm (Ni) and 488 nm (EGFP) **(Fig. 7.4c, d)**.

The results are promising since the expected co-elutions were observed. However, the intensity of the signals corresponding to Ni and EGFP, are weak compared to M13, meaning that the amount of phage eluted together with Ni or EGFP, is very small.

So far, this experiment has been performed a limited number of times, therefore, further investigations to optimise the procedure are necessary to obtain clearer data and give more detailed results.

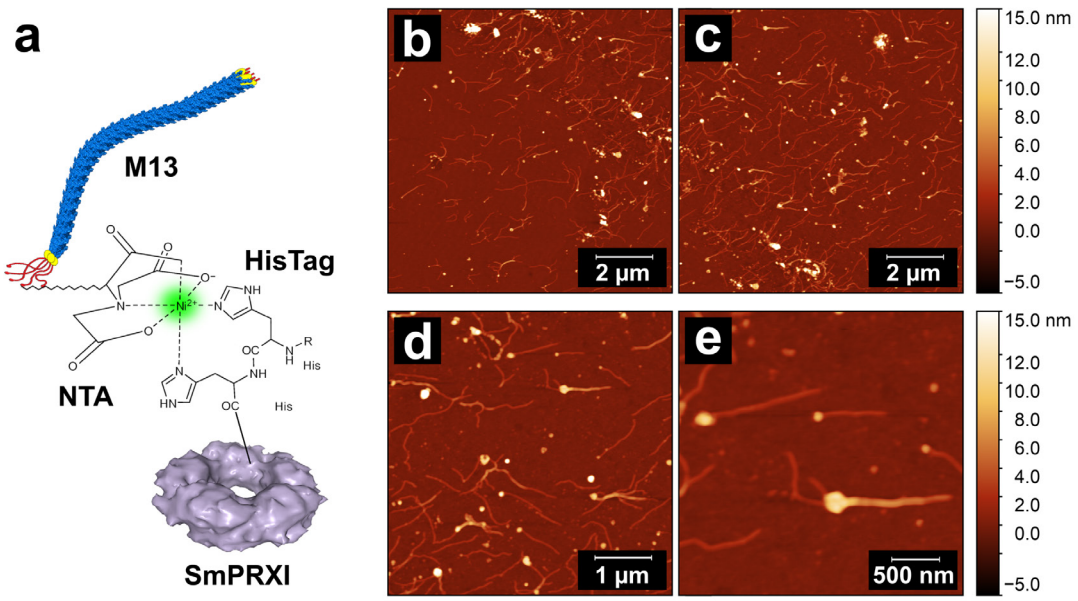


Figure 7.5. AFM analysis of M13-SmPRXI

(a) Schematic representation of M13-SmPRXI and the Ni-NTA-His-Tag interaction. **(b–e)** AFM images of M13-SmPRXI at different magnification where it is possible to see M13 showing a modified end corresponding to the one where the PIII is located.

AFM images **(Fig. 7.5)** provided interesting results, showing that the M13-NTA-SmPRXI is distinguishable compared with the wild type M13 **(Fig. 3.3)**. The presence of a variable-sized particle at one end of the phages indicates that they were modified and that the SmPRXI or multiple copies were connected. Therefore, the visible modified end should correspond to the PIII side, also considering that the PIII is the only protein that shows available Cys residues in the whole M13 virion.[76,367]

7.5. GRX-N13 Self-assembly

Although the purification experiments did not provide clear information about the purity and yields of M13-NTA stocks, the latter were eventually used to assemble the complex M13-SmPRXI and final structure of the GRX-N13.

7.5.1. Experimental Procedure

Several deposition methods were tested to find the optimal assembly conditions for GRX-N13. AFM was employed to study each step of the structure assembly, therefore images of SmPRXI, GO and M13 deposited individually on a silicon wafer functionalised with APTES were acquired **(Fig. 7.6a–c)**. Moreover, two control samples were analysed following the same procedure. The first consisted of silanised silicon with GO and SmPRXI and the second of GO and M13. Lastly, the fully assembled GRX-N13 was deposited on a clean and silanised silicon wafer functionalised with GO. The SmPRXI and M13 were added one after the other, with an intermediate dry and wash step.

Therefore, for the preparation of the aforementioned samples, silicon substrates were cleaned and silanised with APTES **(Chapter 4.2.2)**. Subsequently, three samples containing GO, SmPRXI and M13 individually, were prepared using a concentration of 5 μg mL^{-1}, except for the GO sample, which was 1 μg mL^{-1}. Two separate vials both of 1 mL containing SmPRXI and M13 of 5 μg mL^{-1} in PBS, were prepared from the corresponding stock solutions. Subsequently, 20 μL of diluted SmPRXI was dropped onto a bare silicon surface and air-dried. M13 on a separate substrate was similarly processed. Once dried, the two samples were gently rinsed with DIW to dissolve and remove salt crystals.

Lastly, the two control samples consisting of GO, with SmPRXI or M13 were prepared using the same concentrations and methods described above to deposit the individual components.

7.5.2. Results

M13 and GO **(Fig. 7.5a, c)** were extensively described and characterised in **Chapters 1, 3** and **4**. SmPRXI on the AFM images appears like small spherical particles **(Fig. 7.5b)**, according to the previous studies conducted at the University of L'Aquila.[38]

The control sample with GO and SmPRXI **(Fig. 7.6d)** shows the two components interacting. This complex was not washed away after rinsing the sample with DIW, while the second **(Fig. 7.6e)**, which consisted of M13 deposited onto GO, did not show a specific affinity between each other.

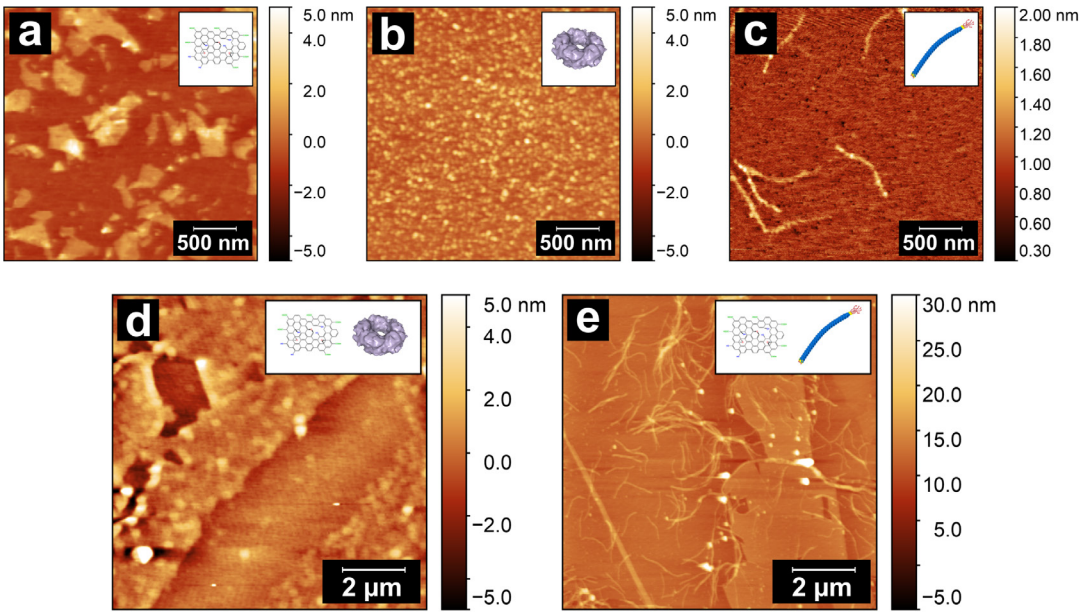


Figure 7.6. AFM analysis of GRX-N13

The figure shows AFM images of **(a)** GO, **(b)** SmPRXI and **(c)** M13, individually deposited on a silicon substrate. Moreover, the two control samples composed of GO **(d)** with SmPRXI or **(e)** M13 deposited on top.

The phages, are randomly distributed on the sample surface and preferentially on the silicon rather than the GO sheets. This, given the chemistry shown on their surfaces, is probably due to the neutral pH conditions, which promote repulsive electrostatic forces between GO and M13.

7.6. Summary and Outlook

The assembly strategy between GO, SmPRXI and M13 proposed in this chapter for the functionalisation of silicon substrates is confirmed as a possible alternative method for the fabrication of nanostructured surfaces, for optics and photonics applications.

The bulk production of recombinant SmPRXI and its purification *via* affinity chromatography are well-established procedures, developed at the University of L'Aquila.

The assembly of GRX-N13 consists of different steps, including the silicon substrate functionalisation with GO, the modification of M13 (M13-NTA), the assembly of M13-NTA-SmPRXI complex and its deposition and binding with the GO surface. While the production of the GO functionalised substrate was easily obtained, the other stages (assembly, templating and characterisation) showed some difficulties. In particular, the modification of M13 and its purification did not show satisfactory yields, probably due to the low pH and other reaction conditions, which need to be optimised and further investigated.

The AFM results were successful as they show morphological differences between wild-type and M13-NTA, the latter displaying one of the two ends rounded due to the selective modification of the PIII protein and its bond with the SmPRXI. However, the poor yield limited the subsequent steps leading to the formation of GRX-N13. In particular, the reduced amount of M13-NTA made it difficult to assemble and identify the complete structure of GRX-N13, preventing the subsequent gold templating process and analysis of optical properties.

Therefore, starting from the optimisation of the M13-NTA modification strategy, further studies are needed to complete all the assembly steps of this new nanostructure.



UNIVERSITY OF
BIRMINGHAM

CHAPTER VIII

SAS-M13 Nanostructured Surface



Abstract

Assuming the same proof of concept for which GRX-N13 was designed, this chapter describes a similar bottom-up strategy to self-assemble M13 onto a silicon substrate forming a structure through covalent bonds, named SAS-M13. This alternative method does not involve other components, but it is merely based on the employment of specific cross-linking molecules.

8.1. Introduction

The following study describes another nanostructured surface for the production of metamaterials, for applications in optics and photonics. The described structure is called SAS-M13 and consists of a chemically modified M13 bound to a silicon substrate by covalent bonds.

Briefly, a silicon substrate is functionalised with APTES and M13 is chemically modified with SMCC, to react with the substrate. Once functionalised, the substrate and the virus are incubated in the same reaction mixture, where they form a covalent bond, due to the functionalisation previously described **(Fig. 7.3)**. The material thus obtained is characterised by a random distribution of bacteriophages on the surface. To increase the level of order, these nanofilaments are aligned by an external streaming force provided by water, which should orient the phages in one direction. Once aligned, the resulting nanostructured surface is subjected to a templating process to fix it and to test its optical properties. Finally, given the nanoscopic dimensions of bacteriophages, due to the topography of the material, it is expected to observe optical properties, within the visible spectrum (380–740 nm).

8.1.1. SAS-M13 Nanostructured Surface

The approach used for the assembly of SAS-M13 takes place in four fundamental steps: (i) the functionalisation of the silicon substrate with APTES,[309] which provides amino groups on the silicon wafer surface **(Chapter 4.2.2)**. (ii) The functionalisation of Si-APTES with SMCC, linked to the amino groups of the substrate, through the presence of the portion, containing the maleimide, of the crosslinker. (iii) The binding between

M13 and Si-APTES-SMCC, mediated by thiol groups made available by the reduction process of disulfide bridges between Cys, in the presence of TCEP **(Chapter 7.4)**. Finally (iv), the process of phage orientation through the application of a streaming force given by water **(Fig. 8.1)**.

Below, in addition to the description of the methodology used, some preliminary results are reported. Numerous assembly approaches have been tested, however, only the one that showed the most promising results for the production of SAS-M13 is reported.

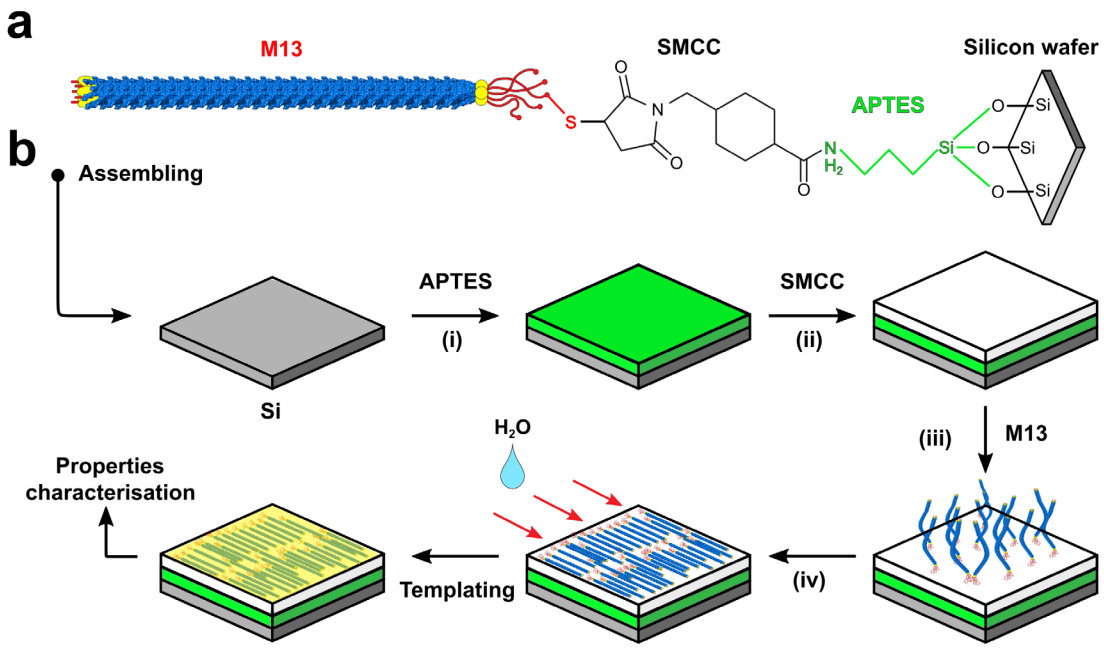


Figure 8.1. Schematic representation of SAS-M13 assembly

(a) Schematic representation of the SAS-M13 unit, followed by **(b)** a step by step summary of the assembly and templating procedure used to assemble it.

8.2. M13 Preparation

For this project, M13 was prepared and characterised following the procedures described in **Chapters 2** and **3**.

8.3. SAS-M13 Self-assembly

(i) The functionalisation of the substrate with APTES was preceded by a series of preliminary steps. Initially, a small silicon substrate was cut and cleaned by snow jet, according to the standard procedure described in **Chapter 2.2.4**. Subsequently, the silicon was placed in glass vials containing toluene and sonicated in a water bath at 37 kHz for 10 min. Lastly, the wafer was sonicated in ultrapure DIW for 5 min to remove any excess toluene and air-dried. At this point, the substrate was modified with APTES, as described in **Chapter 4.2.2**. Following the reaction with APTES the substrate was rinsed and sonicated for a further 5 min in fresh toluene, then in ultrapure DIW for another 5 min and dried in a clean environment. (ii) Si-APTES was immersed for 1 h in 1 mL of 20 mM SMCC and protected from light, using aluminium foil. After the reaction, the wafer was rinsed with ultrapure DIW to remove excess SMCC and dried in a clean environment. (iii) The wafer previously prepared was incubated in 1 mL of a 20 mM TCEP and 0.1 mg mL^{-1} M13 solution at pH 7, for 2.5 h. Then the wafer was gently soaked in 50 mL of ultrapure DIW for 5 min, to remove any excess reagent. (iv) The complex thus obtained was subjected to a water streaming force. A drop of ultrapure DIW was held at the end of a pipette tip and hand-dragged across the sample surface, to facilitate the alignment of the bacteriophages.

Due to time limitations, it was not possible to perform the templating on SAS-M13. However, optical microscopy, AFM, Raman and reflectance spectroscopy in the Vis-NIR range have been carried out to characterise the nanostructured surface, obtained so far.

8.4. SAS-M13 Characterisation

AFM allowed to clearly distinguish the three phases of the assembly. The surface of the clean Si substrate appears free of impurities and extremely uniform **(Fig. 8.2a)**, as can be seen from the corresponding profile **(Fig. 8.2d)**.

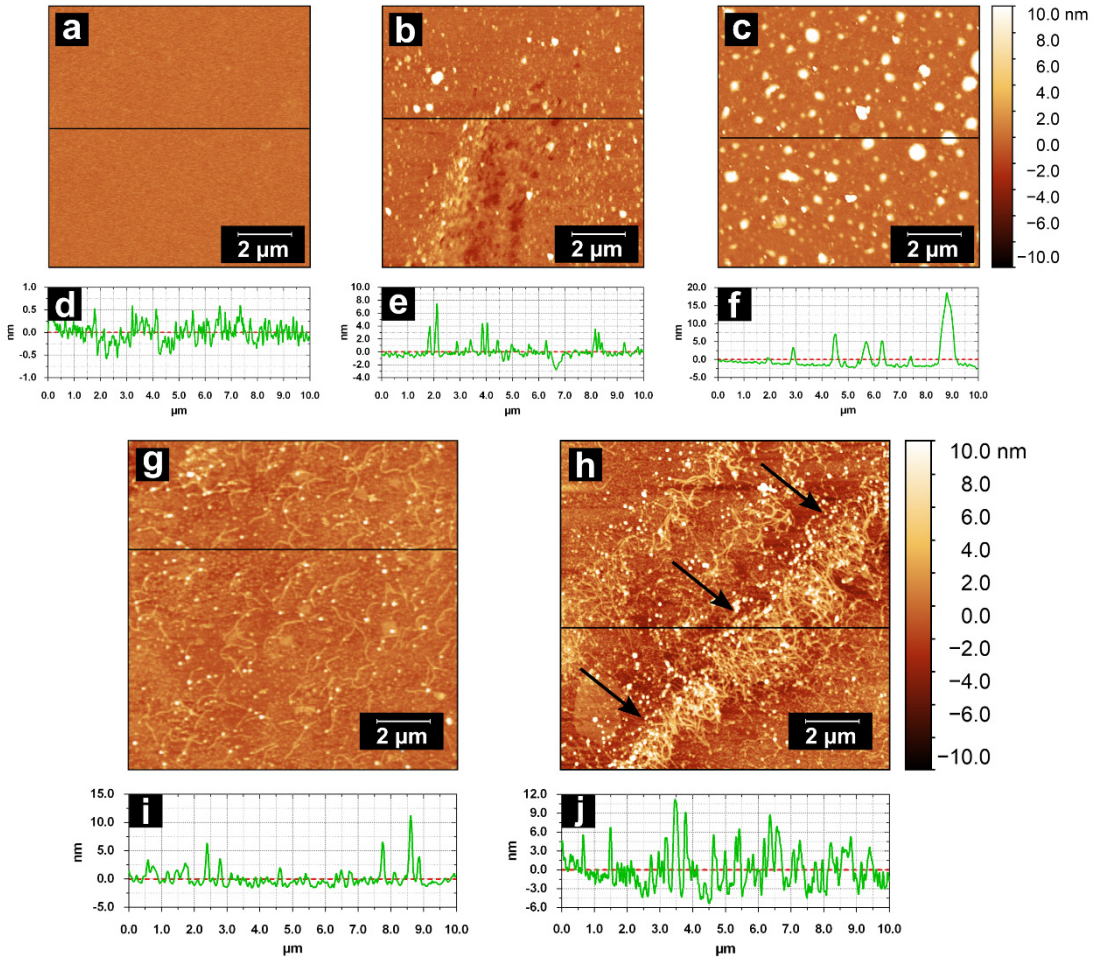


Figure 8.2. AFM analysis of SAS-M13 and the intermediate samples

AFM images of **(a)** Si, **(b)** Si-APTES and **(c)** Si-APTES-SMCC, followed by **(d-f)** their corresponding cross-sections. These samples show clear differences, for instance, Si is characterised by a very smooth and clear surface, while the sample containing SMCC shows circular aggregates distributed on its surface. SAS-M13 was analysed with the AFM before **(g)** and after **(h)** the orienting procedure. The arrows indicate the direction of the streaming force to align M13. Although the cross-sections **(i, j)** are similar, the images show the phages with a spherical portion at one end of their structure as well as a more random orientation of the phages in the sample not subjected to the streaming force.

Si-APTES presents, instead, a more heterogeneous surface with small aggregates, clearly distinguishable from the bare Si **(Fig. 8.2b)**. The sample containing SMCC displays circular aggregates, with variable diameter and height, reaching up to 20 nm **(Fig. 8.2c)**. The complete SAS-M13 sample clearly shows the presence of M13 stochastically distributed on the surface and related to what appear to be the aggregates previously identified in Si-APTES-SMCC **(Fig. 8.2g)**. Finally, the SAS-M13 sample subjected to a streaming force **(Fig. 8.2h)**, presents characteristics similar to the sample with non-aligned M13. Although partially obtained, the level of order and alignment did not reach the anticipated level.

To characterise the samples and confirm the formation of the bonds between the components, the same samples described above were analysed with a Raman spectrometer **(Chapter 2.3.3)**. The components that form SAS-M13 were analysed *via* Raman spectroscopy individually, depositing a small amount obtained from their stocks on a Si substrate **(Fig. 8.3)**.

The spectra thus obtained were compared with those acquired by the samples prepared with the assembly process. Although the components taken from the stocks showed a spectrum with well-defined peaks **(Fig. 8.3a)**, the samples corresponding to the various steps of preparation of SAS-M13 did not show the characteristic peaks of their corresponding control samples **(Fig. 8.3b)**. However, given that the presence of the components was confirmed by AFM, the absence of peaks can be attributed to the small quantity of APTES, SMCC and M13 deposited on the surface, which is probably not enough to be detectable by the instrument.

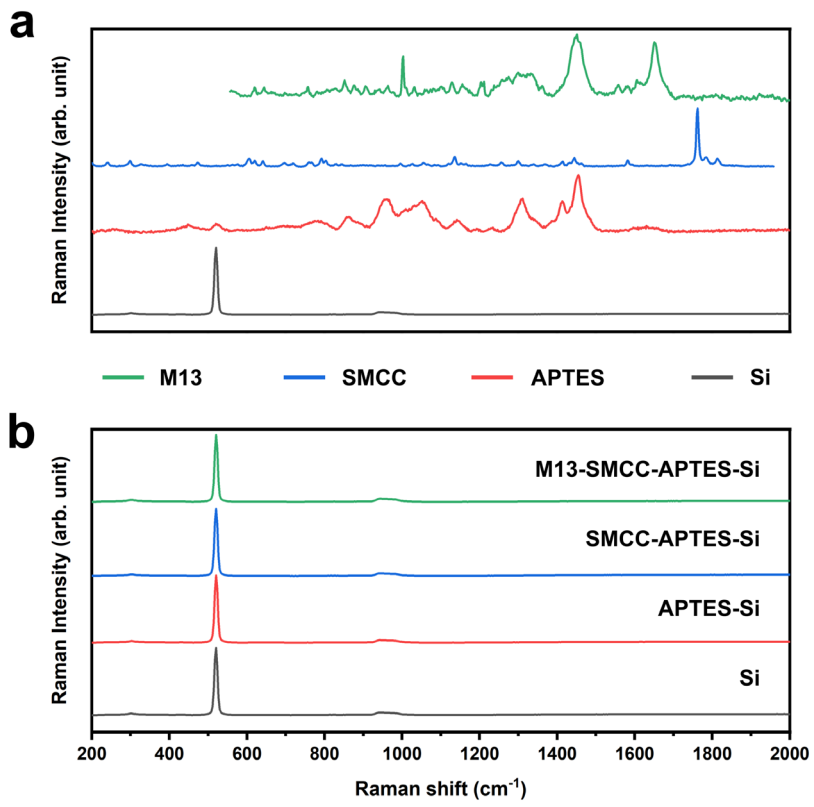


Figure 8.3. Raman analysis of SAS-M13 and the intermediate samples

(a) The Raman spectra of the control samples Si (black), APTES (red), the SMCC (blue) and M13 (green) as well as **(b)** the spectra of SAS-M13 at each stage of the assembly, obtained at 633 nm laser excitations. The controls show clear fingerprint spectra, which was not detected from the SAS-M13 intermediate and final samples, probably due to the detection limit of the instrument. SAS-M13 is assembled on a Si substrate, therefore, its signal is always contained in the spectra of each intermediate step. Note that M13 and SMCC spectra are truncated due to a different acquisition range in static mode, which was necessary to avoid poor signals.

Lastly, the Vis-NIR spectroscopy of the samples showed three different spectra **(Fig. 8.4)**. These show no particularly noticeable absorption peaks, besides being very similar to each other. However, the signal obtained from the SAS-M13 sample has a higher signal intensity than the Si-APTES and Si-APTES-SMCC spectra. This indicates the ability of the SAS-M13 sample to better reflect light, contrary to what was expected, given that for the previous two layers the intensity of the reflected light decreases after the addition of each level.

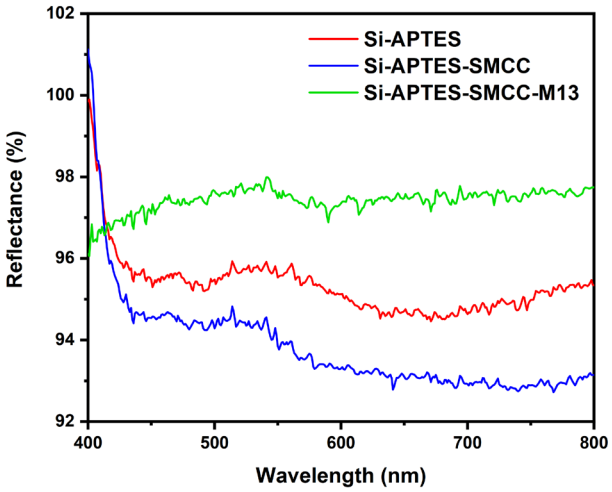


Figure 8.4. Vis-NIR analysis of SAS-M13 and the intermediate samples

The reflectance spectrometry analysis of SAS-M13 and its intermediate samples shows that they have distinguishable spectra, without particular adsorption peaks. However, SAS-M13 shows higher reflectance intensity compared with the two samples without M13 (Si-APTES- SMCC and Si-APTES).

8.5. Summary and Outlook

In this chapter, the self-assembly strategy leading to the successful realisation of SAS-M13 is described. The results shown confirmed that it is possible to functionalise silicon substrates using APTES and SMCC, through the formation of covalent bonds.

Furthermore, the bonding of M13 on the silicon surface by SMCC was successfully carried out, generating the nanostructured surface called SAS-M13.

The next step was to align the viruses with a streaming force, to increase the order level. Under these conditions, given the nanoscopic dimensions, viruses should interact with light, in particular, in the visible range, altering the optical properties of the surface on which they were assembled. Although the AFM results clearly show that the phages bond

to the surface were partially oriented in the direction of the streaming force, SAS-M13 needs to be further investigated.

In particular, a small number of functionalised areas was found, which have proved to be not sufficiently homogeneous, since the functionalisation reactions with APTES and SMCC formed heterogeneous monolayers. Thus, the viruses tend to bind around circular areas where there is a higher concentration of crosslinkers, hampering the alignment process.

The AFM proved to be an excellent method of investigation to study the architecture of SAS-M13, showing clear evidence of the morphological differences existing between the various layers such as Si-APTES and Si-APTES-SMCC.

Nevertheless, further spectroscopic analysis, such as Raman and Vis-NIR spectroscopies were performed. Raman spectroscopy analysis can identify fingerprint spectra for the individual components of SAS-M13. Unfortunately, the thickness of the layers that constitute SAS-M13 may be too thin and consequently, their concentration might be too low to be detected by the Raman spectrometer. Therefore, it is necessary to perform further analyses *via* Raman spectroscopy to find the optimal conditions to study these samples. Moreover, other techniques such as FT-IR and X-ray photoelectron spectroscopy (XPS) should be employed to expand the range of analyses to support that the surface is properly modified.

Finally, the analysis at the Vis-NIR spectrometer showed an increased intensity of the light reflected by SAS-M13, compared to control samples. This unexpected result suggests that further investigation is needed to discover the reasons, which could allow this material to have applications in the field of optics and photonics.



UNIVERSITY OF
BIRMINGHAM

CONCLUSIONS AND OUTLOOK

Paolo Passaretti

This thesis explored and successfully confirmed the versatility of the bacteriophage M13 in the self-assembly of novel nanostructures for the production of functional materials, such as *GraPhage13*, GRX-N13 and SAS-M13. Before summarising the outputs related to these, it is worthwhile highlighting certain results obtained from the studies of M13 and GO, discussed in **Chapters 3** and **4** respectively.

Chapter 3 focused on the successful propagation and purification of high yield of M13. It also described a detailed study of the IEP of M13, which has not been previously reported in the literature, except for filamentous phages (Ff) in general or *fd*.

The isoelectric precipitation performed after PEG purification reduces the amount of contaminating PEG, favouring the purification of high-quality phages. The effectiveness of this method could be studied using Raman and FT-IR, which can easily identify and distinguish M13 and PEG if present simultaneously.

Chapter 4 revolved around the study of GO and, in particular how sonication reduces the size of GO nanosheets while favouring their dispersibility in water. GO could be easily identified and studied for the manufacturing of composite materials with spectroscopic techniques such as UV-Vis, FT-IR and Raman, due to the specific fingerprint spectra obtained with each of these techniques.

The design, assembly, characterisation and some applications of the novel self-assembled composite material *GraPhage13* were described in **Chapters 5** and **6**.

Importantly, *GraPhage13* is the first self-assembled, virus-based hydrogel/aerogel. It opens a new route for the production of graphene-based aerogels, through the employment of biological components and eco-friendly procedures.

The realisation of *GraPhage13* was possible due to the combination of two remarkable nanotools, GO and M13, that not only have individually revolutionised different scientific fields but also once combined, gave rise to this very interesting and exciting new material. It has a 3D porous structure self-assembled through non-covalent interactions. The self-assembly process that leads to its formation is surprisingly simple. It only consists of two essential steps including the formation of a hydrogel, immediately after the two components combine in water or aqueous buffers at permissive pH conditions, and the freeze-drying process, which transforms it into a free-standing 3D aerogel, characterised by porous structure, high-surface-area of 325.147 ± 34.307 m^2 g^{-1} and ultra-low-density of 8.82 ± 0.03 mg cm^{-3}. Furthermore, it was observed that it is possible to modulate the porosity of the aerogel by varying the concentration ratio of the two components and/or employ hydrogels with different densities for the freeze-drying process. However, this is yet to be confirmed and it is subject to further investigations.

During the characterisation of *GraPhage13*, it was found that some aerogels have exhibited hydrophobic properties. It was observed that in some cases, higher contact angles were associated with smaller porosity morphologies, ranging from absence of hydrophobicity in larger pores aerogels, to contact angle greater than 130° for smaller pores aerogels. Although *GraPhage13* is formed *via* M13 and GO, which are easily dispersible in water, with the resulting aerogels being sensitive to degradation in presence of water, its hydrophobic properties can be associated with the micro- nanotexture of the sponges, which hamper the penetration of water in its porous network. However, *GraPhage13* is currently very fragile and therefore, its exploitation for various possible applications is limited at this stage. To overcome these limitations and improve the durability and thermoelectric conductivity performance of *GraPhage13*, gold

electrodeposition as well as the incorporation of the CNTs, have been tested. These results are detailed in **Chapter 6**, which confirm that electrodeposition is a templating strategy which can be pursued for this purpose, yet it is still limited by the instability of *GraPhage13* during this procedure. Similarly, the inclusion of CNTs in the standard *GraPhage13* aerogel produced an 'upgraded' composite, which also needs to be further investigated and it is expected to show better performance in terms of robustness, thermo-electrical conductivity and hydrophobicity.

Given the results demonstrated in this thesis, *GraPhage13* appears to be an interesting material, and even more so due to its versatility. In fact, the surface of M13, as well as that of GO, can be easily modified with chemical groups, chelating agents, nanoparticles, proteins, enzymes, antibodies, etc. This can provide to *GraPhage13* specific additional characteristics and functionalities, enabling it to further be employed in a breadth of applications such as the production of batteries, supercapacitors, catalysis, absorbers, sensors and even scaffolds for tissue regeneration. All of this, with additional benefits of low-cost, shorter production times, scalability, performance and environmental sustainability.

Given the size of M13 (~900 μm long, with a thickness of ~6 nm), the production of functionalised surfaces exposing the filamentous phage was further explored, to exploit the characteristics of the virus for optical and photonic applications.

Chapters 7 and **8** describe preliminary results related to the nanofabrication of the nanostructured surfaces GRX-N13 and SAS-M13, which require silicon supports to facilitate their self-assembly.

In **Chapter 7**, the successful production of the SmPRXI protein (in collaboration with the University of L'Aquila) was described. The modification of the PIII protein of M13, by means of a cross-linker, carrying the NTA chelating group has provided promising preliminary results, observed by FPLC, Raman and AFM. These suggested the feasibility of this modification and the overall self-assembly strategy of GRX-N13.

However, further studies are needed to improve the functionalisation procedure of M13-NTA and its purification as well as establish effective assembly conditions to obtain larger areas of the functionalised surface.

In **Chapter 8** the SAS-M13 is described and discussed. It is essentially a nanostructured silicon surface covalently bound to M13 *via* cross-linking agents such as APTES and SMCC. Although the AFM images showed that the virus was present on the surface even after repeated washings, the Raman analysis did not provide sufficient information probably due to the small amount of each component, which was not detected by the instrument in this condition. Reflectance spectroscopy in Vis-NIR, allowed to distinguish the three levels of the surface functionalisation. However, the higher level of reflected light by SAS-M13 compared to the control samples without M13, require further analysis to identify and characterise the properties of this new material.

While these two materials showed great potential, further studies are necessary to improve the production technique and subsequently, investigate the various applications, especially those for optics and photonics.

Nanotechnology provided alternative strategies to manipulate the matter at the molecular level by producing novel structures having very small components with dimensions of a few nanometers. This is crucial for the manufacturing of new functional materials and

devices with advanced features or even show new properties, not described yet. Furthermore, nanotechnology, together with synthetic biology and the employment of biological molecules, is revolutionising all scientific fields, from medical sciences to new technologies for energy production, conversion and storage. The employment of biological molecules is of great interest due to the high-precision assembly of the components, reduced time and costs of production as well as environmental sustainability.

GRX-N13, SAS-M13 and in particular, *GraPhage13* emerged as new and interesting materials with improved functionalities while opening new possibilities for their exploitation in various applications and miniaturised devices. Given its porous structure, ultra-low density and high-surface-area as well as the possibility of being functionalised, it demonstrates to be a dynamic platform for the fabrication of absorbers, filters, batteries and biosensors. The results related to this study have recently been published in the journal of Nanoscale, a peer-reviewed journal of the Royal Society of Chemistry.

Finally, it is noteworthy to continue studying the characteristics of these newly synthesized materials as well as in-depth testing of their properties and the emerging functionalities. It will also be beneficial to compare *GraPhage13* to other non-viral materials with similar properties, aiming at fabricating more optimised and advanced versions of these micro-nanomaterials which ware envisioned to exhibit superior performance and to be incorporated in advanced miniaturized devices and technologies.



UNIVERSITY OF
BIRMINGHAM

APPENDICES

Paolo Passaretti

Appendix 1

M13 genome and proteins details

In this appendix, the sequences of genes and the respective proteins of M13 bacteriophage are listed. M13 genome was sequenced by Wezenbeek *et al.* that also compared the M13 sequence to the related bacteriophage *fd*. [41,370,371]

The following information about every single gene such as region and length come from Wezenbeek *et al.*,[41] the molecular weight was estimated using the Sequence Manipulation Suite[372] instead. The base pairs (bp) of each gene sequence, includes the stop codon in the count and the MW of single-stranded sequences is assumed to have a 5'–P.[372]

About the corresponding proteins, information such as Protein Data Bank (PDB) ID, sequence, length and measured MW, come from Wezenbeek *et al.*,[41] the theoretical MW (average and monoisotopic) and IEP, were estimated using ExPASy - Compute IEP/MW tool.[373,374] Finally, the molar attenuation coefficient (ε) was calculated by using the **Eq. A1**.[375–377]

$$\varepsilon_{280} = [(n\mathrm{Trp})(5500)] + [(n\mathrm{Tyr})(1490)] + [(n\mathrm{Cys})(125)] \qquad \text{(A1)}$$

The abbreviations *n*Trp, *n*Tyr and *n*Cys are respectively the number of Tryptophans, Tyrosines and Cysteines in the considered amino acid sequence. This method provides an estimation of the coefficient with a standard deviation of ± 5%.[376]

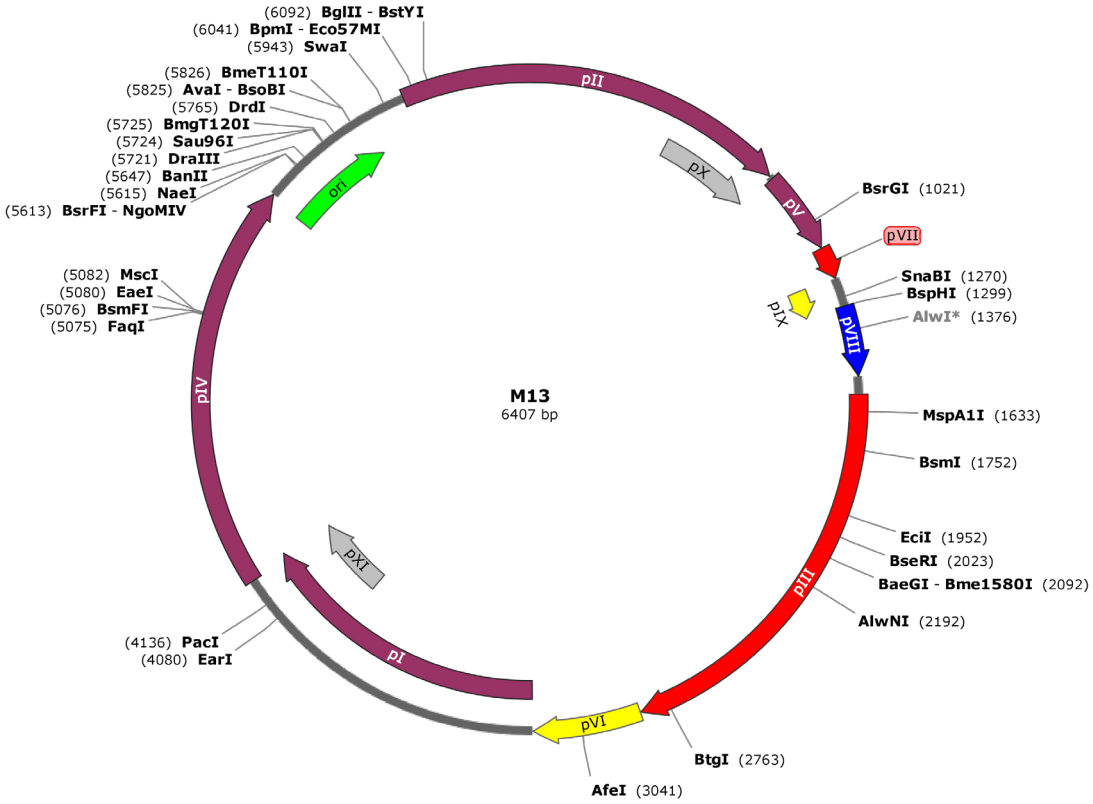


Figure A1 M13 genome map

The figure shows the entire genome of M13, highlighting the genes, several restriction sites and the origin of replication.

Gene I (*pI*)

```
3196 ATGGCTGTTT ATTTTGTAAC TGGCAAATTA GGCTCTGGAA AGACGCTCGT
3246 TAGCGTTGGT AAGATTCAGG ATAAAATTGT AGCTGGGTGC AAAATAGCAA
3296 CTAATCTTGA TTTAAGGCTT CAAAACCTCC CGCAAGTCGG GAGGTTCGCT
3346 AAAACGCCTC GCGTTCTTAG AATACCGGAT AAGCCTTCTA TATCTGATTT
3396 GCTTGCTATT GGGCGCGGTA ATGATTCCTA CGATGAAAAT AAAAACGGCT
3446 TGCTTGTTCT CGATGAGTGC GGTACTTGGT TTAATACCCG TTCTTGGAAT
3496 GATAAGGAAA GACAGCCGAT TATTGATTGG TTTCTACATG CTCGTAAATT
3546 AGGATGGGAT ATTATTTTTC TTGTTCAGGA CTTATCTATT GTTGATAAAC
3596 AGGCGCGTTC TGCATTAGCT GAACATGTTG TTTATTGTCG TCGTCTGGAC
3646 AGAATTACTT TACCTTTTGT CGGTACTTTA TATTCTCTTA TTACTGGCTC
3696 GAAAATGCCT CTGCCTAAAT TACATGTTGG CGTTGTTAAA TATGGCGATT
3746 CTCAATTAAG CCCTACTGTT GAGCGTTGGC TTTATACTGG TAAGAATTTG
3796 TATAACGCAT ATGATACTAA ACAGGCTTTT TCTAGTAATT ATGATTCCGG
3846 TGTTTATTCT TATTTAACGC CTTATTTATC ACACGGTCGG TATTTCAAAC
3896 CATTAAATTT AGGTCAGAAG ATGAAATTAA CTAAAATATA TTTGAAAAAG
3946 TTTTCTCGCG TTCTTTGTCT TGCGATTGGA TTTGCATCAG CATTTACATA
3996 TAGTTATATA ACCCAACCTA AGCCGGAGGT TAAAAAGGTA GTCTCTCAGA
4046 CCTATGATTT TGATAAATTC ACTATTGACT CTTCTCAGCG TCTTAATCTA
4096 AGCTATCGCT ATGTTTTCAA GGATTCTAAG GGAAAATTAA TTAATAGCGA
4146 CGATTTACAG AAGCAAGGTT ATTCACTCAC ATATATTGAT TTATGTACTG
4196 TTTCCATTAA AAAAGGTAAT TCAAATGAAA TTGTTAAATG TAATTAA
```

Region:
3196...4242
Length:
1047 bp
MW:
323 680.96 Da

Protein I (PI)

```
        10         20         30         40         50
MAVYFVTGKL GSGKTLVSVG KIQDKIVAGC KIATNLDLRL QNLPQVGRFA
        60         70         80         90        100
KTPRVLRIPD KPSISDLLAI GRGNDSYDEN KNGLLVLDEC GTWFNTRSWN
       110        120        130        140        150
DKERQPIIDW FLHARKLGWD IIFLVQDLSI VDKQARSALA EHVVYCRRLD
       160        170        180        190        200
RITLPFVGTL YSLITGSKMP LPKLHVGVVK YGDSQLSPTV ERWLYTGKNL
       210        220        230        240        250
YNAYDTKQAF SSNYDSGVYS YLTPYLSHGR YFKPLNLGQK MKLTKIYLKK
       260        270        280        290        300
FSRVLCLAIG FASAFTYSYI TQPKPEVKKV VSQTYDFDKF TIDSSQRLNL
       310        320        330        340
SYRYVFKDSK GKLINSDDLQ KQGYSLTYID LCTVSIKKGN SNEIVKCN
```

Length:
348 aa
Measured MW:
39 500 Da
Theoretical MW:
- **Average**
  39 550.72 Da
- **Monoisotopic**
  39 525.80 Da

IEP:
9.55
ε:
59 540 M^{-1} cm^{-1}
Trp: 5
Tyr: 21
Cys: 6

Gene II (*pII*)

```
6006 ATGATTGACA TGCTAGTTTT ACGATTACCG TTCATCGATT CTCTTGTTTG
6056 CTCCAGACTC TCAGGCAATG ACCTGATAGC CTTTGTAGAC CTCTCAAAAA
6106 TAGCTACCCT CTCCGGCATG AATTTATCAG CTAGAACGGT TGAATATCAT
6156 ATTGATGGTG ATTTGACTGT CTCCGGCCTT TCTCACCCTT TTGAATCTTT
6206 ACCTACACAT TACTCAGGCA TTGCATTTAA AATATATGAG GGTTCTAAAA
6256 ATTTTTATCC TTGCGTTGAA ATAAAGGCTT CTCCCGCAAA AGTATTACAG
6306 GGTCATAATG TTTTTGGTAC AACCGATTTA GCTTTATGCT CTGAGGCTTT
6356 ATTGCTTAAT TTTGCTAATT CTTTGCCTTG CCTGTATGAT TTATTGGATG
6406 TTAACGCTAC TACTATTAGT AGAATTGATG CCACCTTTTC AGCTCGCGCC
  49 CCAAATGAAA ATATAGCTAA ACAGGTTATT GACCATTTGC GAAATGTATC
  99 TAATGGTCAA ACTAAATCTA CTCGTTCGCA GAATTGGGAA TCAACTGTTA
 149 CATGGAATGA AACTTCCAGA CACCGTACTT TAGTTGCATA TTTAAAACAT
 199 GTTGAGCTAC AGCACCAGAT TCAGCAATTA AGCTCTAAGC CATCCGCAAA
 249 AATGACCTCT TATCAAAAGG AGCAATTAAA GGTACTCTCT AATCCTGACC
 299 TGTTGGAGTT TGCTTCCGGT CTGGTTCGCT TTGAAGCTCG AATTAAAACG
 349 CGATATTTGA AGTCTTTCGG GCTTCCTCTT AATCTTTTTG ATGCAATCCG
 399 CTTTGCTTCT GACTATAATA GTCAGGGTAA AGACCTGATT TTTGATTTAT
 449 GGTCATTCTC GTTTTCTGAA CTGTTTAAAG CATTTGAGGG GGATTCAATG
 499 AATATTTATG ACGATTCCGC AGTATTGGAC GCTATCCAGT CTAAACATTT
 549 TACTATTACC CCCTCTGGCA AAACTTCTTT TGCAAAAGCC TCTCGCTATT
 599 TTGGTTTTTA TCGTCGTCTG GTAAACGAGG GTTATGATAG TGTTGCTCTT
 649 ACTATGCCTC GTAATTCCTT TTGGCGTTAT GTATCTGCAT TAGTTGAATG
 699 TGGTATTCCT AAATCTCAAC TGATGAATCT TTCTACCTGT AATAATGTTG
 749 TTCCGTTAGT TCGTTTTATT AACGTAGATT TTTCTTCCCA ACGTCCTGAC
 799 TGGTATAATG AGCCAGTTCT TAAAATCGCA TAA
```

Region:
6006…6407 - 1...831
Length:
1 233 bp
MW:
379 753.04 Da

Protein II (PII)

```
        10         20         30         40         50
MIDMLVLRLP FIDSLVCSRL SGNDLIAFVD LSKIATLSGM NLSARTVEYH
        60         70         80         90        100
IDGDLTVSGL SHPFESLPTH YSGIAFKIYE GSKNFYPCVE IKASPAKVLQ
       110        120        130        140        150
GHNVFGTTDL ALCSEALLLN FANSLPCLYD LLDVNATTIS RIDATFSARA
       160        170        180        190        200
PNENIAKQVI DHLRNVSNGQ TKSTRSQNWE STVTWNETSR HRTLVAYLKH
       210        220        230        240        250
VELQHQIQQL SSKPSAKMTS YQKEQLKVLS NPDLLEFASG LVRFEARIKT
       260        270        280        290        300
RYLKSFGLPL NLFDAIRFAS DYNSQGKDLI FDLWSFSFSE LFKAFEGDSM
       310        320        330        340        350
NIYDDSAVLD AIQSKHFTIT PSGKTSFAKA SRYFGFYRRL VNEGYDSVAL
       360        370        380        390        400
TMPRNSFWRY VSALVECGIP KSQLMNLSTC NNVVPLVRFI NVDFSSQRPD
       410
WYNEPVLKIA
```

Length:
410 aa
Measured MW:
46 117 Da
Theoretical MW:
- **Average:**
  46 166.63 Da
- **Monoisotopic:**
  46 137.50 Da

IEP:
7.63
ε:
50 600 M^{-1} cm^{-1}
Trp: 5
Tyr: 15
Cys: 6

Gene III (*pIII*)

```
1579 ATGAAAAAAT TATTATTCGC AATTCCTTTA GTTGTTCCTT TCTATTCTCA
1629 CTCCGCTGAA ACTGTTGAAA GTTGTTTAGC AAAACCCCAT ACAGAAAATT
1679 CATTTACTAA CGTCTGGAAA GACGACAAAA CTTTAGATCG TTACGCTAAC
1729 TATGAGGGTT GTCTGTGGAA TGCTACAGGC GTTGTAGTTT GTACTGGTGA
1779 CGAAACTCAG TGTTACGGTA CATGGGTTCC TATTGGGCTT GCTATCCCTG
1829 AAAATGAGGG TGGTGGCTCT GAGGGTGGCG GTTCTGAGGG TGGCGGTTCT
1879 GAGGGTGGCG GTACTAAACC TCCTGAGTAC GGTGATACAC CTATTCCGGG
1929 CTATACTTAT ATCAACCCTC TCGACGGCAC TTATCCGCCT GGTACTGAGC
1979 AAAACCCCGC TAATCCTAAT CCTTCTCTTG AGGAGTCTCA GCCTCTTAAT
2029 ACTTTCATGT TTCAGAATAA TAGGTTCCGA AATAGGCAGG GGGCATTAAC
2079 TGTTTATACG GCACTGTTA CTCAAGGCAC TGACCCCGTT AAAACTTATT
2129 ACCAGTACAC TCCTGTATCA TCAAAAGCCA TGTATGACGC TTACTGGAAC
2179 GGTAAATTCA GAGACTGCGC TTTCCATTCT GGCTTTAATG AGGATCCATT
2229 CGTTTGTGAA TATCAAGGCC AATCGTCTGA CCTGCCTCAA CCTCCTGTCA
2279 ATGCTGGCGG CGGCTCTGGT GGTGGTTCTG GTGGCGGCTC TGAGGGTGGT
2329 GGCTCTGAGG GTGGCGGTTC TGAGGGTGGC GGCTCTGAGG GAGGCGGTTC
2379 CGGTGGTGGC TCTGGTTCCG GTGATTTTGA TTATGAAAAG ATGGCAAACG
2429 CTAATAAGGG GGCTATGACC GAAAATGCCG ATGAAAACGC GCTACAGTCT
2479 GACGCTAAAG GCAAACTTGA TTCTGTCGCT ACTGATTACG GTGCTGCTAT
2529 CGATGGTTTC ATTGGTGACG TTTCCGGCCT TGCTAATGGT AATGGTGCTA
2579 CTGGTGATTT TGCTGGCTCT AATTCCCAAA TGGCTCAAGT CGGTGACGGT
2629 GATAATTCAC CTTTAATGAA TAATTTCCGT CAATATTTAC CTTCCCTCCC
2679 TCAATCGGTT GAATGTCGCC CTTTTGTCTT TAGCGCTGGT AAACCATATG
2729 AATTTTCTAT TGATTGTGAC AAAATAAACT TATTCCGTGG TGTCTTTGCG
2779 TTTCTTTTAT ATGTTGCCAC CTTTATGTAT GTATTTTCTA CGTTTGCTAA
2829 CATACTGCGT AATAAGGAGT CTTAA
```

Region:
1579...2853
Length:
1272 bp
MW:
394 236.67 Da

Region:
1632...2853
Length:
1218 bp
MW:
377 763.93 Da

Protein III (PIII)

```
        10         20         30         40         50
MKKLLFAIPL VVPFYSHSAE TVESCLAKPH TENSFTNVWK DDKTLDRYAN
        60         70         80         90        100
YEGCLWNATG VVVCTGDETQ CYGTWVPIGL AIPENEGGGS EGGGSEGGGS
       110        120        130        140        150
EGGGTKPPEY GDTPIPGYTY INPLDGTYPP GTEQNPANPN PSLEESQPLN
       160        170        180        190        200
TFMFQNNRFR NRQGALTVYT GTVTQGTDPV KTYYQYTPVS SKAMYDAYWN
       210        220        230        240        250
GKFRDCAFHS GFNEDPFVCE YQGQSSDLPQ PPVNAGGGSG GGSGGGSEGG
       260        270        280        290        300
GSEGGGSEGG GSEGGGSGGG SGSGDFDYEK MANANKGAMT ENADENALQS
       310        320        330        340        350
DAKGKLDSVA TDYGAAIDGF IGDVSGLANG NGATGDFAGS NSQMAQVGDG
       360        370        380        390        400
DNSPLMNNFR QYLPSLPQSV ECRPFVFSAG KPYEFSIDCD KINLFRGVFA
       410        420
FLLYVATFMY VFSTFANILR NKES
```

Length:
424 aa
Measured MW:
44 748 Da
Theoretical MW:
- **Average:**
  44 651.67 Da
- **Monoisotopic:**
  44 623.61 Da

IEP:
4.37
ε:
54 290 M^{-1} cm^{-1}
Trp: 4
Tyr: 21
Cys: 8

Length:
406 aa
Measured MW:
42 675 Da
Theoretical MW:
- **Average:**
  42 579.09 Da
- **Monoisotopic:**
  42 552.44 Da

IEP:
4.26
ε:
52 800 M^{-1} cm^{-1}
Trp: 4
Tyr: 20
Cys: 8

PDB ID:
1G3P
1TOL

Note: The mature form of the protein does not contain the sequence underlined in red.

Gene IV (*pIV*)

```
4220 ATGAAATTGT TAAATGTAAT TAATTTTGTT TTCTTGATGT TTGTTTCATC
4270 ATCTTCTTTT GCTCAGGTAA TTGAAATGAA TAATTCGCCT CTGCGCGATT
4320 TTGTAACTTG GTATTCAAAG CAATCAGGCG AATCCGTTAT TGTTTCTCCC
4370 GATGTAAAAG GTACTGTTAC TGTATATTCA TCTGACGTTA AACCTGAAAA
4420 TCTACGCAAT TTCTTTATTT CTGTTTTACG TGCTAATAAT TTTGATATGG
4470 TTGGTTCAAT TCCTTCCATA ATTCAGAAGT ATAATCCAAA CAATCAGGAT
4520 TATATTGATG AATTGCCATC ATCTGATAAT CAGGAATATG ATGATAATTC
4570 CGCTCCTTCT GGTGGTTTCT TTGTTCCGCA AAATGATAAT GTTACTCAAA
4620 CTTTTAAAAT TAATAACGTT CGGGCAAAGG ATTTAATACG AGTTGTCGAA
4670 TTGTTTGTAA AGTCTAATAC TTCTAAATCC TCAAATGTAT TATCTATTGA
4720 CGGCTCTAAT CTATTAGTTG TTAGTGCACC TAAAGATATT TTAGATAACC
4770 TTCCTCAATT CCTTTCTACT GTTGATTTGC CAACTGACCA GATATTGATT
4820 GAGGGTTTGA TATTTGAGGT TCAGCAAGGT GATGCTTTAG ATTTTTCATT
4870 TGCTGCTGGC TCTCAGCGTG GCACTGTTGC AGGCGGTGTT AATACTGACC
4920 GCCTCACCTC TGTTTTATCT TCTGCTGGTG GTTCGTTCGG TATTTTTAAT
4970 GGCGATGTTT TAGGGCTATC AGTTCGCGCA TTAAAGACTA ATAGCCATTC
5020 AAAAATATTG TCTGTGCCAC GTATTCTTAC GCTTTCAGGT CAGAAGGGTT
5070 CTATCTCTGT TGGCCAGAAT GTCCCTTTTA TTACTGGTCG TGTGACTGGT
5120 GAATCTGCCA ATGTAAATAA TCCATTTCAG ACGATTGAGC GTCAAAATGT
5170 AGGTATTTCC ATGAGCGTTT TTCCTGTTGC AATGGCTGGC GGTAATATTG
5220 TTCTGGATAT TACCAGCAAG GCCGATAGTT TGAGTTCTTC TACTCAGGCA
5270 AGTGATGTTA TTACTAATCA AAGAAGTATT GCTACAACGG TTAATTTGCG
5320 TGATGGACAG ACTCTTTTAC TCGGTGGCCT CACTGATTAT AAAAACACTT
5370 CTCAAGATTC TGGCGTACCG TTCCTGTCTA AAATCCCTTT AATCGGCCTC
5420 CTGTTTAGCT CCCGCTCTGA TTCCAACGAG GAAAGCACGT TATACGTGCT
5470 CGTCAAAGCA ACCATAGTAC GCGCCCTGTA G
```

Region:
4220…5500
Length:
1278 bp
MW:
395 204.13 Da

Protein IV (PIV)

```
        10         20         30         40         50
MKLLNVINFV FLMFVSSSSF AQVIEMNNSP LRDFVTWYSK QSGESVIVSP
        60         70         80         90        100
DVKGTVTVYS SDVKPENLRN FFISVLRANN FDMVGSIPSI IQKYNPNNQD
       110        120        130        140        150
YIDELPSSDN QEYDDNSAPS GGFFVPQNDN VTQTFKINNV RAKDLIRVVE
       160        170        180        190        200
LFVKSNTSKS SNVLSIDGSN LLVVSAPKDI LDNLPQFLST VDLPTDQILI
       210        220        230        240        250
EGLIFEVQQG DALDFSFAAG SQRGTVAGGV NTDRLTSVLS SAGGSFGIFN
       260        270        280        290        300
GDVLGLSVRA LKTNSHSKIL SVPRILTLSG QKGSISVGQN VPFITGRVTG
       310        320        330        340        350
ESANVNNPFQ TIERQNVGIS MSVFPVAMAG GNIVLDITSK ADSLSSSTQA
       360        370        380        390        400
SDVITNQRSI ATTVNLRDGQ TLLLGGLTDY KNTSQDSGVP FLSKIPLIGL
       410        420
LFSSRSDSNE ESTLYVLVKA TIVRAL
```

Length:
426 aa
Measured MW:
45 791 Da
Theoretical MW:
- **Average:**
  45 864.73 Da
- **Monoisotopic:**
  45 836.61 Da

IEP:
4.94
ε:
15 930 M^{-1} cm^{-1}
Trp: 1
Tyr: 7
Cys: 0

Gene V (*pV*)

```
 843 ATGATTAAAG TTGAAATTAA ACCATCTCAA GCCCAATTTA CTACTCGTTC
 893 TGGTGTTTCT CGTCAGGGCA AGCCTTATTC ACTGAATGAG CAGCTTTGTT
 943 ACGTTGATTT GGGTAATGAA TATCCGGTTC TTGTCAAGAT TACTCTTGAT
 993 GAAGGTCAGC CAGCCTATGC GCCTGGTCTG TACACCGTTC ATCTGTCCTC
1043 TTTCAAAGTT GGTCAGTTCG GTTCCCTTAT GATTGACCGT CTGCGCCTCG
1093 TTCCGGCTAA GTAA
```

Region:
843...1106
Length:
261 bp
MW:
81 332.73 Da

Protein V (PV)

```
        10         20         30         40         50
MIKVEIKPSQ AQFTTRSGVS RQGKPYSLNE QLCYVDLGNE YPVLVKITLD
        60         70         80
EGQPAYAPGL YTVHLSSFKV GQFGSLMIDR LRLVPAK
```

Length:
87 aa
Measured MW:
9666 Da
Theoretical MW:
- **Average:**
  9688.24 Da
- **Monoisotopic:**
  9682.10 Da

IEP:
9.17
ε:
7575 M^{-1} cm^{-1}
Trp: 0
Tyr: 5
Cys: 1
PDB ID:
2GVA
2GVB

Gene VI (*pVI*)

```
2856 ATGCCAGTTC TTTTGGGTAT TCCGTTATTA TTGCGTTTCC TCGGTTTCCT
2896 TCTGGTAACT TTGTTCGGCT ATCTGCTTAC TTTTCTTAAA AAGGGCTTCG
2956 GTAAGATAGC TATTGCTATT TCATTGTTTC TTGCTCTTAT TATTGGGCTT
2996 AACTCAATTC TTGTGGGTTA TCTCTCTGAT ATTAGCGCTC AATTACCCTC
3056 TGACTTTGTT CAGGGTGTTC AGTTAATTCT CCCGTCTAAT GCGCTTCCCT
3096 GTTTTTATGT TATTCTCTCT GTAAAGGCTG CTATTTTCAT TTTTGACGTT
3156 AAACAAAAAA TCGTTTCTTA TTTGGATTGG GATAAATAA
```

Region:
2856…3194
Length:
339 bp
MW:
104 274.79 Da

Protein VI (PVI)

```
        10         20         30         40         50
MPVLLGIPLL LRFLGFLLVT LFGYLLTFLK KGFGKIAIAI SLFLALIIGL
        60         70         80         90        100
NSILVGYLSD ISAQLPSDFV QGVQLILPSN ALPCFYVILS VKAAIFIFDV
       110
KQKIVSYLDW DK
```

Length:
112 aa
Measured MW:
12 264 Da
Theoretical MW:
- **Average:**
  12 350.09 Da
- **Monoisotopic:**
  12 342.07 Da

IEP:
9.17
ε:
11 585 M^{-1} cm^{-1}
Trp: 1
Tyr: 4
Cys: 1

Gene VII (*pVII*)

1108 ATGGAGCAGG TCGCGGATTT CGACACAATT TATCAGGCGA TGATACAAAT 1158 CTCCGTTGTA CTTTGTTTCG CGCTTGGTAT AATCGCTGGG GGTCAAAGAT 1208 GA	**Region:** 1108..1209 **Length:** 102 bp **MW:** 31 685.56 Da

Protein VII (PVII)

10 20 30 MEQVADFDTI YQAMIQISVV LCFALGIIAG GQR	**Length:** 33 aa **Measured MW:** 3587 Da **Theoretical MW:** • **Average:** 3602.24 Da • **Monoisotopic:** 3599.82 Da **IEP:** 4.03 **ε:** 1615 M^{-1} cm^{-1} **Trp:** 0 **Tyr:** 1 **Cys:** 1

Gene VIII (*pVIII*)

```
1301 ATGAAAAAGT CTTTAGTCCT CAAAGCCTCT GTAGCCGTTG CTACCCTCGT
1351 TCCGATGCTG TCTTTCGCTG CTGAGGGTGA CGATCCCGCA AAAGCGGCCT
1401 TTAACTCCCT GCAAGCCTCA GCGACCGAAT ATATCGGTTA TGCGTGGGCG
1451 ATGGTTGTTG TCATTGTCGG CGCAACTATC GGTATCAAGC TGTTTAAGAA
1501 ATTCACCTCG AAAGCAAGCT GA
```

Region:
1301...1522
Length:
222 bp
MW:
68 503.32 Da

Region:
1569...1522
Length:
153 bp
MW:
47 371.66 Da

Protein VIII (PVIII)

```
        10         20         30         40         50
MKKSLVLKAS VAVATLVPML SFAAEGDDPA KAAFNSLQAS ATEYIGYAWA
        60         70
MVVVIVGATI GIKLFKKFTS KAS
```

PDB ID:
2MJZ
2CPB
2CPS

Length:
73 aa
Measured MW:
7622 Da
Theoretical MW:
- **Average:**
  7625.07 Da
- **Monoisotopic:**
  7620.13 Da

IEP:
9.63
ε:
8480 M^{-1} cm^{-1}
Trp: 1
Tyr: 2
Cys: 0

Length:
50 aa
Measured MW:
5234 Da
Theoretical MW:
- **Average:**
  5238.04 Da
- **Monoisotopic:**
  5234.74 Da

IEP:
8.34
ε:
8480 M^{-1} cm^{-1}
Trp: 1
Tyr: 2
Cys: 0

Note: The mature form of the protein does not contain the sequence underlined in red.

Gene IX (*pIX*)

1206 ATGAGTGTTT TAGTGTATTC TTTCGCCTCT TTCGTTTTAG GTTGGTGCCT **1256** TCGTAGTGGC ATTACGTATT TTACCCGTTT AATGGAAACT TCCTCATGA	**Region:** 1206...1304 **Length:** 99 bp **MW:** 30540.83 Da

Protein IX (PIX)

10 20 30 MSVLVYSFAS FVLGWCLRSG ITYFTRLMET SS	**Length:** 32 aa **Measured MW:** 3654 Da **Theoretical MW:** • **Average:** 3653.29 Da • **Monoisotopic:** 3650.80 Da **IEP:** 7.95 **ε:** 8480 M^{-1} cm^{-1} **Trp:** 1 **Tyr:** 2 **Cys:** 0

Gene X (*pX*)

```
496 ATGAATATTT ATGACGATTC CGCAGTATTG GACGCTATCC AGTCTAAACA
556 TTTTACTATT ACCCCCTCTG GCAAAACTTC TTTTGCAAAA GCCTCTCGCT
596 ATTTTGGTTT TTATCGTCGT CTGGTAAACG AGGGTTATGA TAGTGTTGCT
656 CTTACTATGC CTCGTAATTC CTTTTGGCGT TATGTATCTG CATTAGTTGA
696 ATGTGGTATT CCTAAATCTC AACTGATGAA TCTTTCTACC TGTAATAATG
756 TTGTTCCGTT AGTTCGTTTT ATTAACGTAG ATTTTTCTTC CCAACGTCCT
796 GACTGGTATA ATGAGCCAGT TCTTAAAATC GCATAA
```

Region:
496...831
Length:
336 bp
MW:
103 402.26 Da

Protein X (PX)

```
        10         20         30         40         50
MNIYDDSAVL DAIQSKHFTI TPSGKTSFAK ASRYFGFYRR LVNEGYDSVA
        60         70         80         90        100
LTMPRNSFWR YVSALVECGI PKSQLMNLST CNNVVPLVRF INVDFSSQRP
       110
DWYNEPVLKI A
```

Length:
111 aa
Measured MW:
12 670 Da
Theoretical MW:
- **Average:**
  12 680.49 Da
- **Monoisotopic:**
  12 672.36 Da

IEP:
9.00
ε:
20 190 M^{-1} cm^{-1}
Trp: 2
Tyr: 6
Cys: 2

Appendix 2

Protocol for the growth in batch of competent *E. coli* cells

Step 1 – Preparation of the NB2 broth, tetracycline and glycerol 50% solutions

Prepare 55 mL of nutrient broth No. 2 (NB2) solution in DIW using:

✓ Nutrient Broth No. 2 by OXOID CM0067

➢ 25 g of NB2 powder per L → 1.37 g of NB2 + 55 mL of DIW for 55 mL of NB2 solution

- Stir in a 100 mL measuring cylinder until dissolved
- Add 55 mL of NB2 solution in a 250 mL conical flask
- Add the sponge to seal conical flask and top and foil
- Add autoclave tape to the conical flasks
- Label: Quantity, contents, date, initials
- Autoclave at 120°C for 20 min

Prepare 1 mL of tetracycline (TCN) in ethanol 100%, with a final concentration of 5 mg mL^{-1}:

✓ Tetracycline (MW: 444.435 g mol^{-1}) CAS: 60-54-8

➢ TNC $_{5\ mg\ mL^{-1}}$ → 5 mg of TNC for 1 mL of TNC solution

Prepare 50 mL of glycerol 50%:

✓ Glycerol (MW: 92.094 g mol^{-1}) CAS: 56-81-5

➢ Glycerol 50% → 25 mL of glycerol + 25 mL of DIW for 50 mL of glycerol 50% solution

Step 2 – Propagation of *E. coli* Top10F' host cells

Defrost 1 mL Top10F' from -80°C freezer

- Using aseptic technique (Bunsen burner or laminar flow cabinet):
  - Inoculate 55 mL of NB2 flask with 55 µL of TNC$_{5\ mg\ mL-1}$ (TNC final concentration of 5 µg mL^{-1})
  - Add 1 mL of *E. coli* stock solution to the NB2 in the flask
- Incubate at 37°C and 150 rpm checking the $OD_{600\ nm}$ every hour until the value is 0.4-0.5 (usually 5 h)

Step 3 – Stocking and storage

- Move the *E. coli* culture on ice to stop the growth
- Combine 50 mL of the culture with 50 mL of glycerol 50%
- Split the final volume into 50 microtubes (1 mL each tube)
- Snap freeze with liquid nitrogen
- Store in the -80°C freezer

Appendix 3

Protocol for the propagation and purification of M13 through infection of *E. coli* and PEG/NaCl precipitation

Step 1 – Preparation of the NB2 broth and PEG

Prepare 2.22 L of nutrient broth No. 2 (NB2) solution in DIW using:

- ✓ Nutrient Broth No. 2 by OXOID CM0067

➢ 25 g of NB2 powder per L → 55.5 g of NB2 for 2.22 L of NB2 solution

- Stir in a beaker until dissolved
- Add 370 mL of NB2 solution to 6 × 2.0 L conical flasks
- Add the sponge to seal conical flask and top and foil
- Add autoclave tape to the conical flasks
- Label: Quantity, contents, date, initials
- Autoclave at 120°C for 20 min

Prepare 1.0 L of PEG/NaCl solution in DIW using:

- ✓ PEG (MW: 6000 g mol^{-1}) CAS: 25322-68-3
- ✓ NaCl (MW: 58.44 g mol^{-1}) CAS: 7647-14-5

➢ $PEG_{250\ mg\ mL^{-1}}$ + $NaCl_{146\ mg\ mL^{-1}}$ → 250 g of PEG + 146 g of NaCl for 1 L of PEG/NaCl solution

- Stir in a beaker until dissolved
- Move the solution in a glass bottle
- Add autoclave tape to the lid (do not screw the lid tight)
- Label: Quantity, contents, date, initials
- Autoclave at 120°C for 20 min

Step 2 – Propagation of M13 using *E. coli* Top10F' host cells

(One Shot TOP10F´ Chemically Competent *E. coli*)

Prepare 2.22 mL of tetracycline (TCN) in ethanol 100%, with a final concentration of 5 mg mL^{-1}:

- ✓ Tetracycline (MW: 444.435 g mol^{-1}) CAS: 60-54-8

➢ $TCN_{5\ mg\ mL^{-1}}$ → 11.1 mg of TCN for 2.22 mL of TCN solution

- Defrost 3 × 1 mL Top10F' from -80°C freezer
- Using aseptic technique (Bunsen burner or laminar flow cabinet):
  - Inoculate each 370 mL of NB2 flask with 370 µL $TCN_{5\ mg\ mL^{-1}}$ (to have a TCN final concentration of 5 µg mL^{-1})
  - Add 500 µL of *E. coli* stock solution to each 370 mL of NB2 flask
  - Add 0.05 mg of M13 from the stock solution to each 370 mL of NB2 flask
- Incubate at 32°C, 150 rpm for 16–18 h (overnight)

Step 3 – Purification of M13

Separate NB2/*E. coli*/M13 into 6 centrifuge tubes:

- Centrifuge at 8000 rpm (Beckman Coulter JA 10 – RCF = 11 295.1 *g*) for 30 min at 4°C
- Extract all the supernatant
- Discard pellet and wash tubes

- Centrifuge again at 8000 rpm (Beckman Coulter JA 10 – RCF = 11 295.1 *g*) for 30 min at 4°C
- This time collect the top 300 mL from each tube

Addition of PEG/NaCl solution to precipitate the M13:

- Add PEG/NaCl solution at a ratio of 1:5 to the volume of supernatant
    - 6 × 300 mL = 1800 add 360 mL PEG/NaCl solution
- Leave on ice to stir for 90 min

Collection of the precipitated M13:

- Separate the PEG/NaCl with M13 supernatant into 6 centrifuge tubes
- Centrifuge at 10 000 rpm (Beckman Coulter JA 10 – RCF = 17 648.6 *g*) for 30 min at 4°C (Spin again if no white pellet seen)
- Discard supernatant and resuspend pellet trying to use 1 mL of $PBS_{50\ mM\ –\ pH\ 8.0}$ (or DIW) and collect in microtubes

- Centrifuge for 5 min at 15 100 RCF (SciQuip - SciSpin MICRO Centrifuge)
- Transfer supernatant to new microtubes and discard brown pellet (*E. coli*)
- Add PEG at a ratio of 1:5 to the volume of supernatant
    - For 1 mL add 200 µL PEG/NaCl solution
- Leave on ice for 90 min

- Centrifuge for 15 min at 15 100 RCF (SciQuip - SciSpin MICRO Centrifuge)
- Discard supernatant and resuspend M13 pellets using 200 µL of $PBS_{50\ mM\ –\ pH\ 8.0}$ (or DIW) and collect in microtubes
- Collect M13 in a Falcon tube and store in the fridge at 4°C

Step 4 – Results

Results table	
E. coli stock used	
M13 stock date and concentration (mg mL^{-1})	
Dilution Factor	
Absorbance of dilution at 269 nm	
Absorbance of dilution at 320 nm	
New stock concentration (mg mL^{-1})	
New stock volume (mL)	
M13 molar extinction coefficient (ε)	3.84 $cm^2\ mg^{-1}$
M13 Molecular Weight (MW)	16.8×10^6 g mol^{-1}

Appendix 4

Protocol for the propagation and purification of M13 through infection of *E. coli* and PEG/precipitation

Step 1 – Preparation of the NB2 broth and PEG

Prepare 2.22 L of nutrient broth No. 2 (NB2) solution in PBS pH 7.33 using:

- ✓ Nutrient Broth No. 2 by OXOID CM0067
- ✓ Phosphate Buffer Saline (PBS) OXOID BR0014G

- ➢ 25 g of NB2 powder per L → 55.5 g of NB2 for 2.22 L of NB2 solution
- ➢ Prepare PBS by dissolving 1 tab per 100 mL

- Dissolve the NB2 powder in PBS and stir until dissolved
- Add 370 mL of NB2 solution to 6 × 2.0 L conical flasks
- Add sponge to seal conical flask and top and foil
- Add autoclave tape to conical flasks
- Label: Quantity, contents, date, initials
- Autoclave at 120°C for 20 min

Prepare 1.0 L of PEG/NaCl solution in DIW using:

- ✓ PEG (MW: 8000 g mol^{-1}) CAS: 25322-68-3
- ✓ NaCl (MW: 58.44 g mol^{-1}) CAS: 7647-14-5

- ➢ $PEG_{250\ mg\ mL^{-1}}$ + $NaCl_{146\ mg\ mL^{-1}}$ → 250 g of PEG + 146 g of NaCl for 1 L of PEG/NaCl solution

- Stir in a beaker until dissolved
- Move the solution in a glass bottle
- Add autoclave tape to the lid (do not screw the lid tight)
- Label: Quantity, contents, date, initials
- Autoclave at 120°C for 20 min

Step 2 – Propagation of M13 using *E. coli* Top10F' host cells

(One Shot TOP10F´ Chemically Competent *E. coli*)

Prepare 2.22 mL of tetracycline (TCN) in ethanol 100%, with a final concentration of 5 mg mL^{-1}:

- ✓ Tetracycline (MW: 444.435 g mol^{-1}) CAS: 60-54-8

- ➢ $TCN_{5\ mg\ mL^{-1}}$ → 11.1 mg of TCN for 2.22 mL of TCN solution

- Defrost 3 × 1 mL Top10F' from -80°C freezer
- Using aseptic technique (Bunsen burner or laminar flow cabinet):
  - Inoculate each 370 mL of NB2 flask with 370 µL $TCN_{5\ mg\ mL^{-1}}$ (to have a TCN final concentration of 5 µg mL^{-1})
  - Add 500 µL of *E. coli* stock solution to each 370 mL of NB2 flask
  - Add 0.05 mg of M13 from the stock solution to each 370 mL of NB2 flask
- Incubate at 32°C, 150 rpm for 16–20 h (overnight)

Step 3 – Purification of M13

Separate NB2/*E. coli*/M13 into six centrifuge tubes:

- Centrifuge at 8000 rpm (Beckman Coulter JA 10 – RCF = 11 295.1 *g*) for 30 min at 4°C
- Extract all the supernatant
- Discard pellet and wash tubes

- Centrifuge again at 8000 rpm (Beckman Coulter JA 10 – RCF = 11 295.1 *g*) for 30 min at 4°C
- This time collect the top 300 mL from each tube

Addition of PEG/NaCl solution to precipitate the M13:

- Add PEG/NaCl solution at a ratio of 1:5 to the volume of supernatant
    - 6 × 300 mL = 1800 add 360 mL PEG/NaCl solution
- Leave on ice to stir for 90 min

Collection of the precipitated M13:

- Separate the PEG/NaCl with M13 supernatant into 6 centrifuge tubes
- Centrifuge at 10 000 rpm (Beckman Coulter JA 10 – RCF = 17 648.6 *g*) for 30 min at 4°C (Spin again if no white pellet is seen)
- Discard the supernatant and resuspend pellet trying to use 1 mL of DIW and collect in microtubes

- Centrifuge for 15 min at 15 100 RCF (SciQuip – SciSpin MICRO Centrifuge)
- Discard the supernatant and resuspend M13 pellets using 500 µL of DIW and collect in microtubes

- Centrifuge for 5 min at 15 100 RCF (SciQuip – SciSpin MICRO Centrifuge)
- Discard the dark pellets and keep the supernatants
- Add HCl until pH 4.5 and leave for 5 min
- Centrifuge for 5 min at 15 100 RCF (SciQuip – SciSpin MICRO Centrifuge)
- Discard the supernatant and resuspend M13 pellets in PBS o DIW
- Collect M13 in a Falcon tube and store in the fridge at 4°C

Step 4 – Results

Results table	
E. coli stock used	
M13 stock date and concentration (mg mL^{-1})	
Dilution Factor	
Absorbance of dilution at 269 nm	
Absorbance of dilution at 320 nm	
New stock concentration (mg mL^{-1})	
New stock volume (mL)	
M13 molar extinction coefficient (ε)	3.84 cm^2 mg^{-1}
M13 Molecular Weight (MW)	16.8 × 10^6 g mol^{-1}

Appendix 5

GO-5' SEM/EDX

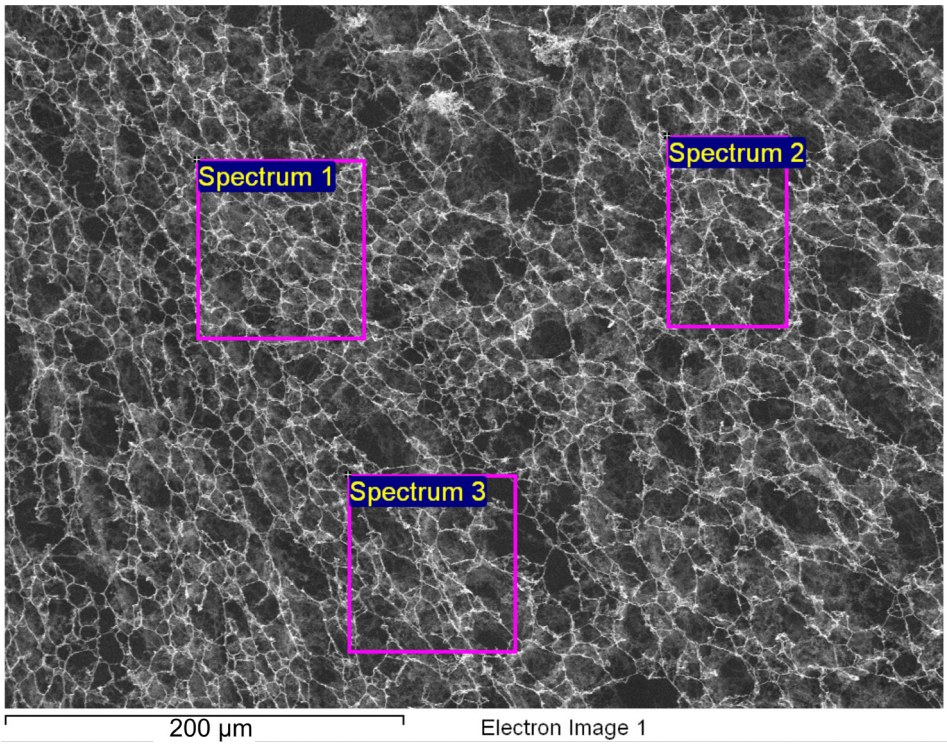


Figure A5 GO-5' SEM/EDX

SEM images of GO-5' with the areas labelled where the EDX spectra **(Fig. 5.9i)** were collected.

Table A5
GO EDX element analysis with results in weight percentage
GO processing option: All elements analysed (Normalised)

	In stats.	Si	C	O	Total (%)
Spectrum 1	Yes	44.71	45.68	9.61	100.00
Spectrum 2	Yes	48.00	41.70	10.30	100.00
Spectrum 3	Yes	49.03	42.75	8.22	100.00
Mean		47.25	43.38	9.38	100.00
Std. deviation		2.26	2.06	1.06	
Max.		49.03	45.68	10.30	
Min.		44.71	41.70	8.22	

Appendix 6

M13 SEM/EDX

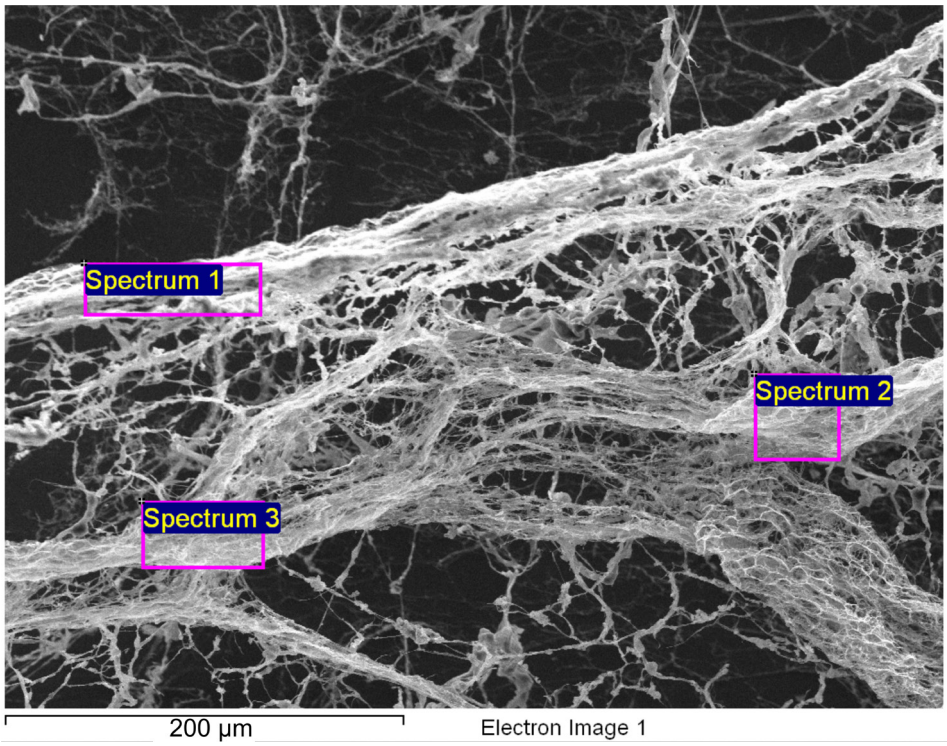


Figure A6 M13 SEM/EDX

SEM images of M13 with the areas where the EDX spectra **(Fig. 5.9j)** were collected.

Table A6
M13 EDX element analysis with results in weight percentage
M13 processing option: All elements analysed (Normalised)

	In stats.	Si	C	O	N	S	P	Na	Cl	Total (%)
Spectrum 1	Yes	36.41	49.31	8.91	4.09	0.01	0.29	0.43	0.55	100.00
Spectrum 2	Yes	21.42	58.06	13.80	4.79	0.04	0.19	0.69	1.01	100.00
Spectrum 3	Yes	28.25	54.30	10.56	5.46	0.05	0.31	0.39	0.68	100.00
Mean		28.69	53.89	11.09	4.78	0.03	0.26	0.50	0.75	100.00
Std. deviation		7.50	4.39	2.49	0.69	0.02	0.06	0.16	0.24	
Max.		36.41	58.06	13.80	5.46	0.05	0.31	0.69	1.01	
Min.		21.42	49.31	8.91	4.09	0.01	0.19	0.39	0.55	

Appendix 7

GraPhag13 SEM/EDX

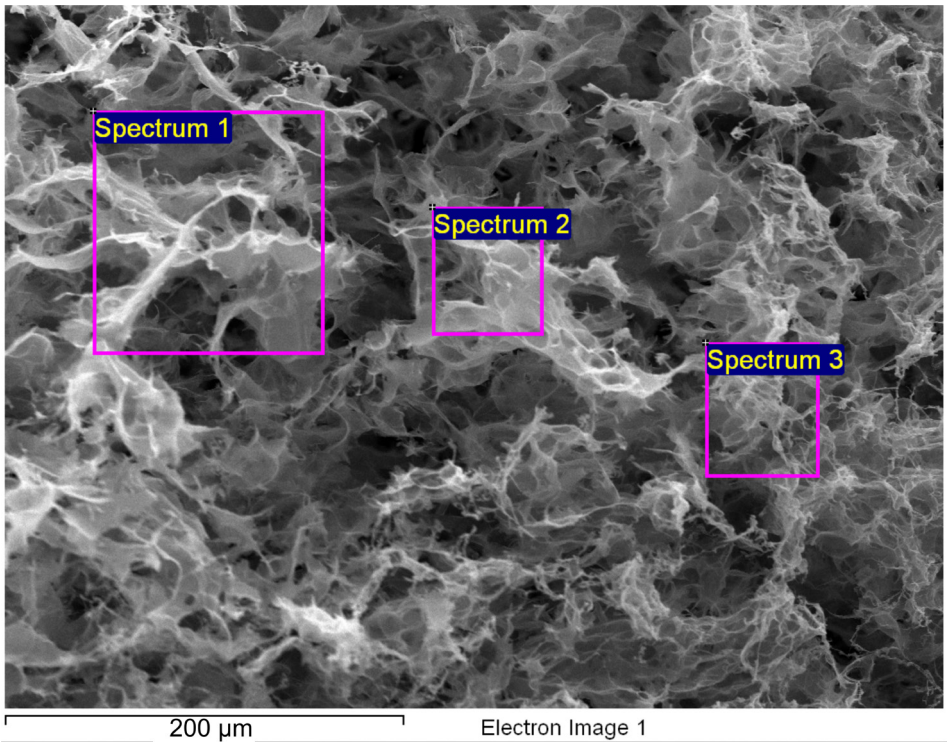


Figure A7 ***GraPhage13*** **SEM/EDX**

SEM images of GO-M13$_{0303\text{-}5'}$ with the areas where the EDX spectra **(Fig. 5.9k)** were collected.

Table A7
GO-M13$_{0303\text{-}5'}$ EDX element analysis with results in weight percentage
GO-M13$_{0303\text{-}5'}$ processing option: All elements analysed (Normalised)

	In stats.	Si	C	O	N	S	P	Na	Cl	Total (%)
Spectrum 1	Yes	2.95	66.25	27.59	1.63	0.29	0.63	0.35	0.30	100.00
Spectrum 2	Yes	2.18	58.89	29.03	8.76	0.20	0.23	0.40	0.31	100.00
Spectrum 3	Yes	1.23	60.92	29.79	6.72	0.26	0.28	0.40	0.40	100.00
Mean		2.12	62.02	28.80	5.70	0.25	0.38	0.38	0.34	100.00
Std. deviation		0.86	3.80	1.12	3.67	0.05	0.22	0.03	0.06	
Max.		2.95	66.25	29.79	8.76	0.29	4.19	0.35	0.40	
Min.		1.23	58.89	27.59	1.63	0.20	1.42	0.40	0.30	

Appendix 8

Raman analysis - Tables

Table A8.1. The position, width and amplitude of the Lorentzians from the best fits of the spectra of the GO, M13, GO-M13$_{PC}$ sample and GO-M13$_{0303\text{-}5'}$ at 633 nm are shown. The fitted position corresponds to the Raman shift. P1 denotes the position of the Lorentzian with the lowest frequency. The width and amplitude of the Lorentzian are labelled corresponding to the positions. W1 and A1 denote the width and amplitude of the peak with the position P1.

	GO	M13	GO-M13$_{PC}$	GO-M13$_{0303\text{-}5'}$
P1 (cm^{-1})	1292.2	1309.2	1339.1	1335.2
P2	1337.7	1450.4	1585.2	1575.8
P3	1586.5	1592.6		1606.2
P4		1652.6		
W1 (cm^{-1})	6.8	47.8	61.5	60.9
W2	60.9	20.5	37.9	34.4
W3	39.6	41.3		20.0
W4		11.0		
A1 (arb. unit)	2.3E+4	5.4E+4	7.1E+5	9.6E+6
A2	1.6E+6	3.7E+4	3.6E+5	3.3E+6
A3	8.3E+5	1.9E+4		1.4E+6
A4		1.7E+4		

Table A8.2. S[*i*] denotes the *i*th coefficients of *sin* term in the Fourier series, and C[*i*] denotes the *i*th *cos* term.

633 nm	GO	M13	GO-M13$_{PC}$	GO-M13$_{0303\text{-}5'}$
S[1]	-166	0.29	-78	-893
S[2]	469	-2.78	177	2339
S[3]	-292	8.49	-127	-1222
S[4]	292	1.12	129	830
S[5]		14.4		1375
C[0]	-97	-2.17	-41	-402
C[1]	289	-1.49	130	2550
C[2]	-98	-6.71	-36	-5
C[3]	94	-0.57	1	545
C[4]	99	-2.48	24	438
C[5]		-17.0		-240

Table A8.3. The positions, width and amplitude of the Lorentzians from the best fits of the spectra of the GO, M13, GO-M13$_{PC}$ and GO-M13$_{0303\text{-}5'}$ at 785 nm are shown. The rule of labelling is the same as that for 633 nm.

	GO	M13	GO-M13$_{PC}$	GO-M13$_{0303\text{-}5'}$
P1 (cm^{-1})	1329.0	1302.7	1323.8	1279.9
P2	1492.5	1341.4	1490.4	1314.4
P3	1589.1	1451.2	1611.2	1368.5
P4		1608.9	1620.7	1510.6
P5		1655.1		1582.6
P6				1606.4
W1 (cm^{-1})	60.6	29.5	63.8	36.0
W2	90.9	26.1	65.2	62.4
W3	44.4	20.4	54.9	50.3
W4		27.2	54.6	69.9
W5		13.0		29.2
W6				17.6
A1 (arb.unit)	2.4E+6	6.0E+3	4.4E+6	5.3E+5
A2	1.9E+6	3.3E+3	6.9E+5	8.5E+6
A3	1.6E+6	6.7E+3	7.2E+6	1.6E+6
A4		1.5E+3	5.5E+6	2.3E+6
A5		3.1E+3		1.8E+6
A6				6.4E+5

Table A8.4. S[*i*] denotes the *i*th coefficients of *sin* term in the Fourier series, and C[*i*] indicates the *i*th *cos* term.

785 nm	GO	M13	GO-M13$_{PC}$	GO-M13$_{0303\text{-}5'}$
S[1]	221	0.327	678	1103
S[2]	297	0.562	-106	-666
S[3]	237	0.665	-313	-790
S[4]	335	1.320	174	438
S[5]	318	2.070		-225
S[6]				-419
C[0]	-119	-0.249	-245	-407
C[1]	-263	-0.715	45	289
C[2]	-170	-0.644	496	1006
C[3]	-53	-0.629	-190	-532
C[4]	111	-0.139	235	24
C[5]	-154	-1.040		-165
C[6]				-204

Appendix 9

SmPRXI details

SmPRXI

```
   1 ATGCGGGGTT CTCATCATCA TCATCATCAT GGTATGGCTA GCATGACTGG
  51 TGGACAGCAA ATGGGTCGGG ATCTGTACGA CGATGACGAT AAGGATCGAT
 101 GGGGATCCAC CATGGTATTG TTGCCTAATA GACCTGCACC AGAATTCAAA
 151 GGACAGGCTG TGATTAATGG TGAATTCAAA GAGATCTGTT TGAAGGATTA
 201 TCGAGGAAAA TATGTTGTAT TATTCTTCTA TCCAGCTGAT TTCACATTCG
 251 TGTGTCCCAC CGAAATCATC GCGTTCAGTG ATCAGGTGGA GGAGTTTAAC
 301 AGTCGAAATT GTCAAGTGAT CGCCTGTTCT ACAGATTCTC AATACAGTCA
 351 TCTTGCATGG GACAATTTGG ATCGTAAATC GGGTGGATTG GGTCATATGA
 401 AAATTCCTCT GTTGGCTGAC CGTAAACAGG AGATTTCCAA AGCATATGGT
 451 GTATTCGATG AAGAGGATGG TAATGCATTC AGAGGTTTAT TCATCATTGA
 501 TCCGAATGGA ATTCTACGTC AAATCACGAT CAATGACAAG CCAGTTGGAC
 551 GATCTGTAGA TGAAACATTA CGACTACTGG ACGCGTTCCA ATTTGTGGAG
 601 AAGCATGGTG AAGTGTGTCC GGTGAACTGG AAACGTGGTC AACATGGGAT
 651 CAAGGTTAAT CAAAAGTAG
```

Length:
669 bp
MW:
20 7810.12 Da

SmPRXI

```
        10         20         30         40         50
MRGSHHHHHH GMASMTGGQQ MGRDLYDDDD KDRWGSTMVL LPNRPAPEFK
        60         70         80         90        100
GQAVINGEFK EICLKDYRGK YVVLFFYPAD FTFVCPTEII AFSDQVEEFN
       110        120        130        140        150
SRNCQVIACS TDSQYSHLAW DNLDRKSGGL GHMKIPLLAD RKQEISKAYG
       160        170        180        190        200
VFDEEDGNAF RGLFIIDPNG ILRQITINDK PVGRSVDETL RLLDAFQFVE
       210        220
KHGEVCPVNW KRGQHGIKVN QK
```

PDB ID:
3ZTL (LMW)
3ZVJ (HMW)

Length:
222 aa
Theoretical MW:
- **Average:**
  25 273.56 Da
- **Monoisotopic:**
  25 257.45 Da

IEP:
6.19
ε:
26 065 $M^{-1}cm^{-1}$
Trp: 3
Tyr: 6
Cys: 5

Length:
185 aa
Theoretical MW:
- **Average:**
  21 043.03 Da
- **Monoisotopic:**
  21 029.67 Da

IEP:
6.10
ε:
19 075 M^{-1} cm^{-1}
Trp: 2
Tyr: 5
Cys: 5

Note: The sequence underlined in red contains the His-Tag and it is not included in the wild type protein.

Appendix 10

Protocol for the production and purification of SmPRXI

Step 1 – Inoculum

Prepare 100 mL of nutrient broth No. 2 (NB2) solution in DIW using:

- ✓ Nutrient Broth No. 2 by OXOID CM0067

➢ 25 g of NB2 powder per L → 2.5 g of NB2 for 100 mL of NB2 solution

- Stir in a 100 mL measuring cylinder until dissolved
- Move the solution in a glass bottle
- Add autoclave tape to the lid (do not screw the lid tight)
- Label: Quantity, contents, date, initials
- Autoclave at 120°C for 20 min

- Pick up with a loop a single colony of BL21(DE3) pLysS pRSETa-SmPRXI from the petri dish and put it into two Falcon tubes containing 5 mL of NB2 AMP+ CAM+ (Ampicillin $_{50\ mg\ mL}^{-1}$ and chloramphenicol $_{35\ mg\ mL}^{-1}$) each
- Incubate at 37°C, 150 rpm overnight

Step 2 – Preparation of antibiotics and BL21 (DE3) pLysS pRSETa-SmPRXI stock

Prepare IPTG, ampicillin (AMP) and chloramphenicol (CAM) solutions:

- ✓ IPTG (MW: 238.30 g mol^{-1}) CAS: 367-93-1
- ✓ Ampicillin (MW: 371.39 g mol^{-1}) CAS: 69-52-3
- ✓ Chloramphenicol (MW: 323.13 g mol^{-1}) CAS: 56-75-7

➢ IPTG $_{1\ M}$ → 1.19 g of IPTG for 5 mL of IPTG solution
➢ Ampicillin $_{50\ mg\ mL}^{-1}$ → 300 mg of ampicillin for 6 mL of ampicillin solution
➢ Chloramphenicol $_{35\ mg\ mL}^{-1}$ → 210 mg of chloramphenicol for 6 mL of chloramphenicol solution

Alternatively: *Ampicillin anhydrous (CAS: 69-53-4 - MW: 349.40 g mol^{-1}) is more freely soluble in a dilute acidic or basic solution (>50 mg mL^{-1}) but can degrade quickly so prepare solutions fresh in 1 M ammonium hydroxide or 1 M HCl for a higher concentration stock solution.*

Once prepared, filter each antibiotic with a sterile filter 0.22 µL (let pass sterile DIW through the filter before the antibiotic) under the fume cupboard in aseptic condition and split both the antibiotic solutions in an appropriate number of microtubes, then store them in the -20°C (6 months) or -80°C (12 months) freezer.

With the spare remaining solutions, prepare AMP and CAM aliquots of 100 µl

Prepare 55 mL of nutrient broth No. 2 (NB2) solution in DIW using:

- ✓ Nutrient Broth No. 2 by OXOID CM0067

➢ 25 g of NB2 powder per L → 1.37 g of NB2 for 55 mL of NB2 solution

- Stir in a 100 mL measuring cylinder until dissolved

- Add 55 mL of NB2 solution in a 250 mL conical flask
- Add sponge to seal conical flask and top and foil
- Add autoclave tape to conical flask
- Label: Quantity, contents, date, initials
- Autoclave at 120°C for 20 min

Prepare 50 mL of glycerol 50%:

✓ Glycerol (MW: 92.094 g mol^{-1}) CAS: 56-81-5

➢ Glycerol 50% → 25 mL of glycerol + 25 mL of H_2O for 50 mL of glycerol 50% solution

Pick up a single colony of from one of the Petri dishes AMP^+ CAM^+ stored in the fridge

- Using aseptic technique (Bunsen burner or fume cupboard):
  - Inoculate 55 mL of NB2 flask with 55 µL of ampicillin $_{50\ mg\ mL}{}^{-1}$ and 55 µL of chloramphenicol $_{35\ mg\ mL}{}^{-1}$ (to have antibiotics with a final concentration respectively of 50 µg mL^{-1} (AMP) and 34 µg mL^{-1} (CAM)
  - Add the single colony of BL21 (DE3) pLysS pRSETa-SmPRXI to the NB2 flask
  - Incubate at 37°C, 150 rpm checking the OD $_{600\ nm}$ every hour until the value is 0.5 (usually, it needs 4 h)
- Move the *E. coli* culture on ice to stop the growth
- Combine 50 mL of the culture with 50 mL of glycerol 50%
- Split the final volume in microtubes, 1 mL each
- Snap freeze with liquid nitrogen if possible

Store in the -80°C freezer

Step 3 – Growth and IPTG induction

Prepare 1 L of nutrient broth No. 2 (NB2) solution in DIW using:

✓ Nutrient Broth No. 2 by OXOID CM0067

➢ 25 g of NB2 powder per L → 25 g of NB2 for 1 L of NB2 solution

- Stir in a 2.0 L beaker until dissolved
- Add 500 mL of NB2 solution to 2 × 2.0 L conical flasks
- Add sponge to seal conical flask and top and foil
- Add autoclave tape to conical flasks
- Label: Quantity, contents, date, initials
- Autoclave at 120°C for 20 min
- Add 500 µL of ampicillin $_{50\ mg\ mL}{}^{-1}$ and 500 µL of chloramphenicol $_{35\ mg\ mL}{}^{-1}$ in each flask

- Move each tube containing 5 mL of NB2 with BL21 (DE3) pLysS pRSETa-SmPRXI prepared in **Step 1** into each flask containing 500 mL of fresh NB2 just prepared.
- Incubate at 37°C, 150 rpm checking the OD $_{600\ nm}$ every hour until the value is 0.5
- Add 500 µL of IPTG $_{1\ M}$ in each flask and let express the protein for 3–5 h at 30°C and 150 rpm
- Centrifuge at 8000 rpm (Beckman JA 10 – RCF = 11 295.1 *g*) for 30 min at 4°C
- Store the pellets in the -20°C freezer

To gain time in the purification process, it could be useful to prepare all the buffers to use in **Step 4**.

Prepare 1 L of filtered and degassed binding buffer pH 8.0 in DIW using:

✓ TRIS base (MW: 121.14 g mol^{-1}) CAS: 2020-02-12
✓ NaCl (MW: 58.44 g mol^{-1}) CAS: 7647-14-5
✓ Imidazole (MW: 68.08 g mol^{-1}) CAS: 288-32-4

- TRIS $_{30\ mM}$ + NaCl $_{0.5\ M}$ + Imidazole $_{25\ mM}$ → 3.63 g of TRIS + 29.22 g of NaCl + 1.71 g of imidazole for 1 L of binding buffer solution

Prepare 1 L of filtered and degassed Elution Buffer pH 8.0 in DIW using:

- TRIS $_{30\ mM}$ + NaCl $_{0.5\ M}$ + Imidazole $_{0.5\ M}$ → 3.63 g of TRIS + 29.22 g of NaCl + 34.04 g of imidazole for 1 L of binding buffer solution

Prepare 1 L of filtered and degassed Stripping Buffer in DIW using:

- ✓ TRIS base (MW: 121.14 g mol^{-1}) CAS: 2020-02-12
- ✓ NaCl (MW: 58.44 g mol^{-1}) CAS: 7647-14-5
- ✓ EDTA (MW: 372.24 g mol^{-1}) CAS: 6381-92-6

- TRIS $_{20\ mM}$ + NaCl $_{0.5\ M}$ + EDTA $_{50\ mM}$ → 2.42 g of TRIS + 29.22 g of NaCl + 18.61 g of EDTA for 1 L of binding buffer solution

Prepare 0.5 L of filtered and degassed $NiSO_4$ solution in DIW using:

- ✓ $NiSO_4 \cdot 6H_2O$ (MW: 262.85 g mol^{-1}) CAS: 10101-97-0

- $NiSO_{4\ 100\ mM}$ → 13.14 g of $NiSO_4$ for 0.5 L of $NiSO_4$ solution

Prepare 1 L of filtered and degassed EtOH 20%

Prepare 1 L of filtered and degassed H_2O

Note: *Filter every solution using a 0.45 or 0.22 µm filter and degas.*

Step 4 – Sonication and purification

Defrost frozen pellets and resuspend each one in the binding buffer to have a final volume of 30-40 mL.

Add to the sample:

- ✓ Triton X100 (MW: 647.00 g mol^{-1}) CAS: 9002-93-1

- Triton X100 → 35 µL of Triton X100 for 35 mL of sample

- Sonication with a pulse to do not overheat the solution until it looks homogeneous
- Split the sonicated sample in an appropriate number of ultracentrifuge tubes
- Centrifuge at 12 500 RCF, 4°C for 30 min
- Discard pellet and collect in one tube all the supernatants

During centrifugation is necessary to prepare the HisTrap column for the elution.

Note: *If it is not possible to perform the purification the same day, ad protease inhibitor and store in the fridge (2 days max).*

The HisTrap column should be found stored at 4°C in EtOH 20% and stripped (column coloured in white, it means that there is no nickel attached on the resin), to equilibrate it for the purification, let pass through the column (manually or with an FPLC system):

- H_2O (5 column volumes)
- $NiSO_4$ (5 column volumes) (column coloured in green)
- H_2O (5 column volumes)
- Binding buffer (5 column volumes) (column coloured in blue)

- Load the sample into the HisTrap column manually with a 10 or 20 mL syringe
- Set up the FPLC and follow the signal at 280 nm (If possible follow also 230–393 nm)
- Equilibrate the system passing through the column binding buffer
- Run the elution program (10 mL binding – gradient from 0% to 100% of elution buffer in 100 mL)
- When the elution program has finished, collect and merge the fraction tubes corresponding to the peak in the 280 nm signal (the correct peak should come between 60–90% of elution buffer)
- Store the sample in the fridge at 4°C

Step 5 – Concentration, dya-filtration and UV-Vis analysis

Concentration and dya-filtration of SmPRXI with Centricon tubes (Millipore):

- Split the eluted sample from the fraction tubes corresponding to the area of the elution peak in an appropriate number of Centricon tubes (4 mL or 15 mL by Millipore)
- Fill the Centricon with the buffer you want to move the protein in and spin at 3 000 RCF for 20–30 min depending on how much solution goes through the filter

  Example: *If you are using 4 mL Centricon, your start volume is 4 ml. After 30 min at 3000 RCF if the volume to filter is still around 4 mL try to spin for longer*
- With a UV-Vis spectrophotometer, measure the absorbance spectrum from 230 nm to 600 nm and calculate the sample concentration (for a good estimation of the concentration, remember to dilute the sample if the measured absorbance exceeds 1, it should be between 0.1 and 1)
- Store the purified SmPRXI in the fridge at 4°C using an appropriate tube depending on the final volume
- To store the SmPRXI for longer periods is better to add 25% glycerol and move the samples in the -20°C (6 months) or the -80°C freezer (more than 6 months) depending on the storage time.

Step 6 – Results

To confirm that the purification was successful, it is necessary to prepare SDS-PAGE

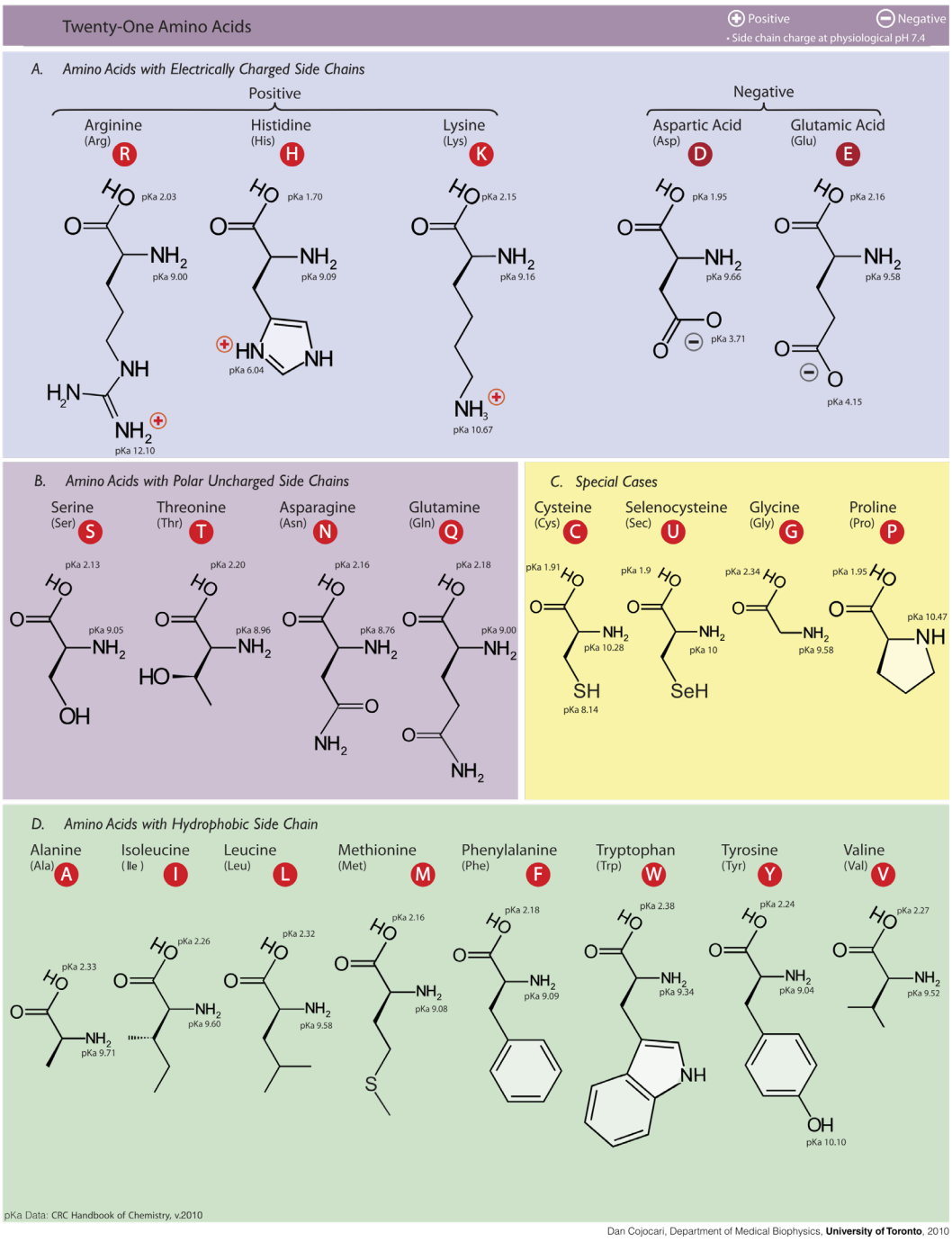
The main things to know are:

- 12% polyacrylamide gel
- A marker that can match 25 kDa (that is the molecular weight of a monomer)
- Protein concentration in reducing buffer around 0.4–0.5 mg mL^{-1} (monomer)

Results table	
E. coli stock used	
Dilution Factor	
Absorbance of dilution at 280 nm	
New stock concentration (mg mL^{-1})	
New stock volume (mL)	
SmPRXI molar extinction coefficient (ε)	1.00 cm^2 mg^{-1}
SmPRXI molar extinction coefficient (ε)	19 075 M^{-1} cm^{-1}
SmPRXI – monomer Molecular Weight (MW)	21 043.03 Da (21 kDa)
SmPRXI – decamer Molecular Weight (MW)	210 430.3 Da (21 kDa)
SmPRXI-His molar extinction coefficient (ε)	1.03 cm^2 mg^{-1}
SmPRXI-His molar extinction coefficient (ε)	26 065 M^{-1} cm^{-1}
SmPRXI-His – monomer Molecular Weight (MW)	25 273.5 Da (25 kDa)
SmPRXI-His – decamer Molecular Weight (MW)	252 735.0 Da (250 kDa)

Appendix 11

Amino acids classification table





UNIVERSITY OF
BIRMINGHAM

REFERENCES

Paolo Passaretti

1. Ratner, M. & Ratner, D. Nanotechnology: A Gentle Introduction to the Next Big Idea. *Mater. Today* **6**, 50 (2003).
2. Wen, A. M., Podgornik, R., Strangi, G. & Steinmetz, N. F. Photonics and Plasmonics go Viral: Self-Assembly of Hierarchical Metamaterials. *Rend. Lincei* **26**, 129–141 (2015).
3. Liu, Z., Qiao, J., Niu, Z. & Wang, Q. Natural Supramolecular Building Blocks: From Virus Coat Proteins to Viral Nanoparticles. *Chem. Soc. Rev.* **41**, 6178–6194 (2012).
4. Fischlechner, M. & Donath, E. Viruses as Building Blocks for Materials and Devices. *Angew. Chemie - Int. Ed.* **46**, 3184–3193 (2007).
5. Flynn, C. E., Lee, S. W., Peelle, B. R. & Belcher, A. M. Viruses as Vehicles for Growth, Organization and Assembly of Materials. *Acta Mater.* **51**, 5867–5880 (2003).
6. Douglas, T. & Young, M. Virus Particles as Templates for Materials Synthesis. *Adv. Mater.* **11**, 679–681 (1999).
7. Baltimore, D. Expression of Animal Virus Genomes. *Bacteriol. Rev.* **35**, 235–41 (1971).
8. Henry, M. & Debarbieux, L. Tools from Viruses: Bacteriophage Successes and Beyond. *Virology* **434**, 151–161 (2012).
9. Wen, A. M. & Steinmetz, N. F. Design of Virus-Based Nanomaterials for Medicine, Biotechnology, and Energy. *Chem. Soc. Rev.* **45**, 4074–4126 (2016).
10. Mohan, K. & Weiss, G. A. Chemically Modifying Viruses for Diverse Applications. *ACS Chem. Biol.* **11**, 1167–1179 (2016).
11. Domingo-Calap, P., Georgel, P. & Bahram, S. Back to the Future: Bacteriophages as Promising Therapeutic Tools. *Hla* **87**, 133–140 (2016).
12. Fagbohun, O. A. *Bacteriophage Fusion Peptides Based Targeted Delivery of Therapeutics to Cancer Cells*. *Afr. J. Biomed. Res* vol. 21 www.ajbrui.org (2018).
13. Lam, P. & Steinmetz, N. F. Plant Viral and Bacteriophage Delivery of Nucleic acid Therapeutics. *Wiley Interdiscip. Rev. Nanomedicine Nanobiotechnology* **10**, 1–18 (2018).
14. Wu, C. H., Liu, I. J., Lu, R. M. & Wu, H. C. Advancement and Applications of Peptide Phage Display Technology in Biomedical Science. *J. Biomed. Sci.* **23**, 1–14 (2016).
15. Lemoine, E. & Thadhani, R. Phage Display: An Overview in Context to Drug Discovery. *Trends Pharmacol. Sci.* **40**, 87–91 (2019).
16. Li, K., Nguyen, H. G., Lu, X. & Wang, Q. Viruses and Their Potential in Bioimaging and Biosensing Applications. *Analyst* **135**, 21–27 (2010).
17. Moon, J. S. *et al.* Recent Progress of M13 Virus-Based Chemical and Biological Sensing. *Toxicol. Environ. Health Sci.* **7**, 251–261 (2015).
18. Cui, Y. Engineered Phages for Electronics. *Biosens. Bioelectron.* **85**, 964–976 (2016).
19. Yuan, H., Lei, T., Qin, Y., He, J.-H. & Yang, R. Design and Application of Piezoelectric Biomaterials. *J. Phys. D. Appl. Phys.* **52**, 194002 (2019).
20. Sanghamitra, N. J. M., Inaba, H., Kitagawa, S. & Ueno, T. Inorganic Design of Protein Assemblies as Supramolecular Platforms. *J. Inorg. Organomet. Polym. Mater.* **23**, 50–60 (2013).
21. Messing, J. *New M13 Vectors for Cloning*. *Methods in Enzymology* vol. 101 (1979).
22. Smith, G. P. Filamentous Fusion Phage: Novel Expression Vectors that Display Cloned Antigens on the Virion Surface. *Science* **228**, 1315–1317 (1985).
23. Smith, G. P. & Petrenko, V. A. Phage Display. *Chem. Rev.* **97**, 391–410 (1997).
24. Merzlyak, A. & Lee, S. W. Phage as Templates for Hybrid Materials and Mediators for Nanomaterial Synthesis. *Curr. Opin. Chem. Biol.* **10**, 246–252 (2006).
25. Lee, S. Y., Lim, J. S. & Harris, M. T. Synthesis and Application of Virus-Based Hybrid

Nanomaterials. *Biotechnol. Bioeng.* **109**, 16–30 (2012).

26. Yang, S. H., Chung, W. J., McFarland, S. & Lee, S. W. Assembly of Bacteriophage into Functional Materials. *Chem. Rec.* **13**, 43–59 (2013).

27. Jo, W., Cheang, U. K. & Kim, M. J. Development of Flagella Bio-Templated Nanomaterials for Electronics. *Nano Converg.* **1**, 10 (2014).

28. Vilona, D. *et al.* Viral Nano-Hybrids for Innovative Energy Conversion and Storage Schemes. *J. Mater. Chem. B* **3**, 6718–6730 (2015).

29. Kim, D., Gu, M., Park, M., Kim, T. & Kim, B.-S. Layer-By-Layer Assembly for Photoelectrochemical Nanoarchitectonics. *Mol. Syst. Des. Eng.* **4**, 65–77 (2019).

30. Yoo, S. Y., Merzlyak, A. & Lee, S. W. Synthetic Phage for Tissue Regeneration. *Mediators Inflamm.* **2014**, 1–11 (2014).

31. Bryksin, A. V., Brown, A. C., Baksh, M. M., Finn, M. G. & Barker, T. H. Learning from Nature - Novel Synthetic Biology Approaches for Biomaterial Design. *Acta Biomater.* **10**, 1761–1769 (2014).

32. Hwang, I. Virus Outbreaks in Chemical and Biological Sensors. *Sensors (Switzerland)* **14**, 13592–13612 (2014).

33. Moon, J.-S. *et al.* M13 Bacteriophage-Based Self-Assembly Structures and Their Functional Capabilities. *Mini. Rev. Org. Chem.* **12**, 271–281 (2015).

34. Peltomaa, R., López-Perolio, I., Benito-Peña, E., Barderas, R. & Moreno-Bondi, M. C. Application of Bacteriophages in Sensor Development. *Anal. Bioanal. Chem.* **408**, 1805–1828 (2016).

35. Passaretti, P. *et al.* Multifunctional Graphene Oxide-Bacteriophage Based Porous Three-Dimensional Micro-Nanocomposites. *Nanoscale* **11**, 13318–13329 (2019).

36. Chabot, V. *et al.* A Review of Graphene and Graphene Oxide Sponge: Material Synthesis and Applications to Energy and the Environment. *Energy Environ. Sci.* **7**, 1564 (2014).

37. Ardini, M. *et al.* Metal-induced self-assembly of peroxiredoxin as a tool for sorting ultrasmall gold nanoparticles into one-dimensional clusters. *Nanoscale* **6**, 8052 (2014).

38. Ardini, M. *et al.* Supramolecular Self-Assembly of Graphene Oxide and Metal Nanoparticles Into Stacked Multilayers by Means of a Multitasking Protein Ring. *Nanoscale* **8**, 6739–6753 (2016).

39. Giovannini, G. *et al.* Chemically-controlled Self-assembly of Hybrid Plasmonic Nanopores on Graphene. (2019).

40. Marvin, D. A. & Hoffmann-Berling, H. Physical and Chemical Properties of Two New Small Bacteriophages. *Nat. Publ. Gr.* **4866**, 517–518 (1963).

41. van Wezenbeek, P. M. G. F. G. F., Hulsebos, T. J. M. M. & Schoenmakers, J. G. G. G. Nucleotide Sequence of the Filamentous Bacteriophage M13 DNA Genome: Comparison with Phage fd. *Gene* **11**, 129–148 (1980).

42. Beck, K. & Duenk, R. M. Flexibility of Bacteriophage M13: Comparison of Hydrodynamic Measurements with Electron Microscopy. *J. Struct. Biol.* **105**, 22–27 (1990).

43. Marvin, D. A. & Hohn, B. Filamentous Bacterial Viruses. *Bacteriol. Rev.* **33**, 172–209 (1969).

44. Ray, D. S., Preuss, A. & Hofschneider, P. H. Replication of the Single-Stranded DNA of the Male-Specific Bacteriophage M13: Circular Forms of the Replicative DNA. *J. Mol. Biol.* **21**, 485–488 (1966).

45. Rakonjac, J., Bennett, N. J., Spagnuolo, J., Gagic, D. & Russel, M. Filamentous Bacteriophage: Biology, Phage Display and Nanotechnology Applications. *Curr. Issues Mol. Biol.* **13**, 51–76 (2011).

46. Van Den Hondel, C. A., Weijers, A., Konings, R. N. H. & Schoenmakers, J. G. G. Studies on Bacteriophage M13 DNA: 2. The Gene Order of the M13 Genome. *Eur. J. Biochem.* **53**, 559–567 (1975).

47. Berkowitz, S. A. & Day, L. A. Mass, Length, Composition and Structure of the Filamentous Bacterial Virus fd. *J. Mol. Biol.* **102**, 531–547 (1976).

48. Ploss, M. & Kuhn, A. Kinetics of Filamentous Phage Assembly. *Phys. Biol.* **7**, 1–8 (2010).

49. Warner, C. M., Barker, N., Lee, S. W. & Perkins, E. J. M13 Bacteriophage Production for Large-Scale Applications. *Bioprocess Biosyst. Eng.* **37**, 2067–2072 (2014).

50. Grieco, S.-H. H., Wong, A. Y. K., Dunbar, W. S., MacGillivray, R. T. A. & Curtis, S. B. Optimization of Fermentation Parameters in Phage Production Using Response Surface Methodology. *J. Ind. Microbiol. Biotechnol.* **39**, 1515–1522 (2012).

51. Tzagoloff, H. & Pratt, D. The Initial Steps in Infection with Coliphage M13. *Virology* **24**, 372–380 (1964).

52. Salivar, W. O., Tzagoloff, H. & Pratt, D. Some Physical-Chemical and Biological Properties of the Rod-Shaped Coliphage M13. *Virology* **24**, 359–371 (1964).

53. Mardis, E. R. High-Throughput Detergent Extraction of M13 Subclones for Fluorescent DNA Sequencing. *Nucleic Acids Res.* **22**, 2173–2175 (1994).

54. Kick, B., Hensler, S., Praetorius, F., Dietz, H. & Weuster-Botz, D. Specific Growth Rate and Multiplicity of Infection Affect High-Cell-Density Fermentation with Bacteriophage M13 for ssDNA Production. *Biotechnol. Bioeng.* **114**, 777–784 (2017).

55. Pratt, D. Genetics of Single-Stranded DNA Bacteriophages. *Annu. Rev. Genet.* **3**, 343–362 (1969).

56. Mai-Prochnow, A. *et al.* Big Things in Small Packages: The Genetics of Filamentous Phage and Effects on Fitness of Their Host. *FEMS Microbiol. Rev.* **39**, 465–487 (2015).

57. Barderas, R. & Benito-Peña, E. The 2018 Nobel Prize in Chemistry: Phage Display of Peptides and Antibodies. *Anal. Bioanal. Chem.* (2019) doi:10.1007/s00216-019-01714-4.

58. Hofschneider, P. H. Untersuchungen über 'kleine' E. coli K 12 Bakteriophagen. *Z. Naturforschg* **18b**, 203–210 (1963).

59. O'Callaghan, R., Bradley, R. & Paranchych, W. The Effect of M13 Phage Infection Upon the F Pili of E. coli. *Virology* **54**, 220–229 (1973).

60. Vajda, B. P. Concentration and Purification of Viruses and Bacteriophages with Polyethylene Glycol. *Folia Microbiol. (Praha).* **23**, 88–96 (1978).

61. Hewitt, J. A. Miniphage: A Class of Satellite Phage to M13. *J. Gen. Virol.* **26**, 87–94 (1975).

62. Griffith, J. & Kornberg, A. Mini M13 Bacteriophage: Circular Fragments of M13 DNA are Replicated and Packaged During Normal Infections. *Virology* **59**, 139–152 (1974).

63. Griffith, J. D., Hester, S. & El Saidy, S. A Duplex Structure Involving Two Non-Complementary DNA Strands can be Formed and Stabilized by M13 Phage Proteins. *J. Mol. Biol.* **157**, 321–330 (1982).

64. Manning, M., Chrysogelos, S. & Griffith, J. Mechanism of Coliphage M13 Contraction: Intermediate Structures Trapped at Low Temperatures. *J. Virol.* **40**, 912–919 (1981).

65. Manning, M., Moore, M., Spremulli, L. & Griffith, J. Coat Protein Conformation in M13 Filaments, I-Forms and Spheroids. *Biochem. Biophys. Res. Commun.* **112**, 349–355 (1983).

66. Manning, M. & Griffith, J. Association of M13 I-Forms and Spheroids with Lipid Vesicles. *Arch. Biochem. Biophys.* **236**, 297–303 (1985).

67. Smith, H. O. & Welcox, K. W. A Restriction Enzyme from Hemophilus influenzae. *J. Mol. Biol.* **51**, 379–391 (1970).

68. Wickner, W., Mandel, G., Zwizinski, C., Bates, M. & Killick, T. Synthesis of Phage M13 Coat Protein and its Assembly into Membranes in vitro. *Proc. Natl. Acad. Sci.* **75**, 1754–1758 (1978).

69. Sidhu, S. S. Engineering M13 for Phage Display. *Biomol. Eng.* **18**, 57–63 (2001).

70. Whaley, S. R., English, D. S., Hu, E. L., Barbara, P. F. & Belcher, A. M. Selection of Peptides with

Semiconductor Binding Specificity for Directed Nanocrystal Assembly. *Lett. to Nat.* **405**, 665–668 (2000).

71. Krumpe, L. R. H. & Mori, T. The Use of Phage-Displayed Peptide Libraries to Develop Tumor-Targeting Drugs. *Int. J. Pept. Res. Ther.* **12**, 79–91 (2006).

72. Länge, K., Rapp, B. E. & Rapp, M. Surface Acoustic Wave Biosensors: A Review. *Anal. Bioanal. Chem.* **391**, 1509–1519 (2008).

73. Seker, U. O. S. & Demir, H. V. Material Binding Peptides for Nanotechnology. *Molecules* **16**, 1426–1451 (2011).

74. Ma, Y., Nolte, R. J. M. & Cornelissen, J. J. L. M. Virus-Based Nanocarriers for Drug Delivery. *Adv. Drug Deliv. Rev.* **64**, 811–825 (2012).

75. Zhi, D., Ling, Z. & Xuemei, M. Application of M13 Phage Coat Proteins. *Agric. Biotechnol.* **2**, 45–47 (2013).

76. Chung, W. J., Lee, D. Y. & Yoo, S. Y. Chemical Modulation of M13 Bacteriophage and its Functional Opportunities for Nanomedicine. *Int. J. Nanomedicine* **9**, 5825–5836 (2014).

77. Wang, L., Sun, Y., Li, Z., Wu, A. & Wei, G. Bottom-up Synthesis and Sensor Applications of Biomimetic Nanostructures. *Materials (Basel).* **9**, 2–28 (2016).

78. Chen, J. *et al.* Early detection of Alzheimer's disease by peptides from phage display screening. *Brain Res.* **1721**, 146306 (2019).

79. Liu, A., Anfossi, L., Shen, L., Li, C. & Wang, X. Non-Competitive Immunoassay for Low-Molecular-Weight Contaminant Detection in Food, Feed and Agricultural Products: A Mini-Review. *Trends Food Sci. Technol.* **71**, 181–187 (2018).

80. Yan, J., Shi, Q., You, K., Li, Y. & He, Q. Phage Displayed Mimotope Peptide-Based Immunosensor for Green and Ultrasensitive Detection of Mycotoxin Deoxynivalenol. *J. Pharm. Biomed. Anal.* **168**, 94–101 (2019).

81. Sharma, R. S., Karmakar, S., Kumar, P. & Mishra, V. Application of Rilamentous Phages in Environment: A Tectonic Shift in the Science and Practice of Ecorestoration. *Ecol. Evol.* **9**, 2263–2304 (2018).

82. Sioud, M. Phage Display Libraries: From Binders to Targeted Drug Delivery and Human Therapeutics. *Mol. Biotechnol.* **61**, 286–303 (2019).

83. Prisco, A. & de Berardinis, P. Filamentous Bacteriophage Fd as an Antigen Delivery System in Vaccination. *Int. J. Mol. Sci.* **13**, 5179–5194 (2012).

84. Konings, R. N. H., Folmer, R. H. A., Folkers, P. J. M., Nilges, M. & Hilbers, C. W. Three-Dimensional Structure of the Single-Stranded DNA-Binding Protein Encoded by Gene V of the Filamentous Bacteriophage M13 and a Model of its Complex with Single-Stranded DNA. *FEMS Microbiol. Rev.* **17**, 57–72 (1995).

85. Marciano, D. K., Marjorie, R. & Sanford, S. M. An Aqueous Channel for Filamentous Phage Export. *Science (80-.).* **284**, 1516–1519 (1999).

86. Alma, N. C. M., Harmsen, B. J. M., de Jong, E. A. M., Ven, J. v.d. & Hilbers, C. W. Fluorescence Studies of the Complex Formation Between the Gene 5 Protein of Bacteriophage M13 and Polynucleotides. *J. Mol. Biol.* **163**, 47–62 (1983).

87. Bulsink, H., Harmsen, B. J. M., Hilbers, C. W. & Wijnaendts van Resandt, R. W. Different DNA-Binding Modes and Cooperativities for Bacteriophage M13 Gene-5 protein Revealed by Means of Fluorescence Depolarisation Studies. *Eur. J. Biochem.* **157**, 329–334 (1986).

88. Stassen, A. P. M., Harmsen, B. J. M., Schoenmakers, J. G. G., Hilbers, C. W. & Konings, R. N. H. Fluorescence Studies of the Binding of Bacteriophage M13 Gene V Mutant Proteins to Polynucleotides. *Eur. J. Biochem.* **206**, 605–612 (1992).

89. Stassen, A. P. M., Zaman, G. J. R., van Deursen, J. M. A., Schoenmakers, J. G. G. & Konings, R. N. H. Selection and Characterization of Randomly Produced Mutants of Gene V Protein of

Bacteriophage M13. *Eur. J. Biochem.* **204**, 1003–1014 (1992).

90. Bulsink, H., Harmsen, B. J. M. & Hilbers, C. W. DNA-Binding Properties of Gene-5 Protein Encoded by Bacteriophage M13: 2. Further Characterization of the Different Binding Modes for Poly- and Oligodeoxynucleic Acids. *Eur. J. Biochem.* **176**, 597–608 (1988).

91. Løset, G. Å. & Sandlie, I. Next Generation Phage Display by Use of pVII and pIX as Display Scaffolds. *Methods* **58**, 40–46 (2012).

92. Hunter, G. J., Rowitch, D. H. & Perham, R. N. Interactions between DNA and Coat Protein in the Structure and Assembly of Filamentous Bacteriophage fd. *Lett. to Nat.* **327**, 252–254 (1987).

93. Pratt, D., Tzagoloff, H. & Beaudoin, J. Conditional Lethal Mutants of the Small Filamentous Coliphage M13: II. Two Genes for Coat Proteins. *Virology* **39**, 42–53 (1969).

94. Samuelson, J. C. *et al.* Function of YidC for the Insertion of M13 Procoat Protein in Escherichia coli: Translocation of Mutants that Show Differences in their Membrane Potential Dependence and Sec Requirement. *J. Biol. Chem.* **276**, 34847–34852 (2001).

95. Stiegler, N., Dalbey, R. E. & Kuhn, A. M13 Procoat Protein Insertion Into YidC and SecYEG Proteoliposomes and Liposomes. *J. Mol. Biol.* **406**, 362–370 (2011).

96. Ohkawa, I. & Webster, R. E. The Orientation of the Major Coat Protein of Bacteriophage f1 in the Cytoplasmic Membrane of Escherichia coli. *J. Biol. Chem.* **256**, 9951–9958 (1981).

97. Papavoine, C. H. M. M., Christiaans, B. E. C. C., Folmer, R. H. A. A., Konings, R. N. H. H. & Hilbers, C. W. Solution Structure of the M13 Major Coat Protein in Detergent Micelles: A Basis for a Model of Phage Assembly Involving Specific Residues. *J. Mol. Biol.* **282**, 401–419 (1998).

98. Russel, M. & Model, P. Filamentous Phage Pre-coat is an Integral Membrane Protein: Analysis by a new Method of Membrane Preparation. *Cell* **28**, 177–184 (1982).

99. Malik, P. *et al.* Role of Capsid Structure and Membrane Protein Processing in Determining the Size and Copy Number of Peptides Displayed on the Major Coat Protein of Filamentous Bacteriophage. *J. Mol. Biol.* **260**, 9–21 (1996).

100. Iannolo, G., Minenkova, O., Petruzzelli, R. & Cesareni, G. Modifying Filamentous Phage Capsid: Limits in the Size of the Major Capsid Protein. *J. Mol. Biol.* **248**, 835–844 (1995).

101. Hofschneider, P. H. & Preuss, A. M13 Bacteriophage Liberation From Intact Bacteria as Revealed by Electron Microscopy. *J. Mol. Biol.* **7**, 450–451 (1963).

102. Smeal, S. W., Schmitt, M. A., Pereira, R. R., Prasad, A. & Fisk, J. D. Simulation of the M13 Life Cycle I: Assembly of a Genetically-Structured Deterministic Chemical Kinetic Simulation. *Virology* **500**, 259–274 (2017).

103. Marvin, D. A. Filamentous Phage Structure, Infection and Assembly. *Curr. Opin. Struct. Biol.* **8**, 150–158 (1998).

104. Stopar, D., Spruijt, R. B., Wolfs, C. J. A. M. & Hemminga, M. A. Protein-Lipid Interactions of Bacteriophage M13 Major Coat Protein. *Biochim. Biophys. Acta - Biomembr.* **1611**, 5–15 (2003).

105. Houbiers, M. C. & Hemminga, M. A. Protein-Lipid Interactions of Bacteriophage M13 Gene 9 Minor Coat Protein. *Mol. Membr. Biol.* **21**, 351–359 (2004).

106. Loh, B., Kuhn, A. & Leptihn, S. The Fascinating Biology Behind Phage Display: Filamentous Phage Assembly. *Mol. Microbiol.* **111**, 1132–1138 (2019).

107. Caro, L. G. & Schnös, M. The Aattachment of the Male-Specific Bacteriophage f1 to Sensitive Strains of Escherichia coli. *Proc. Natl. Acad. Sci.* **56**, 126–132 (1966).

108. Meynell, E., Meynell, G. G. & Datta, N. Phylogenetic Relationships of Drug-Resistance Factors and Other Transmissible Bacterial Plasmids. *Bacteriol. Rev.* **32**, 55–83 (1968).

109. Meynell, G. G. & Lawn, A. M. Filamentous Phages Specific for the I Sex Factor. *Nature* **217**, 1184–1186 (1968).

110. Hsu, Y. C. Propagation or Elimination of Viral Infection in Carrier Cells. *Bacteriol. Rev.* **32**, 387–

38799 (1968).

111. Trenkner, E., Bonhoeffer, F. & Gierer, A. *The Fate of the Protein Component of Bacteriophage fd During Infection*. vol. 28 (1967).

112. Frost, L. S. Conjugative Pili and Pilus-Specific Phages. in *Bacterial Conjugation* 189–221 (Springer US, 1993). doi:10.1007/978-1-4757-9357-4_7.

113. Stengele, I., Bross, P., Garces, X., Giray, J. & Rasched, I. Dissection of Functional Domains in Phage fd Adsorption Protein. *J. Mol. Biol.* **212**, 143–149 (2004).

114. Rakonjac, J., Feng, J. nong & Model, P. Filamentous Phage are Released from the Bacterial Membrane by a Two-Step Mechanism Involving a Short C-Terminal Fragment of pIII. *J. Mol. Biol.* **289**, 1253–1265 (1999).

115. Deng, L.-W. & Perham, R. N. Delineating the Site of Interaction on the pIII Protein of Filamentous Bacteriophage fd with the F-pilus of Escherichia coli. *J. Mol. Biol.* **319**, 603–614 (2002).

116. Zenkin, N., Naryshkina, T., Kuznedelov, K. & Severinov, K. The Mechanism of DNA Replication Primer Synthesis by RNA Polymerase. *Nature* **439**, 617–620 (2006).

117. Kim, M. H., Hines, J. C. & Ray, D. S. Viable Deletions of the M13 Complementary Strand Origin. *Proc. Natl. Acad. Sci.* **78**, 6784–6788 (1981).

118. Pratt, D., Tzagoloff, H. & Erdahl, W. S. Conditional Lethal Mutants of the Small Filamentous Coliphage M13. *Virology* **30**, 397–410 (1966).

119. Asano, S., Higashitani, A. & Horiuchi, K. Filamentous Phage Replication Initiator Protein GPII Forms a Covalent Complex with the 5' end of the Nick it Introduced. *Nucleic Acids Res.* **27**, 1882–1889 (1999).

120. Greenstein, D., Zinder, N. D. & Horiuchi, K. Integration Host Factor Interacts with the DNA Replication Enhancer of Filamentous Phage f1. *Proc. Natl. Acad. Sci.* **85**, 6262–6266 (1988).

121. Horiuchi, K. Initiation Mechanisms in Replication of Filamentous Phage DNA. *Genes to Cells* **2**, 425–432 (1997).

122. Russel, M. Protein-protein Interactions During Filamentous Phage Assembly. *J. Mol. Biol.* **231**, 689–697 (1993).

123. Makowski, L. Structural Constraints on the Display of Foreign Peptides on Filamentous Bacteriophages (Display Vectors; Virus Structure and Assembly; Escherichia coli Phage M13; Pseudomonas Phage Pf1; X-ray Diffraction). *Gene* **128**, 5–11 (1993).

124. Nambudripad, R., Stark, W., Opella, S. J. & Makowski, L. Membrane-Mediated Assembly of Filamentous Bacteriophage Pf1 Coat Protein. *Science (80-.).* **252**, 1305–1308 (1991).

125. Shon, K., Kim, Y., Colnago, L. & Opella, S. NMR Studies of the Structure and Dynamics of Membrane-Bound Bacteriophage Pf1 Coat Protein. *Science (80-.).* **252**, 1303–1305 (1991).

126. Russel, M. Filanmentous Phage Assembly. *Mol. Microbiol.* **5**, 1607–1613 (1991).

127. Guy-Caffey, J. K., Rapoza, M. P., Jolley, K. A. & Webster, R. E. Membrane Localization and Topology of a Viral Assembly Protein. *J. Bacteriol.* **174**, 2460–2465 (1992).

128. Feng, J., Model, P. & Russel, M. A Trans-Envelope Protein Complex Needed for Filamentous Phage Assembly and Export. *Mol. Microbiol.* **34**, 745–755 (1999).

129. Russel, M. Moving Through the Membrane with Filamentous Phages. *Trends Microbiol.* **3**, 223–228 (1995).

130. Loh, B., Haase, M., Mueller, L., Kuhn, A. & Leptihn, S. The Transmembrane Morphogenesis Protein gp1 of Filamentous Phages Contains Walker a and Walker B Motifs Essential for Phage Assembly. *Viruses* **9**, 1–12 (2017).

131. Machida, K. & Imataka, H. Production Methods for Viral Particles. *Biotechnol. Lett.* **37**, 753–760 (2015).

132. Konings, R. N. H. Synthesis of Phage M13 Specific Proteins in a DNA-Dependent Cell-Free System. *FEBS Lett.* **35**, 155–160 (1973).

133. Konings, R. N. H., Jansen, J., Cuypers, T. & Schoenmakers, J. G. G. Synthesis of Bacteriophage M13-Specific Proteins in a DNA-Dependent Cell-Free System II. In vitro Synthesis of Biologically Active Gene 5 Protein. *J. Virol.* **12**, 1466–1472 (1973).

134. Konings, R. N. H., Hulsebos, T. & Van Den Hondel, C. A. Identification and Characterization of the in vitro Synthesized Gene Products of Bacteriophage M13. *J. Virol.* **15**, 570–584 (1975).

135. Wickner, W. & Killick, T. Membrane-Associated Assembly of M13 Phage in Extracts of Virus-Infected Escherichia coli. *Proc. Natl. Acad. Sci.* **74**, 505–509 (1977).

136. Maier, R. M. Bacterial Growth. in *Environmental Microbiology* 37–54 (Academic Press, 2009). doi:10.1016/B978-0-12-370519-8.00003-1.

137. Green, M. R. & Sambrook, J. Growing Bacteriophage M13 in Liquid Culture. *Cold Spring Harb. Protoc.* **2017**, pdb.prot093435 (2017).

138. Grieco, S. H. H., Lee, S., Dunbar, W. S., MacGillivray, R. T. A. & Curtis, S. B. Maximizing Filamentous Phage Yield During Computer-Controlled Fermentation. *Bioprocess Biosyst. Eng.* **32**, 773–779 (2009).

139. Kick, B., Praetorius, F., Dietz, H. & Weuster-Botz, D. Efficient Production of Single-Stranded Phage DNA as Scaffolds for DNA Origami. *Nano Lett.* **15**, 4672–4676 (2015).

140. Kick, B., Behler, K. L., Severin, T. S. & Weuster-Botz, D. Chemostat Studies of Bacteriophage M13 Infected Escherichia coli JM109 for cCntinuous ssDNA Production. *J. Biotechnol.* **258**, 92–100 (2017).

141. Atha, D. H. & Inghamg, K. C. Mechanism of Precipitation of Proteins by Polyethylene Glycols. *J. Biol. Chem.* **256**, 12108–12117 (1981).

142. Reitinger, S., Petriv, O. I., Mehr, K., Hansen, C. L. & Withers, S. G. Purification and Quantitation of Bacteriophage M13 Using Desalting Spin Columns and Digital PCR. *J. Virol. Methods* **185**, 171–174 (2012).

143. McClendon, J. H. The Osmotic Pressure of Concentrated Solutions of Polyethylene Glycol 6000, and its Variation with Temperature. *J. Exp. Bot.* **32**, 861–866 (1981).

144. Beaudoin, J., Henry, T. J. & Pratt, D. Purification of Single- and Double-Length M13 Virions by Polyacrylamide Gel Electrophoresis. *J. Virol.* **13**, 470–7 (1974).

145. Beaudoin, J. & Pratt, D. Antiserum Inactivation of Electrophoretically Purified M13 Diploid Virions: Model for the F-Specific Filamentous Bacteriophages. *J. Virol.* **13**, 466–469 (1974).

146. Salivar, W. O., Henry, T. J. & Pratt, D. Purification and Properties of Diploid Particles of Coliphage M13. *Virology* **32**, 41–51 (1967).

147. Ling, T. C. *et al.* Purification of Filamentous Bacteriophage M13 by Expanded Bed Anion Exchange Chromatography. *J. Microbiol.* **42**, 228–32 (2004).

148. Monjezi, R., Tey, B. T., Sieo, C. C. & Tan, W. S. Purification of Bacteriophage M13 by Anion Exchange Chromatography. *J. Chromatogr. B Anal. Technol. Biomed. Life Sci.* **878**, 1855–1859 (2010).

149. Zakharova, M. Y. *et al.* Purification of Filamentous Bacteriophage for Phage Display Using Size-Exclusion Chromatography. *Biotechniques* **38**, 194–198 (2005).

150. Smrekar, F., Ciringer, M., Štrancar, A. & Podgornik, A. Characterisation of Methacrylate Monoliths for Bacteriophage Purification. *J. Chromatogr. A* **1218**, 2438–2444 (2011).

151. Tang, J. X., Janmey, P. A., Lyubartsev, A. & Nordenskiöld, L. Metal Ion-Induced Lateral Aggregation of Filamentous Viruses fd and M13. *Biophys. J.* **83**, 566–581 (2002).

152. González-Mora, A., Ruiz-Ruiz, F., Benavides, J. & Rito-Palomares, M. Improved Recovery of Bacteriophage M13 Using an ATPS-Based Bioprocess. *Biotechnol. Prog.* **34**, 1177–1184 (2018).

153. Yamamoto, K. R., Alberts, B. M., Benzinger, R., Lawhorne, L. & Treiber, G. Rapid Bacteriophage Sedimentation in the Presence of Polyethylene Glycol and its Application to Large-Scale Virus Purification. *Virology* **40**, 734–744 (1970).

154. Branston, S., Stanley, E., Keshavarz-Moore, E. & Ward, J. Precipitation of Filamentous Bacteriophages for Their Selective Recovery in Primary Purification. *Biotechnol. Prog.* **28**, 129–136 (2012).

155. Dong, D., Sutaria, S., Hwangbo, J. Y. & Chen, P. A Simple and Rapid Method to Isolate Purer M13 Phage by Isoelectric Precipitation. *Appl. Microbiol. Biotechnol.* **97**, 8023–8029 (2013).

156. Zimmermann, J. *et al.* Automated Preparation and Purification of M13 Templates for DNA Sequencing. *Methods Mol. Cell. Biol.* (1989).

157. Eperon, I. C. Rapid Preparation of Bacteriophage DNA for Sequence Analysis in Sets of 96 Clones, Using Filtration. *Anal. Biochem.* (1986) doi:10.1016/0003-2697(86)90273-3.

158. Mardis, E. R. & Roe, B. A. Automated Methods for Single-Stranded DNA Isolation and Dideoxynucleotide DNA Sequencing Reactions on a Robotic Workstation. *Biotechniques* (1989).

159. Alderton, R. P. *et al.* Magnetic Bead Purification of M13 DNA Sequencing Templates. *Anal. Biochem.* **20**, 166–169 (1992).

160. Fry, G. *et al.* A New Approach to Template Purification for Sequencing Applications Using Paramagnetic Particles. *Biotechniques* (1992).

161. Hawkins, T. M13 Single-Strand Purification Using a Biotinylated Probe and Streptavidin Coated Magnetic Beads. *DNA Seq.* **3**, 65–69 (1992).

162. Wilson, R. K. High-Throughput Purification of M13 Templates for DNA Sequencing. *Biotechniques* (1993).

163. Santos, M. A. An Improved Method for the Small Scale Preparation of Bacteriophage DNA Based on Phage Precipitation by Zinc Chloride. *Nucleic Acids Res.* **19**, 5442 (1991).

164. Pelta, J., Livolant, F. & Sikorav, J. L. DNA Aggregation Induced by Polyamines and Cobalthexamine. *J. Biol. Chem.* **271**, 5656–5662 (1996).

165. Sambrook, J. & Russell, D. W. *Molecular Cloning : A Laboratory Manual, III. Red. New York: Cold Spring Harbor Laboratory Press* (2001). doi:10.3724/SP.J.1141.2012.01075.

166. Nummelin, S., Kommeri, J., Kostiainen, M. A. & Linko, V. Evolution of Structural DNA Nanotechnology. *Adv. Mater.* **30**, 1–12 (2018).

167. Bernard, J. M. L. & Francis, M. B. Chemical Strategies for the Covalent Modification of Filamentous Phage. *Front. Microbiol.* **5**, 1–7 (2014).

168. Novoselov, K. S. *et al.* Electric Field Effect in Atomically Thin Carbon Films. *Science (80-.).* **306**, 666–669 (2004).

169. Yang, M., Yao, J. & Duan, Y. Graphene and its Derivatives for Cell Biotechnology. *Analyst* **138**, 72–86 (2013).

170. Allen, M. J., Tung, V. C. & Kaner, R. B. Honeycomb Carbon: A Review of Graphene. *Chem. Rev.* **110**, 132–145 (2010).

171. Krishna, K. V., Ménard-Moyon, C., Verma, S. & Bianco, A. Graphene-Based Nanomaterials for Nanobiotechnology and Biomedical Applications. *Nanomedicine* **8**, 1669–1688 (2013).

172. Kravets, V. G. *et al.* Engineering Optical Properties of a Graphene Oxide Metamaterial Assembled in Microfluidic Channels. *Opt. Express* **23**, 867–871 (2015).

173. Shehzad, K., Xu, Y., Gao, C. & Duan, X. Three-Dimensional Macro-Structures of Two-Dimensional Nanomaterials. *Chem. Soc. Rev.* **45**, 5541–5588 (2016).

174. Mohan, V. B., Lau, K. tak, Hui, D. & Bhattacharyya, D. Graphene-Based Materials and Their Composites: A Review on Production, Applications and Product Limitations. *Compos. Part B Eng.* **142**, 200–220 (2018).

175. Ahmad, H., Fan, M. & Hui, D. Graphene Oxide Incorporated Functional Materials: A Review. *Compos. Part B Eng.* **145**, 270–280 (2018).

176. Novoselov, K. S. *et al.* Two-Dimensional Gas of Massless Dirac Fermions in Graphene. *Nature* **438**, 197 (2005).

177. Zhang, Y., Yan-Wen, T., Stormer, H. L. & Kim, P. Experimental Observation of the Quantum Hall Effect and Berry's Phase in Graphene. *Lett. to Nat.* **438**, 201–204 (2005).

178. Novoselov, K. S. *et al.* Unconventional Quantum Hall Effect and Berry's Phase of 2π in Bilayer Graphene. *Nat. Phys.* **2**, 177–180 (2006).

179. Novoselov, K. S. *et al.* Room-Temperature Quantum Hall Effect in Graphene. *Science (80-.).* **315**, 1379 (2007).

180. Georgakilas, V. *et al.* Functionalization of Graphene: Covalent and non-Covalent Approaches, Derivatives and Applications. *Chem. Rev.* **112**, 6156–6214 (2012).

181. Schedin, F. *et al.* Detection of Individual Gas Molecules Adsorbed on Graphene. *Nat. Mater.* (2007) doi:10.1038/nmat1967.

182. Lee, W. C. *et al.* Origin of Enhanced Stem Cell Growth and Differentiation on Graphene and Graphene Oxide. *ACS Nano* **5**, 7334–7341 (2011).

183. Byun, J. Emerging Frontiers of Graphene in Biomedicine. *J. Microbiol. Biotechnol.* **25**, 145–151 (2015).

184. Elias, A. L. *et al.* Longitudinal Cutting of Pure and Doped Carbon Nanotubes to form Graphitic Nanoribbons Using Metal Clusters as Nanoscalpels. *Nano Lett.* **10**, 366–372 (2010).

185. Chang, Y. *et al.* In vitro Toxicity Evaluation of Graphene Oxide on A549 Cells. *Toxicol. Lett.* (2011) doi:10.1016/j.toxlet.2010.11.016.

186. Zhao, J., Wang, Z., White, J. C. & Xing, B. Graphene in the Aquatic Environment: Adsorption, Dispersion, Toxicity and Transformation. *Environ. Sci. Technol.* **48**, 9995–10009 (2014).

187. Eda, G. & Chhowalla, M. Chemically Derived Graphene Oxide: Towards Large-Area Thin-Film Electronics and Optoelectronics. *Adv. Mater.* **22**, 2392–2415 (2010).

188. Nezakati, T., Cousins, B. G. & Seifalian, A. M. Toxicology of Chemically Modified Graphene-Based Materials for Medical Application. *Arch. Toxicol.* **88**, 1987–2012 (2014).

189. Pinto, A. M., Gonçalves, I. C. & Magalhães, F. D. Graphene-Based Materials Biocompatibility: A Review. *Colloids Surfaces B Biointerfaces* **111**, 188–202 (2013).

190. Bitounis, D., Ali-Boucetta, H., Hong, B. H., Min, D. H. & Kostarelos, K. Prospects and Challenges of Graphene in Biomedical Applications. *Adv. Mater.* **25**, 2258–2268 (2013).

191. Sutter, P. W., Flege, J. I. & Sutter, E. A. Epitaxial Graphene on Ruthenium. *Nat. Mater.* **7**, 406–411 (2008).

192. Mattevi, C., Kim, H. & Chhowalla, M. A review of Chemical Vapour Deposition of Graphene on Copper. *J. Mater. Chem.* **21**, 3324–3334 (2011).

193. Thakare, S. R., Fendarkar, D. A., Bidkar, C., Yadav, J. & Gedam, S. D. Chemical Functionalization of Graphene and Graphene Oxide - A Review. *ISSN* **5**, 1–23 (2017).

194. Wang, Y. *et al.* Conductive Graphene Oxide Hydrogels Reduced and Bridged by l-Cysteine to Support Cell Adhesion and Growth. *J. Mater. Chem. B* **5**, 511–516 (2017).

195. Chen, D., Tang, L. & Li, J. Graphene-Based Materials in Electrochemistry. *Chem. Soc. Rev.* **39**, 3157–3180 (2010).

196. Yi, J. W., Park, J., Kim, K. S. & Kim, B. H. PH-Responsive Self-Duplex of PyA-Substituted Oligodeoxyadenylate in Graphene Oxide Solution as a Molecular Switch. *Org. Biomol. Chem.* **9**, 7434–7438 (2011).

197. Yi, J. W. *et al.* Quencher-Free Molecular Beacon: Enhancement of the Signal-to-Background Ratio

with Graphene Oxide. *Bioorganic Med. Chem. Lett.* **21**, 704–706 (2011).

198. Min, S. K., Kim, W. Y., Cho, Y. & Kim, K. S. Fast DNA Sequencing with a Graphene-Based Nanochannel Device. *Nat. Nanotechnol.* **6**, 162–165 (2011).

199. Goenka, S., Sant, V. & Sant, S. Graphene-Based Nanomaterials for Drug Delivery and Tissue Engineering. *J. Control. Release* **173**, 75–88 (2014).

200. Hu, H., Xin, J. H., Hu, H., Wang, X. & Kong, Y. Metal-Free Graphene-Based Catalyst-Insight into the Catalytic Activity: A Short Review. *Appl. Catal. A Gen.* **492**, 1–9 (2015).

201. Lee, C., Wei, X., Kysar, J. W. & Hone, J. Measurement of the Elastic Properties and Intrinsic Strength of Monolayer Graphene. *Source Sci. New Ser.* **321**, 385–388 (2008).

202. Zhao, J., Wei, N., Fan, Z., Jiang, J. W. & Rabczuk, T. The Mechanical Properties of Three Types of Carbon Allotropes. *Nanotechnology* **24**, (2013).

203. Bolotin, K. I. *et al.* Ultrahigh Electron Mobility in Suspended Graphene. *Solid State Commun.* **146**, 351–355 (2008).

204. Gómez-Navarro, C. *et al.* Electronic Transport Properties of Individual Chemically Reduced Graphene Oxide Sheets. *Nano Lett.* **7**, 3499–3503 (2007).

205. Zhang, P. *et al.* Fracture Toughness of Graphene. *Nat. Commun.* **5**, 3782 (2014).

206. Gao, Y. *et al.* The Effect of Interlayer Adhesion on the Mechanical Behaviors of Macroscopic Graphene Oxide Papers. *ACS Nano* **5**, 2134–2141 (2011).

207. Sepioni, M. *et al.* Limits on Intrinsic Magnetism in Graphene. *Phys. Rev. Lett.* **105**, (2010).

208. Sarkar, S. K., Raul, K. K., Pradhan, S. S., Basu, S. & Nayak, A. Magnetic Properties of Graphite Oxide and Reduced Graphene Oxide. *Phys. E Low-Dimensional Syst. Nanostructures* **64**, 78–82 (2014).

209. Los, J. H., Zakharchenko, K. V., Katsnelson, M. I. & Fasolino, A. Melting Temperature of Graphene. *Phys. Rev. B* **91**, 045415 (2015).

210. Zhu, Y. *et al.* Graphene and Graphene Oxide: Synthesis, Properties, and Applications. *Adv. Mater.* **22**, 3906–3924 (2010).

211. Becerril, H. A. *et al.* Evaluation of Solution-Processed Reduced Graphene Oxide Films as Transparent Conductors. *ACS Nano* **2**, 463–470 (2008).

212. Kang, S.-H., Fang, T.-H. & Hong, Z.-H. Electrical and Mechanical Properties of Graphene Oxide on Flexible Substrate. *J. Phys. Chem. Solids* **74**, 1783–1793 (2013).

213. Konios, D., Stylianakis, M. M., Stratakis, E. & Kymakis, E. Dispersion Behaviour of Graphene Oxide and Reduced Graphene Oxide. *J. Colloid Interface Sci.* **430**, 108–112 (2014).

214. Balandin, A. A. *et al.* Superior Thermal Conductivity of Single-Layer Graphene. *Nano Lett.* **8**, 902–907 (2008).

215. Boehm, V. H. P., Fischer, C. G. O. & Hofmann, U. Das Adsorptionsverhalten sehr dünner Kohlenstoff-Folien. 119–127 (1962).

216. Wei, Z. *et al.* Nanoscale Tunable Reduction of Graphene Oxide for Graphene Electronics. *Source Sci. New Ser.* **328**, 1373–1376 (2010).

217. Chen, W. & Yan, L. Preparation of Graphene by a Low-Temperature Thermal Reduction at Atmosphere Pressure. *Nanoscale* **2**, 559–563 (2010).

218. Dreyer, D. R., Ruoff, R. S. & Bielawski, C. W. From Conception to Realization: An Historial Account of Graphene and some Perspectives for its Future. *Angew. Chemie - Int. Ed.* **49**, 9336–9344 (2010).

219. Dreyer, D. R., Park, S., Bielawski, W. & Ruoff, R. S. The Chemistry of Graphene Oxide. *R. Soc. Chem.* **39**, 228–240 (2010).

220. Hernandez, Y. *et al.* High-Yield Production of Graphene by Liquid-Phase Exfoliation of Graphite.

Nat. Nanotechnol. **3**, 563–568 (2008).

221. Wu, J., Pisula, W. & Müllen, K. Graphenes as Potential Material for Electronics. *Chem. Rev.* **107**, 718–747 (2007).

222. Park, S. & Ruoff, R. S. Chemical Methods for the Production of Graphenes. *Nat. Nanotechnol.* **4**, 217–224 (2009).

223. Bai, H., Li, C. & Shi, G. Functional Composite Materials Based on Chemically Converted Graphene. *Adv. Mater.* **23**, 1089–1115 (2011).

224. Brodie, B. C. XIII. On the Atomic Weight of Graphite. *Philos. Trans. R. Soc. London* **149**, 249–259 (1859).

225. Compton, O. C. & Nguyen, S. T. Graphene Oxide, Highly Reduced Graphene Oxide, and Graphene: Versatile Building Blocks for Carbon-Based Materials. *Small* **6**, 711–723 (2010).

226. Hummers, W. S. & Offeman, R. E. Preparation of Graphitic Oxide. *J. Am. Chem. Soc.* **80**, 1339–1339 (1958).

227. Li, D., Müller, M. B., Gilje, S., Kaner, R. B. & Wallace, G. G. Processable Aqueous Dispersions of Graphene Nanosheets. *Nat. Nanotechnol.* **3**, 101–105 (2008).

228. Zhang, L. *et al.* Size-Controlled Synthesis of Graphene Oxide Sheets on a Large Scale Using Chemical Exfoliation. *Carbon N. Y.* **47**, 3365–3368 (2009).

229. Pan, S. & Aksay, I. A. Factors Controlling the size of Graphene Oxide Sheets Produced via the Graphite Oxide Route. *ACS Nano* **5**, 4073–4083 (2011).

230. Wu, Z. S. *et al.* Synthesis of High-Quality Graphene with a Pre-Determined Number of Layers. *Carbon N. Y.* **47**, 493–499 (2009).

231. Chen, D., Feng, H. & Li, J. Graphene Oxide: Preparation, Functionalization, and Electrochemical Applications. *Chem. Rev.* **112**, 6027–6053 (2012).

232. Gao, H. & Duan, H. 2D and 3D Graphene Materials: Preparation and Bioelectrochemical Applications. *Biosens. Bioelectron.* **65**, 404–419 (2015).

233. Gao, X., Jang, J. & Nagase, S. Hydrazine and Thermal Reduction of Graphene Oxide: Reaction Mechanisms, Product Structures, and Reaction Design. *J. Phys. Chem. C* **114**, 832–842 (2010).

234. Xu, Y., Wu, Q., Sun, Y., Bai, H. & Shi, G. Three-Dimensional Self-Assembly of Graphene Oxide and DNA Into Multifunctional Hydrogels. *ACS Nano* **4**, 7358–7362 (2010).

235. Burrs, S. L. *et al.* A Comparative Study of Graphene-Hydrogel Hybrid Bionanocomposites for Biosensing. *Analyst* **140**, 1466–1476 (2015).

236. Ronkainen, N. J., Halsall, H. B. & Heineman, W. R. Electrochemical Biosensors. *Chem. Soc. Rev.* **39**, 1747–1763 (2010).

237. Logan, B. E. Exoelectrogenic Bacteria that Power Microbial Fuel Cells. *Nat. Rev. Microbiol.* **7**, 375–381 (2009).

238. Chae, H. Z., Chung, S. J. & Rhee, S. G. Thioredoxin-Dependent Peroxide Reductase from Yeast. *J. Biol. Chem.* **269**, 27670–27678 (1994).

239. Hall, A., Karplus, P. A. & Poole, L. B. Typical 2-Cys Peroxiredoxins - Structures, Mechanisms and Functions. *FEBS J.* **276**, 2469–2477 (2009).

240. Wood, Z. A., Schröder, E., Robin Harris, J. & Poole, L. B. Structure, Mechanism and Regulation of Peroxiredoxins. *Trends Biochem. Sci.* **28**, 32–40 (2003).

241. Peshenko, I. V. & Shichi, H. Oxidation of Active Center Cysteine of Bovine 1-Cys Peroxiredoxin to the Cysteine Sulfenic Acid form by Peroxide and Peroxynitrite. *Free Radic. Biol. Med.* **31**, 292–303 (2001).

242. Jang, H. H. *et al.* Two Enzymes in One; Two Yeast Peroxiredoxins Display Oxidative Stress-Dependent Switching from a Peroxidase to a Molecular Chaperone Function. *Cell* **117**, 625–635

(2004).

243. Saccoccia, F. *et al.* Moonlighting by Different Stressors: Crystal Structure of the Chaperone Species of a 2-Cys Peroxiredoxin. *Structure* **20**, 429–439 (2012).

244. Vitha, M. F. *Chromatography: Principles and Instrumentation*. *Chromatographia* vol. 185 (Hoboken, New Jersey : John Wiley & Sons, Inc., 2016).

245. Thanu, D. P. R., Zhao, M., Han, Z. & Keswani, M. Fundamentals and Applications of Sonic Technology. in *Developments in Surface Contamination and Cleaning: Applications of Cleaning Techniques* 1–48 (Elsevier, 2019). doi:10.1016/B978-0-12-815577-6.00001-3.

246. Hoenig, S. A. Cleaning Surfaces With Dry Ice. *Compress. Air Mag.* 22–25 (1986).

247. Sherman, R., Hirt, D. & Vane, R. Surface Cleaning with the Carbon Dioxide Snow Jet. *J. Vac. Sci. Technol. A Vacuum, Surfaces, Film.* **12**, 1876–1881 (1994).

248. Sherman, R. Carbon Dioxide Snow Cleaning. *Part. Sci. Technol.* **25**, 37–57 (2007).

249. Habib, S. B., Gonzalez, E. & Hicks, R. F. Atmospheric Oxygen Plasma Activation of Silicon (100) Surfaces. *J. Vac. Sci. Technol. A Vacuum, Surfaces, Film.* **28**, 476–485 (2010).

250. Stevens, J. *Sputter Coating Technical Brief*. http:///www.quorumtech.com (2002).

251. Kohl, P. A. Modern Electroplating, 5h Edition. in 115–130 (2010).

252. Eliaz, N. & Gileadi, E. *Physical Electrochemistry: Fundamentals, Techniques, and Applications*. (Wiley-VCH, 2019).

253. Metrohm. *Basic Overview of the Working Principle of a Potentiostat/Galvanostat (PGSTAT)-Electrochemical Cell Setup*. (2011).

254. Metrohm. *NOVA User Manual*. www.metrohm-autolab.com (2016).

255. Elgrishi, N. *et al.* A Practical Beginner's Guide to Cyclic Voltammetry. *J. Chem. Educ.* **95**, 197–206 (2018).

256. Skoog, D. A., Holler, F. J. & Crouch, S. R. Principles of Instrumental Analysis. *Anal. Chim. Acta* **152**, 314 (2006).

257. Mäntele, W. & Deniz, E. UV–VIS Absorption Spectroscopy: Lambert-Beer Reloaded. *Spectrochim. Acta Part A Mol. Biomol. Spectrosc.* **173**, 965–968 (2017).

258. Lambert. *Photometerie - Photometria Sive De Mensura et Gradibus Luminis, Colorum et Umbrae*. *Monatshefte für Mathematik* (Leipzig, Verlag von Wilhelm Engelmann, 1892). doi:10.1007/BF01692369.

259. Griffiths, P. R. & de Haseth:, J. A. Fourier Transform Infrared Spectrometry. *Anal. Bioanal. Chem.* **391**, 2379–2380 (2008).

260. Larkin, P. *Infrared and Raman Spectroscopy - Principles and Spectral Interpretation*. *Elsevier* (Elsevier, 2011).

261. Temple, P. A. & Hathaway, C. E. Multiphonon Raman Spectrum of Silicon. *Phys. Rev. B* **7**, 3685–3697 (1973).

262. Borowicz, P. *et al.* Deep-Ultraviolet Raman Investigation of Silicon Oxide: Thin Film on Silicon Substrate Versus Bulk Material. *Adv. Nat. Sci. Nanosci. Nanotechnol.* **3**, 1–7 (2012).

263. Kallay, N., Kovačević, D. & Salac, S. Chapter 6 Thermodynamics of the solid/liquid interface - its application to adsorption and colloid stability. in *Interface Science and Technology* vol. 11 133–170 (2006).

264. Malvern. *Zetasizer Nano User Manual (Man0317-5.0)*. (2009).

265. Sperazza, M., Moore, J. N. & Hendrix, M. S. High-Resolution Particle Size Analysis of Naturally Occurring Very Fine-Grained Sediment Through Laser Diffractometry. *J. Sediment. Res.* **74**, 736–743 (2007).

266. McCave, I. N., Bryant, R. J., Cook, H. F. & Coughanowr, C. A. Evaluation of a Laser-Diffraction-Size Analyzer for use with Natural Sediments. *J. Sediment. Res.* **56**, 561–564 (1986).

267. de Boer, G. B. J., de Weerd, C., Thoenes, D. & Goossens, H. W. J. Laser Diffraction Spectrometry: Fraunhofer Diffraction Versus Mie Scattering. *Part. Part. Syst. Charact.* **4**, 14–19 (1987).

268. Singer, J. K. & J. B. Anderson, M. An Assessment of Analytical Techniques For The Size Analysis of Fine-Grained Sediments. *SEPM J. Sediment. Res.* (1988) doi:10.1306/212f8de6-2b24-11d7-8648000102c1865d.

269. Loizeau, J.-L., Arboutlle, D., Santiago, S. & Vernet, J.-P. Evaluation of a Wide Range Laser Diffraction Grain Size Analyser for Use With Sediments. *Sedimentology* **41**, 353–361 (1994).

270. Wriedt, T. Mie Theory: A Review. in *Springer Series in Optical Sciences* 53–71 (2012). doi:10.1007/978-3-642-28738-1_2.

271. Malvern. *Mastersizer 2000 User Manual*. https://www.malvernpanalytical.com (2007).

272. Marshall, J. L. Scanning Electron Microscopy and Energy Dispersive X-ray (SEM/EDX) Characterization of Solder Solderability and Reliability. in *Solder Joint Reliability* 173–224 (Springer US, 1991). doi:10.1007/978-1-4615-3910-0_6.

273. Johnson, D., Hilal, N. & Bowen, W. R. Basic Principles of Atomic Force Microscopy. in *Atomic Force Microscopy in Process Engineering* 1–30 (2009).

274. Binnig, G. & Quate, C. F. Atomic Force Microscope. *Phys. Rev. Lett.* (1986).

275. Mewis, J. & Wagner, N. J. *Colloidal Suspension Rheology*. (Cambridge University Press, 2011). doi:10.1017/CBO9780511977978.

276. Lowell, S., Shields, J. E., Thomas, M. A. & Thommes, M. Surface Area Analysis from the Langmuir and BET Theories. in 58–81 (Springer, Dordrecht, 2004). doi:10.1007/978-1-4020-2303-3_5.

277. Mitchell, G. H. *Gel Electrophoresis: Types, Applications & Research*. *Nova Science Publishers Inc* (2017).

278. Zimmermann, K., Hagedorn, H., Heuck, C. C., Hinrichsen, M. & Ludwig, H. The Ionic Properties of the Filamentous Bacteriophages Pf1 and fd. *J. Biol. Chem.* **261**, 1653–1655 (1986).

279. Lee, Y. M. *et al.* Nanomesh-Structured Ultrathin Membranes Harnessing the Unidirectional Alignment of Viruses on a Graphene-Oxide Film. *Adv. Mater.* **26**, 3899–3904 (2014).

280. Morag, O., Sgourakis, N. G., Baker, D. & Goldbourt, A. The NMR–Rosetta Capsid Model of M13 Bacteriophage Reveals a Quadrupled Hydrophobic Packing Epitope. *Proc. Natl. Acad. Sci.* **112**, 971–976 (2015).

281. Ji, X., Oh, J., Dunker, A. K. & Hipps, K. W. Effects of Relative Humidity and Applied Force on Atomic Force Microscopy Images of the Filamentous Phage fd. *Ultramicroscopy* **72**, 165–176 (1998).

282. Aubrey, K. L. & Thomas, G. J. Raman Spectroscopy of Filamentous Bacteriophage Ff (fd, M13, f1) Incorporating Specifically-Deuterated Alanine and Tryptophan Side Chains. Assignments and Structural Interpretation. *Biophys. J.* **60**, 1337–1349 (1991).

283. Simpson, R. J. Stabilization of Proteins for Storage. *Cold Spring Harb. Protoc.* (2010) doi:10.1101/pdb.top79.

284. Porterfield, J. Z. & Zlotnick, A. A Simple and General Method for Determining the Protein and Nucleic Acid Content of Viruses by UV Absorbance. *Virology* **407**, 281–288 (2010).

285. Ito, A. & Ito, T. Absorption Spectra of Deoxyribose, Ribosephosphate, ATP and DNA by Direct Transmission Measurements in the Vacuum-UV (150—190 nm) and Far-UV (190—260 nm) Regions Using Synchrotron Radiation as a Light Source. *Photochem. Photobiol.* **44**, 355–358 (1986).

286. Goldfarb, A. R., Saidel, L. J. & Mosovich, E. The Ultraviolet Absorption Spectra of Proteins. *J.*

Biol. Chem. **193**, 397–404 (1951).

287. Aitken, A. & Learmonth, M. Protein Determination by UV Absorption. in *The Protein Protocols Handbook* (ed. Walker, J. M.) 3–6 (2009). doi:10.1007/978-1-60327-259-9.

288. Fornander, L. H., Feng, B., Beke-Somfai, T. & Nordén, B. UV Transition Moments of Tyrosine. *J. Phys. Chem. B* **118**, 9247–9257 (2014).

289. Antosiewicz, J. M. & Shugar, D. UV–Vis Spectroscopy of Tyrosine Side-Groups in Studies of Protein Structure. Part 2: Selected Applications. *Biophys. Rev.* **8**, 163–177 (2016).

290. Day, L. A. & Wiseman, R. L. A Comparison of DNA Packaging in the Virions of fd , Xf , and Pf1. *Cold Spring Harb. Monogr. Arch.* **8**, 605–625 (1978).

291. Simonian, M. H. & Smith, J. A. *Spectrophotometric and Colorimetric Determination of Protein Concentration*. *Current Protocols in Molecular Biology* (2006). doi:10.1002/0471142727.mb1001as76.

292. Lide, D. R. CRC Handbook of Chemistry and Physics 90th Edition. *J. Am. Chem. Soc.* **131**, 12862–12862 (2010).

293. Popović, D. M. Modeling of Conformation and Redox Potentials of Hemes and other Cofactors in Proteins. (2002).

294. Aronson, J. N. The Henderson-Hasselbalch Equation Revisited - Biochemical Education. *Biochem. Mol. Biol. Educ.* **11**, 68 (1983).

295. Li, H., Robertson, A. D. & Jensen, J. H. Very Fast Empirical Prediction and Rationalization of Protein pKa Values. *Proteins Struct. Funct. Bioinforma.* **61**, 704–721 (2005).

296. Bas, D. C., Rogers, D. M. & Jensen, J. H. Very Fast Prediction and Rationalization of pKa Values for Protein-Ligand Complexes. *Proteins Struct. Funct. Bioinforma.* **73**, 765–783 (2008).

297. Olsson, M. H. M., Søndergaard, C. R., Rostkowski, M. & Jensen, J. H. PROPKA3 Consistent Treatment of Internal and Surface Residues in Empirical pKa Predictions. *J. Chem. Theory Comput.* **7**, 525–537 (2011).

298. Dong, D., Zhang, Y., Sutaria, S., Konarov, A. & Chen, P. Binding Mechanism and Electrochemical Properties of M13 Phage-Sulfur Composite. *PLoS One* **8**, 1–10 (2013).

299. Saravanan, L. & Subramanian, S. Surface Chemical Studies on the Competitive Adsorption of Poly(ethylene glycol) and Ammonium Poly(methacrylate) onto Alumina. *J. Colloid Interface Sci.* **284**, 363–377 (2005).

300. Tunç, S. & Duman, O. The Effect of Different Molecular Weight of Poly(Ethylene Glycol) on the Electrokinetic and Rheological Properties of Na-Bentonite Suspensions. *Colloids Surfaces A Physicochem. Eng. Asp.* **317**, 93–99 (2008).

301. Shameli, K. *et al.* Synthesis and Characterization of Polyethylene Glycol Mediated Silver Nanoparticles by the Green Method. *Int. J. Mol. Sci.* **13**, 6639–6650 (2012).

302. Katarzyna, S.-K. *et al.* Modified Filamentous Bacteriophage as a Scaffold for Carbon Nanofiber. *Bioconjug. Chem.* **27**, 2900–2910 (2016).

303. Miyazawa, T., Fukushima, K. & Ideguchi, Y. Molecular Vibrations and Structure of High Polymers. III. Polarized Infrared Spectra, Normal Vibrations, and Helical Conformation of Polyethylene Glycol. *J. Chem. Phys.* **37**, 2764–2776 (1962).

304. Colthup, N. B., Daly, L. H. & Wiberley, S. E. *Introduction to Infrared and Raman Spectroscopy*. (Academic Press, 1990). doi:10.1016/C2009-0-21628-X.

305. Kozielski, M. Conformational Changes in the Chains of Polyoxyethyleneglycols. *J. Mol. Liq.* **128**, 105–107 (2006).

306. Bozzini, B., D'Urzo, L., Mele, C. & Romanello, V. Electrodeposition of Cu From Acidic Sulphate Solutions in the Presence of Polyethylene Glycol and Chloride Ions. *J. Mater. Sci. Mater. Electron.* **17**, 915–923 (2006).

307. Yamini, D., Devanand Venkatasubbu, G., Kumar, J. & Ramakrishnan, V. Raman Scattering Studies on PEG Functionalized Hydroxyapatite Nanoparticles. *Spectrochim. Acta - Part A Mol. Biomol. Spectrosc.* **117**, 299–303 (2014).

308. Lai, Q., Zhu, S., Luo, X., Zou, M. & Huang, S. Ultraviolet-Visible Spectroscopy of Graphene Oxides. *AIP Adv.* **2**, 3–8 (2012).

309. Ou, J. *et al.* Tribology Study of Reduced Graphene Oxide Sheets on Silicon Substrate Synthesized via Covalent Assembly. *Langmuir* **26**, 15830–15836 (2010).

310. Zhang, J. *et al.* Graphene Oxide as a Matrix for Enzyme Immobilization. *Langmuir* **26**, 6083–6085 (2010).

311. Zhang, F. *et al.* Horseradish Peroxidase Immobilized on Graphene Oxide: Physical Properties and Applications in Phenolic Compound Removal. *J. Phys. Chem. C* **114**, 8469–8473 (2010).

312. Ye, S. & Feng, J. The Effect of Sonication Treatment of Graphene Oxide on the Mechanical Properties of the Assembled Films. *RSC Adv.* **6**, 39681–39687 (2016).

313. Konkena, B. & Vasudevan, S. Understanding Aqueous Dispersibility of Graphene Oxide and Reduced Graphene Oxide Through pKa Measurements. *J. Phys. Chem. Lett.* **3**, 867–872 (2012).

314. Wang, X., Chen, Y. P. & Nolte, D. D. Strong Anomalous Optical Dispersion of Graphene: Complex Refractive Index Measured by Picometrology. *Opt. Express* **16**, 1–14 (2008).

315. Zhang, H., Hines, D. & Akins, D. L. Synthesis of a Nanocomposite Composed of Reduced Graphene Oxide and Gold Nanoparticles. *Dalt. Trans.* **43**, 2670–2675 (2014).

316. Ghadim, E. E. *et al.* Adsorption Properties of Tetracycline onto Graphene Oxide: Equilibrium, Kinetic and Thermodynamic Studies. *PLoS One* **8**, 1–9 (2013).

317. Liu, C. *et al.* Low Temperature Reduction of Free-Standing Graphene Oxide Papers with Metal Iodides for Ultrahigh Bulk Conductivity. *Sci. Rep.* **4**, 1–6 (2014).

318. Naebe, M. *et al.* Mechanical Property and Structure of Covalent Functionalised Graphene/Epoxy Nanocomposites. *Sci. Rep.* **4**, 1–7 (2014).

319. Johra, F. T. & Jung, W. G. Hydrothermally Reduced Graphene Oxide as a Supercapacitor. *Appl. Surf. Sci.* **357**, 1911–1914 (2015).

320. Huang, X. *et al.* Graphene-Based Materials: Synthesis, Characterization, Properties, and Applications. *Small* **7**, 1876–1902 (2011).

321. Bae, S. *et al.* Roll-to-Roll Production of 30-Inch Graphene Films for Transparent Electrodes. *Nat. Nanotechnol.* **5**, 574–578 (2010).

322. Kim, K. S. *et al.* Large-Scale Pattern Growth of Graphene Films for Stretchable Transparent Electrodes. *Nature* **457**, 706–710 (2009).

323. Eda, G., Fanchini, G. & Chhowalla, M. Large-Area Ultrathin Films of Reduced Graphene Oxide as a Transparent and Flexible Electronic Material. *Nat. Nanotechnol.* **3**, 270–274 (2008).

324. Bourlinos, A. B., Georgakilas, V., Zboril, R., Steriotis, T. A. & Stubos, A. K. Liquid-Phase Exfoliation of Graphite Towards Solubilized Graphenes. *Small* **5**, 1841–1845 (2009).

325. Khan, U., O'Neill, A., Lotya, M., De, S. & Coleman, J. N. High-Concentration Solvent Exfoliation of Graphene. *Small* **6**, 864–871 (2010).

326. Khan, U. *et al.* Liquid-Phase Exfoliation of Graphite Towards Solubilized Graphenes. *Langmuir* **27**, 9077–9082 (2011).

327. Marcano, D. C. *et al.* Improved Synthesis of Graphene Oxide. *ACS Nano* **4**, 4806–4814 (2010).

328. Zhang, H.-B. *et al.* Vacuum-Assisted Synthesis of Graphene from Thermal Exfoliation and Reduction of Graphite Oxide. *J. Mater. Chem.* **21**, 5392 (2011).

329. Fan, Z.-J. *et al.* Facile Synthesis of Graphene Nanosheets via Fe Reduction of Exfoliated Graphite Oxide. *ACS Nano* **5**, 191–198 (2011).

330. Chen, C., Long, M., Xia, M., Zhang, C. & Cai, W. Reduction of Graphene Oxide by an in-Situ Photoelectrochemical Method in a dye-Sensitized Solar Cell Assembly. *Nanoscale Res. Lett.* **7**, 101 (2012).

331. He, H., Klinowski, J., Forster, M. & Lerf, A. A New Structural Model for Graphite Oxide. *Chem. Phys. Lett.* **287**, 53–56 (1998).

332. Lerf, A., He, H., Forster, M. & Klinowski, J. Structure of Graphite Oxide Revisited. *J. Phys. Chem. B* **102**, 4477–4482 (1998).

333. Sahu, A., Choi, W. Il & Tae, G. A Stimuli-Sensitive Injectable Graphene Oxide Composite Hydrogel. *Chem. Commun.* **48**, 5820 (2012).

334. Cong, H.-P., Wang, P. & Yu, S.-H. Stretchable and Self-Healing Graphene Oxide–Polymer Composite Hydrogels: a Dual-Network Design. *Chem. Mater.* **25**, 3357–3362 (2013).

335. Zhang, Y., Wu, C., Guo, S. & Zhang, J. Interactions of Graphene and Graphene Oxide with Proteins and Peptides. *Nanotechnol. Rev.* **2**, 27–45 (2013).

336. Henry, T. J. & Pratt, D. The Proteins of Bacteriophage M13. *Proc. Natl. Acad. Sci.* **62**, 800–807 (1969).

337. Roth, T. A., Weiss, G. A., Eigenbrot, C. & Sidhu, S. S. A Minimized M13 Coat Protein Defines the Requirements for Assembly Into the Bacteriophage Particle. *J. Mol. Biol.* **322**, 357–367 (2002).

338. Micromeritics. *AccuPyc II 1340 Pycnometer Service Manual*. (2009).

339. du Plessis, A., Broeckhoven, C., Guelpa, A. & le Roux, S. G. Laboratory X-ray Micro-computed Tomography: A User Guideline for Biological Samples. *Gigascience* **6**, (2017).

340. Sun, H., Xu, Z. & Gao, C. Multifunctional, Ultra-flyweight, Synergistically Assembled Carbon Aerogels. *Adv. Mater.* **25**, 2554–2560 (2013).

341. Xu, Z., Sun, H., Zhao, X. & Gao, C. Ultrastrong Fibers Assembled from Giant Graphene Oxide Sheets. *Adv. Mater.* **25**, 188–193 (2013).

342. Ye, S., Feng, J. & Wu, P. Highly Elastic Graphene Oxide-epoxy Composite Aerogels via Simple Freeze-drying and Subsequent Routine Curing. *J. Mater. Chem. A* **1**, 3495–3502 (2013).

343. Zhao, Y. *et al.* Highly Compression-tolerant Supercapacitor Based on Polypyrrole-mediated Graphene Foam Electrodes. *Adv. Mater.* **25**, 591–595 (2013).

344. El-Kady, M. F., Strong, V., Dubin, S. & Kaner, R. B. Laser Scribing of High-performance and Flexible Graphene-based Electrochemical Capacitors. *Science (80-.).* **335**, 1326–1330 (2012).

345. Zhang, X. *et al.* Mechanically Strong and Highly Conductive Graphene Aerogel and its use as Electrodes for Electrochemical Power Sources. *J. Mater. Chem.* **21**, 6494–6497 (2011).

346. Luan, V. H. *et al.* Synthesis of a Highly Conductive and Large Surface Area Graphene Oxide Hydrogel and its use in a Supercapacitor. *J. Mater. Chem. A* **1**, 208–211 (2013).

347. Worsley, M. A. *et al.* High Surface Area, sp2-cross-linked Three-dimensional Graphene Monoliths. *J. Phys. Chem. Lett.* **2**, 921–925 (2011).

348. Zhao, J., Ren, W. & Cheng, H. M. Graphene Sponge for Efficient and Repeatable Adsorption and Desorption of Water Contaminations. *J. Mater. Chem.* **22**, 20197–20202 (2012).

349. Tuinstra, F. & Koenig, J. L. Raman Spectrum of Graphite. *J. Chem. Phys.* **53**, 1126–1130 (1970).

350. Parobek, D. & Liu, H. Wettability of Graphene. *2D Mater.* **2**, 032001 (2015).

351. Green, T. A. & Roy, S. Speciation Analysis of Au(I) Electroplating Baths Containing Sulfite and Thiosulfate. *J. Electrochem. Soc.* **153**, C157 (2006).

352. Baltrūnas, G. *et al.* Electrochemical Gold Deposition from Sulfite Solution: Application for Subsequent Polyaniline Layer Formation. *J. Appl. Electrochem.* **38**, 1519–1526 (2008).

353. Iijima, S. Helical Microtubules of Graphitic Carbon. *Nature* **354**, 56–58 (1991).

354. Meo, M. & Rossi, M. Prediction of Young's Modulus of Single Wall Carbon Nanotubes by Molecular-mechanics Based Finite Element Modelling. *Compos. Sci. Technol.* (2006) doi:10.1016/j.compscitech.2005.11.015.

355. Tans, S. J. *et al.* Individual Single-wall Carbon Nanotubes as Quantum Wires. *Nature* (1997) doi:10.1038/386474a0.

356. Hayashi, Y., Shinawaki, A., Nishino, S., Tanaka, Y. & Morita, M. Gas Phase Syntheses of Single-Walled Carbon Nanotubes by Chemical Vapor Deposition Using Hot filament and Plasma. *Jpn. J. Appl. Phys.* **43**, L1237–L1240 (2004).

357. Bhaviripudi, S. *et al.* CVD Synthesis of Single-Walled Carbon Nanotubes from Gold Nanoparticle Catalysts. *J. Am. Chem. Soc.* **129**, 1516–1517 (2007).

358. Duan, W. H., Wang, Q. & Collins, F. Dispersion of Carbon Nanotubes with SDS Surfactants: A Study from a Binding Energy Perspective. *Chem. Sci.* **2**, 1407 (2011).

359. Moon, J.-S., Choi, J., Hwang, Y.-H. & Oh, J.-W. Liquid Sensing of a M-13 Bacteriophage-Based Colorimetric Sensor. *Macromol. Res.* **26**, 775–779 (2018).

360. Manivannan, S., Seo, Y., Kang, D. K. & Kim, K. Colorimetric and Optical Hg(ii) Ion Sensor Developed With Conjugates of M13-Bacteriophage and Silver Nanoparticles. *New J. Chem.* **42**, 20007–20014 (2018).

361. Wang, Z., Cheng, F., Winsor, T. & Liu, Y. Optical Chiral Metamaterials: A Review of the Fundamentals, Fabrication Methods and Applications. *Nanotechnology* **27**, 412001 (2016).

362. Gwo, S., Chen, H.-Y., Lin, M.-H., Sun, L. & Li, X. Nanomanipulation and Controlled Self-Assembly of Metal Nanoparticles and Nanocrystals for Plasmonics. *Chem. Soc. Rev.* **45**, 5672–5716 (2016).

363. Jutz, G. & Böker, A. Bionanoparticles as Functional Macromolecular Building Blocks - A New Class of Nanomaterials. *Polymer (Guildf).* **52**, 211–232 (2011).

364. Krajina, B. A., Proctor, A. C., Schoen, A. P., Spakowitz, A. J. & Heilshorn, S. C. Biotemplated Synthesis of Inorganic Materials: An Emerging Paradigm for Nanomaterial Synthesis Inspired by Nature. *Prog. Mater. Sci.* **91**, 1–23 (2018).

365. Aumiller, W. M., Uchida, M. & Douglas, T. Protein Cage Assembly Across Multiple Length Scales. *Chem. Soc. Rev.* **47**, 3433–3469 (2018).

366. Matsuura, K. Synthetic Approaches to Construct viral Capsid-Like Spherical Nanomaterials. *Chem. Commun.* **54**, 8944–8959 (2018).

367. Lee, B. Y. *et al.* Virus-Based Piezoelectric Energy Generation. *Nat. Nanotechnol.* **7**, 351–356 (2012).

368. Angelucci, F. *et al.* Switching Between the Alternative Structures and Functions of a 2-Cys Peroxiredoxin, by Site-Directed Mutagenesis. *J. Mol. Biol.* **425**, 4556–4568 (2013).

369. Li, X. *et al.* Generation of Destabilized Green Fluorescent Protein as a Transcription Reporter. *J. Biol. Chem.* **273**, 34970–34975 (1998).

370. Beck, E. *et al.* Nucleotide Sequence of Bacteriophage fd DNA. *Nucleic Acids Res.* **5**, 4495–4504 (1978).

371. Beck, E. & Zink, B. Nucleotide Sequence and Genome Organisation of Filamentous Bacteriophages fl and fd. *Gene* **16**, 35–58 (1981).

372. Stothard, P. The Sequence Manipulation Suite: JavaScript Programs for Analyzing and Formatting Protein and DNA Sequences. *Biotechniques* **28**, (2000).

373. Bjellqvist, B. *et al.* The Focusing Positions of Polypeptides in Immobilized pH Gradients can be Predicted from their Amino Acid Sequences. *Electrophoresis* (1993) doi:10.1002/elps.11501401163.

374. Gasteiger, E. *et al. The Proteomics Protocols Handbook - Chapter 52: Protein Identification and*

Analysis Tools on the ExPASy Server. *The Proteomics Protocols Handbook* (2005). doi:10.1385/1592598900.

375. Edelhoch, H. Spectroscopic Determination of Tryptophan and Tyrosine in Proteins. *Biochemistry* **6**, 1948–1954 (1967).

376. Gill, S. C. & von Hippel, P. H. Calculation of Protein Extinction Coefficients from Amino Acid Sequence Data. *Anal. Biochem.* **182**, 319–326 (1989).

377. Pace, C. N., Vajdos, F., Fee, L., Grimsley, G. & Gray, T. How to Measure and Predict the Molar Absorption Coefficient of a Protein. *Protein Sci.* **4**, 2411–2423 (1995).